2006

INITIAL ASSESSMENT OF THE "COMPRESSIBLE POOR MAN'S NAVIER{STOKES (CPMNS) EQUATION" FOR SUBGRID-SCALE MODELS IN LARGE-EDDY SIMULATION

Chetan Babu Velkur
University of Kentucky, vcbabu@uky.edu

ABSTRACT OF THESIS

INITIAL ASSESSMENT OF THE "COMPRESSIBLE POOR MAN'S NAVIER–STOKES (CPMNS) EQUATION" FOR SUBGRID-SCALE MODELS IN LARGE-EDDY SIMULATION

Large-eddy simulation is rapidly becoming the preferred method for calculations involving turbulent phenomena. However, filtering equations as performed in traditional LES procedures leads to significant problems. In this work we present some key components in the construction of a novel LES solver for compressible turbulent flow, designed to overcome most of the problems faced by traditional LES procedures. We describe the construction of the large-scale algorithm, which employs fairly standard numerical techniques to solve the Navier–Stokes equations. We validate the algorithm for both transonic and supersonic flow scenarios. We further explicitly show that the solver is capable of capturing boundary layer effects. We present a detailed derivation of the chaotic map termed the "compressible poor man's Navier–Stokes (CPMNS) equation" starting from the Navier–Stokes equations themselves via a Galerkin procedure, which we propose to use as the fluctuating component in the SGS model. We provide computational results to show that the chaotic map can produce a wide range of temporal behaviors when the bifurcation parameters are varied over their ranges of stable behaviors. Investigations of the overall dynamics of the CPMNS equation demonstrates that its use increases the potential realism of the corresponding SGS model.

KEYWORDS: LES, Turbulence, Compressible Flow, Discrete Dynamical Systems, Shock-tube problem

Chetan Babu Velkur
November 7, 2006

INITIAL ASSESSMENT OF THE "COMPRESSIBLE POOR MAN'S NAVIER–STOKES (CPMNS) EQUATION" FOR SUBGRID-SCALE MODELS IN LARGE-EDDY SIMULATION

By

Chetan Babu Velkur

James M. McDonough, PhD
Director of Thesis

S. Stephens, PhD
Director of Graduate Studies

November 7, 2006

RULES FOR THE USE OF THESES

Unpublished theses submitted for the Master's degree and deposited in the University of Kentucky Library are as a rule open for inspection, but are to be used only with due regard to the rights of the authors. Bibliographical references may be noted, but quotations or summaries of parts may be published only with the permission of the author, and with the usual scholarly acknowledgments.

Extensive copying or publication of the thesis in whole or in part also requires the consent of the Dean of the Graduate School of the University of Kentucky.

THESIS

Chetan Babu Velkur

The Graduate School

University of Kentucky

2006

INITIAL ASSESSMENT OF THE "COMPRESSIBLE POOR MAN'S NAVIER–STOKES (CPMNS) EQUATION" FOR SUBGRID-SCALE MODELS IN LARGE-EDDY SIMULATION

THESIS

A thesis submitted in partial fulfillment of the
requirements for the degree of Master of Science in Mechanical Engineering
in the College of Engineering at the University of Kentucky

By

Chetan Babu Velkur

Director: Dr. James M. McDonough, Professor of Mechanical Engineering and Mathematics

Lexington, Kentucky

2006

Dedicated

To my parents(s) at Chittoor and Bangalore

Acknowledgments

The satisfaction and euphoria that accompany the successful completion of any task would not be complete without the mention of people who made it possible, whose constant encouragement and guidance crowned the effort with success.

I would like to express my deepest gratitude to my academic advisor Dr. J. M. McDonough for his enthusiastic supervision throughout the course of this work. He gave me the opportunity to work on this incredibly interesting and challenging research topic. I would like to thank Dr. Raymond LeBeau for discussions on turbulence and for serving on my final examination committee. I would also like to thank my defense committee member Dr. Zhongwei Shen for his valuable time for being on my committee and evaluating my work.

I am grateful to my many student colleagues who have made my stay at RGAN 210A a memorable one. I am especially grateful to Abhishek Tiwari, Anand Palki, Chaitanya Penugonda, Narendra Beliganur, and Ying Xu for their stimulating discussions, emotional support, entertainment and caring they provided.

I am forever indebted to my friends at 823, Press Avenue and 110 Conn Terrace, Lexington for being the surrogate family during my period of stay here at Lexington and for their moral support there after. Finally, I would like to thank caffeine, for getting me through many sleepless nights and making this work possible.

Table of Contents

List of Figures

List of Tables

List of Files

Chapter 1
INTRODUCTION

Feynman said turbulence is the last unsolved problem in classical physics. Nearly a hundred years have come and gone, but turbulence still remains far from being "solved." Advances in computing power over the last 50 years (teraflops clock time and terabyte storage now available) have led to another branch of turbulence study apart from theoretical and experimental, that of computer simulations of turbulence. The computational approach to turbulence is based on the Navier–Stokes (N.–S.) equations, the governing equations for fluid flow. Well-established computational techniques such as direct numerical simulation (DNS), large-eddy simulation (LES) and Reynolds-averaged Navier–Stokes (RANS) are available at the present day. Even with such advances in computing power and numerical techniques, application of such techniques to compressible turbulent flow have been significantly fewer when compared to its incompressible counterpart. This is in part because of the coupling of the energy equation with the momentum and continuity equations in a compressible fluid flow, which increases storage and complexity especially if 3-D simulations have to be performed. LES is rapidly becoming the preferred approach for turbulent flow calculations, as witnessed by the fact that many commercial CFD code vendors are now incorporating versions of this into their software suites. However, one should recognize that filtering of equations as done in traditional LES results in two main problems: lack of commutativity of filter with differential operators and action of the filter on nonlinear terms producing correlations (statistics) which must be modeled. By trying to model statistics, we are, in fact, trying to invert the mapping between physics and statistics, which is not one-to-one; *i.e.,* many different physical flows can give rise to the same statistics. In this research effort we have developed some key components for the construction of a novel LES solver for compressible flow based on a new LES formalism which allows us to circumvent most of the problems arising from filtering the governing equations. The new LES formalism is based on filtering solutions rather than equations, while keeping the formal LES decomposition of resolved and unresolved scales. In order to account for the unresolved scales we have developed a subgrid-scale model based on deconvolution, Kolmogorov's theories and discrete dynamical systems, with which the subgrid-scale dependent variables are modeled directly (model physics not statistics).

In this chapter, a brief overview of turbulence is given. Included is a historical perspective on turbulence research over the past century. We also present the governing equations for incompressible and compressible flow, and indicate the complexities one encounters while trying to solve the full compressible N.–S. equations. A brief overview on studies of compressible turbulence is also given. We then present the objective of our research effort, which has consummated into this thesis. Following this the framework of thesis will be discussed briefly.

1.1 Introduction to Turbulence

Turbulence is a complex phenomenon that goes largely unnoticed despite frequent encounters in daily life (flow of water from a faucet for example). As a matter of fact it is

the most common state of fluid motion, and more often than not, turbulence dominates all the important physics of the flow. It is of extreme importance in real life and in most scientific and engineering disciplines: in aeronautics, ship building, oceanography, combustion, geophysics, meteorology, mixing of pollutants (environmental), astrophysics, cosmology and even the structure of the universe. The problem of turbulence is so difficult that is has even defied the formulation of a consistent and rigorous definition. Turbulence has had many colorful descriptions over the years, from Lamb's [1] scholarly "chief outstanding difficulty of our subject" to Bradshaw's [2] inspired "invention of the devil on the seventh day of creation." This apparent frustration results largely from the mixture of chaos, order, and the wide range of length and time scales that a turbulent flow possesses. In order to visualize a turbulent flow with a spectrum of scales one can think of what are known as turbulent eddies. A turbulent eddy can be thought of as a local swirling motion in a fluid flow whose characteristic dimension would be the local turbulence length scale. There can be eddies of varying sizes in a turbulent fluid flow, but the sizes of these eddies are bounded above by the characteristic length scale of the flow under consideration and below by the molecular length scale. Turbulence features a cascade of energy whereby, as turbulence decays, its kinetic energy is transferred from larger eddies to the smaller ones. Ultimately, the smallest eddies dissipate the kinetic energy into heat through the action of molecular viscosity.

Mankind has noticed turbulence in fluid flow as early as the 15th century. Leonardo Da Vinci's sketches (see *e.g.,* Richter [3]) of chaotic whirlpools—eddies as in Fig. 1.1, are believed by most to be the first attempt at describing turbulence. Such phenomena were termed "turbolenza" by da Vinci, based probably on the Latin root words, *turba*, meaning

Figure 1.1 Whirpool sketch by Leonardo Da Vinci.

disturbance or *turbo*, meaning whirl. The modern scientific study of turbulence as noted by Frisch [4] dates back to the late 1800s in the works of Saint-Venant, Boussinesq [5] and the seminal work of Osborne Reynolds [6]. Since then, it has attracted the attention of some of the best minds in fields of mathematics, physics and engineering. By now, in the 21st century all researchers accept that the Navier–Stokes (N.–S.) equations for both compressible and incompressible flows provide the exact description of turbulence, or indeed any nonrelativistic

motion of a Newtonian fluid. Even the smallest length scales occurring in a turbulent flow are large compared to the mean free path between molecular collisions in most flows; so the continuum hypothesis holds, and hence the constitutive equations are not in doubt.

To discern between a compressible and incompressible fluid we now introduce the formal definition of compressibility τ,

$$\tau = \frac{1}{\rho}\frac{\partial \rho}{\partial p}\,, \tag{1.1}$$

where ρ is density, and p is the pressure. Fluids that require very large changes in pressure to cause even minor changes in density are termed incompressible. In a mathematical sense we can say that an incompressible flow occurs when $\tau \to 0$, so that $\Delta\rho = \rho\tau\Delta p \to 0$. We note that this would imply that motion in "stratified" media such as the ocean or atmosphere, whose densities vary with depth and height, respectively, should be classified as "compressible." This, however, is incorrect; probably a better practical definition of compressible flow is high Mach number (M) flow, where Mach number is the ratio of flow speed U to the speed of sound a:

$$M = \frac{U}{a}\,. \tag{1.2}$$

This is a far better indicator of compressibility, and is satisfactory for most practical applications.

We now present the N.–S. equations for a compressible flow:

$$\frac{\partial \rho}{\partial t} + \frac{\partial \rho u_j}{\partial x_j} = 0\,, \qquad (continuity - mass\, conservation) \tag{1.3a}$$

$$\frac{\partial \rho u_i}{\partial t} + \frac{\partial \rho u_i}{\partial x_j} = -\frac{\partial p}{\partial x_j} + \frac{\partial \tau_{ij}}{\partial x_j}\,, \qquad (momentum) \tag{1.3b}$$

$$\frac{\partial \rho E}{\partial t} + \frac{\partial \rho u_j E}{\partial x_j} = -\frac{\partial p u_j}{\partial x_j} + \frac{\partial q_j}{\partial x_j} + \frac{\partial u_j \tau_{ij}}{\partial x_j}\,. \qquad (energy) \tag{1.3c}$$

In Eq. (1.3) the Einstein summation convention is used. For a Newtonian fluid, the viscous shear stress tensor is of the form

$$\tau_{ij} = \mu\left(\frac{\partial u_i}{\partial x_j} + \frac{\partial u_j}{\partial x_i}\right) + \lambda\delta_{ij}\frac{\partial u_k}{\partial x_k}\,, \tag{1.4}$$

where δ_{ij} is the Kronecker delta, and μ and λ are two coefficients which are to be determined empirically. From Newton's law of viscosity, the proportionality factor between the shear stress and the velocity gradients is the dynamic viscosity. Hence the quantity μ appearing in Eq. (1.4) is the dynamic viscosity. The coefficient λ is usually referred to as the second viscosity. We note that the difference between the thermodynamic pressure and the mechanical pressure is proportional to the divergence of the velocity vector. The proportionality factor is usually referred to as the bulk viscosity and is denoted by K, where $K = \lambda + \frac{2}{3}\mu$ (the reader is referred to the text by Currie [7] for details). If the fluid is a monoatomic gas, the mechanical pressure and thermodynamic pressure are the same; hence K is zero. This implies that $\lambda = -\frac{2}{3}\mu$, which is called the Stokes' relation. Even for polyatomic gases and for liquids the departure from $K = 0$ is frequently small, and many researchers incorporate the Stokes' relation.

The shear stress tensor can now be written as

$$\tau_{ij} = 2\mu S_{ij} \,. \tag{1.5}$$

Here, the viscous strain-rate tensor S_{ij} is defined by

$$S_{ij} = \frac{1}{2}\left(\frac{\partial u_i}{\partial x_j} + \frac{\partial u_j}{\partial x_i}\right) - \frac{1}{3}\frac{\partial u_k}{\partial x_k}\delta_{ij} \,. \tag{1.6}$$

The heat flux, q_j, is given by Fourier's Law

$$q_j = -k\frac{\partial T}{\partial x_j} \,. \tag{1.7}$$

In Eqs. (1.3–1.7) ρ, p and T are the usual density, pressure and temperature; $\boldsymbol{u} \equiv (u_1, u_2, u_3) = (u, v, w)^T$ is the velocity vector; the quantity $E \equiv (e + \boldsymbol{u}^2 \backslash 2)$, corresponds to total energy with $\boldsymbol{u}^2$ denoting $\boldsymbol{u} \cdot \boldsymbol{u}$. Finally, k is thermal conductivity.

We will also need an equation of state for the fluid to relate the various thermodynamic properties. At temperatures and pressures characteristic of many compressible flow applications, the gas particles are, on the average, widely separated. The average distance between particles is usually more than 10 molecular diameters, which corresponds to a weak attractive force. As a result, for a large number of engineering applications, the effect of intermolecular forces on the gas properties is negligible. By definition, a perfect gas is one in which intermolecular forces can be neglected. By ignoring intermolecular forces, the equation of state for a perfect gas can be derived from theoretical concepts of modern statistical mechanics or kinetic theory. However, historically it was synthesized from laboratory measurements by Robert Boyle in the 17th century, Jacques Charles in the 18th century, Joseph Gay-Lussac and John Dalton around 1800 (Anderson [8]). The empirical result which unfolded from these observations is the well-known equation of state for a perfect gas

$$p = \rho R T \,, \tag{1.8}$$

where R is the specific gas constant.

In the incompressibility (very low Mach number) limit, Eq. (1.3) can be reduced to give the governing equations for an incompressible flow:

$$\frac{\partial u_i}{\partial x_i} = 0 \,, \tag{1.9a}$$

$$\rho\frac{\partial u_i}{\partial t} + \rho\frac{\partial u_i u_j}{\partial x_j} = -\frac{\partial p}{\partial x_i} + \frac{\partial \tau_{ij}}{\partial x_j} \,, \tag{1.9b}$$

$$\rho\frac{\partial E}{\partial t} + \rho\frac{\partial u_j E}{\partial x_j} = -\frac{\partial p u_j}{\partial x_j} + \frac{\partial q_j}{\partial x_j} + \frac{\partial u_j \tau_{ij}}{\partial x_j} \,. \tag{1.9c}$$

The shear stress tensor is again given by

$$\tau_{ij} = 2\mu S_{ij} \,; \tag{1.10}$$

however, in the case of an incompressible flow, as a result of the divergence-free condition Eq. (1.9a), the strain rate tensor S_{ij} is defined as

$$S_{ij} = \frac{1}{2}\left(\frac{\partial u_i}{\partial x_j} + \frac{\partial u_j}{\partial x_i}\right) . \tag{1.11}$$

The heat flux q_j is again given by Fourier's law.

It should be noted that in the case of a cold (without any heat transfer) incompressible flow the energy equation Eq. (1.9c) is uncoupled from the momentum equations. Hence, in such a flow there is no need to solve the energy equation. Even in cases where heat transfer has to be included, Eq. (1.9c) can be reduced to a simpler equation in terms of temperature when compared with Eq. (1.3c) using the divergence-free condition. On the other hand, in the case of a compressible flow, the energy equation is coupled with the other equations via the equation of state, thus adding one more equation to the already complex system of equations. Therein lies the complexity of trying to solve or analyze the N.–S. equations for a compressible flow. This complexity is further amplified if turbulence and three dimensionality have to be taken into consideration. We further comment that from a numerical standpoint the incompressible equations are much more problematic than the compressible equations, since numerical algorithms have to satisfy the divergence-free constraint.

Given any flow configuration, a nondimensional parameter known as the Reynolds number (Re) provides a good representation of the qualitative behavior of the flow. This parameter is given by

$$Re = \frac{\rho U L}{\mu} , \tag{1.12}$$

where ρ is the fluid density; U is the characteristic flow speed; L is the characteristic length scale, and μ is the dynamic viscosity. Re defines the relative role of inertia effects (arising due to the nonlinear terms) and dissipative effects (arising from the diffusion terms) in the equations of motion. In the case of low-Re flows, the viscosity has a considerable effect on the entire flow, smoothing all existing small-scale irregularities; such flows with low-Re are termed laminar. In the case of high-Re flows, the dominant role is played by inertia effects whose action leads to transfer of energy from large-scale components of motion to small-scale components, and consequently to the formation of local irregularities. Moreover, as the value of the Re increases, flows typically progress from a steady state to a time-dependent one (usually first a periodic flow as seen in the famous Karman vortex street for flow past a cylinder at moderate Re; see Van Dyke [9]). Eventually, with further increase in Re, the flow becomes erratic (chaotic), and this state is generally associated with turbulence.

A good review on the history of turbulence research starting with the work of O. Reynolds in 1894 to the then present time in 1985 can be found in Chapman and Tobak [10]. They identify three overlapping "movements" characterized by a definite viewpoint of turbulence, and a reasonably well-defined beginning into what they term statistical, structural and deterministic movements.

Reynolds' observation of transition to turbulence in pipe flow, and his subsequent analyzes led him to decompose the velocity field into a mean and fluctuating component (a perturbation). Considering the perturbation flow too complicated or unpredictable (nondeterministic) he spatially averaged the N.–S. equations. However subsequent researchers

chose to time average the N.–S. equations—in retrospect probably not the best thing to do—which led to what we now call the Reynolds-averaged Navier–Stokes equations. This viewpoint, which is formalized in a statistical theory of random perturbations, was also bolstered by advances in kinetic theory of gases using statistical mechanics, and also by the success achieved in theoretical physics by quantum mechanics. There is an extensive body of literature on the study of turbulence within the statistical framework. Some of the major contributions have come from von Karman [11], Taylor [12], Kolmogorov [13], [14], [15], [16]—his celebrated K41 and K62 theories for incompressible turbulence, Obukhov [17], Prandtl [18]—his mixing-length model, Kraichnan [19], [20], among many others. A much more detailed summary can be found in Monin and Yaglom [21] and Pouquet [22].

The fact that a turbulent flow contains a great deal of organization was probably first articulated by Liepmann [23]. This was, in fact, preceded by observation of Tollmien-Schlicting waves in transitional flow by Schubauer and Skramstad [24]. Many experimentalists exploited this idea, both from the point of observing structures and analyzing turbulent flows, notably Townsend [25] in his book in 1956, and Lumley ([26], [27]) among numerous others. The idea of coherent structures in a turbulent flow proliferated in the 1970s with improvements made in experimental measurement techniques. This brought deeper understanding and additional structures to light (see, *e.g.,* Grass [28]). Structures in turbulent free shear flows were studied extensively by Roshko [29]. The interested reader is referred to Cantwell [30] and references therein for a good review of organized motion in a turbulent flow. Computer simulations have also aided analysis and visualization of structures over the last three decades. Examples are results of Rogallo [31] for homogeneous turbulence, and those of Moin and Kim [32] for turbulent channel flow, again among numerous others.

In the last 15 to 25 years, the techniques of dynamical systems theory have been applied to study turbulence, and literature has been inundated with talk of chaos, strange attractors, fractals, bifurcation theory and so on, but these have been criticized for not having produced practically useful results. Discussion of such techniques will be taken up in an entire subsection in Chapter II.

Over the past 100 years, by applying every tool and technique available to the problem of turbulence there has been some progress in our understanding of low-speed flows which are essentially incompressible. Efforts to study compressible turbulent flow have been significantly fewer due its greater complexity.

1.2 Compressible Turbulence

Swedish engineer Carl G. P. de Laval's single-stage steam turbine with a convergent-divergent nozzle in 1889 probably opened the door to the study of compressible flow. The possibility of supersonic (greater than the speed of sound, $M > 1$) movement through air brought about fundamental research in this area. For a good overview on the beginnings of research on compressible flow, the interested reader is referred to Busemann [33]. Although Chuck Yeager achieved supersonic flight in his small but beautiful Bell XS-1 (named *Glamorous Glennis* after his wife) in 1947, since the 1950s interest in high-speed civilian and military aircraft, ramjets, supersonic combustion ramjets (scramjets), interest in propulsion systems and most recently pulse-detonation engines has invigorated fundamental research in compressible turbulence.

In a compressible fluid, density fluctuates together with the velocity and pressure; and the turbulent field when Fourier analyzed includes longitudinal (parallel) and transverse (orthogonal) components to the wavenumber vector. The longitudinal components unlike the transverse components, propagate in all directions as sound waves. The transverse components are known as *shear turbulence*, and the longitudinal components may be called *compression turbulence*. Moreover, the structure of compression turbulence itself is sensitive to M. So long as M is small, compression turbulence takes the form of an assembly of ordinary sound waves. At M of finite magnitude of unity or larger, however, the compression sides of sound waves rapidly steepen and become shock fronts, while the expansion sides become less and less steep. The spectral representation of homogeneous, isotropic turbulence in a compressible fluid was first studied by Moyal [34]. He decomposed the velocity field in spectral space into a longitudinal component, and a transverse component to the wavenumber vector. This is, in fact, equivalent in physical space to the Helmholtz decomposition, which states that any vector field, meeting certain criteria (of decay towards infinity) can be resolved into irrotational (curl-free) and solenoidal (divergence-free) components (note that in physical space the decomposition is generally performed with respect to the flow direction). The longitudinal component in physical space is also known as the *acoustic component* or compression turbulence, and the transverse component is known as the *solenoidal component*.

Moyal showed that for small values of M the governing equations can be broken up into two distinct groups, one referring to the transverse velocity spectrum, and the other to the longitudinal spectra, which includes the longitudinal velocity components, the density and the temperature. The broad conclusion of this work was that the interaction between these two groups is exclusively due to the nonlinear terms, and such interactions are strongest at high Re. In order to explain the dynamics of weakly compressible turbulence, Carrier and Carlson [35] and Kovàsznay [36] decomposed the turbulent flow field into three modes—the vorticity mode, the entropy mode and the acoustic mode—that evolve independently of each other. For details regarding this decomposition the reader is referred to [21]. Chu and Kovàsznay [37] then analyzed the mutual interactions of these three basic modes and found that the combination of any two modes generates higher-order ones even for a weakly compressible turbulent field. For homogeneous compressible turbulence, Sarkar *et al.* [38] have performed an asymptotic analysis of the N.–S. equations that is formally valid in the limit of small turbulent Mach numbers (M_t). Their analysis shows that for moderate M_t, the compressible component of turbulence evolves on a fast time scale, and it is in near equilibrium with respect to the incompressible component. Sarkar [39] has also studied the effects of the presssure-dilatational term which appears explicitly as a compressibility term in the equation for mean temperature and turbulence kinetic energy. In recent years, the method of Eddy-Damped-Quasi-Normal-Markovian (EDQNM) models of Orszag [40] are being used to study energy transfer and triadic interactions of compressible turbulence (*e.g.,* Bataille *et al.* [41]). This has proved to give insights into the energy transfer process among different modes in compressible turbulence.

Over the years with the development of supersonic wind tunnels, a large volume of useful data has been accumulated through experiments. Good reviews on compressible shear layers can be found in Bradshaw [42] and references therein, and in Morkovin [43]; supersonic turbulent boundary layers are considered by Spina *et al.* [44] and [43]. Issues

regarding interactions of shocks and turbulent boundary layers can be found in Green [45] and Adamson and Messiter [46]. A detailed review of the effects of compressibility on turbulence may be found in Lele [47] and references therein.

Advances in computing power have led to another branch in studying turbulence, that of computer simulations of turbulence. All computational approaches are based on the Navier–Stokes equations. Numerous computational methods such as direct numerical simulation (DNS), large-eddy simulation (LES) and Reynolds-averaged Navier–Stokes (RANS), to name a few important techniques, are available at the present day, all having their own advantages and disadvantages. We will discuss in fair detail the various numerical procedures for simulating/modeling turbulence in Chapter II.

1.3 Objective

It is widely accepted that LES in some form will soon become the method of choice for industrial and environmental applications involving computations of turbulent flow. Direct numerical simulation is good for theoretical studies at low Re number; however, even for simple cold incompressible flows the required amount of arithmetic scales at least as Re^3, Piomelli [48]. Therefore calculations using DNS are not feasible for compressible flow at supersonic and hypersonic Mach numbers on current or even near-term foreseeable machines. These problems are exacerbated if 3-D simulations are required, which is generally the case for turbulence-related phenomena. RANS methods on the other hand are known to have fundamental flaws (see, *e.g.,* McDonough [49]) especially if unsteady phenomena are to be modeled; and it is only the lack of viable alternatives that has led to their widespread utilization.

LES provides a compromise between DNS and RANS by not resolving all the physical scales. As a consequence the required arithmetic is roughly proportional to Re^2 [48]; this is an acceptable level to permit solutions to a wide range of practical problems in a realistic time frame. The separation of scales in LES is peformed by the use of a low-pass filter which eliminates fluctuations at scales smaller than the mesh size h. Due to the very nature of LES the effects at the subgrid-scales (*scales smaller than the grid size* h) must be modeled. There are a number of excellent reviews on the theory and practice of SGS modeling in the traditional framework, especially for incompressible flows: Lesieur and Mètias [50], Meneveau and Katz [51] and Piomelli [52]. However, applications of LES to compressible flow have been significantly fewer owing to increased complexity introduced by the need to solve an additional energy equation (usually expressed in terms of total energy), which in the traditional framework results in extra unclosed terms that must be modeled in addition to the usual SGS stresses that must be modeled even in incompressible flows (see Martin *et al.* [53]).

It has been known since its very inception that the filtering process in LES leads to significant problems. Filtering equations, as is done in usual LES, results in two main problems. First, if the governing equations are nonlinear, the action of the filter on the nonlinear terms produces correlations (statistical, rather than physical quantities) which must be modeled. Second, if non-uniform gridding is employed, the filter will no longer commute with the differential operators; so errors arise from this source even if the equations are linear. Moreover, the traditional SGS models tend to model correlations (*statistics*)

rather than primitive variables (*physics*) at the small scale, thus removing any possibility of accounting for interactions between turbulence and other physics on the sub-grid scale. These shortcomings of traditional LES have resulted in an increasing interest in so called "synthetic-velocity" SGS models wherein the unresolved primitive variables are computed as secondary quantities directly from the resolved-scale results (see Domaradzski and Adams [54] for a review). Experiments, both numerical—Guzmàn and Amon [55], Pulliman and Vastano [56] and physical—Gollub and Benson [57], Wulf *et al.* [58] (see the subsection 'Routes to chaos: Experiments' in [59]) have provided support for the "strange-attractor" theory of turbulence. This has resulted in a dynamical systems approach to turbulence especially in the context of what are known as shell models of turbulence (see Bohr *et al.* [60] and references therein for theory and applications), and it has been our contention that since deterministic chaotic solutions to the Navier–Stokes (N.–S.) equations are known to exist (mathematically proven by Ruelle and Takens [61] in 1971), it is reasonable to use this knowledge in SGS models. McDonough *et al.* [62] introduced what could be called a new approach to LES in 1995. This is based on three key ideas: 1) filter solutions, not equations; 2) model primitive variables (physics), not correlations (statistics), and 3) do not discard subgrid-scale model results; instead use them to augment the resolved scale. However, the approach retains the usual LES decomposition of the dependent variable vector into resolved and unresolved scales,

$$\boldsymbol{Q}(\boldsymbol{x},t) = \boldsymbol{q}(\boldsymbol{x},t) + \boldsymbol{q}^*(\boldsymbol{x},t)\,, \tag{1.13}$$

where $\boldsymbol{q}(\boldsymbol{x},t)$ corresponds to the resolved (large) scale and $\boldsymbol{q}^*(\boldsymbol{x},t)$ corresponds to the unresolved (small) scale. Moreover, in this approach the large-scale dependent variables are calculated on the given grid and each component of the small-scale dependent variable vector are modeled directly. It is evident that such an approach to LES would eliminate most of the problems caused by filtering the equations of motion, and moreover it would retain the physics on the sub-grid scale. In this thesis we have developed a subgrid-scale model for compressible turbulent flow based on deconvolution, Kolmogorov's theories and discrete dynamical systems (DDS) for such an approach to LES, which accounts for the the unresolved scales $\boldsymbol{q}^*(\boldsymbol{x},t)$. We have also developed a large-scale solver to calculate $\boldsymbol{q}(\boldsymbol{x},t)$ on the given grid. An initial assessment of the subgrid-scale model has also been performed by supplying it with a large-scale data set. However, we have not investigated the effect of the small-scale field on the large-scale. This would require an implementation of the complete multi-scale approach proposed above, which has not been achieved in this work.

1.4 Framework of Thesis

In Chapter II, we present overviews on current state-of-the art numerical procedures in turbulence. Included are discussions on DNS, RANS, LES, detached-eddy simulation (DES) and implicit large-eddy simulation (ILES). Following this, applications of nonlinear dynamical systems theory to turbulence simulations will be discussed briefly. We will also discuss the new generation of SGS models known as synthetic-velocity models.

Once a solid framework for the study is laid, we proceed with specific discussions on the solution procedures developed in this research for unsteady, three-dimensional compressible Navier–Stokes turbulence. We begin, in Chapter III, with a detailed solution procedure for

the large-scale part of the calculations in 3-D. Included is the predictor-corrector methodology employed to solve the compressible N.–S. equations, the linearization procedure adopted to linearize the equations of motion, and the δ-form Douglas–Gunn time splitting algorithm [63] employed to dimensionally split the N.–S. equations and subsequently solve them efficiently. We end Chapter III by validating our 3-D solver with standard test problems, the 1-D shock-tube problem described by Sod in [64] and the 3-D blast-wave problem [65].

In Chapter IV, we describe the construction of the novel subgrid-scale (SGS) model developed in this work. We begin with a detailed derivation of a discrete dynamical system termed the "compressible 'poor man's Navier–Stokes (CPMNS) equation" from the 3-D compressible N.–S. equations, which provides small-scale fluctuations for the small-scale dependent variables. To familiarize the reader with general behaviors produced by such a discrete dynamical system studied here, we employ tools such as time series, power spectra, phase portraits, and regime maps (bifurcation diagrams) among others. Special attention will be paid to the physics retained by the CPMNS equation and the generic relationship between bifurcation parameters and the true physical variables. The approach employed to construct the amplitude factors which forms an important part of the proposed model is also discussed. We end Chapter IV with an initial assessment of the SGS model.

We conclude in Chapter VI with a summary of our findings and conclusions drawn from the various studies presented, along with proposals for future studies.

Chapter 2
PREVIOUS WORK

2.1 Numerical Procedures in Turbulence

Since the 1970s computer capacity has increased significantly, and so have the number of workers in the field. At first, researchers turned, naturally, to the most well known and earliest treatment of the N.–S. equations—time averaging—resulting in the Reynolds Averaged Navier–Stokes (RANS) procedures. In time, improvement in computer resources allowed one to solve the full N.–S. equations. The inherent property of turbulent flows, whose range of scales increases rapidly with Reynolds number, restricts the use of such solvers only to low *Re*, whereas typical industrial applications require much higher *Re*. When the scale range exceeds that allowed by computer capacity, some scales must be discarded and the influence of the discarded scales modeled. We shall distinguish between completely resolved and partly resolved simulations by referring to these as direct numerical simulation (DNS) and large-eddy simulation (LES), respectively.

In the following sections we will briefly discuss each of the above mentioned procedures in turn. Emphasis will be laid on LES due to reasons alluded to in Chapter I, and subgrid-scale modeling techniques will also be discussed. We also present two fairly recent numerical approaches, detached-eddy simulation (DES) and implicit large-eddy simulation (ILES). Current trends including applications of discrete dynamical systems theory to turbulence simulation and a new generation of SGS models known as synthetic-velocity models are presented towards the latter half of the chapter.

2.1.1 Reynolds–averaged Navier–Stokes (RANS) procedures

Traditionally, it was thought that turbulence consists of random fluctuations of the various flow variables; hence statistical approaches were used. Such an approach was formally first presented by Reynolds [6] in which all quantities are expressed as a sum of a mean and a fluctuating part. Time averaging as considered by many early researchers is appropriate for stationary turbulence, *i.e.,* a turbulent flow that, on an average, does not vary with time. Let a flow variable $\Phi(\boldsymbol{x}, t)$ be well defined in a domain $\Omega \subset \mathbb{R}^d$, $d = 1, 2, 3$ and for $t \in [\,0, t_f]$, then the Reynolds decomposition of $\Phi(\boldsymbol{x}, t)$ is

$$\Phi(\boldsymbol{x}, t) = \overline{\Phi}(\boldsymbol{x}) + \Phi'(\boldsymbol{x}, t)\,, \tag{2.1}$$

where the mean $\overline{\Phi}(\boldsymbol{x})$ is defined as

$$\overline{\Phi}(\boldsymbol{x}) = \lim_{T\to\infty} \int_0^T \Phi(\boldsymbol{x}, t) dt\,; \tag{2.2}$$

this allows the fluctuating part to be expressed as

$$\Phi'(\boldsymbol{x}, t) = \Phi(\boldsymbol{x}, t) - \overline{\Phi}(\boldsymbol{x})\,. \tag{2.3}$$

It is clear from the definition of the time average that the Reynolds decomposition possesses the following two properties:

$$\overline{\overline{\Phi}}(\boldsymbol{x}) = \overline{\Phi}(\boldsymbol{x}) \qquad \text{and} \qquad \overline{\Phi'}(\boldsymbol{x}, t) = 0. \tag{2.4}$$

Substituting the Reynolds decomposition into the continuity equation and performing the time average yields:

$$\frac{\partial \overline{\rho}}{\partial t} + \frac{\partial}{\partial x_j}\left(\overline{\rho}\,\overline{u_j} + \overline{\rho' u_j'}\right) = 0\,. \tag{2.5}$$

This suggests that the use of the primitive–variable form of the Reynolds decomposition for the compressible N.–S. equations leads to triple correlations involving ρ', u_i' and u_j' when averaging the product $\rho u_i u_j$ that appears in the convective acceleration. Clearly, this increases the complexity of establishing closure approximations for the unknown fluctuating components. The problem of establishing the appropriate form of the time-averaged equations for compressible flow can be simplified dramatically by using the density-weighted averaging procedure suggested by Favre [66]. In Favre averaging an instantaneous flow variable is decomposed into a mass-averaged part, $\widetilde{\Phi}(\boldsymbol{x},t)$ and a fluctuating part $\Phi''(\boldsymbol{x},t)$. The mass-averaged quantity, $\widetilde{\Phi}(\boldsymbol{x},t)$, is defined by

$$\widetilde{\Phi}(\boldsymbol{x}) = \frac{1}{\overline{\rho}} \lim_{T\to\infty} \int_0^T \rho(\boldsymbol{x},t)\Phi(\boldsymbol{x},t)dt = \frac{\overline{\rho\Phi}}{\overline{\rho}}\,, \tag{2.6}$$

where $\overline{\rho}$ is the conventional Reynolds-averaged density. Note that with the above definition $\overline{\Phi''} \neq 0$.

In order to mass average the conservation equations, we now decompose the various flow variables as follows:

$$\begin{aligned}
\rho &= \overline{\rho} + \rho'\,,\\
p &= P + p'\,,\\
q_j &= qL_j + q_j'\\
,u_i &= \widetilde{u}_i + u_i''\,,\\
h &= \widetilde{h} + h''\,,\\
e &= \widetilde{e} + e''\,,\\
T &= \widetilde{T} + T''\,.
\end{aligned} \tag{2.7}$$

Note that we decompose p, ρ, and q_j in terms of the conventional mean and fluctuating parts. Substituting Eqs. (2.7) into Eq. (1.3) and performing the mass-averaging operations (see, Wilcox [67] for details), we arrive at what are referred to as the Favre (mass)-averaged mean conservation equations:

$$\frac{\partial}{\partial t}\left(\overline{\rho}\widetilde{u}_i\right) + \frac{\partial}{\partial x_i}\left(\overline{\rho}\widetilde{u}_i\right) = 0\,, \tag{2.8a}$$

$$\frac{\partial}{\partial t}\left(\overline{\rho}\widetilde{u}_i\right) + \frac{\partial}{\partial x_j}\left(\overline{\rho}\widetilde{u}_j\widetilde{u}_i\right) = -\frac{\partial P}{\partial x_j} + \frac{\partial}{\partial x_j}\left(\tau_{ji} + \tau_{ji}^{turb}\right)\,, \tag{2.8b}$$

$$\begin{aligned}
\frac{\partial}{\partial t}\left(\overline{\rho}E\right) + \frac{\partial}{\partial x_j}\left(\overline{\rho}\widetilde{u}_j H\right) &= \frac{\partial}{\partial x_j}\left(-qL_j - qT_j + \overline{\tau_{ji}u_i''} - \overline{\rho u_j''\frac{1}{2}u_i''u_i''}\right)\\
&\quad + \frac{\partial}{\partial x_j}\left[\widetilde{u}_i\left(\overline{\tau_{ij}} + \tau_{ij}^{turb}\right)\right]\,,
\end{aligned} \tag{2.8c}$$

$$P = \overline{\rho}R\widetilde{T}\,, \tag{2.8d}$$

where $i, j = 1, 2, 3$, $\tau_{ij}^{turb} = \overline{-\rho u_i'' u_j''}$ and $qT_j = \overline{\rho u_j'' h''}$. The quantities E and H are total energy and total enthalpy respectively.

The decomposition of the variables into mean and fluctuating components has isolated the effect of fluctuations on the mean flow. However, the equations for the mean flow now contain six components of τ_{ij}^{turb} (τ_{ij}^{turb} is a symmetric tensor) and three components of qT_j as unknowns additional to the mean density, three components of velocity, pressure and energy. We thus obtain a total of 15 unknowns with only six mean conservation equations, plus an equation of state to specify them. This illustrates the so-called "turbulence closure problem" which has led to extensive modeling efforts form the early part of the 20th century to the present day. We notice that in order to close the system of mean-flow equations, we need a prescription for computing τ_{ij}^{turb}, the Reynolds-stress tensor and qT_j, the turbulent heat flux vector.

As noted by Wilcox [67] there are four main categories of turbulence models which provide approximations for the Reynolds stress tensor and the turbulent heat flux vector: algebraic (zero-equation) models, one-equation models, two-equation models and second-order closure models. Turbulence models are termed algebraic if they do not use any additional ODEs or PDEs to provide closure approximations. One- and two-equation models use one and two additional PDEs, respectively, to provide closure approximations. The second-order closure models are so named because they include equations for each of the second-order statistical quantities comprising the Reynolds stress tensor and the turbulent heat flux vector. A good review on each of these classes of models can be found in Speziale [68]. For zero-, one-, and two-equation models nearly all researchers use the Boussinesq eddy-viscosity hypothesis with suitable generalizations for compressible flows [67]. Denoting the turbulent eddy-viscosity by μ_T, the following form is generally assumed for the Reynolds stress:

$$\tau_{ij}^{turb} = \overline{-\rho u_i'' u_j''} = 2\mu_T \left(S_{ij} - \frac{1}{3}\delta_{ij} \frac{\partial \widetilde{u}_k}{\partial x_k} \right) - \frac{2}{3}\overline{\rho} k \delta_{ij} \,, \tag{2.9}$$

where S_{ij} is the mean strain rate tensor, k is the turbulence kinetic energy, and δ_{ij} is the kronecker delta. Note that the second term on the right-hand side of the above equation is needed to obtain the proper trace of τ_{ij}^{turb}, *i.e.,* $\tau_{ii}^{turb} = -2\,\overline{\rho} k$. Further this means that the "second eddy viscosity" must be $-2/3\mu_T$. We should also recognize that the construction of Eq. (2.9) is somewhat similar in construction to the Newton's law of viscosity given by

$$\tau = \mu \frac{\partial u}{\partial y} \,. \tag{2.10}$$

But it is important to bear in mind that the physical situation is very different for the two cases. In the laminar flow case, Eq. (2.10) is an empirical relationship, and moreover viscosity μ is a property of the fluid. However, in the turbulent flow case, Eq. (2.9) is not a empirically-supported physical result and μ_T is not a property of the fluid. The most commonly used approximation for the turbulent heat-flux vector, qT_j, follows from appealing to the classical analogy between momentum and heat transfer, *i.e.,* turbulent motions transfer heat in much the same way as transporting momentum. It is thus assumed to be proportional to the mean temperature gradient; hence

$$qT_j = \overline{\rho u_j'' h''} = -\frac{\mu_T c_p}{Pr_T} \frac{\partial \widetilde{T}}{\partial x_j} \,, \tag{2.11}$$

where Pr_T is the turbulent Prandtl number usually set to a constant value, and c_p is specific heat at constant pressure.

Some of the popular models are zero-equation models—Baldwin–Lomax [69], one-equation models—Spalart–Allmaras model [70] which uses one PDE to model the turbulent kinetic energy, two-equation models, which are by far the most widely used models: $k-\varepsilon$ model of Jones and Launder [71], $k-\varepsilon$ model of Rubesin [72]—the same model as Jones and Launder but with compressibility corrections, $k-\omega$ of Wilcox [67] uses two PDEs to model the turbulence quantities. Here k, ε, and ω represent turbulence kinetic energy, the dissipation rate of turbulence kinetic energy, and the dissipation per unit turbulence kinetic energy respectively. We note that a partitioning of the isotropic dissipation rate can be performed by assimilating the deviatoric part of the tensor dissipation rate into the pressure-strain correlation (see Zeman [73], Sarkar *et al.* [38] for details) to account explicitly for compressibility effects. For a review on the use of the above mentioned models for compressible high-speed flows the reader is referred to Barre *et al.* [74], Wilcox [67] and references therein.

Although use of the above-mentioned models does provide fairly accurate results in certain situations, there are many situations of practical interest for which these models will fail due to the underlying assumptions in their construction—most notably the Boussinessq eddy-viscosity hypothesis. Wilcox [67] provides a fairly detailed discussion of the Boussinessq hypothesis, emphasizing its shortcomings. Generally speaking, models using the Boussinesq hypothesis fail in the following physical situations: flows with sudden changes in mean-strain rate, flow over curved surfaces, flows with boundary-layer separation, among others (see, *e.g.,* [67] for further listings). We further mention a difficulty arising from the Boussinesq hypothesis that is of a more mathematical nature. Recall that the source of the Reynolds stresses was averaging the nonlinear advective terms in the N.–S. equations. But, the Boussinesq hypothesis leads to replacing these with linear diffusive terms. While this is obviously good for numerical computation, it is bad physics, and in the context of the modern view of N.–S. equations it will alter bifurcation sequences. This essentially precludes any chance of predicting transition to turbulence using RANS models; separate, *ad hoc* models must be implemented to account for this. On the other hand, second-order closure models do not explicitly use the Boussinessq eddy-viscosity hypothesis, but instead model the six individual components of the Reynolds stress using six additional transport equations. Even though such models naturally include effects of stream line curvature, sudden changes in strain rate, *etc.,* a significant price is paid in complexity and computational cost for these gains, and hence these models are not widely used.

Finally, we comment that strictly speaking, from the definition of the time-average, the RANS equations should not contain the temporal term (*i.e.,* we would have to consider only steady state flows). However, in practice it is present in essentially all formulations. Although Wilcox [67] provides arguments for retaining the temporal term in certain cases (flows for which the mean flow varies slowly with time), he also recognizes that very few unsteady flows of engineering interest actually satisfy this condition. He further recommends using rigorous approaches like LES for such flows.

It is also interesting to consider the mathematics of the Reynolds decomposition. A simple Fourier series representation of a flow variable, followed by time-averaging the Fourier representation allows us to determine that the fluctuating component ϕ' represents all of the solution (a very wide range of scales) except the zeroth temporal modes. As a consequence,

we should expect that it would be quite difficult to model. But at least in principle this is precisely what must be modeled in RANS formulations; that is, essentially the entire solution must be modeled. While the small-scales tend to depend only on viscosity, and may be somewhat universal, the large ones are affected very strongly by the boundary conditions. Thus, it does not seem possible to model the effect of the large-scales of turbulence in the same way in flows that are very different. Not surprisingly, it has been shown by McDonough [49] that intrinsic errors are present in RANS formulations. In particular, he shows the inequality of RANS solutions to the time-averaged N.–S. solutions.

2.1.2 Direct numerical simulation (DNS)

The main purpose of a DNS is to solve for the velocity field and scalars of a turbulent flow without the use of a "turbulence model," thus avoiding the curse of closure which comes up in almost every modeling procedure. To do so, one has to resolve the entire range of scales in a turbulent flow. The largest scales are generally determined by physical parameters such as channel width, boundary layer thickness, mixing layer thickness and so on. The physics (*e.g.,* dissipation spectrum) dictates the smallest scale that needs to be resolved, and the accuracy with which it needs to be represented. Generally the Kolmogorov length scale $\eta = (\nu/\varepsilon)^{1/4}$, where ν is the dynamic viscosity and ε is the kinetic energy dissipation rate, is the smallest scale that needs to be resolved. This wide range of scales compounded by accuracy requirements which are determined by the numerical method chosen to solve the N.–S. equations give DNS its two obvious problems: memory and computational speed requirements (amount of arithmetic). For cold incompressible flow the required arithmetic for a DNS scales at least as $\mathcal{O}(Re^3)$. The range of scales in a turbulent flow increases rapidly with Re, thus rendering DNS impractical for applications of engineering interest. For compressible flows, this low Re restriction is compounded by several additional factors: (1) at least one additional thermodynamic variable, *e.g.,* mass density, must be retained and time advanced, and this increases the storage problem; (2) as Mach number increases, the average diagonal component of the Taylor microscale decreases, which implies the requirement of more refined discretization as the Mach number increases (see Zang *et al.* [75]). All these drawbacks are further exacerbated if 3-D simulations are to be performed. However, DNS should be regarded as the best research tool available to the fluids community, and in this context the capabilities of this tool are impressive.

The earliest DNS can be traced back to Orszag and Patterson [76] in 1972. They performed a 32^3 computation of isotropic turbulence at a Re_λ (based on Taylor microscale length) of 35. As we should expect, in contrast to its incompressible counterpart, DNS of compressible turbulence has been fairly recent. The DNS of homogeneous compressible turbulent flow was initiated in 1981 by Feiereisen *et al.* [77].

Shock waves and related phenomena which feature prominently in compressible flows have been studied in fair detail. Lee *et al.* [78] conducted 3-D simulations of isotropic turbulence in order to investigate the existence of eddy shocklets. Results were reported for 64^3 and 128^3 grids with a peak turbulent Mach number $M_t = q/c$ (q is a velocity scale characteristic of the turbulence and c is a representative speed of sound) of 0.6 (subsonic) and Re_λ of 50. Their results substantiate the existence of eddy shocklets, that were found to satisfy the same properties of shock waves. Furthermore, those authors have demonstrated

that shocklets are more likely to occur as M_t and Re are increased. Ravi Samtaney *et al.* [79] conducted simulations of decaying compressible, isotropic turbulence at fluctuating Mach numbers 0.1–0.5 and a Re_λ $\mathcal{O}$ $(50-100)$ on 128^3 and 256^3 grids and quantified shocklet statistics. In particular, they found the shock thickness statistics to scale on the Kolmogorov length scale rather than on that of the mean free path in a gas.

Direct simulations of compressible shear layers have also been performed to understand fundamental aspects of compressibility effects on turbulence. Perhaps the most significant effect of compressibility on a free shear flow is a suppressed growth rate, which has important implications for applications such as scramjet engines and abatement of supersonic jet noise. Identification of the mechanisms responsible for the inhibited shear layer growth at high Mach number may also be used to derive insights into possible mixing enhancement strategies. Freund *et al.* [80] performed simulations of time evolving annular mixing layers. They conducted an extensive study involving nine cases with convective Mach number $M_c = (U_1 - U_2)/\overline{c}$ (where U_1 and U_2 are the velocities of the two flows forming the mixing layer and $\overline{c}$ is the average sound velocity between the two layers—in general M_c is a Mach number defined on a moving frame of reference) ranging from $0.1 - 0.8$ and M_t reaching as high as 0.8. They offer an acoustic timescale limitation of deforming eddies as a possible explanation for decrease in transverse length scale. Direct simulations of fully developed turbulent shear layers was performed by Pantano and Sarkar [81]. In agreement with previous studies they found the thickness growth rate of the shear layer to exhibit a large reduction with increase in convective Mach number. However, they also found that all components of turbulence intensities decrease with increase in M_c (for further details the reader is referred to [81]).

A good review related to numerical issues such as boundary conditions, spatial and temporal discretizations can be found in Moin and Mahesh [82] and references therein. For discussions on consistent initial conditions for DNS of compressible turbulence, the reader is referred to Ristorcelli and Blaisdell [83].

We remark that although the complexity of flows that are being computed by DNS today has considerably increased, the Reynolds number is still low. Another development has been the increased investigation of turbulence physics by computing idealized flows that cannot be produced in the laboratory. Moreover, availability of raw DNS data has allowed scientists to develop new ideas and theories that can be readily tested. In this context DNS is becoming an invaluable tool to provide reliable data for model validation and development (for both LES and RANS). Perhaps the most significant contribution of DNS to date has been the identification of turbulent structures. In particular, we mention the classical results by Rogallo [31] for homogeneous turbulence, and those of Moin and Kim [32] for turbulent channel flow among numerous others.

2.1.3 Large-eddy simulation

Large-eddy simulation is a technique intermediate between the direct simulation of turbulent flows and the solution of the Reynolds-averaged equations. In LES the contribution of the large, energy-carrying structures to momentum and energy transfer is computed exactly, and only the effect of the smallest scales of turbulence is modeled. Since the small scales tend to be more homogeneous and universal, and less affected by boundary conditions than the large ones, there is hope that their models can be simpler and require fewer adjustments

when applied to different flows than similar models for the RANS equations.

LES is similar to DNS; in fact, it can be shown that as the grid spacing is decreased a correctly-implemented LES converges to a DNS. LES also provides three-dimensional, time dependent solutions to the N.–S. equations. Thus, its use still requires fairly fine meshes. However, LES can be used at much higher Reynolds numbers than DNS. Among the objectives of LES is to study more complex physics than can be addressed by DNS, in configurations closer to that of engineering interest.

To separate the large from the small scales, LES uses a filtering operation. If $f(\boldsymbol{x})$ is a function containing all the scales we define, the large-scale or resolved-scale component of f, denoted as $\overline{f}$ is given by a convolution of f with a filter function $G(\boldsymbol{x})$ (Leonard [84])

$$\overline{f}(\boldsymbol{x}) = \int_D f(\boldsymbol{x}') G\left(\boldsymbol{x}, \boldsymbol{x}'; \overline{\Delta}\right) d\boldsymbol{x}' \,, \tag{2.12}$$

where D is the entire domain, G is the filter function, and $\overline{\Delta}$ is the filter-width associated with the wavelength of the smallest scale retained by the filtering operation. Thus, the filter function implicitly sets the size and structure of the small scales. These small scales (subgrid-scales) should be modeled in some fashion to overcome the problem of closure. For some commonly used filters in LES see Piomelli [85].

In compressible flows it is convenient to use Favre-filtering [66] to avoid the introduction of subgrid-scale (SGS) terms in the continuity equation. A Favre-filtered variable is defined as $\widetilde{f} = \overline{\rho f}/\overline{\rho}$. Applying the Favre-filtering operation to Eqs. (1.3a–1.3c) we obtain the resolved scale equations:

$$\frac{\partial \overline{\rho}}{\partial t} + \frac{\partial}{\partial x_j}\left(\overline{\rho}\widetilde{u}_j\right) = 0 \,, \tag{2.13a}$$

$$\frac{\partial \overline{\rho}\widetilde{u}_i}{\partial t} + \frac{\partial}{\partial x_j}\left(\overline{\rho}\widetilde{u}_i\widetilde{u}_j\right) = -\frac{\partial}{\partial x_j}\left(\,\overline{p}\delta_{ij}\right) + \frac{\partial}{\partial x_j}\left(\sigma_{ji}\right) + \frac{\partial}{\partial x_j}\left(\tau_{ji}\right) \,, \tag{2.13b}$$

$$\frac{\partial \overline{\rho}\widetilde{E}}{\partial t} + \frac{\partial}{\partial x_j}\left(\overline{\rho}\widetilde{E}\widetilde{u}_j\right) = -\frac{\partial}{\partial x_j}\left(\overline{p}\widetilde{u}_j\right) - \frac{\partial}{\partial x_j}\left(\widetilde{q}_j\right) + \frac{\partial}{\partial x_j}\left(\widetilde{\sigma}_{ij}\widetilde{u}_i\right) \tag{2.13c}$$

$$- \frac{\partial}{\partial x_j}\left(\gamma c_v Q_j + \frac{1}{2}\Im_j - D_j\right) \,. \tag{2.13d}$$

Here E is the total energy per unit mass, and the diffusive fluxes are given by

$$\widetilde{\sigma}_{ij} = 2\widetilde{\mu}\widetilde{S}_{ij} - \frac{2}{3}\widetilde{\nu}\delta_{ij}\widetilde{S}_{kk} \,, \tag{2.14}$$

$$\widetilde{q}_j = -\widetilde{k}\frac{\partial \widetilde{T}}{\partial x_j} \,. \tag{2.15}$$

The effect of the subgrid-scale terms appears on the right-hand side of the governing equations through the SGS stresses τ_{ij}, SGS heat flux Q_j, and SGS viscous diffusion $\partial D_j/\partial x_j$.

These quantities are defined as

$$\tau_{ij} = \overline{\rho}\left(\widetilde{u_i u_j} - \widetilde{u}_i\widetilde{u}_j\right) , \tag{2.16}$$

$$Q_j = \overline{\rho}\left(\widetilde{u_j T} - \widetilde{u}_j\widetilde{T}\right) , \tag{2.17}$$

$$\Im_j = \overline{\rho}\left(\widetilde{u_j u_k u_k} - \widetilde{u}_j\widetilde{u_k u_k}\right) , \tag{2.18}$$

$$D_j = \overline{\sigma_{ij}u_i} - \widetilde{\sigma_{ij}}\widetilde{u}_i . \tag{2.19}$$

For solving the energy equation, one can choose from formulations based on internal energy or enthalpy apart from total energy that we have considered. For such formulations the interested reader is referred to [53].

In order for the dynamics of the resolved scales to remain correct, the subgrid terms have to be taken into consideration, and thus have to be modeled. The modeling consists of approximating the subgrid-scale terms on the basis of the information contained in the resolved scales.

The first LES dates back to the mid to late 1960s and early 1970s with the pioneering work on incompressible flows by Smagorinsky [86], Lilly [87] and Deardorff [88]. Since then, subgrid-scale modeling has matured considerably and can be broadly classified into three general categories (among many other possible classifications): eddy-viscosity models, scale-similarity models, and so called mixed models which combine eddy-viscosity and scale-similarity expressions. There are a number of excellent reviews on the theory and practice of SGS modeling in the traditional framework, especially for incompressible flows, *e.g.,* Lesieur and Mètias [50], Meneveau and Katz [51] and Piomelli [52].

Eddy-viscosity models rely on the assumption that the subgrid-scale stress is proportional to the resolved-scale strain rate tensor, the proportionality factor being referred to as the eddy-viscosity—again, the Bousinessq hypothesis. Eddy-viscosity models try to reproduce the global exchange of energy between resolved and unresolved stresses by mimicking the drain of energy associated with the turbulence energy cascade. The most famous eddy-viscosity model was proposed by Smagorinsky [86] and was motivated by meteorological applications. Yoshizawa [89] proposed an eddy-viscosity model for weakly compressible turbulent flows using a multiscale direct-interaction approximation method. The anisotropic part of the SGS stresses is parametrized using the Smagorinsky (1963) model, while its trace τ_{kk} is modeled separately:

$$\tau_{ij} - \frac{\delta_{ij}}{3}\tau_{kk} = -C_s^2 2\overline{\Delta}^2\overline{\rho}|\widetilde{S}|\left(\widetilde{S}_{ij} - \frac{\delta_{ij}}{3}\widetilde{S}_{kk}\right) , \tag{2.20}$$

$$\tau_{kk} = C_I 2\overline{\Delta}^2\overline{\rho}|\widetilde{S}|^2 . \tag{2.21}$$

with $C_s = 0.16$, $C_I = 0.09$ and $|\widetilde{S}| = \left(2\widetilde{S}_{ij}\widetilde{S}_{ij}\right)^{1/2}$.

We see from this, that the subgrid-scale stress tensor is now completely specified; but we should expect that from the simplicity of the above model that it is not likely to be very accurate except for homogeneous turbulence. Moreover, the model is completely dissipative, and it is due to this that it performs very badly for wall-bounded flows. In particular, it is now known that for such flows as much of one third of the turbulence kinetic energy

cascaded to the small scales returns to the large scales without being dissipated. This is termed "backscatter," and the above model is unable to produce such behavior.

Moin *et al.* [90] generalized the dynamic subgrid-scale model of Germano *et al.* [91] for the LES of compressible flow, in which the two model coefficients C_s and C_I are determined dynamically, rather than input *a priori*. To accomplish this, additional information is needed, and Germano *et al.* obtain this by means of a second filtering operation. This second filter is usually known as a *test filter*. The Germano identity [91] $L_{ij} = T_{ij} - \widehat{\tau_{ij}}$, relates the SGS stresses τ_{ij} to the "resolved scale stresses." For the compressible equations $L_{ij} = \left(\widehat{\overline{\rho u_i}\ \overline{\rho u_j}}/\overline{\rho}\right) - \widehat{\overline{\rho u_i}}\ \widehat{\overline{\rho u_j}}/\overline{\rho}$, and the subset stress $T_{ij} = \widehat{\overline{\rho}}\widetilde{\widehat{u_i}}\widetilde{\widehat{u_j}} - \widehat{\overline{\rho}}\breve{\widehat{u}}_i\breve{\widehat{u}}_j$ (where $\breve{\widehat{f}} = \widehat{\overline{\rho f}}/\widehat{\overline{\rho}}$, and the hat represents the application of the test filter $\widehat{G}$ of typical width $\widehat{\Delta} = 2\overline{\Delta}$). Moin *et al.* determined the model coefficients by substituting Eq. (2.20) and Eq. (2.21) into the Germano identity and contracting with $\widetilde{S}_{ij}$. However, the contraction with the strain rate tensor $\widetilde{S}_{ij}$ leads to difficulties at flow field locations where the strain rate is very small (or zero). To overcome this difficulty Lilly [92], proposed a contraction with the error itself, which results in a least-squares problem of minimizing error with respect to the model constants. Accordingly, the two model coefficients for the dynamic eddy-viscosity model will be given by:

$$C = C_s^2 = \frac{\langle L_{ij} M_{ij} \rangle}{\langle M_{kl} M_{kl} \rangle}\,, \tag{2.22}$$

$$C_I = \frac{\langle L_{kk} \rangle}{\langle \beta - \widehat{\alpha} \rangle}\,, \tag{2.23}$$

where $\beta_{ij} = -2\widehat{\Delta}^2\ \widehat{\overline{\rho}}|\breve{\widetilde{S}}|\left(\breve{\widetilde{S}}_{ij} - \delta_{ij}\breve{\widetilde{S}}_{kk}/3\right)$, $M_{ij} = \beta_{ij} - \widehat{\alpha_{ij}}$, and $\beta = 2\widehat{\Delta}^2\ \widehat{\overline{\rho}}|\breve{\widetilde{S}}|^2$. We note that $\langle\ \rangle$ indicates an averaging procedure.

As noted in Sagaut [93], the coefficient C (without the averaging) has the following two properties. The constant can take negative values, so the model can have an anti-dissipative effect—in fact, the PDE problem is ill-posed. This is a characteristic that is often interpreted as a model of the backward energy cascade mechanism—"backscatter." The second property is that C can become unbounded, since in principle the denominator can become zero. These two properties have important practical consequences on the numerical solution because they are both potentially destructive of the stability of the simulation. Numerical experiments have shown that the constant can remain negative over long time intervals, causing an exponential growth in the high-frequency fluctuations of the resolved field. The constant therefore needs an *ad hoc* process to ensure the model's good numerical properties. This is generally achieved by averaging, typically in directions in which the flow exhibits homogeneity—if such directions exist (see [93] for various options). Thus, while dynamic models tend to seemingly reproduce physics better than do the simple Smagorinsky type models, especially for wall-bounded shear flows, the underlying reasons are not well founded, leaving open the question whether such models, or any others based on eddy-viscosity, could be truly predictive.

Scale-similar models are based on the scale similarity hypothesis as proposed by Bardina *et al.* [94], who assume that the statistical structure of the tensors constructed on the subgrid-scales is similar to that of their equivalents evaluated on the smallest resolved scales. This amounts to saying that the most active SGSs are those closer to the cutoff, and that the scales

with which they interact are those immediately above the cutoff wavenumber. Thus, scale similar models employ multiple operations to identify the smallest resolved scales and use the smallest "resolved" stresses to represent SGS stresses. Although these models account for the local energy events, they underestimate the dissipation. Indeed, they generally produce far too much backscatter and as a consequence are numerically unstable.

Speziale *et al.* [95] proposed the addition of a scale-similar part to the eddy-viscosity model of Yoshizawa introducing the "mixed" model. In this way, the eddy-viscosity contribution provides the dissipation that is underestimated by purely scale-similar models. This model was used by Erlebacher *et al.* [96] and Zang *et al.* [97], and is given by

$$\tau_{ij} - \frac{\delta_{ij}}{3}\tau_{kk} = C_s\alpha_{ij} + A_{ij} - \frac{\delta_{ij}}{3}A_{kk}\,, \tag{2.24}$$

$$\tau_{kk} = C_I\alpha + A_{kk}\,, \tag{2.25}$$

where $A_{ij} = \overline{\rho}\left(\widetilde{\widetilde{u}_i\widetilde{u}_j} - \widetilde{\widetilde{u}}_i\widetilde{\widetilde{u}}_j\right)$. Erlebacher *et al.* tested the model *a priori* by comparing DNS and LES results of compressible isotropic turbulence and found good agreement in the dilatational statistics of the flow, as well as a high correlation between the exact and modeled stresses. Zang *et al.* compared the DNS and LES results of isotropic turbulence with various initial ratios of compressible to total kinetic energy. They obtained good agreement for the evolution of quantities such as compressible kinetic energy and fluctuations of thermodynamic variables.

It should also be noted that dynamic model adjustment can also be applied to mixed models Eqs. (2.24) and (2.25), to yield dynamic mixed models. We remark that the combination of Boussinesq-based eddy-viscosity models and scale-similarity models presents a fundamental contradiction. Any eddy-viscosity method implicitly relies on scale separation since such models incorporate the notion that eddy viscosity "acts like" molecular viscosity. The former plus the latter appear in the diffusion terms of the governing equations, and this physical molecular behavior takes place on scales that are not directly influenced by the macroscopic scales of motion. In contrast to this, the scale-similarity approaches attempt to bridge this gap near the cutoff wavenumber, and in particular require resolution well into the inertial subrange to be effective.

2.1.4 Detached-eddy simulation (DES)

Detached-eddy simulation (DES) is a hybrid technique first proposed by Spalart *et al.* [98] for prediction of turbulent flows at high Reynolds numbers (see, also Spalart [99]). Development of this technique was motivated by estimates which indicate that the computational cost of applying LES to simulate flow over complete configurations such as an airplane, submarine, or road vehicles is prohibitive. The high cost of LES when applied to complete configurations at high Reynolds number arises because of the resolution requirements in the boundary layers, an issue that remains even with fully successful wall-layer modeling. On the other hand, RANS models tend to be able to predict attached flows with a low computational cost. However, RANS (statistical) models are not capable of predicting massively separated flows. The advantages then offered by LES provide strong motivation for its application, *i.e.,* direct resolution of the dominant unsteady structures though at a higher computational cost than RANS. In DES, the aim is to combine the most favorable aspects of the two techniques,

i.e., application of RANS models for predicting attached boundary layers and LES for resolution of time-dependent, three-dimensional large eddies. The cost scaling of the method is then favorable since LES is not required to resolve the relatively smaller structures that populate the boundary layer. In natural applications of this method, the entire boundary layer is treated by RANS, with an LES treatment of the separated regions.

The base model employed in a majority of DES applications to date is the Spalart–Allmaras one-equation model [70] (henceforth referred to as S–A). The S–A model solves a single partial differential equation for a variable $\widetilde{\nu}$ which is the turbulent viscosity. The differential equation is derived "using empiricism and arguments of dimensional analysis, Galilean invariance and selected dependence on molecular viscosity." The model includes a wall-destruction term that reduces the turbulent viscosity in the log layer and laminar sub-layer, and trip terms that are supposed to provide a smooth transition from laminar to turbulent states. For compressible flow Spalart suggested using the compressibility correction proposed by Secundov [100]. This amounts to adding an extra destruction term to the right-hand side of the S–A model equation:

$$-C_5\widetilde{\nu}^2 U_{ij}U_{ij}/a^2\,, \tag{2.26}$$

where a is the speed of sound, and C_5 is an empirically determined constant.

The wall-destruction term in the S–A model is proportional to $(\widetilde{\nu}/d)^2$, where d is the distance to the closest wall. When this term is balanced with the production term, the eddy-viscosity becomes proportional to $\boldsymbol{S}d^2$ ($\widetilde{\nu} \propto \boldsymbol{S}d^2$), where $\boldsymbol{S}$ is the local strain rate. Recall that the Smagorinsky LES model varies its subgrid-scale turbulent viscosity with the local strain rate and the grid spacing Δ. If, therefore, d is replaced by Δ in the wall destruction term, the S–A model will act as a Smagorinsky model.

To exhibit both RANS and LES behavior, d in the S–A model is replaced by

$$\widetilde{d} = min\,(d, C_{DES}\Delta)\,, \tag{2.27}$$

where C_{DES} is a model constant. When $d \ll \Delta$, the model acts as a RANS model. When $d \gg \Delta$, the model acts as a Smagorinsky LES model.

Strelets [101] introduced a DES model based on Menter's shear stress transport model (SST) (see Menter [102], and [103] for details). The SST model is a combination of $k-\varepsilon$ and $k-\omega$ models, utilizing the best features of each model. Wilcox's $k-\omega$ model is well-behaved in the near-wall region, where low Reynolds number corrections are not required. However, the model is generally sensitive to freestream values of ω. On the other hand, $k-\varepsilon$ equations are relatively insensitive to freestream values of ε, but behave poorly in near wall regions. The SST model uses a parameter F_1 to switch from $k-\omega$ to $k-\varepsilon$ in the wake region to prevent the model from being sensitive to freestream conditions. Menter did not include compressibility corrections in his model. Suzen and Hoffmann [104], however, added compressible dissipation and dilatation terms to the $k-\varepsilon$ portion of Menter's SST model. In the SST model, the turbulent length scale is given by $l_{k-\omega} = k^{1/2}/\beta^*\omega$ (see [102] for details). The DES modification replaces the length scale by $\widetilde{l} = min\,(l_{k-\omega}, C_{DES}\Delta)$ in the dissipation term of the k-transport equation.

Most applications of DES have been for flows with separation. Constantinescu and Squires [105] applied DES to turbulent flow over a sphere at several Reynolds numbers.

Strelets [101] presented numerous cases using DES: a cylinder, airfoil, backstep, triangle in channel, raised runaway section, and landing gear. Some cases showed very little improvement over RANS calculations; but none performed worse than RANS, and many performed better. Forsythe *et al.* [106] performed a DES of an axisymmetric base flow at supersonic conditions. Their work incorporated compressible shear layer corrections in both S–A and SST models. They also tested the sensitivity of the models to grid-refinement, and even grid type (structured and unstructured). They found that all the results looked similar when comparing S–A based DES to SST based DES and the fine structured *vs* unstructured grid for this particular flow scenario.

As we should expect, applications of DES have been successful only in flow scenarios where there is a clear demarcation between the RANS and LES regions. For other scenarios one of the issues confronting DES is the "grey area" in which a shear layer, after separation, must generate "LES content" which it did not possess in the boundary layer upstream. Moreover, in general, a Smagorinsky type model is used as the subgrid-scale model in a DES; hence, one should expect all the disadvantages of using eddy-viscosity assumptions to also occur for a DES. We also note, on the other hand, that disadvantages of using eddy-viscosity models are somewhat alleviated, since they are not used at the wall. In DES, the turbulence is treated by RANS in the boundary layer and slightly beyond separation. Therefore the accuracy in RANS mode in a DES is no more than it is in pure RANS. We further emphasize that RANS and LES procedures are fundamentally different. In particular, the Reynolds decomposition results in having to model the entire range of length scales of the flow, whereas in a LES decomposition the modeling is confined only to the small-scales—hence we should expect that it should be difficult to combine them.

2.1.5 Implicit large-eddy simulation (ILES)

As alluded to throughout this material, large-eddy simulation was developed within the framework of spatial filtering. In particular, virtually all developments of large-eddy simulation consider spatial filters with constant filter width, *e.g.,* convolution filters. Though the LES approach promises to be a relevant engineering simulation strategy, in order to efficiently extend the capabilities of LES to turbulent flows with complex geometries, one must allow for filters whose properties vary in space, time or both space and time. We note that the advantages of local refining or coarsening of the filter width shows some similarity to those exhibited by the use of non-uniform grids.

The introduction of a spatially non-uniform filter or the use of an uniform filter on a non-uniform grid, complicates the development of the corresponding large-eddy approach since additional closure terms emerge. In particular, these terms are generally referred to as commutator-error terms and originate from the fact that non-uniform filtering and differentiation do not commute. Fedderik *et al.* [107] have analyzed the large-eddy simulation equations that are obtained from the application of a spatially non-uniform filter to the incompressible N.–S. equations. They show that the turbulent stress contributions and the commutator-errors display the same scaling behavior on the filter width and its derivative. The authors conclude from the order of magnitude of the commutator-error terms that it is necessary to explicitly model the commutator-error terms along with traditional subgrid-scale modeling. They further propose models for the error terms (see [107] for further details).

This is nothing but a headache when considering LES of compressible turbulence.

Furthermore, difficulties with conventional LES arise from modeling of the SGS term itself and the (possible) masking of the SGS terms by the truncation error. This suggests that we must understand how numerical methods contribute implicitly to turbulence modeling; otherwise we may end up double-counting the effects of turbulence through the explicit turbulence model as well as through the properties of the numerical method. Moreover, the under-resolution of a LES will also result in "aliasing errors." A relatively large-amount of filtering (smoothing) is needed to ensure that the short wavelength does not contribute very much to the error. This filtering in some formulations can have a significant dissipative effect even on scales that can be resolved well.

The above properties of conventional LES has provided a rationale for using high-resolution methods (for definition of high-resolution methods see Harten [108]), without any explicit filtering of the governing equations for simulating turbulent flows. These methods appear to have many of the properties of subgrid-scale models due to their numerical analytic properties. The idea to use these methods as an implicit way to numerically model turbulent flows is referred to as monotonically integrated LES (MILES), implicit large-eddy simulation (ILES), or embedded turbulence modeling.

Reynolds [109] discussed the notion of LES being performed without explicit subgrid-scale models, but he did not address the interpretation that monotone schemes may already have a minimal built-in subgrid model. Boris *et al.* [110] provided the first detailed discussion regarding the use of high-resolution monotone computational fluid dynamic algorithms such as flux-corrected transport (FCT) [111] or piecewise parabolic methods (PPM) [112] as alternatives to conventional LES. They recognized that these algorithms, which were designed to satisfy the physical requirements of positivity and causality, have a minimal nonlinear LES filter and hence, a matching SGS model. In particular, they provide evidence to substantiate their notion of a "built-in" subgrid model (see, [110] for further details). Over the past one and a half decades a number of such algorithms have been used by various researchers over a wide range of problems, especially at high Re involving compressible phenomena. A recent extensive review on the use of high resolution methods for such simulations is presented in Drikakis [113]. Moreover, most of these algorithms were designed for compressible flow simulations, and hence this kind of interpretation of LES blends almost perfectly for simulating compressible Navier–Stokes turbulence.

All this being said, the use of high-resolution methods as an implicit way to model and compute turbulent flows is indeed an evolving area of research. In particular, there is a need for better understanding of the physics encompassed by such numerical methods. Though there has been significant progress in the theory of high-resolution methods for one-space dimension, there is a need to understand the nonlinear behavior of the schemes in multi-dimensional problems (where we are lacking in theory). This nonlinear behavior is also closely related to the numerical mechanisms leading to the formation of spurious solutions in under-resolved simulations [113]. In particular, the question "why certain schemes evince spurious solutions while others do not" [113], still eludes a scholastic answer. Such questions in turn lead to dilemmas regarding the fidelity of the use of a particular scheme over a wide range of flow scenarios.

2.2 Current Trends

While involved in the Statistical Forecasting project at MIT, Lorenz [114] exhibited that a simple deterministic dynamical model of a fluid system can yield flow properties having bounded aperiodic behavior in time, of a form apparently so chaotic, that in current terminology is said to indicate the presence of a "strange attractor." This (re)discovery by Lorenz of deterministic systems that are long term unpredictable led to a class of systems that have come to be known as "chaotic dynamical systems." These systems are characterized by *sensitivity to initial conditions*, that is, exponential separation of nearby trajectories in phase space, which is considered by many to be the hallmark of a strange attractor.

Although Poincare [115] studied "nonlinear dynamical systems" in the 19th century, the discovery by Lorenz provided an impetus to researchers to draw parallels between mathematics and physical systems that were previously beyond description. Since then, one of the main goals for the development of theory of chaotic dynamical systems has been to make progress in the understanding of turbulence. For a complete review on the history of dynamical systems and chaos, the interested reader is referred to Aubin and Dalmedico [116]. Here we will give special attention to the relationship between turbulence and chaotic phenomena. We also consider a new generation of turbulence models known as synthetic-velocity models.

2.2.1 Dynamical systems, chaos and turbulence

One of the goals of science is to predict how a system will evolve as time progresses. The theory of dynamical systems allows one to do just that. In fluid dynamics a general evolution equation can be written down as follows

$$\frac{d\boldsymbol{x}}{dt} = F(\boldsymbol{x}(t), \lambda)\,, \tag{2.28}$$

where $\boldsymbol{x}(t)$ is the velocity field, and λ is a parameter (*e.g.,* Reynolds number, angle of attack, Mach number). As λ varies, particular equilibrium solutions, periodic orbits, or other more complicated invariant sets, may appear or their stability may change. These are considered to be what are called bifurcations. There are two ways in which the stability of an equilibrium can change: an eigenvalue of its linearization can pass through zero, or a pair of nonzero eigenvalues may cross the imaginary axis. In the first case, the simplest bifurcation is called a *saddle-node* or *limit-point* bifurcation. It describes the birth or collapse of two equilibria (of different stability) as a parameter is varied. The second process, in which nonzero eigenvalues cross the imaginary axis, is called *Hopf bifurcation* and involves a family of periodic orbits that grow from equilibrium. So, as the parameter λ is varied, a viscous fluid progresses through a collection of increasingly complicated flow patterns. Often, primary interest is directed towards the asymptotic behavior of the system. Then it is necessary to study the dynamics of the attractor (a set in phase space to which the system evolves after a long enough time) to describe the asymptotic behavior of the system.

Originally, Landau [117] and Hopf [118] (see, Landau and Lifschitz [119]) proposed that the time evolution of a turbulent fluid flow is asymptotically given by

$$\boldsymbol{X}(t) = f_k(\omega_1 t, \omega_2 t, ..., \omega_k t)\,, \tag{2.29}$$

where f_k is a periodic function of period 2π in each of its arguments, and $\omega_1, ..., \omega_k$ are independent frequencies. A function of the form of Eq. (2.29) is called quasiperiodic (the corresponding quasiperiodic attractor is a k-dimensional torus) if two, or more, of the ω_k are incommensurate. A quasiperiodic function has a non-periodic, irregular aspect, suggestive of turbulence, but it is not sensitive to initial conditions. In their seminal paper Ruelle and Takens [61] mathematically proved that by a small perturbation of Eq. (2.28), one can destroy a quasiperiodic attractor and if $k \geq 3$ obtain a strange attractor (an attractor with chaotic dynamics). This new progression from steady to turbulent states was termed as the Ruelle–Takens–Newhouse (RTN) scenario—where a system starting from a steady state undergoes Hopf bifurcations leading to a quasiperiodic trajectory, which, if made of more than two incommensurate frequencies, needs only to be perturbed to become attracted by a strange attractor. We note that if the time evolution is governed by a strange attractor one may obtain a continuous frequency spectrum (the function giving the square of the amplitude versus the frequency is called frequency spectrum). It is well known that the frequency spectrum of a turbulent fluid flow is continuous. However, until the mathematical discovery by Ruelle and Takens and the direct experimental evidence presented by Swinney and Gollub [120], Fenstermacher *et al.* [121], and Gollub and Benson [57], nearly everyone attributed this fact to the accumulation of a large number of independent frequencies simulating, in the limit, a continuous spectrum. The RTN scenario for the first time proved otherwise; if one increases the parameter λ describing the system, the transition to the continuous spectrum is rapid. There is no progressive accumulation of many independent discrete frequencies. This discovery established what we now call the "strange attractor theory of turbulence." In addition, the modern mathematical theory of turbulence also incorporates the Feignbaum scenario [122]—where a turbulent state is reached through a series of pitchfork bifurcations and the Pomeau–Manneville scenario [123]—through intermittency.

Laboratory experiments, Gollub and Benson [57], Wulf *et al.*, and [58] Guckenheimer [59] (see the subsection 'Routes to chaos: Experiments' and references therein) have provided support for the strange attractor theory in turbulence. Numerical simulations (e.g., turbulent channel flow [55] and open unforced 2-D flow [56]) have demonstrated the transition to low-dimensional chaos. For further reading on chaos and dynamical systems, the interested reader is referred to the text by Alligood *et al.* [124].

Progress in the utilization of these theories as models for simulating turbulence has been slow. However, there has been an increasing interest in the so called "shell models" of turbulence (see Bohr *et al.* [60] and references therein for theory and applications) which have been developed based on the dynamical systems approach to turbulence. There has also been some success in modeling the large-scales of wall-bounded turbulent flow by low-dimensional dynamical systems (see, *e.g.,* Aubry *et al.* [125]). We comment that the tools which have been developed mostly for low-order dynamical systems (Lyapunov exponents, dimensions of attractors *etc.*) are not very useful for fully developed turbulence, which has very large number of degrees of freedom. We are of the belief that the attempts to oversimplify turbulence by analogy with low-dimensional nonlinear systems that have been shown to be chaotic is not entirely correct. Here, we take the position of McDonough and coworkers (see, *e.g.,* [126], [127]) that a subspace of fully developed turbulence, the small scales, may be effectively described locally in space and time by lower-order dynamical systems without belying the complexity of fully-developed turbulence.

2.2.2 Synthetic-velocity models

In all the SGS models discussed in Section 2.1.3 we notice the failure of the models to incorporate more detailed information about the SGS interactions, and this has been one of their major shortcomings. To gain information about SGS interactions one has to explicitly evaluate the subgrid-scales. Models which explicitly evaluate the dependent variables at the subgrid-scale are sometimes termed "synthetic-velocity models." Such models not only improve the quality of the SGS model, but also provide us with the opportunity to study small-scale turbulence, which would not be possible if traditional SGS models are used. There now exist several possible formulations of this type. For more on the methodology behind such models, the reader is referred to the review article by Domaradzki and Adams [128], and the text by Sagaut [93]. We will now discuss some prominent models in brief.

In Scotti and Meneveau's fractal interpolation model [129] the sub-grid velocity is reconstructed by using two pieces of information: 1) the resolved velocity field, which is known on the finest grid and 2) the fractality of the velocity field. The fluctuations on the small scale are evaluated by interpolating the resolved velocity field on the fine grid using a fractal interpolation technique (see [129] for details). This model is based on geometric considerations only, and does not take into account any information dealing with the flow dynamics, which clearly is a major drawback. As a result of lack of flow dynamics information and high computational cost associated with model implementation, the model has not been widely used.

Kerstein *et al.* [130] developed what they call the one-dimensional turbulence (ODT) model. The essence of ODT is to represent a three-dimensional turbulent field through a one-dimensional line of data which in LES would extend across a volume determined by neighboring mesh points. The fields defined on the one-dimensional domain evolve by two mechanisms, molecular evolution and a stochastic process representing (replacing) advection. The stochastic process consists of a sequence of events, each of which involves an instantaneous transformation of velocity and scalar fields. During the time interval between each event and its successor, molecular evolution occurs, governed by the equations

$$\left(\partial_t - \nu\partial_y^2\right) v_i(y,t) = 0\,, \tag{2.30}$$

$$\left(\partial_t - \kappa\partial_y^2\right) \theta_i(y,t) = 0\,, \tag{2.31}$$

where $v_i(y,t)$ is a three-component vector velocity field defined on a one-dimensional domain (parametrized by the spatial coordinate y), $\theta_i(y,t)$ is a scalar field, ν is the kinematic viscosity, and κ is the scalar diffusivity.

The advection submodel is specified by defining the mathematical operations performed during an "eddy event" and by formulating the rules that govern the random selection of such events. An eddy event consists of two mathematical operations. One is a measure-preserving map representing the fluid motions associated with a notional turbulent eddy. The other is a modification of the velocity profiles in order to implement energy transfers prescribed by dynamical rules. These operations are represented symbolically as

$$v_i(y) \to v_i\left(f(y) + c_i K(y)\right)\,, \qquad \theta \to \theta\left(f(y)\right)\,, \tag{2.32}$$

where $f(y)$ is the measure preserving triplet map (see Kerstein [131] for further details regarding the triplet map and also for other options). The mapping takes a line segment

$[y_0, y_0 + l]$, and shrinks it into an interval of a third of its original length and adds two identical copies rearranged such that the continuity of the advected fields is maintained. This simulates the process of decreasing length scale and increasing gradients during the (hypothesized) turbulent energy cascade. Eddy sizes of length l, and the times and locations of their occurrence for mapping events, are chosen at random from a specified probability distribution function based on the turbulence production mechanisms. The modeled SGS quantities are then used to provide SGS fluxes needed to advance in time the LES equations.

The SGS estimation model of Domaradzki and Saiki [132], and Domaradzki and Loh [133], provides an estimate of the unfiltered fluctuating velocity field appearing in the definition of the SGS stress tensor and consists of two steps. In the first (kinematic) step, an approximate inversion of the filter operator is performed, providing the value of the defiltered velocity field $\tilde{u}_i^0$ on an auxiliary grid. It is assumed in the procedure that the filter width Δ is twice the LES mesh size Δ_{LES}. This "deconvolution" is followed by the second (nonlinear dynamic) step, which generates scales twice smaller than the smallest scales resolved on the original LES mesh. In order to capture these scales a finer mesh is required. The fine mesh is constructed by halving the LES mesh in each Cartesian direction, *i.e.,* the fine mesh spacing is $\Delta_{LES}\backslash 2$. The previously computed $\tilde{u}_i^0$ is first interpolated from the coarse LES mesh to the fine mesh. Next, the small scales are produced as a result of nonlinear interactions among large scales resulting in a perturbation velocity $\tilde{u}_i'$ is given by

$$\tilde{u}_i' = \theta N_i' \,. \tag{2.33}$$

Here, N_i' is the growth rate of sub-grid scale velocities due to nonlinear interactions among resolved scales. It is computed as

$$N_i' = N_i^0 - \overline{N_i^0} \,, \tag{2.34}$$

where N_i^0 is the nonlinear term from which the advection effects by the large scales are removed:

$$N_i^0 = -\left(\tilde{u}_j^0 - \overline{u_j^0}\right) \frac{\partial}{\partial x_j} \tilde{u}_i^0 \,. \tag{2.35}$$

The timescale θ can be interpreted as large-eddy turnover time, and its value may vary with the position in a flow to reflect local conditions of turbulence. The estimated velocity $\tilde{u}_i = \tilde{u}_i' + \tilde{u}_i^0$ is given on the fine mesh and is used to compute the SGS stress on the coarse LES mesh directly from the definition.

We note that both the ODT of Kerstein and SGS estimation model of Domaradzki *et al.* have been applied to simulate turbulence in compressible flows.

Chapter 3
LARGE-SCALE SOLUTION PROCEDURE

In this chapter, the solution procedure employed to solve the unsteady, 3-D compressible N.–S. equations will be discussed. This constitutes the large-scale part of the overall multi-scale LES algorithm. Shocks and other phenomena unique to compressible flows are also captured in this part of the algorithm. Various schemes that have been developed to solve the compressible N.–S. equations will also be discussed in brief. We will further present results and validate the solver with standard test problems, the 1-D shock-tube problem described by Sod in [64] and the 3-D blast-wave problem [65].

3.1 Background

It is well-known that solutions to the compressible N.–S. equations admit discontinuities (shock waves). Therefore any numerical algorithm designed to solve the compressible N.–S. equations must also be capable of admitting such solutions. If the concept of the derivative is generalized in the spirit of distribution theory, it has been shown by Lax [134] in 1954 that the governing equations in PDE form admit "weak solutions" (that is, solutions not sufficiently regular to satisfy the PDE—*e.g.,* solutions containing discontinuities) and that such jumps appear in the right places.

To compute flows with shocks one can proceed along two different lines of thought resulting in two different methods/approaches. The first, which are known as "shock capturing" methods, relies on the proven mathematical legitimacy of weak solutions. These methods are designed to have shock waves appear naturally within the computational domain as a direct result of the overall flow field solution, *i.e.*, as a direct result of the general algorithm, without any special treatment to take care of the position of the shocks themselves. This is in contrast to the "shock fitting" approach, where shock waves are explicitly introduced into the flow field solution; the exact Rankine–Hugoniot relations for changes across a shock are used to relate the flow immediately ahead of and behind the shock, and the governing equations are used to calculate the remainder of the flow field. Although both these methods have inherent advantages and disadvantages, shock capturing methods are best suited for complex flow problems involving shock waves for which we do not know either the location or number of shocks—a typical scenario for engineering applications. The interested reader is referred to the text by Anderson [135], and the review by Moretti [136] for further details regarding these two classes of methods.

Shock capturing methods

Use of shock capturing methods allows us to develop algorithms to solve only the governing system of PDEs over the entire domain. Generally time-dependent PDEs are solved using time-marching procedures. Such procedures fall into one of two different classes or categories, explicit or implicit. The time step size in an explicit scheme is governed by the Courant number for high-Re problems, which must not be greater than unity for stable calculations. For low-Re problems the time step size is set by the viscous stress terms. The

stability limit for explicit schemes is set by regions in the domain where wave speeds are high. These regions drastically reduce the time step possible for explicit schemes. Implicit schemes, on the other hand, can maintain stability with much larger time steps when compared to their explicit counterparts. For coupled nonlinear PDEs, such as the compressible N.–S. equations, the use of implicit schemes results in having to iteratively solve a coupled system of linearized equations at each time step. Hence, a reduction in the number of time steps may be outweighed by increase in the number of arithmetic operations at each time step. Hybrid schemes containing both implicit and explicit approaches have also been developed to abate the disadvantages of the above mentioned approaches.

Numerical solutions to the N.–S. equations at high Re rely largely on methods developed for the Euler equations—the governing equations for inviscid flows. Most of the schemes applied to the Euler equations can be used for the N.–S. equations by applying centered discretizations of the viscous and heat conduction terms. Generally, such schemes employ a cell-centered unstaggered grid arrangement. In such a grid arrangement, the dependent variables are computed at cell centers, and the fluxes needed for these calculations are obtained at the cell walls (see, *e.g.,* the text by Hirsch [137]). Numerical algorithms designed to obtain solutions to the Euler equations can be categorized into two broad categories based on their ability to use wave propagation information.

Space-centered algorithms for the Euler equations were historically the first to be derived and still form the basis and reference for all other schemes derived since then. These schemes generally have centered spatial discretizations, and they do not distinguish upstream from downstream influences. Hence, the physical propagation of perturbations along characteristics, typical of all hyperbolic equations, is not considered in the definition of the numerical model. The entire Lax–Wendroff family of space-centered schemes and MacCormak's schemes fall under this category (see the texts by Hirsch [137] and Anderson [135] for derivations and analysis of such schemes). All second-order, three-point schemes generate oscillations in the vicinity of discontinuities due to the Gibbs phenomenon (see, *e.g.,* the relatively recent review by Gottlieb and Shu [138] for further details regarding this phenomenon). In order to remove the unavoidable oscillations around discontinuities in second-order centered schemes, Von Neumann and Richtmeyer [139] introduced the concept of artificial viscosity (artificial dissipation), wherein additional terms are added to smooth out oscillations. These additional artificial dissipation terms simulate the effects of physical viscosity on the scale of the mesh locally around discontinuities, and the effects are negligible (that of an order equal to or higher than the dominant truncation error) in smooth regions of the flow. Several formulations of this type are possible, and the interested reader is referred to [137] for different options. First-order schemes have dominant truncation errors proportional to the second-derivative which acts as a numerical viscosity. Therefore, these schemes will damp out high-frequency oscillations. However, even second-order implementations of space-centered schemes still appear to be unsatisfactory to achieve the best possible resolution of discontinuities. In order to capture the discontinuities to the sharpest possible extent, one needs to make use of wave propagation information embedded in the governing equations. Such schemes are known as upwind schemes to which we now turn.

Since the 1970s numerical analysts have focused their attention on a variety of schemes that can all be categorized as belonging to the same family because all are based on the theory of characteristics. The concept itself is far from being new, and an application using finite-

difference techniques had been proposed long ago by Courant *et al.* [140] in 1952. The related scheme is known as the CIR scheme (an acronym on the authors' names). Their procedure consists of tracing back from a solution at $(i\Delta x, (n+1)\Delta t)$ all three of the characteristic paths. Since the governing equations are nonlinear, the directions of these paths are not known exactly, but to a first approximation they can be taken equal to their known directions at $(i\Delta x, n\Delta t)$. Then each characteristic equation is solved using interpolated data at time $n\Delta t$ in an interval to the left of i for characteristics with positive speed and in an interval to the right of i for characteristics with negative speed. A major drawback of this method is that it is only first-order accurate.

In 1959, Godunov [141] suggested an approach for the numerical solution of the Euler equations that was philosophically different from the methods invented until then. Instead of solving for a general flow field by directy implementing a numerical method to solve the Euler equations written in PDE form, he suggested that the exact solutions to the Euler equations for a local region of the flow be pieced together to synthesize the overall flow field. In Godunov's method the solution is considered as a piecewise constant over each mesh cell at a fixed time, and the evolution of the flow to the next time results from solving a Riemann problem at the cell boundaries. A Riemann problem consists of finding the flow at $t + \Delta t$ if a flow consisting of two semi-infinite states is given at time t. If the Riemann problem is solved exactly in each interval, assuming that the two initial states are defined by the values at its end points, the slopes of all the characteristics, contact discontinuities, and shock waves are defined, and all the fluxes across boundaries are computable. The new piecewise constant at time $(n+1)\Delta t$ is then obtained by averaging the fluid states over each cell. However, Godunov's original method was only first-order accurate—which led to smearing of discontinuities; but it had the important property of monotonicity. Monotonicity is crucial when dealing with compression waves; it ensures that the only shock waves which develop result from the local collapse of continuous compressions, and it excludes any spurious shocks resulting from the numerical scheme (*e.g.,* "expansion" shocks). A detailed description of the method and applications to numerous flow problems as analyzed by Godunov and his co-workers over a time span of nearly twenty years are given in Godonov *et al.* [142].

Extension of Godonov-type methods to second-order accuracy was undertaken by van Leer. Passage from first-order to second-order accuracy in line with the Godunov method is accomplished in the representation of the state-variables in each cell. Van Leer's MUSCL approach (monotonic upstream-centered scheme for conservation laws) [143] generalized the Godunov method to second-order accuracy. As in Godunov's method the gas is divided into cells, and the interaction of these cells at their interfaces (boundaries) is considered in detail. Whereas in Godonov's method the distribution of the state quantities inside the cell are taken to be uniform, in the MUSCL approach the distributions are taken to be linear. The information contained in the slopes of these distributions makes it possible to attain second-order accuracy.

Higher-order geometrical approaches such as the piecewise parabolic method (PPM) [112] of Colella and Woodward have also been proposed. In the PPM method, the average value of the state variable in each cell is first interpolated using a piecewise parabolic distribution. With these interpolation functions a first guess is produced for the initial left and right states for the Riemann problem. These initial guesses for the left and right states are then corrected by solving the Riemann problem iteratively. The left and right states (values of the state

variables at the cell walls) are then used to construct fluxes. The solution now can be time advanced by conservative differencing. A review of some important second-order Godonov methods such as the PPM of Collela and Woodward, MUSCL approach of van Leer and the characteristic-based scheme of Roe, including explicit formulae to compute the fluxes, are discussed at length in Holt [144].

The disadvantage of higher-order extensions of Godunov's method is the difficulty of exactly solving the nonlinear Riemann problem at each interface. The exact solution of the Riemann problem requires an iterative procedure, which leads to relatively complex and time consuming numerical codes. Since computational efficiency is a major requirement for applied numerical methods, this results in restricted the use of such methods.

To overcome this drawback, several approximations to the Riemann problem have been developed. The most important approximate Riemann solvers have been developed by Roe [145], Osher [146], and Osher and Solomon [147]. A review on characteristic-based schemes for the Euler equations such as approximate Riemann solvers of Roe, flux-vector splitting of Steger and Warming [148] and other nonconservative schemes is given by Roe in [149]. We comment that even these schemes generate oscillations in the vicinity of discontinuities; they are designed to obtain second-order accuracy by representing the state variables in each cell as piecewise linear, thereby adding the slope of the linear variation as an additional variable to be determined. However, oscillations will be created when the slope in a cell becomes larger than the difference of adjacent mean values (see, *e.g.,* [137] for further details).

The motivation for the development of so called high-resolution methods which attempt to provide both high-order of accuracy and absence of oscillations in the vicinity of large gradients emerges from the efforts of numerical analysts to circumvent Godunov's theorem which states: *There are no monotone, linear schemes for the linear advection equation of second or higher-order accuracy.*. In other words, second-order accuracy and monotonicity are contradictory requirements (within the framework of linear methods).

This represents a severe limitation since first-order accurate schemes are too diffusive for practical applications. Hence, conditions less severe than monotonicity have been defined, allowing schemes with an accuracy higher than one, which generate entropy-satisfying solutions (*i.e.*, absence of spurious expansion shocks) without overshoots at shocks and contact discontinuities. Schemes of this type are called "high-resolution schemes." The development of such schemes started with the work of Boris and Book on flux corrected transport (FCT) methods [111], and van Leer on MUSCL schemes [143]. The introduction of the concept of total variation nonincreasing (TVNI) (now referred to as total variation diminishing, or more popularly as TVD) by Harten [108] proved to be a major step forward in the development of such procedures.

Intuitively, one can think of total variation as a measure of the overall amount of oscillation in a function over some prescribed interval; it is defined as:

$$TV(u(\cdot,t)) = sup_{_P} \sum_{i=-\infty}^{\infty} |u(x_{i+1},t) - u(x_i,t)|$$

for each fixed time t, with the supremum running over all partitions $P = \{x_1, \ldots, x_n\}$ of the interval. The supremum of a bounded set $\boldsymbol{S}$, $sup(\boldsymbol{S})$, is defined as the the smallest upper bound of the set $\boldsymbol{S}$. We note that TVD implies monotonicity preservation. To see this,

consider a monotone function; then the total variation has a particular value. If the function does not remain monotone, say as t increases, and instead develops new maxima and minima (oscillations), the total variation increases. However, of course, the total variation cannot increase in a TVD method, and thus the solution must remain monotone.

Harten [108] proved that any linear TVD scheme is monotone and hence only first-order accurate. This restriction does not apply to nonlinear schemes, which can be made TVD while having second-order accuracy. This possibility explains the importance of the TVD concept in the generation of high-resolution methods.

Despite their excellent stability and high-resolution properties, TVD schemes have a serious deficiency in that they degenerate to first order at smooth extrema of a solution [150]. In [151] Harten and Osher relaxed the TVD restriction and replaced it by a UNO (uniformly nonoscillatory) restriction; in this context the total number of numerical extrema does not increase, and their amplitudes could be allowed to increase slightly. It was soon realized that even the UNO restriction was still too strong since it excluded schemes of higher than second-order accuracy. Thus, the concept of essentially nonoscillatory (ENO) schemes was first given by Harten *et al.* [152] in 1987. Any ENO scheme uses an adaptive stencil which is chosen based on the local smoothness of the solution—measured by the Newton divided differences of the numerical solution. Thus the accuracy of the scheme is never reduced, but the local stencil automatically avoids crossing discontinuities. Such schemes allow both the number of numerical extrema and their amplitudes to increase; however, such additional oscillations are controlled to the level of truncation errors even if the solution is not smooth. ENO schemes have been extremely successful in applications because they allow arbitrary orders of accuracy and generate sharp (nearly) monotone shock transitions. The ENO scheme described in [152] is a finite-volume scheme; Shu and Osher ([153], [154]) have also developed finite-difference based ENO schemes in conservation form. Analysis of ENO schemes is given in Harten *et al.* [152], and applications of ENO schemes to 2-D and 3-D compressible turbulent flow calculations are given in Shu *et al.* [155].

An improvement over the ENO scheme is the WENO (weighted ENO) scheme, which was first developed by Liu *et al.* [156]. Like ENO, WENO uses adaptive stencils based on local smoothness of the numerical solution to automatically achieve high-order accuracy and nonoscillatory properties near discontinuities. While ENO uses just one (optimal in some sense) out of many candidate stencils when doing the reconstruction, WENO uses a convex combination of all candidate stencils, each being assigned a nonlinear weight that depends on the local smoothness of the numerical solution based on that stencil.

Hybrid schemes

In 1981 MacCormack [157] presented an explicit-implicit predictor-corrector method that involved the "inversion" of bi-diagonal matrices in an effort to reduce computer time. The algorithm was formally second-order accurate in space and time. While marching in time, the direction of the one-sided finite differencing was switched between predictor and corrector steps. Implicit steps were taken as forward differencing in the predictor and backward differencing in the corrector. Fourth-order artificial dissipation, expressed in terms of pressure, was used in the explicit part. Implicit damping was also added to prevent oscillations around sharp discontinuities, such as shocks (see [157] for further details).

An implicit-explicit hybrid scheme which extended Godonov schemes to the implicit regime was developed by Fryxell *et al.* [158]. Dai *et al.* [159] implemented an iterative version of the scheme developed in [158] for solving the Euler equations. This scheme is of Godunov type in both the implicit and explicit regimes, is conservative, is accurate to second order in both space and time for all Courant numbers, and is able to switch smoothly between the implicit and explicit calculations. These switches are determined based on the Courant number: if the Courant number is less than unity, the equations are solved explicitly; if it is greater than unity, the equations are solved implicitly since the domain of dependence extends beyond a cell interface (see [159] for further details). We have by no means attempted a comprehensive discussion of the various types of schemes developed for the Euler equations. There is an overwhelming amount of literature on such schemes built up over a period of more than 60 years, and the ambitious reader is referred to texts by Laney [160] and Hirsch [137] for a comprehensive review.

Our solver is based on a predictor-corrector methodology. The predictor part of the scheme consists of a half time step explicit forward Euler time integration of the Euler equations followed by a full time step implicit backward Euler time integration of the complete N.–S. equations. Spatial discretization is second-order centered for both predictor and corrector parts of the scheme with dependent variables being evaluated at cell centers and fluxes evaluated at cell walls. The nonlinearities in the N.–S. equations are handled iteratively by δ-form quasilinearization; and δ-form Douglas–Gunn time-splitting [63] is used to solve the linearized equations at each time step. Shocks are captured by using MacCormack and Baldwin higher-order artificial viscosity as given in [137]. The classic shock-tube problem described by Sod [64] and the three-dimensional blast wave problem as given in Toro [65] are employed to validate the solver.

The rest of this chapter is organized as follows. In the next section we provide an overview of the governing equations in conservation form and the mathematical formulation of the hybrid scheme based on δ-form Douglas–Gunn time splitting. An overview of the test cases (shock tube problem and 3-D blast-wave problem) and the pseudo-language algorithm is presented in the third section. We then present results to validate the solver using the above test cases in the last section.

3.2 Mathematical Formulation

3.2.1 Governing equations

We begin by presenting the compressible N.–S. equations in their generic form:

$$\frac{\partial \boldsymbol{U}}{\partial t} + \frac{\partial \boldsymbol{F}}{\partial x} + \frac{\partial \boldsymbol{G}}{\partial y} + \frac{\partial \boldsymbol{H}}{\partial z} = 0\,. \tag{3.1}$$

Equation (3.1) represents the entire system of governing equations in conservation form if $\boldsymbol{U, F, G, H}$ are interpreted as column vectors given by

$$\boldsymbol{U} = \begin{bmatrix} \rho \\ \rho u \\ \rho v \\ \rho w \\ \rho E \end{bmatrix}, \tag{3.2a}$$

$$\boldsymbol{F(U)} = \begin{bmatrix} \rho u \\ \rho u^2 + p - \tau_{xx} \\ \rho uv - \tau_{xy} \\ \rho uw - \tau_{xz} \\ \rho Eu + pu - k\frac{\partial T}{\partial x} - u\tau_{xx} - v\tau_{xy} - w\tau_{xz} \end{bmatrix}, \tag{3.2b}$$

$$\boldsymbol{G(U)} = \begin{bmatrix} \rho v \\ \rho vu - \tau_{yx} \\ \rho v^2 + p - \tau_{yy} \\ \rho vw - \tau_{yz} \\ \rho Ev + pv - k\frac{\partial T}{\partial y} - u\tau_{yx} - v\tau_{yy} - w\tau_{yz} \end{bmatrix}, \tag{3.2c}$$

$$\boldsymbol{H(U)} = \begin{bmatrix} \rho w \\ \rho wu - \tau_{zx} \\ \rho wv - \tau_{zy} \\ \rho w^2 + p - \tau_{zz} \\ \rho Ew + pw - k\frac{\partial T}{\partial z} - u\tau_{zx} - v\tau_{zy} - w\tau_{zz} \end{bmatrix}. \tag{3.2d}$$

Elements of the stress tensor are given in Cartesian tensor notation by

$$\tau_{ij} = \mu\left(\frac{\partial u_i}{\partial x_j} + \frac{\partial u_j}{\partial x_i}\right) + \delta_{ij}\lambda\frac{\partial u_k}{\partial x_k}, \qquad i, j = 1, 2, 3, \tag{3.3}$$

and the equation of state for a perfect gas is used:

$$p = \rho RT. \tag{3.4}$$

To relate Eq. (3.3) to the subscript notation of (3.2) note that, *e.g.,* i=1 and j=2 in the shear stress tensor corresponds to the shear stress component τ_{xy}. Further the first subscript, *e.g*, the x subscript implies that we are considering a component acting on a face perpendicular to the x axis, and the y subscript indicates that this stress is in the y direction. In Eq. (3.2) ρ, p and T are the usual density, pressure and temperature; $\boldsymbol{u} \equiv (u_1, u_2, u_3) = (u, v, w)^T$ is the velocity vector; the quantity $E \equiv (e + \boldsymbol{u}^2/2)$, corresponds to total energy (per unit mass) with $\boldsymbol{u}^2$ denoting $\boldsymbol{u} \cdot \boldsymbol{u}$, and e is internal energy. Finally, k is thermal conductivity; μ is dynamic viscosity; λ is second viscosity, and δ_{ij} is the Kronecker delta. The corresponding Euler equations are obtained by setting $\mu, \lambda, k \equiv 0$.

The column vectors $\boldsymbol{F, G, H}$ in Eq. (3.2) are called the flux terms (or flux vectors). The column vector $\boldsymbol{U}$ is the solution vector, and its elements are conserved variables. This is in contrast with *u, v, w* and E which by themselves are examples of primitive variables. The

primitive variables are obtained from the flux variables via the following relationships

$$\begin{aligned} \rho &= \rho\,, \\ u &= \frac{\rho u}{\rho}\,, \\ v &= \frac{\rho v}{\rho}\,, \\ w &= \frac{\rho w}{\rho}\,, \\ E &= \frac{\rho E}{\rho}. \end{aligned} \tag{3.5}$$

3.2.2 Predictor stage

We first present the standard cell-centered unstaggered grid arrangement employed. In

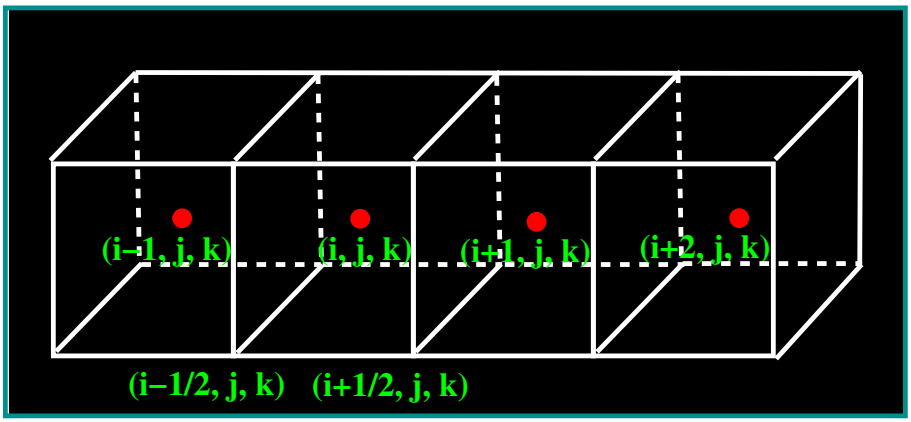

Figure 3.1 Schematic of computational Grid.

Fig. 3.1 full grid point indices (*e.g.*, i, j , k) correspond to cell-centers, and half grid point indices (*e.g.*, $i+\frac{1}{2}$, j , k) correspond to cell walls. Horizontal fluxes $\boldsymbol{F}$ are evaluated on vertical cell walls; vertical fluxes $\boldsymbol{G}$ are evaluated on horizontal cell walls; transverse fluxes $\boldsymbol{H}$ are evaluated on transverse cell walls. These are evaluated using

$$\boldsymbol{F}_{i+\frac{1}{2}} = \tfrac{1}{2}\left(\boldsymbol{F}_{i-1,\,j\,,k} + \boldsymbol{F}_{i,\,j\,,k}\right)\,, \tag{3.6}$$

$$\boldsymbol{G}_{j+\frac{1}{2}} = \tfrac{1}{2}\left(\boldsymbol{G}_{i,\,j-1\,,k} + \boldsymbol{G}_{i,\,j\,,k}\right)\,, \tag{3.7}$$

$$\boldsymbol{H}_{k+\frac{1}{2}} = \tfrac{1}{2}\left(\boldsymbol{H}_{i,\,j\,,k-1} + \boldsymbol{H}_{i,\,j\,,k}\right)\,. \tag{3.8}$$

The predictor stage consists of a half time step forward time integration of the Euler equations with a centered discretization in space. On discretizing Eq. (3.1) with appropriate definitions for $\boldsymbol{F}$, $\boldsymbol{G}$, and $\boldsymbol{H}$ we obtain a discrete formula for the unknown $\boldsymbol{U}_{i,j,k}$ as

$$\boldsymbol{U}^{n+1/2}_{i,j,k} = \boldsymbol{U}^{n}_{i,j,k} - \Delta t d_{0,x}\boldsymbol{F}^{n}_{i,j,k} - \Delta t d_{0,y}\boldsymbol{G}^{n}_{i,j,k} - \Delta t d_{0,z}\boldsymbol{H}^{n}_{i,j,k}\,. \tag{3.9}$$

The difference operator $d_{0,x}$ is defined as $d_{0,x}\left(u_{i,j,k}\right) = \left(u_{i+1,j,k} - u_{i,j,k}\right)/\Delta x$ with corresponding definitions for $d_{0,y}$ and $d_{0,z}$. We also note that the time-step $\Delta t = \Delta t/2$, *i.e.,* time advancement in the predictor is performed only for half a time-step. The value of $\boldsymbol{U}_{i,j,k}^{n+\frac{1}{2}}$ now serves as an initial guess for the corrector step.

3.2.3 Corrector stage

In the corrector stage of the algorithm we implicitly solve the complete N.–S. equations; hence, there is a need to linearize the nonlinear terms in the equations. This is achieved by employing the Newton–Kantorovich procedure (see, *e.g.,* Kantorovich and Akilov [161]). The form that we shall employ here is often termed quasilinearization (even though it is actually linearization and not quasilinearization). The simplest form of quasilinearization from a conceptual standpoint was introduced by Bellman and Kalaba [162] whereby the dependent variables, as well as their derivatives, are viewed as independent variables in a Fréchet–Taylor expansion of any nonlinear terms present in the problem. We comment that, though this formulation is a very general and effective way to treat nonlinear PDEs, there is considerable arithmetic involved in evaluating the resulting equations. We therefore consider an alternative (and equivalently accurate) formulation, often called δ-form quasilinearization, to which we now proceed.

Quasilinearization

Notice that the fluxes are nonlinear functionals of the solution vector $\boldsymbol{U}$. We first linearize the fluxes by constructing Fréchet–Taylor expansions in δ-form. For the general m^{th} iteration we have

$$\begin{aligned}
\boldsymbol{F}(\boldsymbol{U})^{(m+1)} &= \boldsymbol{F}(\boldsymbol{U})^{(m)} + \left(\frac{\partial \boldsymbol{F}}{\partial \boldsymbol{U}}\right)^{(m)} \delta \boldsymbol{U}\,, \\
\boldsymbol{G}(\boldsymbol{U})^{(m+1)} &= \boldsymbol{G}(\boldsymbol{U})^{(m)} + \left(\frac{\partial \boldsymbol{G}}{\partial \boldsymbol{U}}\right)^{(m)} \delta \boldsymbol{U}\,, \\
\boldsymbol{H}(\boldsymbol{U})^{(m+1)} &= \boldsymbol{H}(\boldsymbol{U})^{(m)} + \left(\frac{\partial \boldsymbol{H}}{\partial \boldsymbol{U}}\right)^{(m)} \delta \boldsymbol{U}\,,
\end{aligned} \tag{3.10}$$

where $\delta \boldsymbol{U} = \boldsymbol{U}^{(m+1)} - \boldsymbol{U}^{(m)}$ is the difference between two successive iterates. In general, for a time-dependent calculation we have $\delta \boldsymbol{U} = \mathbf{U}^{n+1(m+1)} - \boldsymbol{U}^{n+1(m)}$. Substituting Eq. (3.10) into Eq. (3.1) and discretizing the resulting linearized system, leads to

$$\begin{aligned}
\boldsymbol{U}^{n+1(m+1)} = \boldsymbol{U}^{n} &- \Delta t d_{0,x}(\boldsymbol{F}^{(m)}) - \Delta t d_{0,y}(\boldsymbol{G}^{(m)}) - \Delta t d_{0,z}(\boldsymbol{H}^{(m)}) - \Delta t D_{0,x}\left(\frac{\partial \boldsymbol{F}^{(m)}}{\partial \boldsymbol{U}} \delta \boldsymbol{U}\right) \\
&- \Delta t D_{0,y}\left(\frac{\partial \boldsymbol{G}^{(m)}}{\partial \boldsymbol{U}} \delta \boldsymbol{U}\right) - \Delta t D_{0,z}\left(\frac{\partial \boldsymbol{H}^{(m)}}{\partial \boldsymbol{U}} \delta \boldsymbol{U}\right)\,.
\end{aligned} \tag{3.11}$$

The centered-difference operator $D_{0,x}$ is defined as $D_{0,x}\left(u_{i,j,k}\right) = \left(u_{i+1,j,k} - u_{i-1,j,k}\right)/2\Delta x$ with corresponding definitions for $D_{0,y}$ and $D_{0,z}$.

We now observe that the unknown time level $n+1$ solution occurs in two different ways in the above equation, namely both as $\boldsymbol{U}^{n+1}$ and as $\delta\boldsymbol{U}$. We need the expression to be entirely in terms of $\delta\boldsymbol{U}$ so we write $\boldsymbol{U}^{n+1}$ as $\boldsymbol{U}^{(m+1)} = \delta\boldsymbol{U} + \boldsymbol{U}^{(m)}$ and substitute into Eq. (3.11) to obtain

$$\begin{aligned}\delta\boldsymbol{U}^{n+1(m+1)} &= \boldsymbol{U}^n - \boldsymbol{U}^{n+1(m)} - \Delta t d_{0,x}(\boldsymbol{F}^{(m)}) - \Delta t d_{0,y}(\boldsymbol{G}^{(m)}) - \Delta t d_{0,z}(\boldsymbol{H}^{(m)}) \\ &\quad - \Delta t D_{0,x}\left(\frac{\partial \boldsymbol{F}}{\partial \boldsymbol{U}}\delta\boldsymbol{U}\right) - \Delta t D_{0,y}\left(\frac{\partial \boldsymbol{G}}{\partial \boldsymbol{U}}\delta\boldsymbol{U}\right) - \Delta t D_{0,z}\left(\frac{\partial \boldsymbol{H}}{\partial \boldsymbol{U}}\delta\boldsymbol{U}\right). \qquad (3.12)\end{aligned}$$

The solution vector now becomes $\delta\boldsymbol{U}$ instead of $\boldsymbol{U}$. $\partial\boldsymbol{F}/\partial\boldsymbol{U}$, $\partial\boldsymbol{G}/\partial\boldsymbol{U}$, and $\partial\boldsymbol{H}/\partial\boldsymbol{U}$ result in three 5×5 matrices which are the Jacobian matrices for the 3-D compressible N.–S. equations. We next rearrange Eq. 3.12as

$$\begin{aligned}&\left\{I + \Delta t D_{0,x}\left(\frac{\partial F_\ell}{\partial U_\ell}\cdot\right)^{(m)} + \Delta t D_{0,y}\left(\frac{\partial G_\ell}{\partial U_\ell}\cdot\right)^{(m)} + \Delta t D_{0,z}\left(\frac{\partial H_\ell}{\partial U_\ell}\cdot\right)^{(m)}\right\}\delta U_\ell \\ &\quad = U_\ell^n - U_\ell^{n+1(m)} - \Delta t d_{0,x}(F_\ell^{(m)}) - \Delta t d_{0,y}(G_\ell^{(m)}) - \Delta t d_{0,z}(H_\ell^{(m)}) \\ &\quad - \Delta t D_{0,x}\left(\frac{\partial F_\kappa}{\partial U_\kappa}\delta U_\kappa\right)^{(m)} - \Delta t D_{0,y}\left(\frac{\partial G_\kappa}{\partial U_\kappa}\delta U_\kappa\right)^{(m)} - \Delta t D_{0,z}\left(\frac{\partial H_\kappa}{\partial U_\kappa}\delta U_\kappa\right)^{(m)}, \\ &\quad \forall\ \ell, \kappa \in \{1,2,3,4,5\},\ \kappa \neq i\,. \qquad (3.13)\end{aligned}$$

There are several remarks to be made regarding Eq. (3.13). The obvious one is that it contains five unknowns: $\delta U_1, \ldots, \delta U_5$. We further note that, the δUs have been arranged such that the unknown corresponding to the equation under consideration appears on the left-hand side and all other unknowns appear on the right-hand side. As an example, if we were solving the continuity equation (which corresponds to ℓ=1) only δU_1=$\delta\rho$ appears on the LHS, and the other unknowns such as $\delta\rho u$, $\delta\rho v$, $\delta\rho w$ and $\delta\rho E$ appear on the RHS. In particular, the equations are now decoupled and will be solved sequentially. We should also observe that as $U_\ell^{n+1(m)} \to U_\ell^{n+1}$, $\delta U_\ell \to 0$. Thus, if the Newton–Kantorovich iterations converge, they converge to a solution of the original nonlinear problem. Moreover, in the context of using time-splitting methods within this solution process, the splitting errors are automatically removed because it is the convergence of the unsplit equations that is tested.

Using compact notation, Eq. (3.13) can be rewritten as

$$[I + A_{1_\ell} + A_{2_\ell} + A_{3_\ell}]\,\delta U_\ell = S^{(m)} \qquad \ell = 1, \ldots, 5\,, \qquad (3.14)$$

with obvious definitions for A_{1_ℓ}, A_{2_ℓ}, A_{3_ℓ}, and S^m. An important consequence of the above rearrangement is that we obtain a form to which time-splitting procedures can be directly applied; this is considered in the sequel.

δ-form Douglas–Gunn time splitting

We comment at the outset that the reason for choosing a time-splitting method such as Douglas–Gunn is its efficiency in solving multi-dimensional problems. This is achieved by decomposing multi-dimensional problems into sequences of 1-D problems. We begin by

recalling that the standard form for any two-level difference scheme applied to a δ-form equation is given by

$$\left[I + A^{(n+1)}\right] \delta u + B u^{(n)} = s^{(n)} \,, \tag{3.15}$$

where in 3-D, typically, $A = A_1 + A_2 + A_3$ corresponding to the three spatial directions, modulo treatment of mixed derivatives. Once we arrive at this form for any problem that we may wish to solve, splitting can be done in the usual way. In general, we have

$$[I + A_p] \, \delta u^{(p)} + \sum_{r=1}^{p-1} A_r \delta u^{(r)} + \sum_{r=p+1}^{q} A_r \delta u^{(n)} + B u^{(n)} = s^{(n)} \,, \qquad p = 1, 2, 3 \,. \tag{3.16}$$

We note that the index q corresponds to the number of the split steps per equation. If iterations have been carried to convergence in the preceding time step, then $\delta u^{(n)} \cong 0$. Then for the first split step it follows that

$$[I + A_1] \, \delta u^{(1)} = s^{(n)} - B u^{(n)} \,, \tag{3.17}$$

and in general,

$$[I + A_p] \, \delta u^{(p)} + \sum_{r=1}^{p-1} A_r \delta u^{(r)} = s^{(n)} - B u^{(n)} \,. \tag{3.18}$$

Similarly,

$$[I + A_{p-1}] \, \delta u^{(p-1)} + \sum_{r=1}^{p-2} A_r \delta u^{(r)} = s^{(n)} - B u^{(n)} \,, \tag{3.19}$$

and subtracting this from Eq. (3.18) yields

$$[I + A_p] \, \delta u^{(p)} - [I + A_{p-1}] \, \delta u^{(p-1)} + A_{p-1} \delta u^{(p-1)} = 0 \,. \tag{3.20}$$

Thus,

$$[I + A_p] \, \delta u^{(p)} = \delta u^{(p-1)} \quad \forall \quad p = 2, \ldots, q \,, \tag{3.21}$$

with

$$\delta u \equiv \delta u^{(q)} \,. \tag{3.22}$$

Then

$$u^{n+1(m+1)} = u^{n+1(m)} + \delta u \,. \tag{3.23}$$

Now recall from Eq. (3.14) that the δ-form quasilinearization of the equations of motion gave us the standard form to which the δ-form time-splitting procedure can be applied. For the first split step we obtain

$$[I + A_{p_\ell}] \, \delta U_\ell^{(1)} = S^m \qquad p = 1 \,; \tag{3.24}$$

and the second split step is

$$[I + A_{p_\ell}] \, \delta U_\ell^{(2)} = \delta U_\ell^{(1)} \qquad p = 2 \,, \tag{3.25}$$

and the third split step is

$$[I + A_{p_\ell}] \, \delta U_\ell^{(3)} = \delta U_\ell^{(2)} \qquad p = 3 \,. \tag{3.26}$$

The update formula

$$U_\ell^{(m+1)} = \delta U_\ell^{(3)} + U_\ell^{(m)} \,, \tag{3.27}$$

provides the new approximation to the solution. We further notice that the time-splitting along with the second-order centered discretization employed herein leads to a tri-diagonal system, that can be solved efficiently using LU decomposition at each split step. Further, the dimensional splitting of the equations leads to an algorithm that is easily parallelized.

Artificial dissipation and filtering

As alluded to in the Background section, all second-order schemes generate oscillations around sharp discontinuities. In order to remove the unavoidable high-frequency oscillations, we use the concept of artificial viscosity. We apply a third-order artificial viscosity developed by MacCormack and Baldwin. We will follow [137] for the formulation of the dissipation term D. This term is made proportional to a second derivative of the pressure field in order to enhance the effects of dissipation in the presence of strong pressure gradients (shocks, expansion waves) and to reduce it in smooth flow regions. The factor D is defined as

$$D = \epsilon \Delta x^2 \frac{|\boldsymbol{u}| + c}{p} \left| \frac{\partial^2 p}{\partial x^2} \right| \,.$$

The modified numerical flux denoted by f now becomes (in 1D)

$$f^*_{i+\frac{1}{2}} = f_{i+\frac{1}{2}} - \epsilon \Delta x^3 \frac{|\boldsymbol{u}| + c}{p} \left| \frac{\partial^2 p}{\partial x^2} \right| \frac{\partial \boldsymbol{U}}{\partial x} \,.$$

This is generally computed as

$$f^*_{i+\frac{1}{2}} = f_{i+\frac{1}{2}} - \epsilon \Delta x^2 \left(|\boldsymbol{u}| + c \right)_{i+\frac{1}{2}} \frac{|p_{i+1} - 2p_i + p_{i-1}|}{p_{i+1} + 2p_i + p_{i-1}} \left(U_{i+1} - U_i \right) \,, \tag{3.28}$$

with direct extension to multi-dimensions. We note that the parameter ϵ in the above equations has to be prescribed *apriori* by the user at the time of the simulation. In our case, in three dimensions we end up with five such parameters (one for each equation) which have to be assigned values.

Since solutions to the compressible N.–S. equations are nonsmooth, we take explicit measures to treat the effects of "aliasing." It is well known that since aliasing arises from an inability to represent high-wavenumber components of a solution in its numerical approximation (which is inherent in a LES methodology), the remedy must always be some kind of smoothing or mollification that introduces additional dissipation into the numerical scheme, thus damping higher-wavenumber effects. Although artificial dissipation methods discussed previously provide additional dissipation (which handles aliasing effects to some extent), they are specifically designed to mitigate the Gibbs phenomenon oscillations in the presence of shocks (a rather different problem). To treat the "aliasing" problem we take the filtering approach, *i.e.,* use of post-processing filters as is routinely done in essentially all signal processing by the electrical engineering community. A collection of numbers comprising a discrete solution can be easily interpreted as a "signal." The simple linear filter to be used

herein was probably first introduced by Shuman [163] in the context of smoothing meteorological measurements and analyzed in detail by Shapiro [164]. In particular, we make use of the Shuman filter as our post-processing filter. The Shuman filter is very simple; it employs dependent variable values in a small neighborhood of grid points in "physical" space to remove the effects of aliasing. The mathematical formula for the Shuman filter is as follows in 1D (see Shuman [163]):

$$u_i = \frac{u_{i+1} + \beta u_i + u_{i+1}}{2 + \beta}, \qquad i = 2, \ldots, N-1, \tag{3.29}$$

where β is a filter parameter, and $u_{i=1}^{N}$ is the grid function. Yang and McDonough [165] have demonstrated the effectiveness of the filtering approach involving a Burgers' equation model of turbulence. They compared the performance of the Shuman filter with two other filters that are widely used in LES. They found that the Shuman filter provided results that were superior to those of either a Gaussian filter or a Fourier sharp cut-off filter. Investigations involving the influence of the parameter value was also undertaken; it was discovered through numerical experiments that proper choice of the value is important; but once it is in the correct range the quantitative features of the computed results are not extremely sensitive to this value.

3.2.4 Pseudo-language algorithm

In this subsection we will present the pseudo-language algorithm corresponding to the foregoing treatment of the mathematical formulation of the large-scale solution procedure. **Algorithm 1:** *Suppose n time steps have been completed. To advance the solution to time level n+1, perform the following steps.*

1 *Calculate Euler cell-wall fluxes from their definitions.*

2 *Add artificial dissipation to the fluxes to obtain modified fluxes.*

3 *Obtain an initial guess for solving the N.–S. equations by first solving the Euler equations, i.e., solve the discrete system Eq.* (3.9).

4 *Do m=1,nlitr*

- i *Calculate N.–S. fluxes from their definitions.*
- ii *Add artificial dissipation to the fluxes to obtain modified fluxes to be used in evaluating the solution vector.*
- iii *Solve discrete continuity, momentum and energy equations, i.e., solve Eq.* (3.14) *i=1, ...,5 by following the time splitting procedure Eq.* (3.24)*–Eq.* (3.27) *for each equation separately (sequentially)*
- iv *Test convergence: If max* $(||\delta \boldsymbol{U}||) \leq \epsilon$*, then goto 6*
- v *If* $m > nlitr$ *then*
  Write error message
  stop

5 *Repeat m*

6 *Filter solution using the Shuman filter*

7 *Calculate primitive variables from Eqs.* (3.5)

3.3 Test Cases

To validate our solver we have chosen the shock-tube problem described by Sod [64] and the 3-D blast-wave problem described by Toro [65]. The two test cases serve two distinct purposes for evaluating the performance of our solver. The shock-tube problem provides us with an opportunity to evaluate the capability of the solver to simulate the boundary layer; however, this test case is inherently one-dimensional. The 3-D blast-wave problem on the other hand provides us with a scenario to generally assess the 3-D capability of the solver. Towards the end of this section we will also specify values for the transport properties, artificial dissipation parameters, and Shuman filter parameters employed in these simulations.

3.3.1 Shock tube problem

The shock-tube problem is an interesting test case because the exact time-dependent solution is known for the Euler equations in 1-D, and, hence, we can compare our computed viscous solution at least qualitatively to the exact inviscid solution. The initial data for the shock-tube problem are composed of two uniform states (generally known as left and right states) separated by a discontinuity, physically a diaphragm. When the diaphragm is broken, two pressure waves appear (a shock wave and an expansion fan) and propagate into the initial fluid states, resulting in two uniform states 2 and 3 as shown in Fig. 3.2. The final

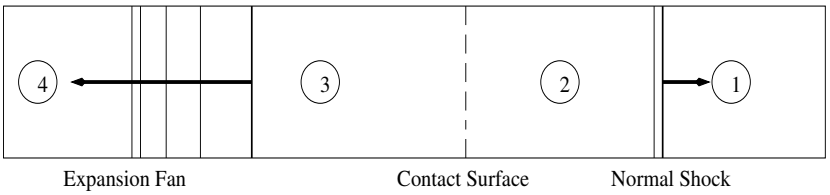

Figure 3.2 Schematic of a shock tube.

states 2 and 3 are separated by a contact discontinuity (discontinuity in first derivatives), implying that the pressure and the velocity of these states are equal, but density jumps across the discontinuity. The governing equations Eq. (3.1) are solved on a domain Ω (a rectangular tube) with dimensions $L \times H \times W \equiv 1 \times 0.2 \times 0.2$ in x-y-z space, respectively, with boundary conditions consisting of the no-slip condition imposed at $y = 0$, $y = H$, $z = 0$, and $z = W$, an inflow condition $\partial \boldsymbol{U}/\partial n = 0$, and outflow condition $\partial \boldsymbol{U}/\partial n = 0$ applied at $x = 0$ and $x = L$, respectively.

We validate the solver in a shock tube set up for three different pressure ratios across the initial discontinuity at time t_0. Test 1 is the popular Sod's test with an initial pressure ratio

of 10, whereas Test 2 employs a much stronger initial pressure ratio of 100. In the first case the shock (more appropriately a strong gradient) is of moderate strength, while the second case corresponds to a strong shock and supersonic Mach numbers after the expansion. Test 3 is designed to assess the robustness of the numerical method—it has a pressure ratio of 100000; its solution consists of a strong right traveling shock wave, a contact surface and a left rarefaction wave. The initial conditions in the left and right sections of the shock tube are given in Table 3.1.

Table 3.1 Initial conditions for shock-tube problem.

Test	ρ_l	u_l	p_l	ρ_r	u_r	p_r
1	1.0	0	1.0	0.125	0	0.1
2	1.0	0	1.0	0.01	0	0.01
3	1.0	0	1000.0	1	0	0.01

3.3.2 Blast-wave problem

The 3-D blast wave problem is like a three-dimensional extension of the shock-tube problem described above. The initial conditions consist of a cube $\Omega = 2 \times 2 \times 2$ in x-y-

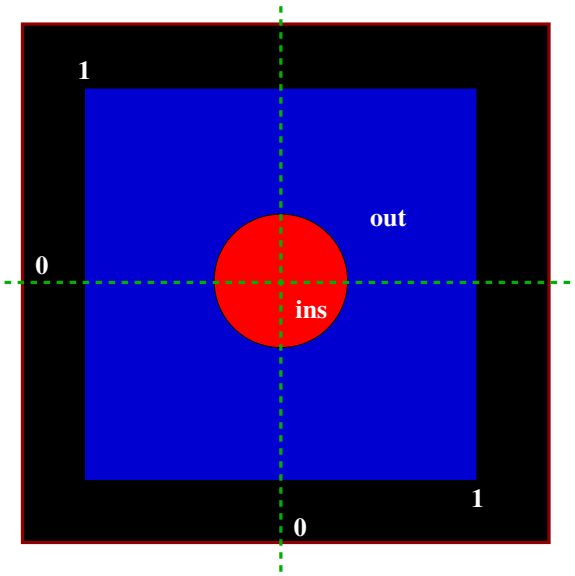

Figure 3.3 Schematic of initial condition for spherical explosion; red circular zone has high pressure and density.

z space, inside which there is a sphere of radius $R = 0.4$ centered at $(0, 0, 0)$ with high pressure and density. The flow variables take constant values in each of these regions (inside and outside the sphere) and are joined by a spherical discontinuity at time $t = 0$. This is represented in Fig. 3.3. The two constant states are given in Table 3.2.

Table 3.2 Initial conditions for blast-wave problem.

Test	ρ_{ins}	u_{ins}	p_{ins}	ρ_{out}	u_{out}	p_{out}
4	1.0	0	1.0	0.125	0	0.1

3.3.3 Transport properties, artificial dissipation parameters and other constants

In this subsection we will give values for the transport properties, artificial dissipation parameters, and Shuman filter parameters, which are employed in obtaining numerical solutions to the test cases described in the previous subsection.

We note that the code was developed within the framework of incorporating constant transport properties. For solving the four test cases whose initial data are dimensionless, the values of these properties were nondimensionalized by a reference value of unity with corresponding SI units. In particular, the dynamic viscosity of air μ was taken to be $1.73e-5$ (viscosity of air at standard conditions). The second viscosity λ is related to μ via the Stokes relation given by $\lambda = -\frac{2}{3}\mu$. The thermal conductivity k of air is given by 0.03 (thermal conductivity of air at standard conditions). Consistent with our assumption that we are dealing with perfect gases, the ratio of specific heats for air at standard conditions is given by $\gamma = 1.4$, and the specific gas constant $R = 287$.

Recall that the dissipation term D in the MacCormack and Baldwin artificial viscosity incorporates a parameter ϵ in its construction, which has to be assigned a value *a priori* in the simulation. For solving the 3-D N.–S. equations we have to assign values for five such parameters (one for each equation). This process of assigning multiple values immediately suggests that it would take a concentrated effort to obtain optimal values for these parameters for each problem over a wide range of test cases employed herein. Hence, we tuned the artificial dissipation parameters only for Test Case 1 and employed the same values for Test Cases 2 and 3. Since Test Case 4 is a three-dimensional extension of Test Case 1, we used some of the values from Test Case 1, but we set the parameter values to be identical in the three momentum equations due to the symmetry present in Test Case 4. In particular, the artificial dissipation parameter values used in simulations of Test Cases 1 to 3 are: $\epsilon_\rho = 2.0$, $\epsilon_{\rho u} = 2.0$, $\epsilon_{\rho v} = 28.0$, $\epsilon_{\rho w} = 28.0$, $\epsilon_E = 4.0$. The values assigned to the parameters for Test Case 4 are: $\epsilon_\rho = 2.0$, $\epsilon_{\rho u} = 4.0$, $\epsilon_{\rho v} = 4.0$, $\epsilon_{\rho w} = 4.0$, $\epsilon_E = 4.0$.

Also, in the context of implementing the Shuman filter to handle aliasing errors we have to assign values to the filter parameter β for each component of the solution vector. We conducted numerical tests to choose the values of these filter parameters. In particular, the values of these parameters were chosen such that the large-scale solution did not blow up, and smearing of the large-scale solution was not considerable. We remark that the same kind of conflict arises even in traditional LES procedures where the user has to specify a filter width Δ. The filter parameters for the test cases were chosen to be: $\beta_\rho = 10000$, $\beta_{\rho u} = 7000$, $\beta_{\rho v} = 7000$, $\beta_{\rho w} = 7000$, and $\beta_{\rho E} = 10000$.

3.4 Results and Discussions

Most 1-D and 2-D results presented in this section are extracted from positions in the domain as shown in Fig. 3.4 unless noted otherwise. The 3-D calculations were performed on a grid consisting of 201 $\times$ 81 $\times$ 81 points in the x, y and z directions for the shock-tube problem. We further note that the shock wave will be represented by '1', the contact discontinuity by '2', the head of the rarefaction fan by '3' and the tail of the rarefaction by '4' throughout the discussions in this section.

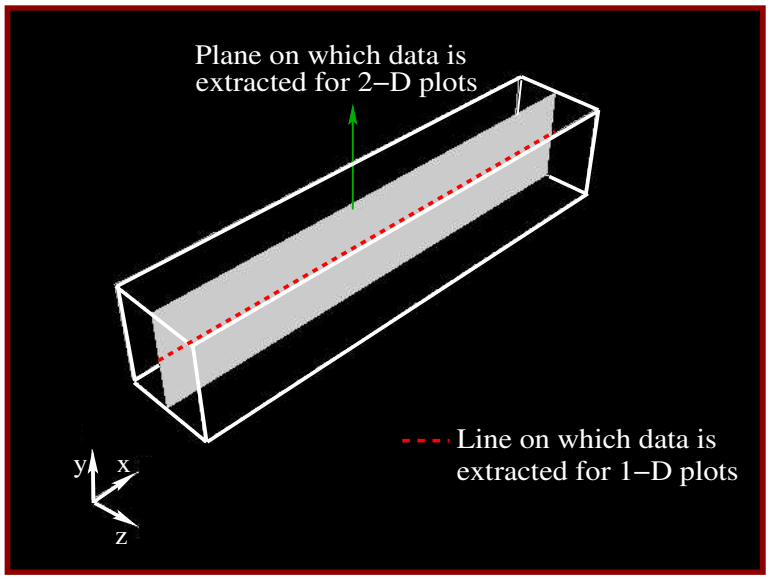

Figure 3.4 Schematic of positions in the computational domain for presenting results.

3.4.1 Test Case 1

We begin by providing an overall three-dimensional qualitative view of the flow field inside the shock tube. We then display two-dimensional contour plots associated with specific slices of the overall 3-D domain to provide better insight into the distribution of the flow variables. Finally, we present comparisons of computed results with the exact 1-D, inviscid solution in the form of 1-D plots. Data for the 1-D plots is extracted from a region, which would be the 1-D case if the 3-D aspect were neglected, as suggested from Fig. 3.4.

In Fig. 3.5 we present a 3-D visualization of the flow field after a time interval of 0.2 units from the initial breaking of the diaphragm. As alluded to previously, the pressure difference across the diaphragm induces a pressure wave to propagate into the quiescent gas to the right. The speed at which the pressure wave propagates depends on the initial pressure ratio across the diaphragm. Along with the initial condition this pressure ratio uniquely determines the strength of the incident shock wave and expansion wave that are set up after the diaphragm is ruptured. In particular, for this test case, the diaphragm pressure ratio is 10 (see Table 3.1). If this pressure ratio is high enough, then the resulting pressure wave is propagated at speeds comparable to the speed of sound in the medium. This results in a wave steepening effect since the speed at which disturbances can be transmitted is limited by the sound speed. As time evolves the compressive region generated by propagation of

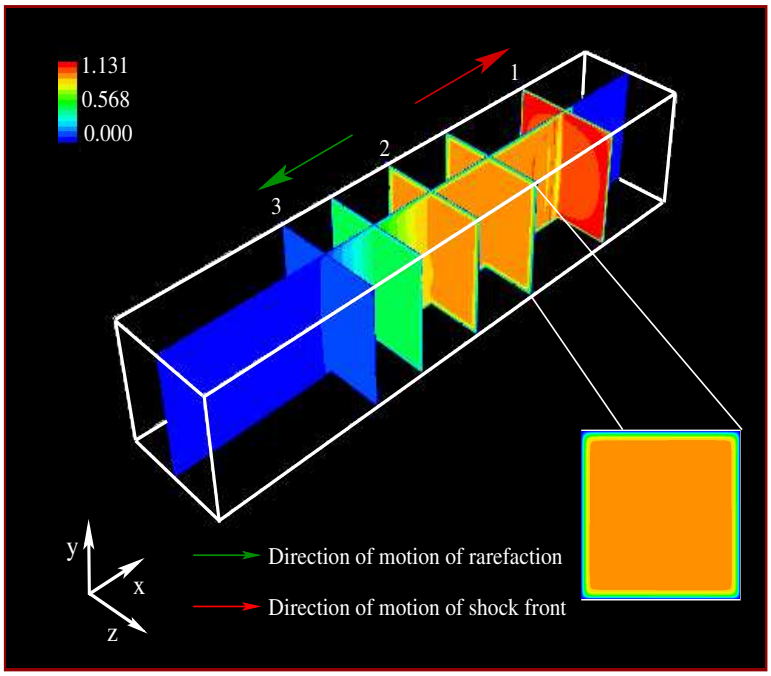

Figure 3.5 Test Case 1: 3-D visualization of flow field. Contours colored with velocity magnitude.

the pressure wave tends to become steeper and narrower, thus forming a normal shock wave. This compressive motion to the right of the tube also results in an expansion or rarefaction wave propagating into the quiescent gas to the left. To understand why this happens, think of the initial discontinuity as a piston. To produce the shock front the piston has to move to the right. Once the piston moves to the right, the gas to the left of the piston also moves to the right to fill up the space previously occupied by the piston resulting in an expansion (feels like withdrawal of the piston).

Figure 3.5 shows the shock wave, which moves to the right and the rarefaction fan which moves to the left. Distribution of the velocity magnitude at cross sections of the tube corresponding to the positions of the shock wave and the head and tail of the rarefaction are also shown. The contour plots at the cross sections of the tube demonstrate the nearly one-dimensional nature of the solution. In the inset we present the velocity contour, which displays the development of the boundary-layer on the tube walls. Variation of the velocity magnitude along a 2-D slice running the length of the tube is also shown to make the jumps more evident.

In Fig. 3.6 we present 2-D contour plots of certain dependent variables at time $t = 0.2$ units. For a compressive shock wave, the kind produced in this shock tube setup, the magnitudes of dependent variables are always greater behind the shock front than ahead of it (from a laboratory frame of reference). The degree of this increase can be used in various ways to measure the strength of the corresponding shock wave. Based on the ratio of the pressure immediately behind and ahead of the shock, the strength of the shock for Test Case 1 is 3. We comment that this shock is not very strong. The jumps in magnitude of the dependent variables from a quiescent zone at the right end of the tube to a region behind the shock wave can be deduced from Fig. 3.6. As the normal shock wave propagates to the right,

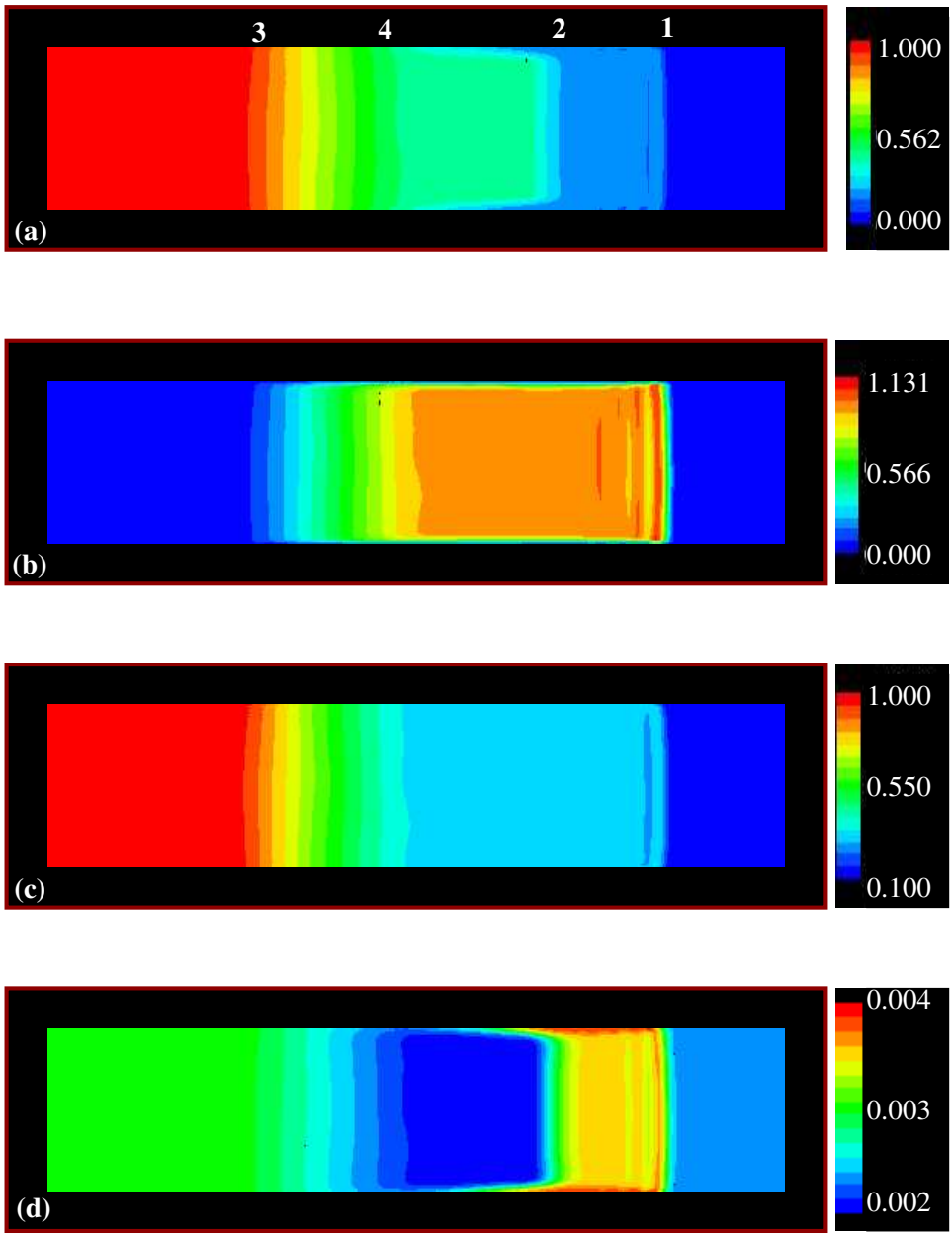

Figure 3.6 Test Case 1: 2-D contour plots at $t = 0.2$ units; (a) density, (b) u-velocity, (c) pressure, (d) temperature.

it begins to envelope more and more of the quiet gas, which, after being overtaken, follows the shock front at a constant velocity. This results in a column of fluid (region between 1 and 2 of Fig. 3.6(b)) moving to the right at constant velocity. Careful observation of the density and temperature contours within the same interval reveals the contact discontinuity which the separates two zones of different density and temperature. Figure. 3.6(b) suggests that the contact discontinuity follows the shock wave at a constant velocity. Across the contact discontinuity, pressure and velocity are preserved, but density and temperature vary discontinuously. The plots in Fig. 3.6 clearly indicate the presence of these features. The rarefaction wave propagates to the left, and it smoothly and continuously decreases the

pressure of the fluid at the head of the rarefaction to a lower pressure behind the rarefaction. This phenomenon is clearly observed in part(c) of the figure and further suggests that the gas particles move at increasing speeds from the rarefaction wave head, towards the tail. This increase can be inferred from Fig. 3.6(b). Furthermore, the Gibbs oscillations behind the shock front are also visible in the contour plots presented above.

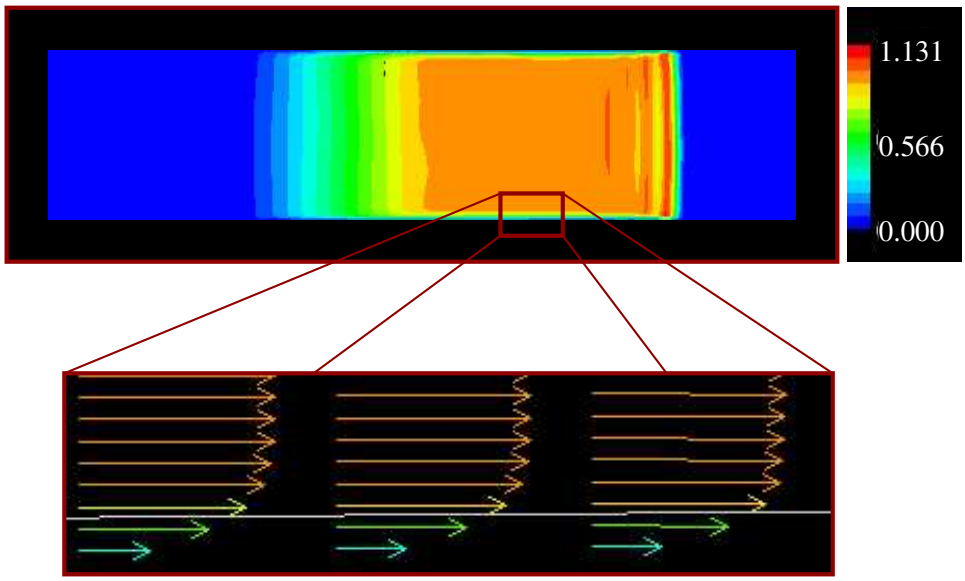

Figure 3.7 Test Case 1: Boundary layer profile.

In Fig. 3.7 we display a zoomed vector plot of the computed boundary-layer profile. It is clear that the solver is able to capture the boundary-layer profile with reasonable accuracy. Due to constraints regarding grid-sizes in 3D, we were able to put only three gridpoints within the boundary-layer. Even with such a coarse grid spacing the solver was able to capture the general shape of the boundary layer, which is particularly encouraging.

In Fig. 3.8 we present comparisons between computed and exact solutions, again at time $t = 0.2$ units. It should be noted that although the inviscid discontinuities are now transformed to sharp but continuous variations due to physical viscosity and heat conduction effects, these cannot be resolved using typical gridding; hence, artificial dissipation still must be used to capture these discontinuities. We notice from the u-velocity profile (part (a) of the figure) that the computed results are in agreement with the exact solution with respect to predicting the position of the shock front. However, the solver overpredicts the velocity at the contact surface. A grid function convergence study, which is considered in the sequel, shows that the overshoot decreases as we decrease grid spacing. Furthermore, the presence of Gibbs oscillations in the immediate vicinity of the shock wave is evident. Although one could mitigate these oscillations to a greater extent by using high-resolution methods, considering the complexities involved in implementing such schemes in 3D, we chose to use artificial dissipation. Post-processing filters like digital total variation (DTV) filtering (see Chan *et al.* [166]) are also being used to provide sharper shock capturing. However, implementation of such filters is not straightforward even in one-dimensional cases. Moreover, the effectiveness of these filters in 3D has also not been studied. In part(b) of the figure we notice that there is a visible smearing at the contact discontinuity. The resolution of the rarefaction is

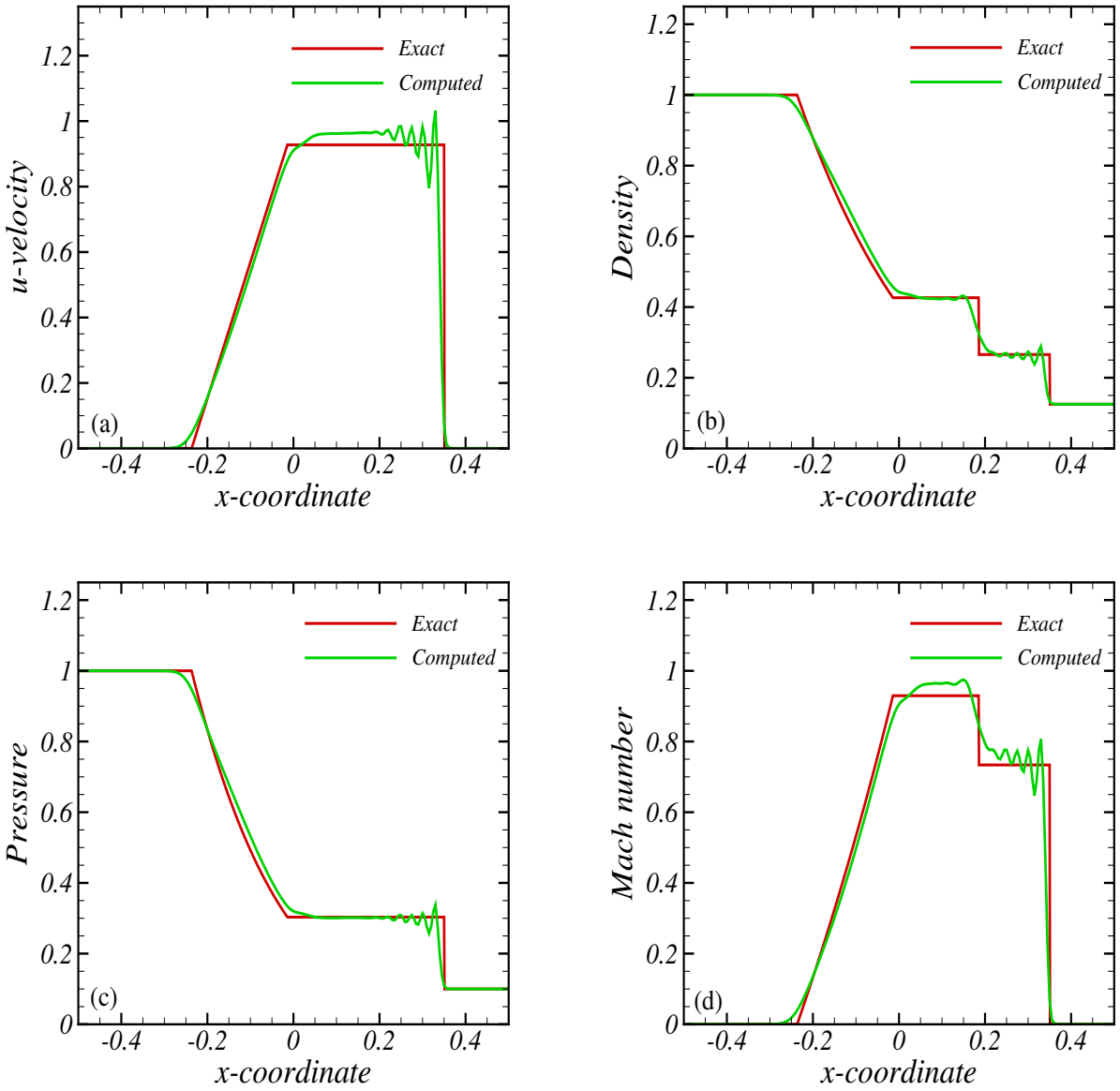

Figure 3.8 Test Case 1: Comparison of numerical with exact solution at $t = 0.2$ units; (a) u-velocity, (b) density, (c) pressure, (d) Mach number.

satisfactory, but there is still some smearing at the head and tail of the rarefaction. The agreement of the computed pressure profile (part(c)) with the exact solution is generally good, but again we see the smearing at the head and tail of the rarefaction. From the Mach number profile (part(d)) it is evident that the maximum Mach number of the fluid in the tube is 0.95; this corresponds to a transonic case. This is to be expected considering the strength of the shock wave in this test case. The Gibbs oscillations and the effects of the overshoot of velocity at the contact discontinuity in the velocity profile has also fed into inaccuracies of the Mach number profile as should be expected.

Grid function convergence study

To determine the convergence rate of the method we perform convergence tests on the grid functions as the discretization step sizes are decreased. In particular, we use three grids denoted as H_c, H_m and H_f—coarse, medium and fine, respectively. Discretization step sizes are sequentially reduced by a factor of two in each separate direction in going from one grid to the next finer one. With a grid spacing of $\Delta x = 0.02$, $\Delta y = 0.01$, and $\Delta z = 0.01$, H_c is the coarsest grid, corresponding to $51 \times 21 \times 21$ points in x-,y- and z coordinate directions, respectively. With a grid spacing of $\Delta x = 0.01$, $\Delta y = 0.005$, and $\Delta z = 0.005$, H_m is the medium grid containing $101 \times 41 \times 41$ points. Finally, $\Delta x = 0.005$, $\Delta y = 0.0025$, and $\Delta z = 0.0025$ for H_f, the finest grid with $201 \times 81 \times 81$ points.

In Fig. 3.9 we present one-dimensional plots comparing the solutions computed on the three grids with the exact solution. The u-velocity plot is displayed in Fig. 3.9(a), density in Fig. 3.9(b), pressure in Fig. 3.9(c) and Mach number in Fig. 3.9(d). Figure 3.9 indicates that the computed solutions approach the exact solution as grid spacing is decreased, indicating the convergence of the solution in a qualitative sense. But, of importance to us in the u-velocity profile (part(a)) is the overprediction of the velocity at the contact surface. A blow up presented as an inset in Fig. 3.9(a) indicates the decrease in the overshoot with decreasing grid spacing. Moreover, with the decrease in overshoot the u-velocity profile approaches the exact solution. This further suggests that our grid spacing even on our finest grid is not fine enough so as to match the exact solution. However, with the resources at our disposal this is the best that could be achieved. Moreover, an exact viscous solution is not available. From the blow up in part (b) of the figure it is evident that the solution computed on the H_f grid captures the shock front much more sharply than the solutions computed on the H_m and H_c grids. Comparison of the amplitudes of Gibbs oscillations present behind the shock front in the density profiles computed on the three grids reveals that the amplitude of the oscillations is somewhat lower on the H_f grid (seen clearly in zoomed view in Fig. 3.9(b)), but the frequency is higher. Also, both the pressure and Mach number profiles illustrate that decreasing grid spacing provides superior results in tracking the profile of the expansion fan.

Even though the above plots illustrate that the computed solution appears to converge to the exact solution as the discretization step size is decreased, it is also important to determine the rate at which error is reduced. For grid functions, we generally have available qualitative information, derived from the numerical method itself about the theoretical convergence rate of the grid functions generated by the method. In particular, we always have the truncation error at our disposal. In our case, since we have used second-order discretizations, the leading truncation error is $\mathcal{O}(h^2)$, *i.e.*, the order of convergence is 2. Hence, a reduction in the step size by a factor of two should reduce the error by a factor of four.

For finite-difference approximations, even for PDEs, the formal convergence rate of the method should be achieved, provided the solutions to the problem are smooth. However, in general, the solutions to the compressible N.–S. equations involve shock waves, and hence, the solutions are inherently nonsmooth. Finite-difference approximations to such solutions are dominated by $\mathcal{O}(1)$ errors, which are introduced in a few cells in the vicinity of discontinuities (contact discontinuity and shocks). Engquist and Sjögreen [167] have shown that this error can affect even the smooth part of the solution away from the shock such that only $\mathcal{O}(h)$

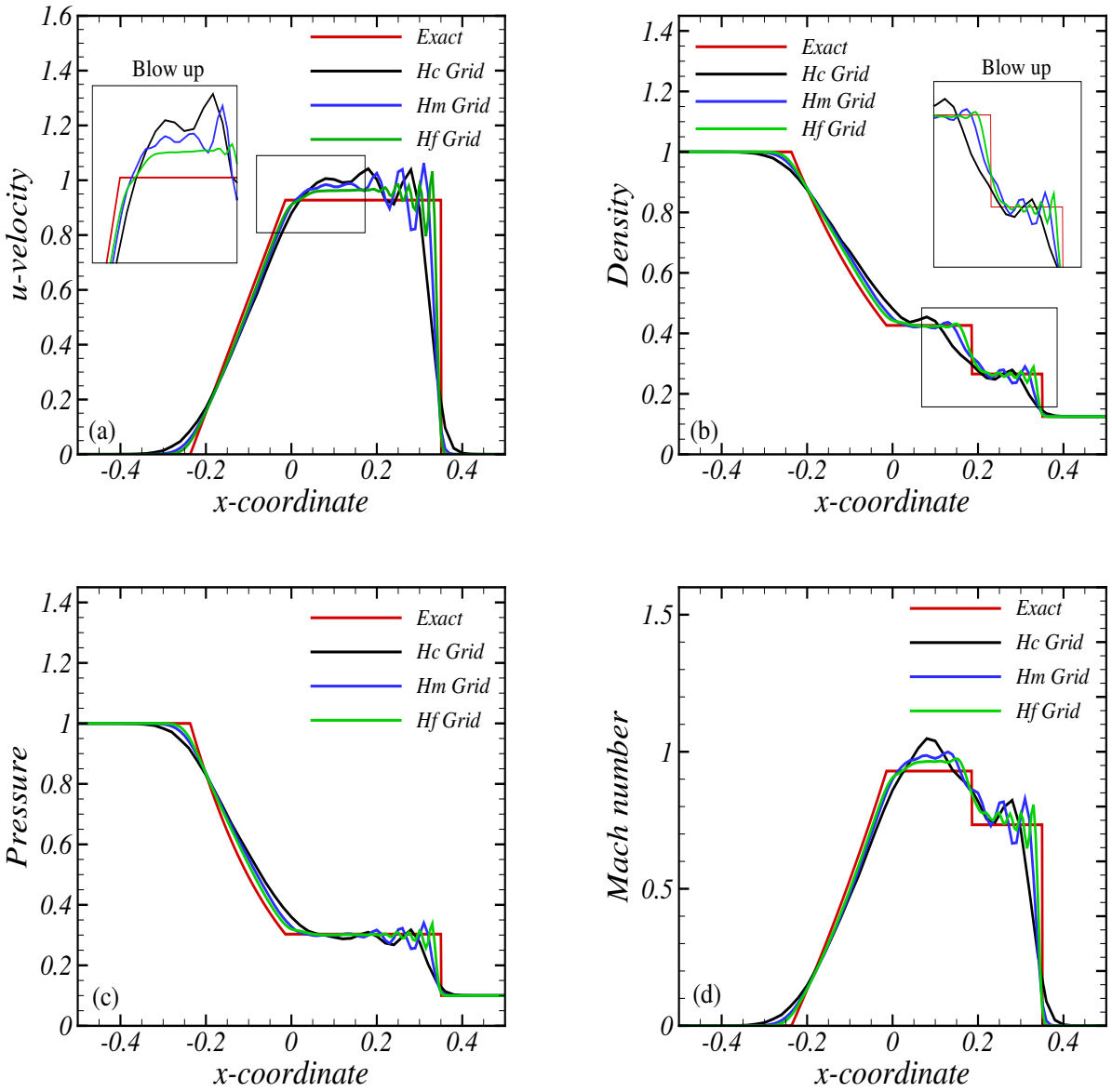

Figure 3.9 Test Case 1: Comparison of numerical solution on three different grids with exact solution at $t = 0.2$ units; (a) u-velocity, (b) density, (c) pressure, (d) Mach number.

accuracy be achieved even for formally higher-order methods. They further give a theorem that proves for scalar problems (1-D cases) that one can expect the formal order of accuracy. But for a system of equations, or problems with source terms, or both, the order of accuracy for even formally higher-order methods is at the most $\mathcal{O}(h)$. The interested reader is referred to [167] for further details. We will show that, this is in fact the case for the 3-D system of equations that we solve.

The L^2 error, which was calculated based on the results obtained on the three grids is presented in Table. 3.3. We note we have used the strong L^2 norm for our calculations, *i.e.*, with the L^2 norm of a variable ϕ defined as $|| \phi ||_2 = \left[\int_0^W \int_0^H \int_0^L |\phi|^2 \, dx \, dy \, dz \right]^{1/2}$, the

corresponding order of convergence p is given by the formula:

$$p = \frac{\frac{||\phi_h - \phi_{h/2}||}{||\phi_{h/2} - \phi_{h/4}||}}{\log(2)} \tag{3.30}$$

Table 3.3 Test Case 1: Results from grid function convergence tests.

ϕ	$\|\|\phi_h - \phi_{h/2}\|\|$	$\|\|\phi_{h/2} - \phi_{h/4}\|\|$	$\frac{\|\|\phi_h - \phi_{h/2}\|\|}{\|\|\phi_{h/2} - \phi_{h/4}\|\|}$	p
ρ	$1.633e-3$	$1.52e-3$	1.41759	0.50344
ρu	$2.33103e-3$	$1.48494e-3$	1.56977	0.65055
ρv	$2.51795e-4$	$1.55105e-4$	1.62338	0.699
ρw	$2.51782e-4$	$1.55101e-4$	1.62334	0.68896
ρe	$4.8756e-3$	$2.81203e-4$	1.73381	0.79395
u	$5.30295e-3$	$3.3059e-3$	1.60405	0.68172
v	$6.51714e-4$	$4.19e-4$	1.551441	0.63636
w	$6.51714e-4$	$4.19271e-4$	1.55439	0.63635
p	$1.62789e-3$	$9.84054e-4$	1.65427	0.72619
T	$1.15398e-5$	$9.32563e-6$	1.23742	0.30734

As mentioned earlier, the obtained order of convergence p is what should be expected for such kinds of problems. In particular, we observe that the order of convergence varies from 0.30734—0.79395 for the various dependent variables. These values for p imply that nearly only $\mathcal{O}(h)$ convergence is achieved. We further comment that the artificial dissipation parameters were tuned for this particular test case.

3.4.2 Test Case 2

The pressure ratio across the diaphragm for this test case is a 100. Figure 3.10 displays a three-dimensional visualization of the flow field at a time $t = 0.1$ units after the initial rupturing of the diaphragm. The normal shock front and the head and tail of the rarefaction are also displayed. Velocity vectors colored with velocity magnitude are also shown to emphasize that the flow is from left to right. This information allows us to discern that the shock wave propagates to the right into the low pressure section of the tube and the rarefaction fan propagates to the left into the high pressure section. We further present the velocity contours, which displays the development of the boundary-layer profile at a specific cross section of the shock tube.

Two-dimensional contour plots of density, u-velocity, pressure, and temperature are presented in Fig. 3.11. The discontinuous jumps in the values of the dependent variables across the shock and contact discontinuity, and the continuous variation in the profile of the dependent variables across the rarefaction fan are evident even for this test case. We further note that for this case we did not attempt to tune the artificial dissipation parameters; they were set to the same values as those used for Test Case 1.

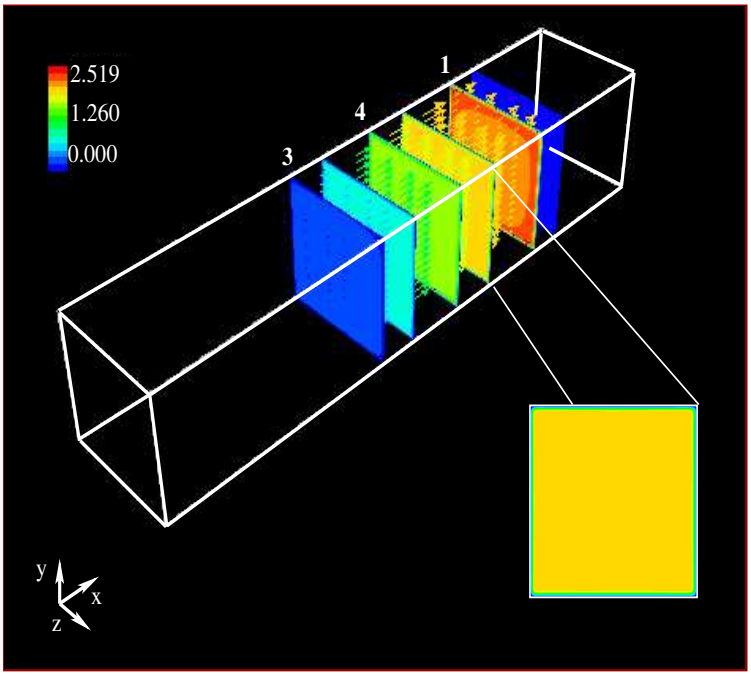

Figure 3.10 Test Case 2: 3-D visualization of flow field. Contours colored with velocity magnitude.

As done earlier, the positions of the different waves generated as part of the solution are shown in Fig. 3.11(a). We comment that in the density (part(a)) and pressure (part(c)) contours the shock front is not actually visible. This is because in this test case the magnitudes of density and pressure are low (0.01 in the present case). Therefore, even after the jump across the shock front they attain magnitudes that are still relatively low when compared to their maxima, thus leading to the difficulty of these jumps being distinguishable in the color table. However, the shock front is easily distinguished in the u-velocity (part(b)) and temperature contours (part(d)). From the u-velocity plot we observe that the the column of fluid between the shock wave and the tail of the rarefaction that follows the shock wave moves at supersonic velocity. In comparison to Test Case 1 the fluid follows the shock front at about double the speed. This is due to an increase in the initial pressure ratio across the diaphragm, which is 100 for this test case. Correspondingly, there is an increase in strength of the incident shock wave as well. In particular, the shock strength for the present test case is 6, as compared to 3 for the first test case. The increase in pressure across the shock front can be seen clearly in the 1-D plots which are presented in the sequel.

From Figs. 3.11(a), (b) and (c), we notice that there is a visible steepening of the rarefaction fan when compared to Test Case 1. Visually, this effect can be seen much more clearly in the line plots presented below, but we will attempt to explain the rationale behind the steepening here, as we have a larger data set. Even though the shock strength in the present test case is twice that of Test Case 1, the initial pressure distribution in the right section of the tube is an order of magnitude lower. So, even after the pressure jump across the shock, the magnitude of the pressure behind the shock is much lower when compared to that of Test Case 1. In particular, the magnitude of the pressure behind the shock is around 0.06 for Test Case 2, whereas it is 0.3 for Test Case 1. This implies that the gas at the left section of

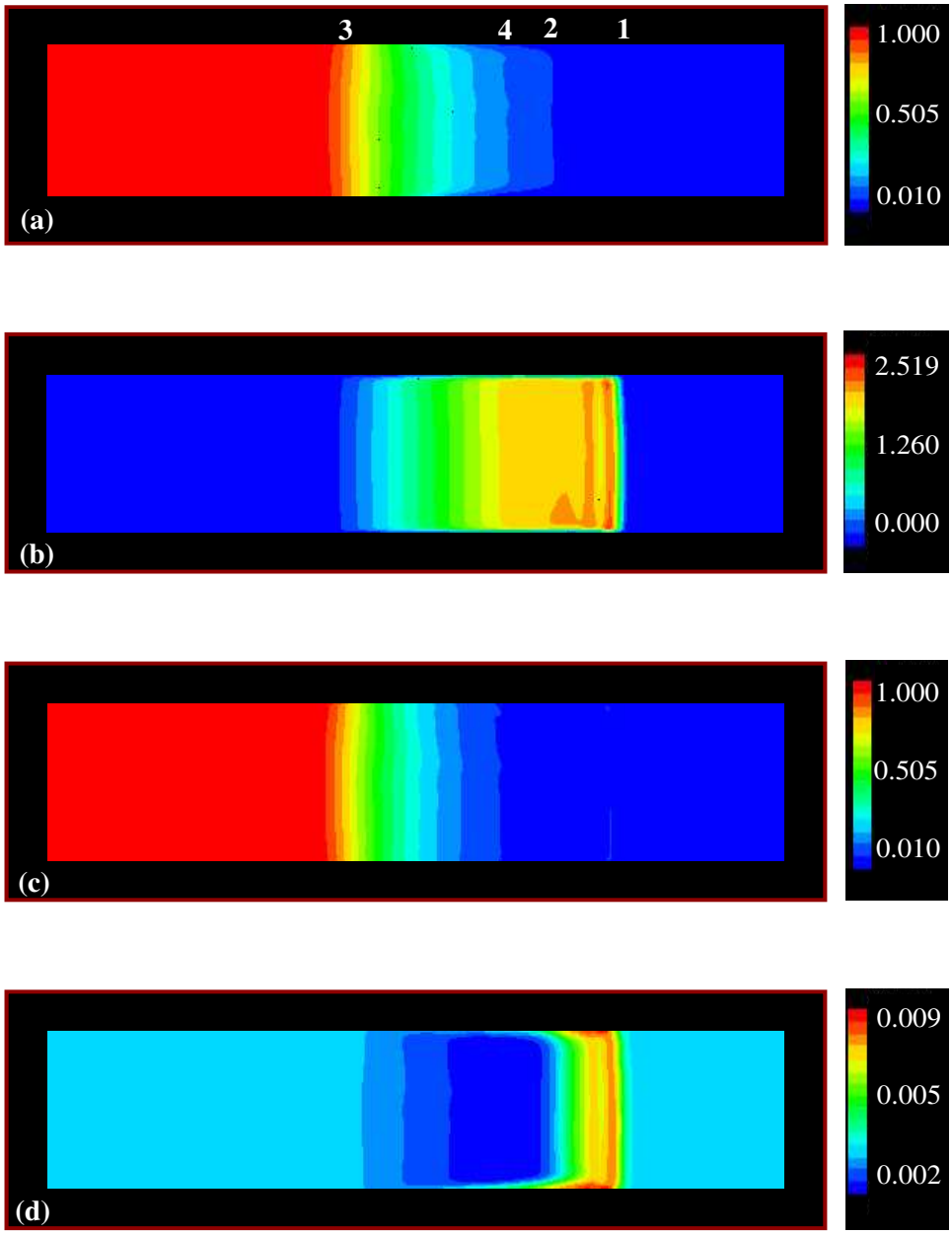

Figure 3.11 Test Case 2: 2-D contour plots at $t = 0.1$ units; (a) density, (b) u-velocity, (c) pressure, (d) temperature.

the tube should expand to a much lower pressure after the expansion when compared to Test Case 1. Therefore, we observe a steepening in the profile of the rarefaction. We remark that even though there is a steepening effect, the variation of the dependent variables across the rarefaction fan is still continuous. We further comment that, although it would seem intuitive to attribute the increase in the velocity of the contact surface to supersonic velocities due the steeping in the pressure profile (increase in pressure gradient), both these phenomena occur simultaneously, and hence, it would not be appropriate to attribute a cause-and-effect relationship. Figures 3.11(a) and (d) illustrate that the jump in density and temperature across the contact discontinuity also increases when compared to Test Case 1. Artifacts of

the Gibbs oscillation can also be seen clearly in all the contour plots displayed in the figure.

A zoomed plot, displaying the velocity vectors of the computed boundary-layer profile, is presented in Fig. 3.12. The plot demonstrates the capability of the solver to capture the boundary layer even at supersonic Mach numbers.

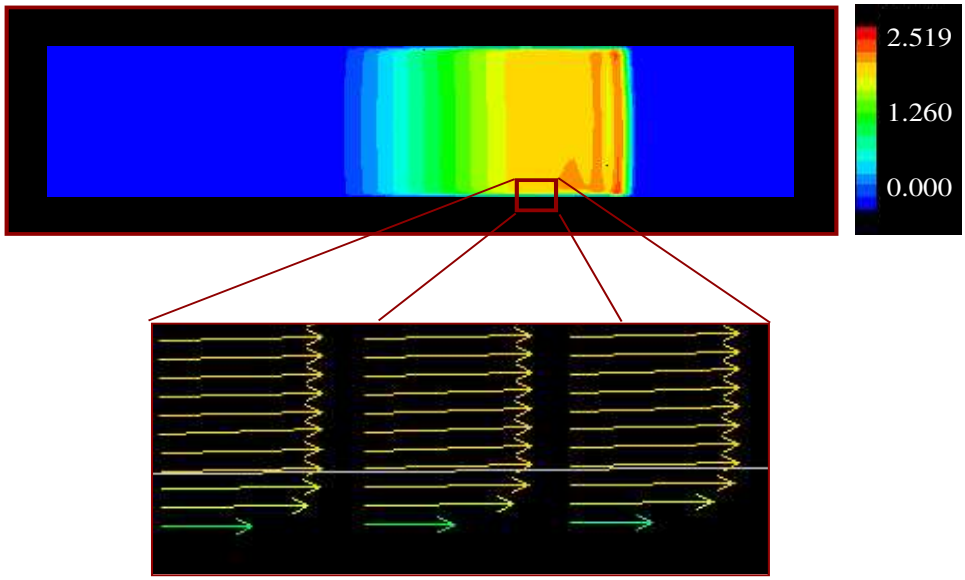

Figure 3.12 Test Case 2: Boundary layer profile.

Results for u-velocity, density, pressure, and Mach number plotted as a function of the x-coordinate at a time t=0.1 units are presented in Fig. 3.13. The exact 1-D, inviscid solution is shown by a red continuous line and the computed solution by a green line. At the outset we would again like to bring to the attention of the reader that although the density and pressure plots displayed suggest that these variables have a magnitude equal to 0 at the right section of the tube, this is not true. In particular, the magnitudes in both the cases are 0.01 (see Table 3.1). From Fig. 3.13 we observe that we are able to capture the position of the shock front and rarefaction fan with fairly good accuracy except in the case of density. Again, we observe the overprediction of the computed u-velocity profile at the contact surface (see part(a) of the figure). In the density profile (Fig. 3.13(b)) we observe a heavy smearing at the contact discontinuity. Although one could attribute this to viscous heat conduction effects, which are far more pronounced in Test Case 2 than in 1, we remark that this is essentially not correct since we cannot resolve the contact discontinuity using typical gridding. This contact smearing is caused by numerical error, and it is inherent in almost all methods, including high-resolution methods unless specific steps are taken to combat it. The most popular measure to decrease contact smearing is probably Harten's artificial compression (see the text by Laney [160] for further details and more options). Furthermore, the resolution of the rarefaction is fairly satisfactory. The agreement between the computed solution and the exact solution is good with respect to the pressure profile. Comparison of Fig. 3.8(c) and Fig. 3.13(c) illustrates the steepening of the rarefaction fan as suggested previously. The Mach number profile (Fig. 3.13(d)) illustrates that the solver underpredicts the peak M. However, we comment that the difference is fairly small, 0.1 in

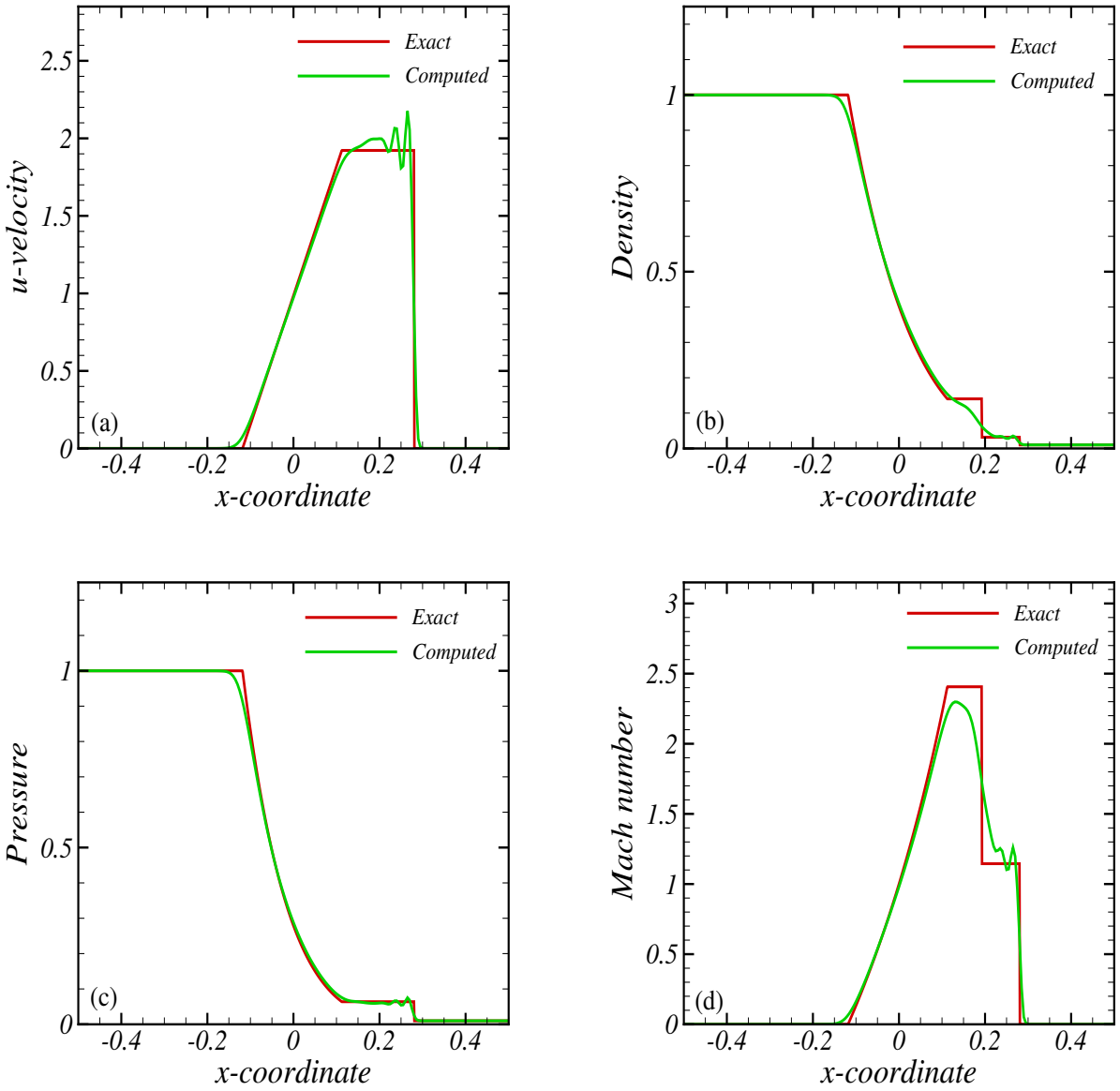

Figure 3.13 Test Case 2: Comparison of numerical with exact solution at $t = 0.1$ units; (a) u-velocity, (b) density, (c) pressure, (d) Mach number.

the present case. Furthermore, the smearing at the contact surface and the Gibbs oscillations behind the shock wave are also displayed clearly.

Grid function convergence study

We use the same methodology and notation described in fair detail for Test Case 1 to conduct grid function convergence tests on solutions to Test Case 2. One-dimensional line plots on three different grid sizes for u-velocity, density, pressure, and Mach number are presented in Fig. 3.14.

In each of the plots presented in the figure, we see much better prediction of the position

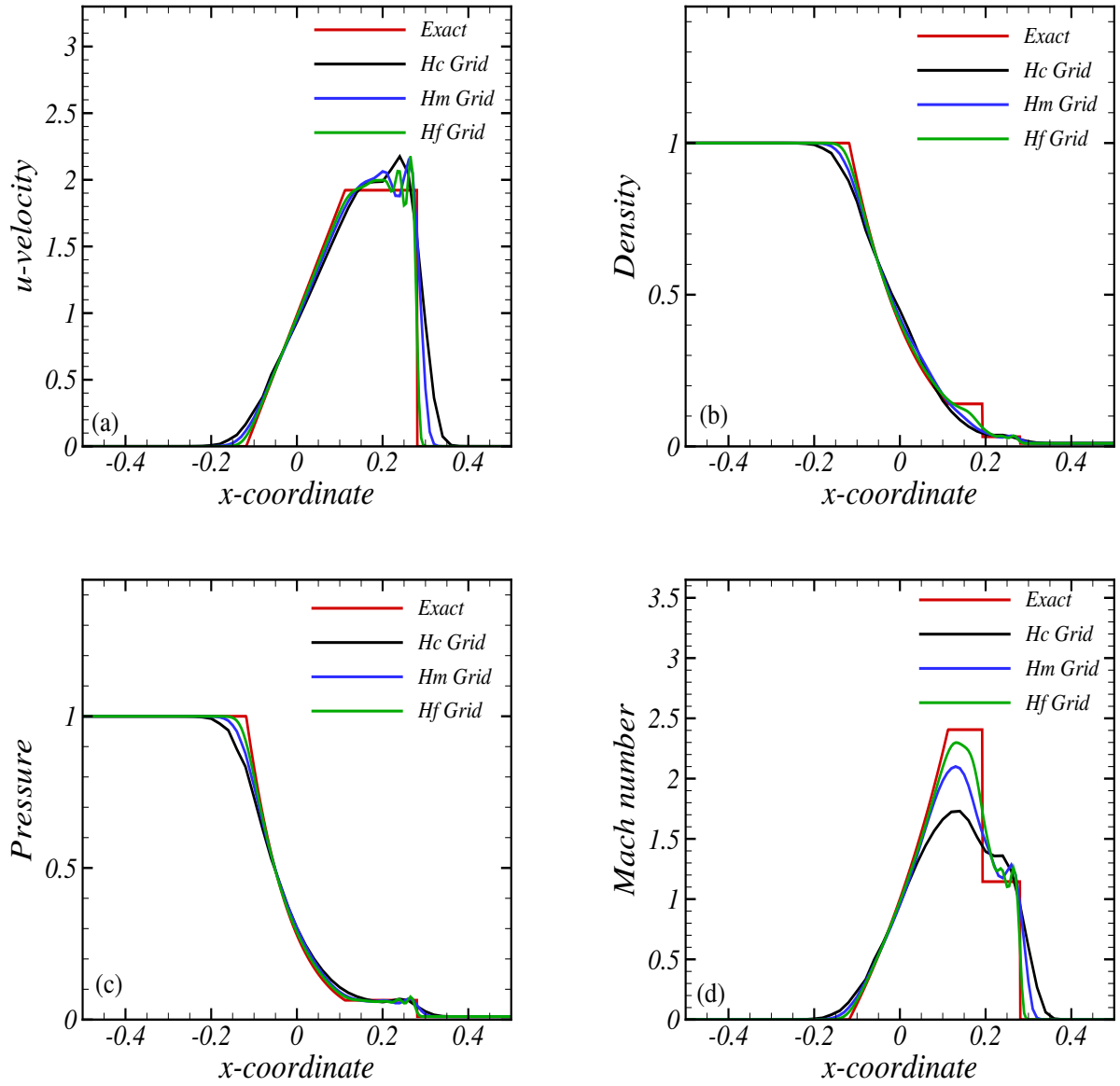

Figure 3.14 Test Case 2: Comparison of numerical solution on three different grids with exact solution at $t = 0.1$ units; (a) u-velocity, (b) density, (c) pressure, (d) Mach number.

of the shock front and the rarefaction fan as the discretization step-sizes are decreased. The decrease in the overshoot of the u-velocity profile as the grid spacing is decreased is evident from Fig. 3.14(a). In part(b) we observe that the ineffectiveness of the artificial dissipation terms at the contact surface, has resulted in a complete smearing of the contact discontinuity on the H_c and H_m grids. The solution on the H_f grid is only marginally better; we can at least observe an attempt by the computed density profile to follow the exact solution at the contact discontinuity. From both the pressure and density plots (parts (b) and (c)) we notice that the smearing at the head of the rarefaction fan is reduced as we go to finer and finer grids. Figure 3.14(d), which displays the M profile, clearly demonstrates the convergence of the computed solution towards the exact solution.

The order of convergence of the scheme is also found in a fashion analogous to Test Case 1. The order of convergence for the various dependent variables is given in Table 3.4. Comparing Table 3.3 with Table 3.4, we infer that the order of convergence for all the

Table 3.4 Test Case 2: Results from grid function convergence tests.

ϕ	$\|\|\phi_h - \phi_{h/2}\|\|$	$\|\|\phi_{h/2} - \phi_{h/4}\|\|$	$\frac{\|\|\phi_h - \phi_{h/2}\|\|}{\|\|\phi_{h/2} - \phi_{h/4}\|\|}$	p
ρ	$1.01412e-3$	$8.8329e-4$	1.14812	0.19927
ρu	$1.4757e-3$	$1.17529e-3$	1.2556	0.32838
ρv	$1.49634e-4$	$1.30836e-4$	1.14367	0.193672
ρw	$1.49633e-4$	$1.30833e-4$	1.14369	0.193697
ρe	$2.67729e-3$	$1.95168e-3$	1.371785	0.456054
u	$8.61486e-3$	$8.51916e-4$	1.011234	0.01611
v	$1.23389e-3$	$1.16e-3$	1.06306	0.08822
w	$1.23e-3$	$1.16e-3$	1.063063	0.088227
p	$1.03597e-3$	$6.69613e-4$	1.547121	0.629593
T	$3.19854e-5$	$3.82972e-5$	0.835188	-0.25982

dependent variables in Test Case 2 is lower than those in Test Case 1. At the start of the discussion on the present test case, we mentioned that the artificial dissipation parameters were not tuned. As a result, the reduction in the amplitude of the Gibbs oscillations with decreasing grid spacing may not have been as effective. Moreover, the shock strength and the peak M for Test Case 2 are higher than those in Test Case 1. We further comment that analysis of the convergence rates will be considered after presenting the rates for Test Case 3 since we will then have more data available to make appropriate arguments.

3.4.3 Test Case 3

Test case 3 is severe in that the initial shock strength is 100000. This test is designed to assess the robustness and accuracy of the solver. Its solution consists of a strong right traveling shock wave, a contact discontinuity, and a left running rarefaction wave.

We note that for this test case use of the explicit predictor in the large-scale algorithm proved to be unstable, *i.e.,* the solution blew up after finite time even on our finest grid. However, we were able to obtain better stability properties from our algorithm, when we used the implicit corrector by itself. Since we only used the corrector, the initial guesses for the nonlinear iterations were taken to be equal to the values of the dependent variables at the previous time step.

We again begin our discussion on the computed results by providing a 3-D visualization of the flow field in Fig. 3.15. The figure demonstrates that even for such a severe test case, the solver exhibits the right traveling shock wave, a contact discontinuity and a rarefaction. The boundary layer along the tube walls can be seen in the inset of the u-velocity contour provided in the figure.

Contours of density, u-velocity, pressure, and temperature are displayed as 2-D plots in Fig. 3.16. From the pressure contour (part(c)) we can deduce that the shock strength

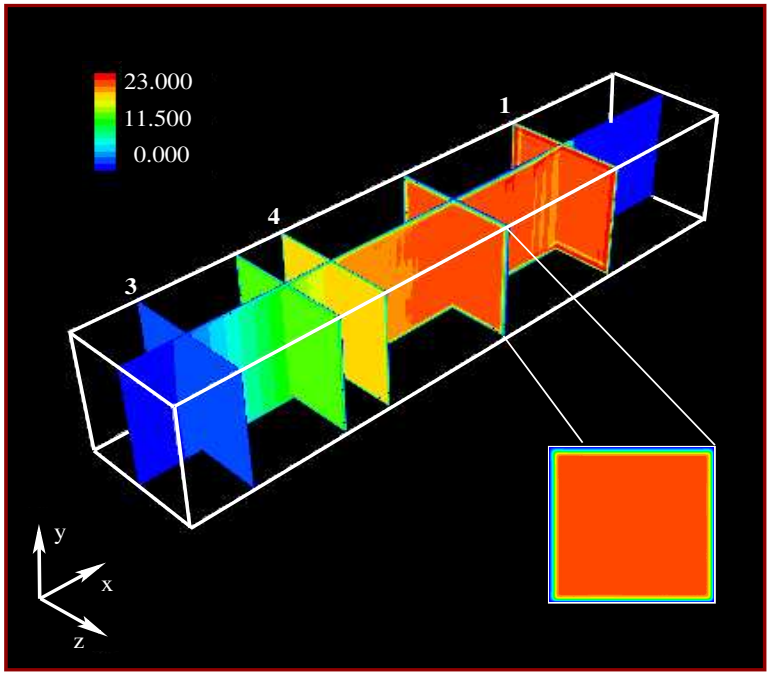

Figure 3.15 Test Case 3: 3-D visualization of flow field. Contours colored with velocity magnitude.

for this particular test case is around 45000 (a strong shock!! indeed, compare this shock strength with those of cases 1 and 2). The shock strength explains the big jumps in the magnitudes of the dependent variables across the shock front. We immediately also notice that the contours of density (part(a)) and the temperature (part(d)) are different in this case than the other two. In particular, the fluid density is at its maximum just behind the shock, and its minimum value is lower than what was even present in the initial conditions. Also, the presence of the rarefaction fan is not very evident and the contact discontinuity is not easily distinguishable in both density and temperature contours.

In the case of the density contour, unlike the other two test cases, the distribution of density along the length of the tube at time $t = 0$ is uniform. Hence, the maximum fluid density will always be at a location just behind the shock front. The red band seen in Fig. 3.16(a) corresponds to this jump. Also, since the rarefaction fan continuously reduces the values of all dependent variables, the magnitude of the density in this case is reduced to a value below that which was present in the domain at the initial time after the expansion. In principle, the region between the the shock front and the region where the fluid density is around 0.015 should have been at a constant density (maximum in this case). The location at which the discontinuous transition from the constant value of fluid density to some other values occurs would correspond to the location of the contact discontinuity, since a contact discontinuity separates two zones of different density and temperature. However, the solver heavily dissipates the location of the contact discontinuity. The light green region corresponding to a fluid density value of around 3.5 between the two regions alluded to above clearly indicates the presence of heavy dissipation. The rarefaction fan can be clearly seen in the u-velocity profile (part(b)), pressure contour (part(c)), and also somewhat in the temperature contour (part(d)). Also, from part(b) of the figure we observe that the contact surface moves at

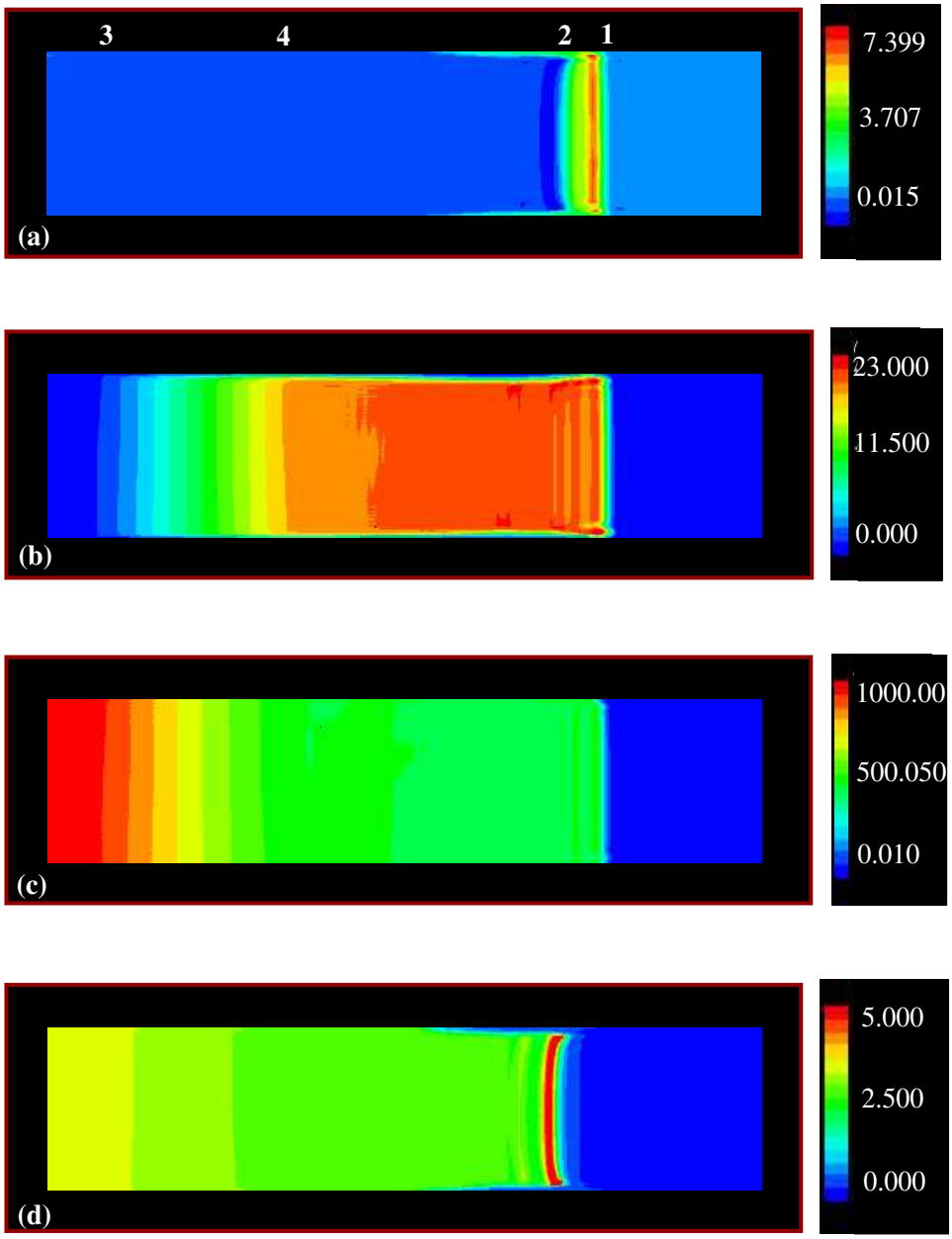

Figure 3.16 Test Case 3: 2-D contour plots at $t = 0.012$ units; (a) density, (b) u-velocity, (c) pressure, (d) temperature.

supersonic velocity. In fact, the contact surface moves at a velocity that is ten times faster that what was achieved in Test Case 2. However, this should not lead us to think that the corresponding M is also very high. From the temperature contour (Fig. 3.16(d)) it is evident that the temperature in the tube is also higher in comparison. Obviously increase in temperature increases sound speed, hence, lowering the corresponding values of M. We further comment that the features described above can also be seen clearly in the line plots.

In Fig. 3.17 we display the velocity vectors of the computed boundary-layer profile. We note that for the grid resolution we are computing with, the solver provides a reasonably good boundary-layer profile.

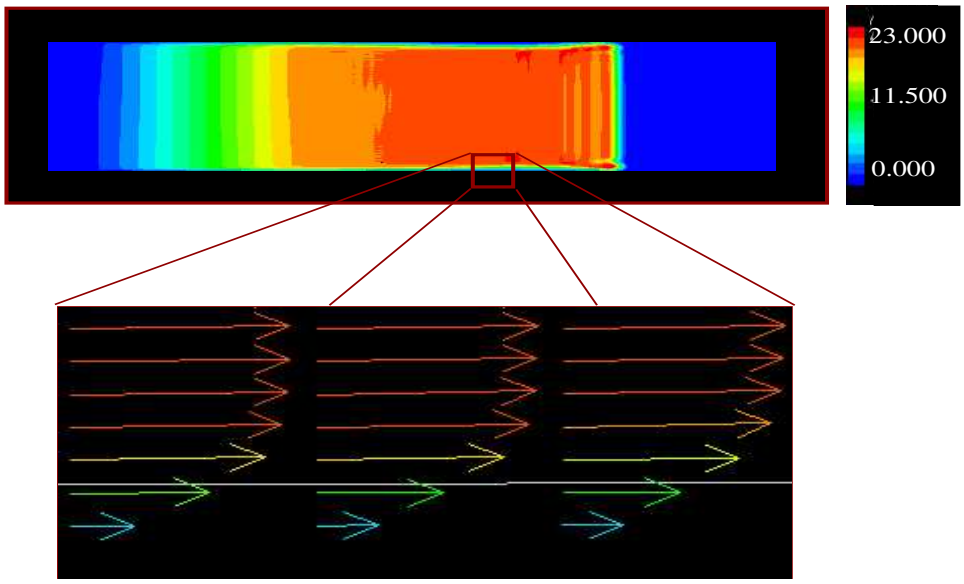

Figure 3.17 Test Case 3: Boundary layer profile.

Comparisons of computed results with exact 1-D solutions are displayed in Fig. 3.18. In general, even for this test case the solver produces results consistent with features observed in the numerical solutions of Test Cases 1 and 2. That is, the the right-traveling shock front and left-traveling rarefaction wave are positioned in the correct locations. Also, resolution of the rarefaction fan is fairly satisfactory in all the plots displayed in Fig. 3.18. We can still observe the overshoot in the u-velocity profile from part(a) of the figure, which we know by now is due to lack of finer grid spacing. Other than the overshoot at the contact surface, the computed u-velocity profile agrees well with the exact solution. From part(b) of the figure we observe that the resolution of the shock is fairly sharp, but as previously suggested, there is a fair bit of smearing at the contact discontinuity. Moreover, an overshoot in the peak value of the density is evident. Evidence of Gibbs oscillations can be seen at the contact surface. This is evident from the Mach number plots also. The features that were discussed in the contour plots can also be clearly seen in the density profile. From the pressure profile displayed in part(c) of the figure, we note that although the profile is in fairly good agreement with the exact solution, there is a small but visible deviation of the pressure in the rarefaction fan. Moreover, we also see some smearing at the head of the rarefaction fan. The Mach number profile is also satisfactory, minus the Gibbs oscillations, which is to be expected considering the strength of the incident shock wave. As alluded to before, even though the velocity of the contact surface is high the peak Mach number is lower than that in Test Case 2. In particular, the peak M is near 2 for this test case.

Grid function convergence study

Figure 3.19 shows the 1-D plots on three different grid sizes for u-velocity, density, pressure and temperature. From the figure, we notice that the solutions obtained on the H_c grid are highly dissipative. The resolution of the discontinuities on this grid is far from satisfactory for all solution components presented. Moreover, as noted previously for the other two test cases, the overshoot of the u-velocity profile decreases as we compute on finer

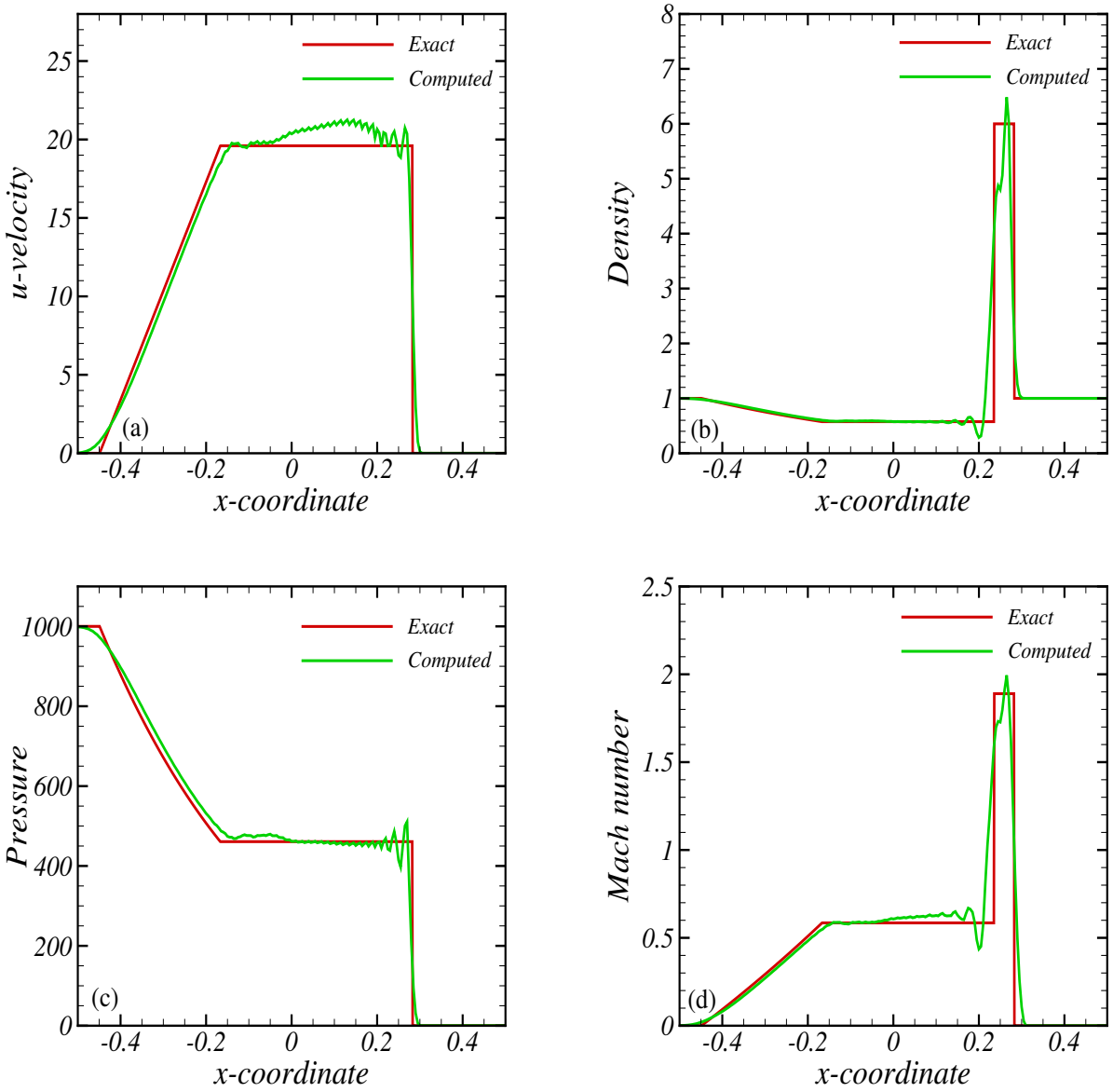

Figure 3.18 Test Case 3: Comparison of numerical with exact solution at $t = 0.012$ units; (a) u-velocity, (b) density, (c) pressure, (d) Mach number.

grids. However, we note that the resolution of the head of the rarefaction fan is not good, no matter which grid we are on. In fact, this feature can be observed in the other plots of the figure as well. From the density profile (part(b)) it is evident that we obtain a better resolution of the contact discontinuity and the shock wave on the H_f grid when compared to the other two grids, but these are still far from being adequately resolved. Convergence of the pressure profile to the exact solution is evident from part(c) of the figure (see the portion of the plot at the rarefaction fan). The same features discerned above especially for density, are also evident in the Mach number profiles.

The order of convergence for Test Case 3 is given in Table 3.5. One can immediately notice that the order of convergence for this test case has significantly dropped when compared to

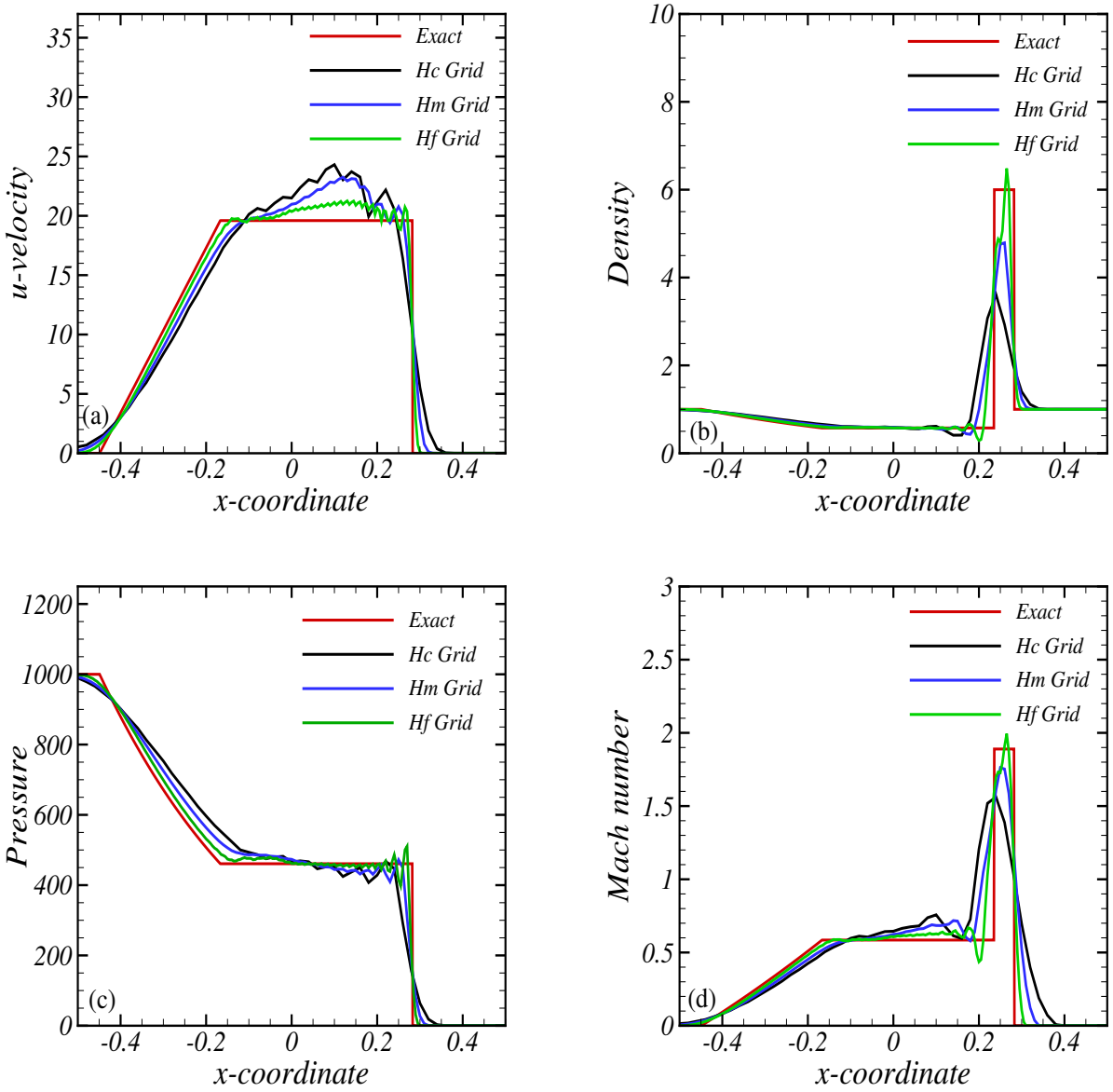

Figure 3.19 Test Case 3: Comparison of numerical solution on three different grids with exact solution at $t = 0.012$ units; (a) u-velocity, (b) density, (c) pressure, (d) Mach number.

the orders obtained for the other test cases. Moreover, the negative values present in Table 3.4 seem to indicate that the resolution of at least the H_c grid is not sufficient to provide meaningful results. This in turn suggests this grid should not have been used for the above calculations, but we were forced to so because of computing resources. Even for this test case we did not tune the artificial dissipation parameters, so the comments made regarding this in Test Case 2 will also hold here.

Table 3.5 Test Case 3: Results from grid function convergence tests.

ϕ	$\|\|\phi_h - \phi_{h/2}\|\|$	$\|\|\phi_{h/2} - \phi_{h/4}\|\|$	$\frac{\|\|\phi_h - \phi_{h/2}\|\|}{\|\|\phi_{h/2} - \phi_{h/4}\|\|}$	p
ρ	$2.87773e-2$	$2.28391e-2$	1.26	0.33342
ρu	$6.5508e-1$	$4.256e-1$	1.53917	0.62216
ρv	$2.6242e-2$	$3.18524e-2$	0.82298	-0.281054
ρw	$2.6214e-2$	$3.18524e-2$	0.822984	-0.28106
ρe	$1.30642e1$	$7.26125e0$	1.79917	0.84733
u	$1.1625e-1$	$1.6475e-1$	0.70559	-0.50308
v	$2.01406e-2$	$2.22284e-2$	0.90607	-0.14229
w	$2.01e-2$	$2.22e-2$	0.90605	-0.14232
p	$2.73473e0$	$1.9063e0$	1.43457	0.52062
T	$2.66466e-2$	$5.67685e-2$	0.46939	-1.091136

Remarks on convergence studies

In the following paragraphs we will try to provide some justification for the convergence rates obtained for the three test cases. The convergence rates achieved for Test Case 1 are within acceptable limits for problems whose solutions are inherently nonsmooth (see [167] for details). However, as already noted the rates for the other two test cases are far from satisfactory considering that we should be able to achieve first-order convergence.

Recall that our coarsest grid has a grid spacing of $\Delta x = 0.02$, $\Delta y = 0.01$, and $\Delta z = 0.01$. We also know that in the last two test cases the velocity of the gas in the tube is higher than that in Test Case 1. Moreover, we know that as Reynolds number (Re) increases, the number of length scales (especially the smaller scales) in a flow increases. This then suggests that one needs finer grids to resolve these scales to be able to obtain meaningful results; otherwise there will be loss of physical information. Hence, use of coarse grids in calculations involving convergence rates at high Re degenerates the results that could be expected.

The length scale for the Re calculations was chosen to be the hydraulic diameter of the rectangular tube under consideration, which is 0.2 for the shock-tube problem. Moreover, in our computations the dynamic viscosity is assumed to be constant; *i.e.,* we prescribe a specific value. With the length and dynamic viscosity set, the only other variables required to build the Re are the density and velocity magnitude, which are readily available at each grid point in our calculations.

Two-dimensional contour plots of Reynolds number profiles for Test Cases 1 to 3 are shown in Fig. 3.20. The distribution of Re was obtained by supplying the formula for Re to our post-processing visualization package (FieldView). We note that for Test Case 1 and Test Case 2 the maximum Re is approximately the same. In particular, it is near 4840. For Test Case 3 the maximum Re is 1600000, which is significantly higher. Since the Reynolds numbers are the same in both Test Cases 1 and 2, intuition would lead us to expect the order of convergence of the solutions to be nearly the same, since in all test cases we computed on identical grids.

However, contrary to our intuition, the orders of convergence for Test Case 2 is fairly far

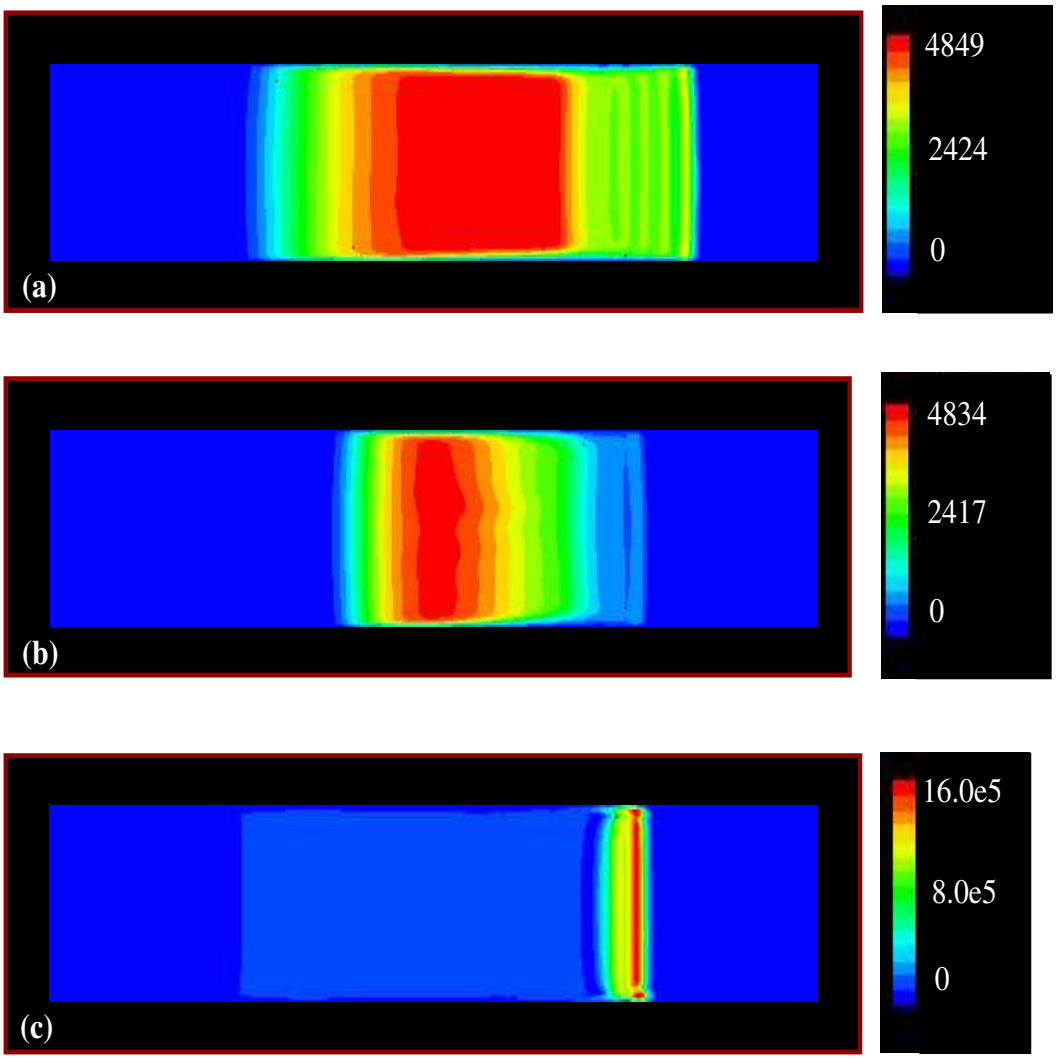

Figure 3.20 Contour plots of Re; (a) Test Case 1, (b) Test Case 2, (c) Test Case 3.

from those obtained in Test Case 1. The maximum Mach number of the flow in Test Case 2 is approximately 2.45 (supersonic), whereas that in Test Case 1 is only 0.95 (transonic). We remark that irrespective of the value of Re, an increase in the value of M increases the nonsmoothness of the solution, which is detrimental to the convergence rates. Hence, the decrease in convergence rates in Test Case 2 when compared to Test Case 1, should be expected. For Test Case 3 we have three main concerns as far as convergence rates are concerned. The first is an increase in Re, which is now considerably higher than in the other two cases. Also, the maximum M is two, which is approximately twice as high as that of Test Case 1. Also, the incident shock wave is 15000 times stronger when compared to the shock in Test Case 1 and around 7500 times stronger than the one that is formed in Test Case 2. All these factors play their own role in the deterioration of convergence rates. The result of these effects are clearly visible in orders of convergence presented in Table 3.5.

3.4.4 Test Case 4

With this test case we are concerned with assessing the capability of the solver to simulate a multi-dimensional problem. Although, in the previous test cases the simulated results were three-dimensional, the solutions mainly depended on only the x-coordinate (see contour plots at the cross sections of the shock tube). The test case considered here is a three-dimensional blast-wave problem described in [65]. The initial conditions for the problem are given in Table 3.2. This problem setup suggests that even this test case is essentially one-dimensional; if we were to employ spherical coordinates with velocity and other scalars variables of the flow depending only on the radial distance r from the origin. However, our code was developed in Cartesian coordinates, thereby, introducing a three-dimensional aspect to the problem.

One may consider the spherical motion alluded to above as being analogous to the one-dimensional motion in the tube under the influence of a piston, with the piston being replaced by an expanding sphere, which impresses a motion on the medium outside. One should bear in mind, however, that in three-dimensional space energy at an increasing rate is required to maintain the constant speed of the piston. Moreover, This is not the scenario being considered here since at $t = 0$ we have a region in the domain having finite energy, which is released instantaneously. In better agreement with the present test scenario is the analogy with the case of spherical blast waves caused by the explosion of a given mass of explosive. However, one should not confuse this scenario with the typical "point" explosion problem, where like in our case there is an instantaneous release of energy, but at a specific space point. Our test case considers the problem of shock wave propagation in air, caused by the explosion of some charge of spherical shape, *i.e.,* a sphere of finite radius. In our case the sphere has a radius of 0.4 units.

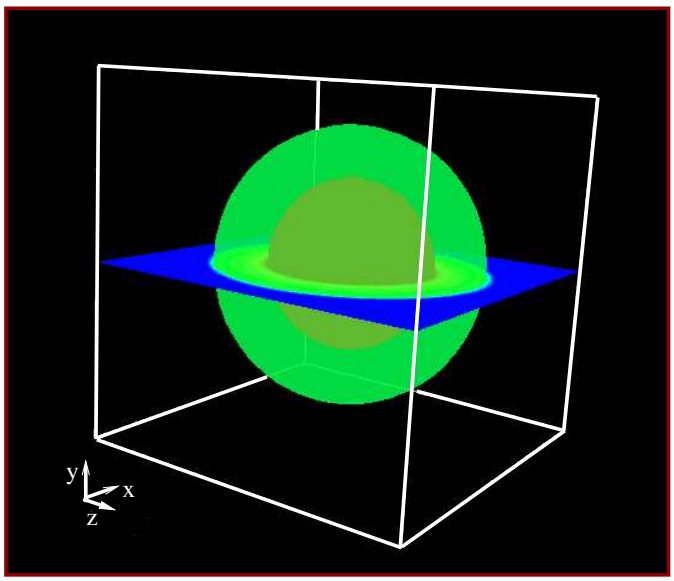

Figure 3.21 Test Case 4: 3-D visualization of spherical waves.

We begin by presenting in Fig. 3.21 a three-dimensional rendering of the total velocity magnitude at time t=0.25 units. The solutions for this test case were calculated on a grid of $101 \times 101 \times 101$ points. We were forced to use the same gridding in all three directions

because of the intrinsic symmetry of the problem. The figure clearly demonstrates the ability of the solver to resolve the spherical waves generated as part of the solution. In particular, the solution to this test case consists of a spherical shock wave traveling outwards, a spherical contact surface traveling in the same direction, and a spherical rarefaction traveling inwards. This is to be expected based on the nature of the initial conditions. The spherical structures (waves) present in the figure are isosurfaces, which were generated at specific values of the velocity magnitude. The transparency of the outer surface was increased so as to allow the visualization of the surface within. We note that we have not used a definitive color table since the transparency of the surfaces would obscure interpretation. Moreover, we have not made an attempt to delineate the different spherical waves since there is no easy way of presenting the visualization.

To demonstrate that an explosion-like scenario occurs, we display in Fig. 3.22 total velocity vectors colored with velocity magnitude in the xy-plane at a value of z=0. We note that all the velocity vectors point outwards, indicating the movement of fluid away from the high pressure center, just as would be the case due to an explosion.

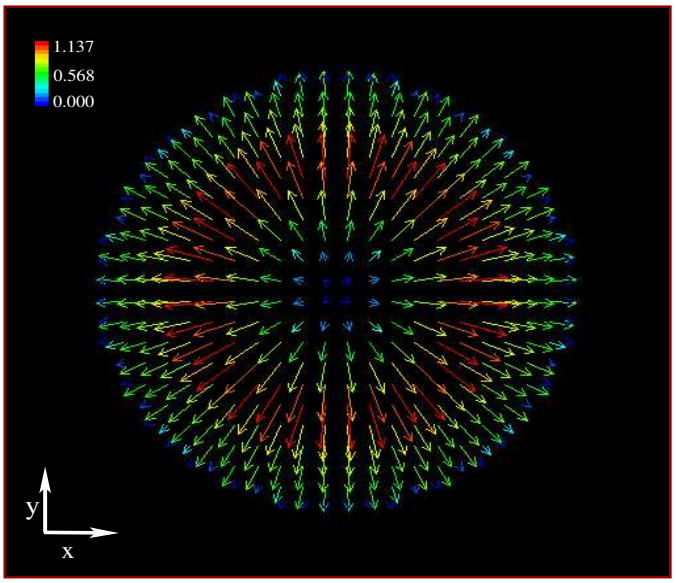

Figure 3.22 Test Case 4: Velocity vectors colored with velocity magnitude displaying the explosion scenario.

Figure 3.23 shows the velocity magnitude as a function of x and y on the plane z=0 at output time t=0.25. The figure exhibits a shock wave traveling outwards, a contact surface traveling in the same direction, and a rarefaction wave traveling inwards. The white arrow pointing inwards (towards the center) indicates the direction of motion of the rarefaction wave, and the white arrow pointing outwards (towards the quiescent zone) indicates the direction of motion of the shock wave and contact discontinuity. Unlike the contour plots in the previous test cases, the features of the solution for this test case are not readily comprehensible. We have, therefore, made explicit comments in the plots themselves to provide better clarity to the reader. The problem in distinguishing the features of the solution is in part due to the slightly more complicated physics of the explosion, compared with that of the shock tube. Herein, we will make a humble effort to at least provide an

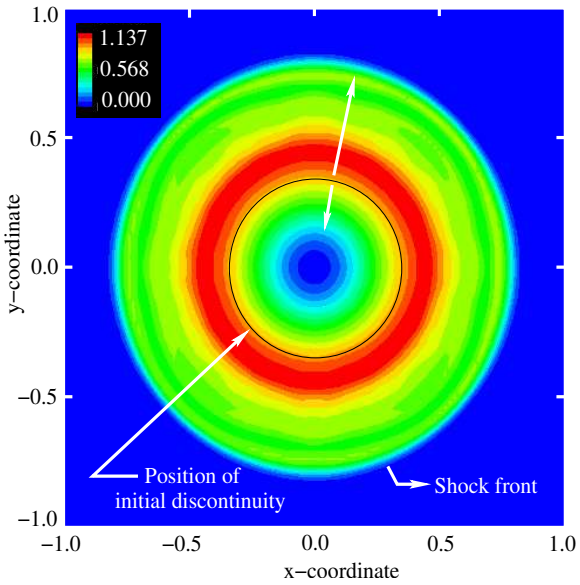

Figure 3.23 Test Case 4: 2-D contour plot of velocity magnitude at $t = 0.25$ units.

overview of the overlying physics of the problem.

Recall that this test case is analogous to that of an explosion, *i.e.,* the total energy available is given in the initial data. Hence, as time evolves we should expect that the energy available to push the shock wave through the medium should reduce. This will in effect result in weakening of the shock wave itself, thereby decreasing the jumps across it as time progresses. This is clearly visible in the velocity magnitude plot (see the region between the position of the initial discontinuity and the shock front). Note that at regions near the initial discontinuity we see the maximum velocity, and the velocity gradually decreases as we move outwards to the present location of the shock front at t=0.25. This is because at early times the shock front is located at regions near the initial discontinuity when the shock is strong, but as the shock moves outwards the shock weakens resulting in decreasing jumps across the shock. The inward moving rarefaction fan is also clearly visible in the figure.

In Fig. 3.24((a),(b),(c)) we show the corresponding density, pressure and temperature distributions, respectively, on the same plane (z=0) at the same time. As expected, we see a jump in density and temperature at the contact discontinuity, whereas the pressure is continuous across it. The rarefaction wave across which density and pressure decreases continuously is also evident from the plots. Moreover, after the air in a blast wave has been crossed by the shock front, and thereby compressed, it expands rapidly to a pressure, which is in general below the pressure in front of the shock wave (see the text by Courant and Fredrichs [168]). This so called suction phase is an important feature of fluid motion caused by explosions. This feature can be seen in the pressure contour (see region just behind the shock), thus demonstrating that the solver is able to predict such physics. The temperature contour also shows the same basic features. Furthermore, in all plots presented we observe that the spherical nature of the solutions has not been perfectly resolved.

This should be expected since the rectangular cells will cut the initial discontinuity so as to result in a staircase representation of the data. Such representation directly leads to the formation of small amplitude waves. These waves are also propagated by the numerical

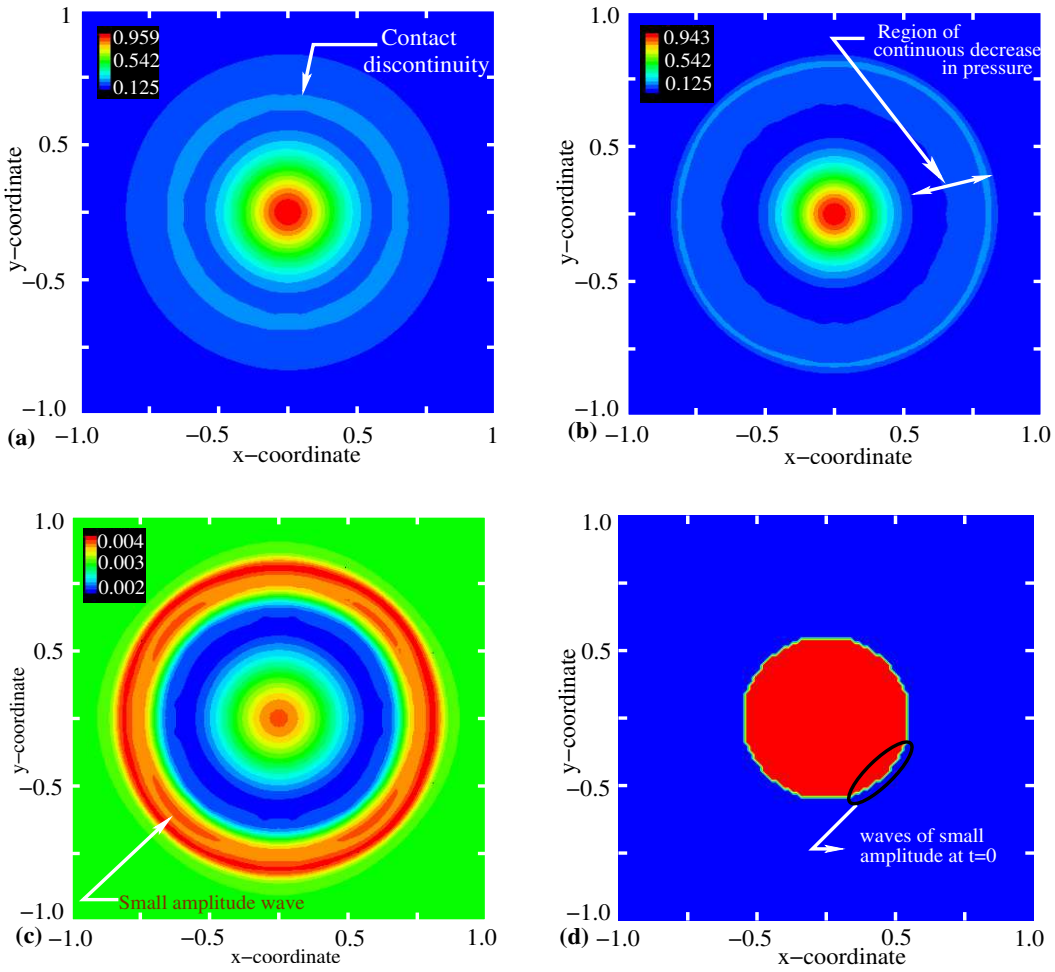

Figure 3.24 Test Case 4: 2-D contour plots at $t = 0.25$; (a) density, (b) pressure, (c) temperature. (d) Manifestation of small amplitude waves at initial time

method (see Fig. 3.24(c)), since such waves are not actually spurious as they result from the data as given. The source of the small amplitude waves generated due to the staircase representation of data is clearly shown in Fig. 3.24(d). The plot was generated at $t = 0$, and it represents the distribution of the initial conditions at that time.

To display the symmetric character of the numerical solution, we display 1-D plots of the u-velocity profile, v-velocity profile and w-velocity profile in Fig. 3.25. We note that the u-velocity plot was extracted from the horizontal centerline of the xy plane at a location where z=0, the v-velocity plot was extracted on the vertical centerline of the same plane, and the w-velocity vector was extracted from the horizontal centerline of the zy plane at a location where x=0. The symmetries in the velocity components are clearly evident from the figure.

We also present the density and pressure contours on each of the three orthogonal planes to demonstrate the three-dimensional, but still symmetric aspect of the problem. The figures displaying the contours are particularly interesting because they allow us to view the interior in its most natural way, *i.e.,* as a sphere with one-eight of it being removed. It is evident from both part(a) and part(b) of the figure that the solver is able to capture the spherical

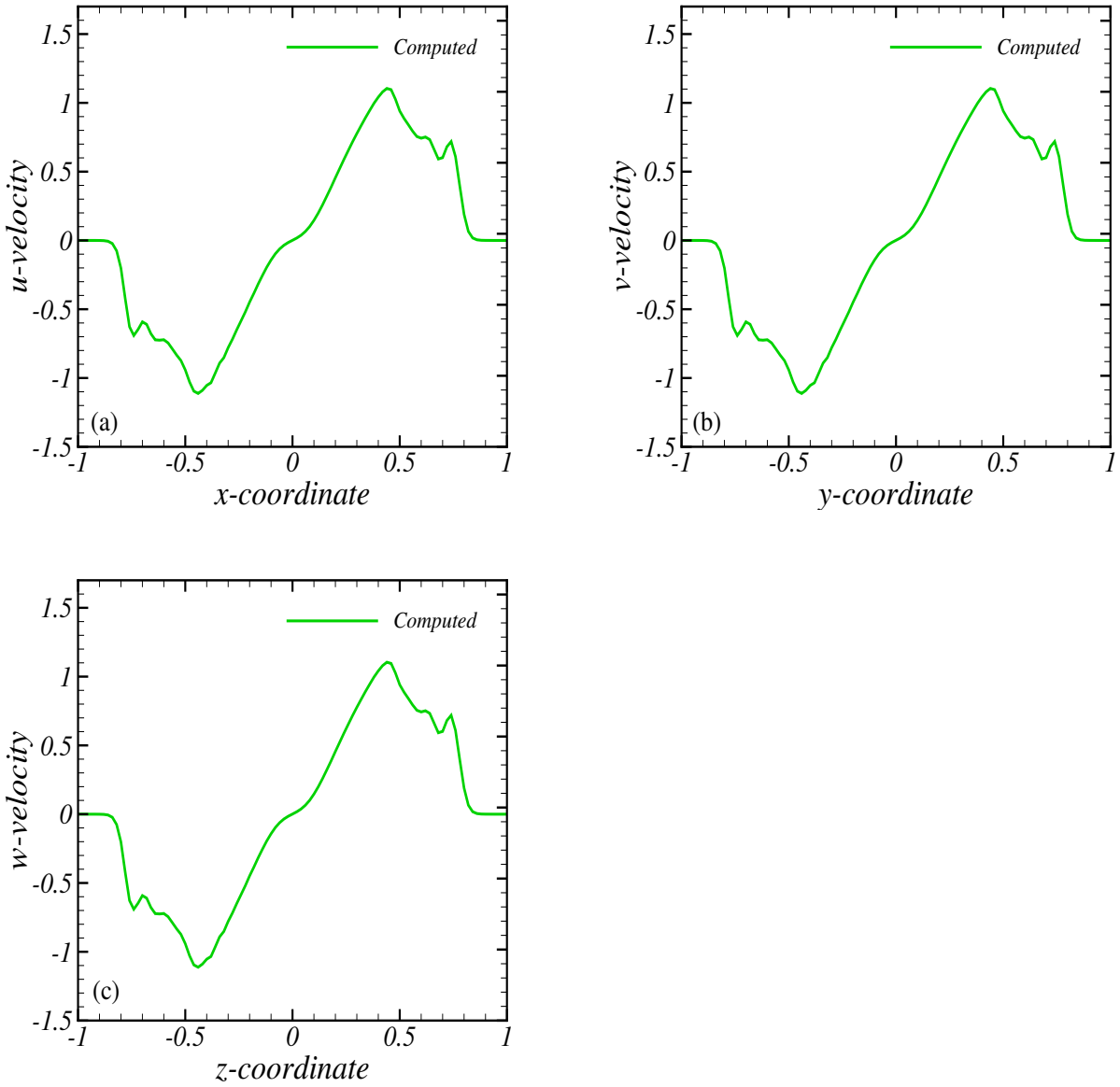

Figure 3.25 Test Case 4: 1-D plots of (a) u-velocity, (b) v-velocity, and (c) w-velocity at $t = 0.25$ units displaying symmetries.

symmetries present in the problem.

In Fig. 3.27 we present one-dimensional plots of the velocity magnitude, density, and pressure. We note that for this test case, we could not find any resources that would allow us to produce an exact solution to the Riemann problem in spherical coordinates, although we are sure that such resources exist. Moreover, keeping in mind the performance of the solver for the previous three test cases we are confident that the solver produces solutions that are in fairly good agreement with the exact solutions. For a qualitative comparison of the computed solutions with "exact" solutions, the reader is referred to the chapter on multi-dimensional test problems in [65]. We remark that the general profile of the computed solutions are in fairly good agreement with the solutions given in [65].

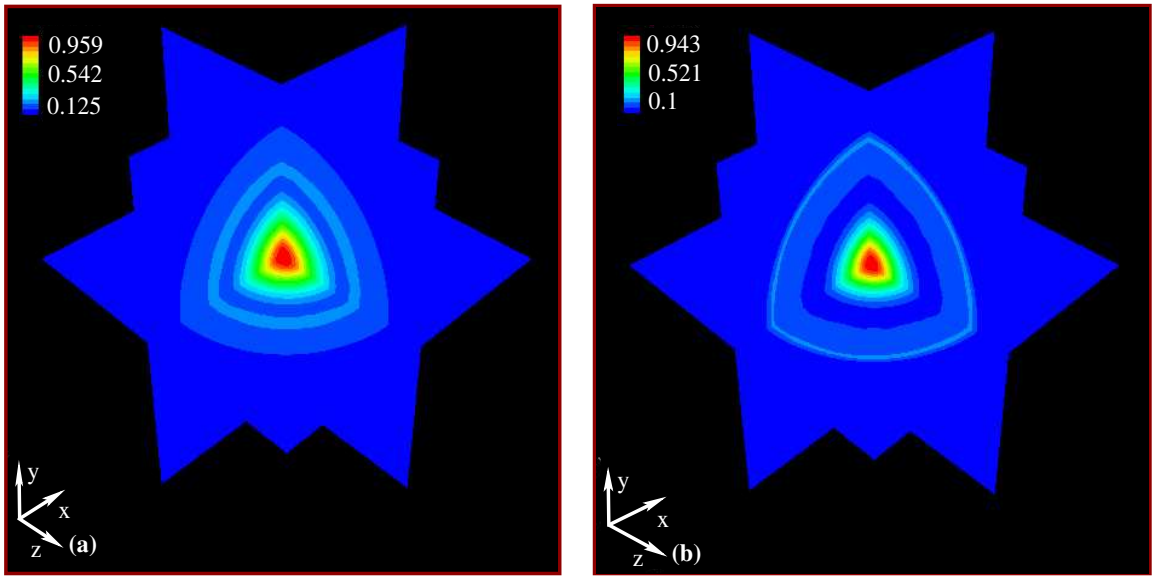

Figure 3.26 Test Case 4: 3-D visualization of (a) density contour and (b) pressure contour.

We remark that data for the plots presented were extracted from a radial line coincident with the x-axis. We further note that comparisons of the solution along other radial directions gave virtually the same result. This is confirmed by the very symmetric nature of the solution as shown in Figs. 3.26(a) and (b). Furthermore, the shock front, contact discontinuity and the rarefaction fan can all be easily delineated from the plots. The shock weakening effect is evident in the velocity magnitude plot. One can clearly observe that the magnitude of velocity behind the shock front gradually decreases as the shock moves away from the initial discontinuity (as time evolves). The jump in density at the contact discontinuity is evident from the density profile; as expected the pressure is continuous across the contact discontinuity. The phenomenon of the fluid rapidly expanding to a pressure comparable to the quiescent region (suction phase) after the pressure increase across the shock can also be seen clearly in the pressure profile. The rarefaction fan be clearly seen in each of the plots presented in the figure. The Gibbs oscillations at discontinuities is also evident in the plots. We further note that the Gibbs oscillations in the case of the shock tube problem are far more pronounced when compared to that of the blast-wave problem. This is seen clearly by comparing the 1-D plots in Fig. 3.27 to any of the 1-D plots presented for the shock tube problem. We should recognize that the shock tube problem is a wall-bounded shear flow, *i.e.,* there is a formation of boundary layer. The presence of a boundary layer then suggests there must be at least two length scales associated with this flow; one corresponding to the rather thin region adjacent to the tube walls and the other can be related to the nearly uniform part of the flow farther away from the walls. On the other hand in the blast-wave problem there is no such formation of the boundary layer and hence it possesses only a single length scale. This problem of multiple length scales in a wall-bounded shear flow results in an increase in aliasing effects due to under-resolution, whereas in the blast-wave problem the effects are relatively lower. Moreover, these problems will be exacerbated near the shock due to interactions between the Gibbs oscillations and aliasing errors. This is the reason for the Gibbs oscillations in the blast wave problem to be somewhat less pronounced when

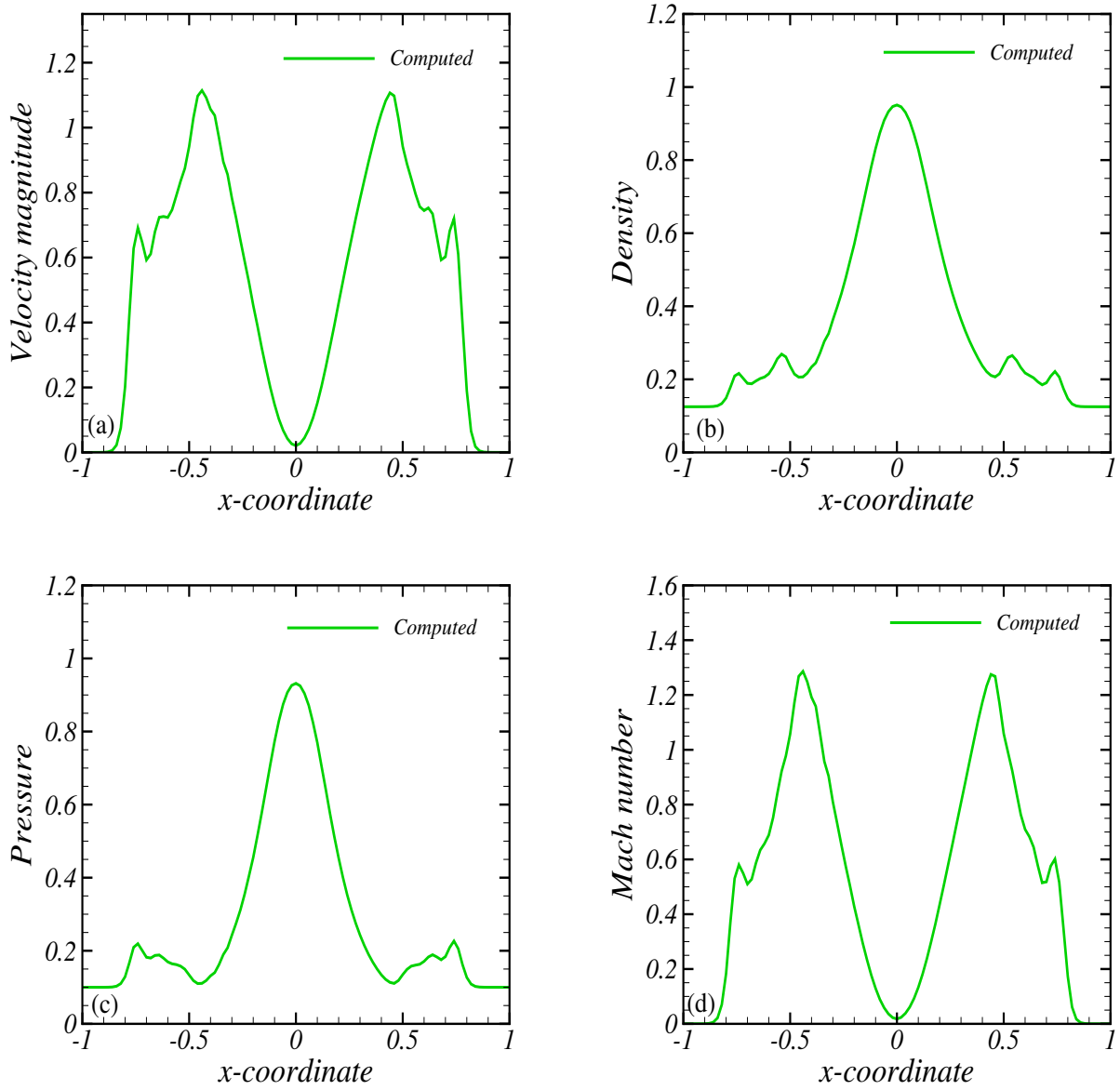

Figure 3.27 Test Case 4: Numerical solution at $t = 0.25$ units; (a) u-velocity, (b) density, (c) pressure, (d) Mach number.

compared to that of the shock tube.

Grid function convergence study

We perform a grid function convergence study using three grids with a refinement ratio 2. Since our finest grid has $101 \times 101 \times 101$ points, the medium grid will have $51 \times 51 \times 51$ gridpoints, and the coarse grid will have $26 \times 26 \times 26$ gridpoints. These grid resolve a domain $\Omega = 2 \times 2 \times 2$ in x-y-z space. We remark that for this test case since we were unable to obtain a source providing us with the exact solution, we did not deem it as appropriate to present 1-D plots of solutions obtained on the three different grids. However, we provide

results of the order of convergence in Table 3.6. The entries in the table indicate that the

Table 3.6 Test Case 4: Results from grid function convergence tests.

ϕ	$\|\|\phi_h - \phi_{h/2}\|\|$	$\|\|\phi_{h/2} - \phi_{h/4}\|\|$	$\frac{\|\|\phi_h - \phi_{h/2}\|\|}{\|\|\phi_{h/2} - \phi_{h/4}\|\|}$	p
ρ	$5.58955e-2$	$3.44658e-2$	1.62167	0.69756
ρu	$4.1169e-2$	$1.855506e-2$	2.21927	1.15
ρv	$4.11689e-2$	$1.85507e-2$	2.21925	1.15
ρw	$4.1169e-2$	$1.85506e-2$	2.21927	1.15
ρe	$1.411e-1$	$7.98e-2$	1.76889	0.82285
u	$1.6532e-1$	$7.25579e-2$	2.27854	1.18811
v	$3.26755e-3$	$1.434e-3$	2.27855	1.18811
w	$1.6532e-2$	$7.25578e-2$	2.27854	1.18811
p	$5.4853e-2$	$2.9505e-2$	1.85906	0.89457
T	$4.8e-4$	$2.1668e-4$	2.21558	1.14768

convergence rates obtained for the blast-wave problem are better than those obtained for the cases involving the shock-tube. This is not entirely surprising since the initial conditions were a three-dimensional extension of those in Test Case 1, although the Re and M values obtained for this test case would suggest quite the contrary.

A contour plot of Re is presented in Fig. 3.28. The Re was calculated in the same fashion as discussed previously for the other test cases. However, the length scale for this case was chosen to be the length of one side of the physical domain (cube), which is equal to two. The figure indicates that the peak Re for this case is around 33310, which when compared with that of Test Case 1 is significantly higher. Also, from Fig. 3.27(c) the peak M of 1.3 is higher. These parameters then suggest that the convergence rates for the blast wave problem should have been poorer.

However, we comment that, although the intervals within which the magnitudes of density and velocity magnitude lie are the same in both cases, the length scales chosen for the calculation of Re are completely different. In particular, the length scale for Test Case 1 based on the hydraulic diameter is 0.2, whereas that for the blast wave problem based on the scale of the physical domain is 2. This order of magnitude increase in the length scale immediately indicates the reason for the increase in Re for Test Case 4, although the values of the initial conditions are the same at $t = 0$.

Moreover, as discussed in fair detail at the start of this subsection, Test Case 4 corresponds to an explosion where there is an instantaneous release of a finite amount of energy. This results in the weakening of the shock wave as time evolves. This effect can be seen in both the velocity magnitude plot (Fig. 3.27(a)) and Mach number plot (Fig. 3.27(d)). That is, both the velocity magnitude and M decrease as time progresses. We note that although the peak M is higher in the blast wave problem, the M is not at its peak value for a long time. The M decreases to a value of 0.55 behind the shock wave within a time interval of 0.25, whereas the M behind the shock wave in Test Case 1 is 0.75 (see Fig. 3.8(d)) even at $t = 0.2$ units. Since the flow in Test Case 1 is inherently one-dimensional, this M will be

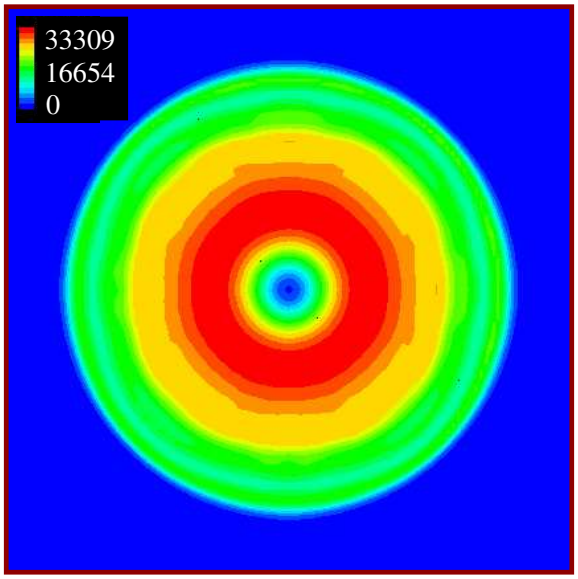

Figure 3.28 Test Case 4: Contour plot of Re on the xy plane at $z = 0$.

sustained at later times also. This then suggests that, in comparison, the shock wave in Test Case 1 is stronger than that of Test Case 4.

Even though the above discussions provide reasonable arguments for improved convergence rates for the blast wave problem, analysis of a more fundamental nature clearly demonstrates the reason why. For this we have to look back into the basic differences between the nature of fluid flow for a shock tube and blast wave problem. Previously we alluded to the fact that the shock tube flow is a wall-bounded shear flow having multiple scales, whereas the blast-wave problem possess a single length scale. Hence in the shock tube problem there is an increasing number of small (unresolvable) scales, thus suggesting that meaningful results can only be obtained on grids that are fine enough. The blast-wave problem has no such problem. This clearly demonstrates the reason for the improvement in convergence rates for the blast wave problem when compared to the shock tube problem (even in comparison to Test Case 1).

3.5 Concluding Remarks

This chapter was entirely devoted to the development of an algorithm to calculate the large-scale part '$\boldsymbol{q}(\boldsymbol{x}, t)$' of the usual LES decomposition (into large and small scales) employed in our multi-scale approach to LES of compressible turbulence. Shocks and other phenomena unique to compressible flows are also captured in this part of the algorithm. Theoretically, physical viscosity and heat conduction effects should result in sharp but continuous variations in shock waves and other discontinuities. However, these cannot be resolved using typical gridding; hence some method must still be used to capture these discontinuities in the large-scale algorithm.

We began by providing a brief review on shock-capturing methods, which are designed to have shock waves appear naturally within the computational domain as a direct result of the overall flow field solution. Although most (if not all) of these schemes/methods were

developed for solving the Euler (inviscid) equations of compressible gas dynamics, they can be applied to the full Navier–Stokes equations by employing centered discretizations for the viscous and heat conduction terms. We concluded that even though high-resolution methods such as ENO, WENO *etc.*, provide superior shock capturing properties when compared to using artificial dissipation, we chose to use the latter in our scheme keeping in mind the complexities and difficulties involved in implementing, for *e.g.,* an ENO scheme in multi-dimensions.

In Sec. 3.2 we presented the governing equations followed by a detailed mathematical formulation of the numerical scheme developed in this work. Our solver is based on a predictor-corrector methodology. The governing equations, Euler in the predictor stage and full N.–S. in the corrector stage, are solved in conservation form on a cell-centered unstaggered grid arrangement. The predictor part of the scheme consists of a half time-step forward Euler time integration of the Euler equations. This step is followed by the corrector part, which employs a full time-step implicit backward Euler time integration of the N.–S. equations. In both predictor and corrector parts of the algorithm, spatial discretization is second-order centered with dependent variables being evaluated at cell-centers and fluxes at cell walls. The 3-D implicit solves are performed by employing Douglas–Gunn time splitting, and the nonlinearities of the N.–S. equations are treated via δ-form quasilinearization. To capture shocks we used the MacCormack and Baldwin higher-order artificial viscosity. Since our LES methodology entails the application of a filter to the large-scale solution rather than to the equations, we used the Shuman filter to handle effects of aliasing. A coarse grained pseudo-language algorithm describing the implementation of this scheme was also provided towards the end of Sec. 3.2.

Several numerical tests were performed to test the solver and assess its performance. In particular, we used the standard shock-tube and three-dimensional blast wave problems. Boundary and initial conditions were also presented to construct a well-posed problem. Test Cases 1, 2 and 3 correspond to the shock-tube problem with an initial pressure ratio of 10, 100, and 100000, respectively. This increase in pressure ratio results in an increase in the strength of the incident shock wave, thus subjecting the solver to a sequence of tests with an increasing degree of difficulty. Test Case 4 is a blast-wave problem where there is a sphere of finite radius with high pressure and energy inside a quiescent region. This initial spherical discontinuity results in generation of spherical discontinuities as part of the solution as time evolves.

We presented 3-D and 2-D visualizations of the flow field inside the shock tube to provide a qualitative view of the typical wave patterns (shock waves, contact discontinuities, and rarefaction fans) seen in the evolution of the flow field subsequent to the removal of the diaphragm at $t = 0$. Comparisons of computed 1-D results with the exact inviscid solution are presented in Figs. 3.8, 3.13, and 3.18 Test Cases 1, 2, and 3 respectively. These figures indicate that we are able to capture that positions of the shock wave and rarefaction fan with fairly reasonable accuracy in Test Cases 1, 2 and 3. Although the resolution of the contact discontinuity for Test Case 1 was satisfactory, we observed a fair amount of smearing in Cases 2 and 3. This contact smearing is caused by numerical error, and it is inherent in almost all methods, including high-resolution methods unless specific steps are taken to combat it. The most popular measure to decrease contact smearing is probably Harten's artificial compression (see the text by Laney [160] for further details and more options).

Some smearing at the head and tail of the rarefaction fan is also seen. This smearing is to be expected since expansions typically have corners at their head and tail. Moreover, in all the u-velocity profiles (Figs. 3.8(a), 3.13(a), and 3.18(a)) we observe an overshoot in the computed results. However, we showed that this overshoot decreases with decrease in grid spacing. We were also able to resolve the boundary-layer with reasonable accuracy for both transonic (Test Case 1) and supersonic cases (Test Cases 2 and 3). The boundary layer profiles for the three test cases are presented in Fig. 3.7, Fig. 3.12, and Fig. 3.17, respectively. The presence of Gibbs oscillations is also evident in the plots presented. Moreover, interaction of aliasing error with the Gibbs oscillations make the oscillations in the solution more pronounced in the shock-tube problem.

Comparisons of density, u-velocity, pressure and Mach number profiles obtained on the H_c, H_m and H_f grids with the exact 1-D, inviscid solution were presented in Fig. 3.9 for Test Case 1, Fig. 3.14 for Test Case 2, and Fig. 3.19 for Test Case 3. These figures indicate that the computed solution approaches this solution as grid-spacing is decreased, indicating convergence of the solution in a qualitative sense. To determine the convergence rate of the solver we calculated the L^2 error based on the results obtained on the three grids. The convergence rates for Test Case 1 were found to be within acceptable limits for problems whose solutions are inherently nonsmooth. Cited references also corroborated our findings. However, there was a significant drop in the convergence rates for Test Cases 2 and 3. For Test Case 2, this reduction was due to effects of increase in M, and in Test Case 3 it was due to effects of increase in both M and Re, when compared to Test Case 1. One should recognize the roles played by the increase in shock strength and aliasing errors associated with increasing M and Re in further reducing the convergence rates in Test Cases 2 and 3.

To assess the capability of the solver to simulate a confirmedly three-dimensional problem (at least with respect to Cartesian coordinates) we used the 3-D blast-wave problem. Even for this case we were able to obtain the spherical waves generated as part of the solution. We were also able to simulate some of the physics that is unique to the 3-D blast-wave problem. In particular, in Fig. 3.23 we demonstrated that the solver is able to simulate the weakening of the shock wave as time progresses. The so called suction phase wherein the air after being crossed by the shock front, and thereby compressed, expands rapidly to a pressure present in front of shock wave can also be clearly seen in Fig. 3.24(b). Furthermore, the symmetries present in Test Case 4 were displayed in Fig. 3.25 and Fig. 3.26. Grid function convergence studies indicated that the convergence rate achieved for the blast-wave problem are better than those achieved for the shock tube problem. This increase in convergence rates is due to the fact that the blast-wave problem possesses a single length scale; hence, the effects due to aliasing are significantly lower than those present in the shock tube problem.

Taking into consideration the wide range of test cases that have been employed, we conclude that the solver is reasonably accurate, robust and multi-dimensional. However, use of artificial dissipation to capture shocks implies that the numerical solutions will always display oscillations. Moreover, in the context of implementing our LES methodology which requires high-pass filtering of the grid-scale results, these oscillations will also feed into the subgrid-scale model. These findings suggest that the user has to be judicious when analyzing the subgrid-scale results.

Chapter 4
SMALL-SCALE SOLUTION PROCEDURE

The novel subgrid-scale model developed in this work, which is based on deconvolution, discrete dynamical systems (DDS) and Kolmogorov's theories is presented in this chapter. We begin by providing some background on the work conducted by McDonough and his co-workers in the development of such models for incompressible flow simulations and the form of the SGS model developed by them. Next, we present a detailed derivation of the discrete dynamical system termed the compressible 'poor man's Navier–Stokes (CPMNS) equation' starting from a non-dimensionalized form of the full viscous Navier–Stokes equation. We then establish the relationships between the bifurcation parameters present in the CPMNS equation and the resolved-scale results via deconvolution thus eliminating the "closure" problem. The approach employed to construct the amplitude factors which forms an important part of the proposed model is also discussed. We will then characterize the different types of temporal behavior produced by the DDS in parameter space via time-series and power spectra. Using so called "regime maps" we provide insight into the overall dynamics of the CPMNS equation when the bifurcation parameters are varied over their ranges of stable behavior. Finally, we perform some preliminary testing of the subgrid-scale (SGS) model developed in this chapter.

4.1 Background

As emphasized throughout this work and recalled here for completeness, the motivation and objective to develop a subgrid-scale model to be described in the following sections is to overcome as much as possible the many shortcomings of traditional LES. It has been known since its very inception that the filtering process in LES leads to significant problems. Filtering equations, as is done in usual LES, results in two main problems. First, if the governing equations are nonlinear, the action of the filter on the nonlinear terms produces correlations (statistical, rather than physical quantities) which must be modeled. Second, if non-uniform gridding is employed, the filter will no longer commute with the differential operators; so errors arise from this source even if the equations are linear. Hence, in general the traditional SGS models tend to model correlations (*statistics*) rather than primitive variables (*physics*) at the small-scale, thus removing any possibility of accounting for interactions between turbulence and other physics on the sub-grid scale.

Moreover, applications of LES to compressible flow have been significantly fewer owing to increased complexity introduced by the need to solve an additional equation (usually expressed in terms of total energy), which in the traditional framework results in extra unclosed terms that must be modeled in addition to the SGS stresses. Complexities involved in developing such models was demonstrated in Sec. 2.1.3. Although implicit large-eddy simulation (ILES) procedures, which use implicit filters and the notion of a corresponding "built-in" SGS model associated with the filter are being widely used for simulations involving compressible turbulence, there are several compelling reasons to adopt a more systematic approach. While discrete derivative operators have a low-pass filtering effect, they act only in the spatial direction in which the derivative is taken. Of a more serious nature is the

inability of the implicit filtering approach to control numerical error. Without the use of an explicit filter there is no way of controlling the energy in the high-wavenumber portion of the energy spectrum. Significant energy in this part of the spectrum coupled with the non-linearities in the N.–S. equations can produce significant aliasing errors in such methods.

To eliminate most of the problems caused by filtering the equations of motion and also to provide better control over the energy at the small scales, McDonough *et al.* [62] introduced an alternative approach to LES. This is based on three key ideas: 1) filter solutions, not equations; 2) model primitive variables (physics), not correlations (statistics), and 3) do not discard subgrid-scale model results; instead use them to augment the resolved scale via a multi-scale formulation. Hylin and McDonough [169] provide a detailed analysis of this approach, and a summary is presented in the text by Sagaut [93]. In all of these works the small-scale components were constructed as a product of three factors:

$$q_i^* = A_i \zeta_i M_i \,, \tag{4.1}$$

where q_i^* is the fluctuating component of the i^{th} dependent variable at the small scale; A_i is an amplitude factor constructed on-the-fly during a LES from Kolmogorov's theories of isotropic turbulence; ζ_i is an anisotropy correction factor; and M_i is a 'chaotic map'—a discrete dynamical system (DDS) that introduces "turbulent-like" temporal fluctuations. Details of the derivation and method of calculation of A_i and ζ_i can be found in [169]. The M_is were constructed using the logistic map (May [170]) for all solution components.

However, it was found in McDonough *et al.* [171] that the practice of using only the logistic map did not provide correct predictions for passive scalar fluctuations, which led McDonough and Huang [172] to produce a 'first-principles' derivation of the fluctuating factor in Eq. (4.1). The resulting DDS, termed the 'poor man's Navier–Stokes (PMNS) equation' in deference to the comment made by Frisch [4] regarding quadratic maps, was derived directly from the equations of motion, thus endowing the M_is with some of the actual small-scale physics. A detailed derivation of the DDS for 2-D incompressible flow, including a thorough computational analysis of the system, is given by McDonough and Huang in [173]. They identified 14 kinds of behaviors characterized by time series and power spectra that the DDS could produce; these appear to encompass the known temporal behaviors of incompressible N.–S. flows. Analysis of the DDS was furthered by Bible and McDonough [174] and McDonough *et al.* [175]; and McDonough and Joyce [176] presented a subgrid-scale model based on this first-principles approach for turbulent convection. In recent work the small-scale components were constructed as a product of only two factors, as proposed by McDonough [177] and Holloway and McDonough [178]:

$$q_i^* = A_i M_i \,, \qquad i = 1, 2, \ldots, N_v \,, \tag{4.2}$$

where, as before, q_i^* is the small-scale portion of the decomposition of the usual LES dependent variable vector

$$\boldsymbol{Q}(\boldsymbol{x}, t) = \boldsymbol{q}(\boldsymbol{x}, t) + \boldsymbol{q}^*(\boldsymbol{x}, t) \,, \tag{4.3}$$

containing N_v components. Removal of ζ_i, the anisotropy correction in Eq. (4.1), was enabled by employing an extension of Kolmogorov's approach to nonisotropic, nonhomogeneous flows, as described in [178].

Successful comparisons of time series produced by the PMNS equations with those of the classical experimental data of Gollub and Benson [57] is shown in [176]. The motivation to transfer the concept to compressible flow was mainly due to the success of the incompressible PMNS equations as subgrid-scale models, both with and without chemistry and the general difficulty of constructing subgrid-scale models for compressible flow by traditional approaches. We now proceed to derive the discrete dynamical system for compressible flow from the compressible N.–S. equations.

4.2 Mathematical Formulation

We begin with a non-dimensional form of the 3-D N.–S. equations,

$$\frac{\partial \rho}{\partial t} + \nabla \cdot (\rho \boldsymbol{U}) = 0\,, \tag{4.4a}$$

$$\rho \frac{D\boldsymbol{U}}{Dt} = -\frac{1}{\gamma M^2}\nabla p + \frac{1}{Re}\nabla \cdot \tau\,, \tag{4.4b}$$

$$\rho \frac{DE}{Dt} = -\frac{1}{\gamma M^2}\nabla \cdot (p\boldsymbol{U}) + \frac{1}{Pe}\nabla \cdot (k\nabla T) + \frac{1}{Re}\phi\,. \tag{4.4c}$$

The equation of state is given by

$$p = \rho T\,. \tag{4.5}$$

In the above equations ρ, p and T are the usual density, pressure and temperature; $\boldsymbol{U} \equiv (u, v, w)^T$ is the velocity vector; E is total energy (internal plus kinetic); ∇ is the gradient operator, and D/Dt is the substantial (material) derivative. Elements of the stress tensor are given in Cartesian tensor notation by

$$\tau_{ij} = \mu\left(\frac{\partial u_i}{\partial x_j} + \frac{\partial u_j}{\partial x_i}\right) + \delta_{ij}\lambda\nabla \cdot \boldsymbol{U}\,, \quad i, j = 1, 2, 3\,, \tag{4.6}$$

and the dissipation function ϕ is defined by:

$$\phi = \tau_{ij}\frac{\partial u_i}{\partial x_j}\,, \tag{4.7}$$

with Einstein summation. Finally, k is the thermal conductivity; μ is dynamic viscosity; λ is second viscosity; γ is the ratio of specific heats, and δ_{ij} is the Kronecker delta. The velocity components u, v, w have been scaled with a reference velocity magnitude U_{ref}, spatial coordinates (x, y, z) by a fixed length scale L, pressure by the equation of state for a perfect gas and temperature by a reference temperature T_{ref}. In the above set of governing equations presented in dimensionless form, Re is the Reynolds number, $Re \equiv UL/\nu$; Pe is the Péclet number defined as $Pe \equiv UL/\kappa$, and finally M is the Mach number given by $M \equiv U/a$. Here, ν is the kinematic viscosity; κ is thermal diffusivity, and a is the speed of sound in the medium.

4.2.1 The discrete dynamical system

In this subsection we will present a detailed derivation that converts the set of PDEs Eq. (4.4) into an algebraic system that can be very efficiently evaluated. We start by assuming that all dependent variables can be represented by Fourier series. The Fourier representations for ρ, $\boldsymbol{U}$, p, E and T respectively can be expressed as

$$\rho(\boldsymbol{x},t) = \sum_{\boldsymbol{k}=-\infty}^{\infty} a_{\boldsymbol{k}}(t)\varphi_{\boldsymbol{k}}(\boldsymbol{x},t) \ , \tag{4.8a}$$

$$u(\boldsymbol{x},t) = \sum_{\boldsymbol{k}=-\infty}^{\infty} b_{\boldsymbol{k}}(t)\varphi_{\boldsymbol{k}}(\boldsymbol{x},t) \ , \tag{4.8b}$$

$$v(\boldsymbol{x},t) = \sum_{\boldsymbol{k}=-\infty}^{\infty} c_{\boldsymbol{k}}(t)\varphi_{\boldsymbol{k}}(\boldsymbol{x},t) \ , \tag{4.8c}$$

$$w(\boldsymbol{x},t) = \sum_{\boldsymbol{k}=-\infty}^{\infty} d_{\boldsymbol{k}}(t)\varphi_{\boldsymbol{k}}(\boldsymbol{x},t) \ , \tag{4.8d}$$

$$p(\boldsymbol{x},t) = \sum_{\boldsymbol{k}=-\infty}^{\infty} p_{\boldsymbol{k}}(t)\varphi_{\boldsymbol{k}}(\boldsymbol{x},t) \ , \tag{4.8e}$$

$$E(\boldsymbol{x},t) = \sum_{\boldsymbol{k}=-\infty}^{\infty} e_{\boldsymbol{k}}(t)\varphi_{\boldsymbol{k}}(\boldsymbol{x},t) \ , \tag{4.8f}$$

$$T(\boldsymbol{x},t) = \sum_{\boldsymbol{k}=-\infty}^{\infty} T_{\boldsymbol{k}}(t)\varphi_{\boldsymbol{k}}(\boldsymbol{x},t) \ . \tag{4.8g}$$

Here $\boldsymbol{k} = (k_1, k_2, k_3)^T$ is a 3-D wavevector with all three components in the range $-\infty \leq k_i \leq \infty$. We will assume the basis set $\varphi_{\boldsymbol{k}}$ used in the construction of these series is complete in L^2 and orthonormal, but only the orthonormality will be specifically used in what follows. Also, despite the possible differences in the components of $\varphi_{\boldsymbol{k}}$, we will treat all of them as complex exponentials with respect to differentiation, and we will assume indexing has been done in such a way as to cancel imaginary parts from corresponding wavevectors. Next, application of the Galerkin procedure consists of the following steps:

i) substitute solution representations into governing equations, *i.e.,* substitute Eqs. (4.8) into Eqs. (4.4) ;

ii) commute differentiation and summation ;

iii) calculate Galerkin inner products ;

iv) supply the orthogonality constraint ;

v) reduce to a single wavevector ;

vi) construct forward Euler temporal discretization ;

vii) transform and rearrange to define bifurcation parameters and obtain the compressible poor man's Navier–Stokes equation (CPMNS equation).

We will give details on application of the Galerkin procedure only for the x-momentum equation—Eq. (4.4a); treatment of other equations is similar. Substituting the required solution representations given by Eqs. (4.8) into the x-momentum equation yields

$$\begin{aligned}
&\left(\sum_{\boldsymbol{l}} b_{\boldsymbol{l}}\varphi_{\boldsymbol{l}}\right)_t + \left(\sum_{\boldsymbol{l}} b_{\boldsymbol{l}}\varphi_{\boldsymbol{l}}\right)\left(\sum_{\boldsymbol{m}} b_{\boldsymbol{m}}\varphi_{\boldsymbol{m}}\right)_x + \left(\sum_{\boldsymbol{l}} c_{\boldsymbol{l}}\varphi_{\boldsymbol{l}}\right)\left(\sum_{\boldsymbol{m}} b_{\boldsymbol{m}}\varphi_{\boldsymbol{m}}\right)_y \\
&+ \left(\sum_{\boldsymbol{l}} d_{\boldsymbol{l}}\varphi_{\boldsymbol{l}}\right)\left(\sum_{\boldsymbol{m}} b_{\boldsymbol{m}}\varphi_{\boldsymbol{m}}\right)_z = -\frac{1}{\gamma M^2}\frac{1}{\sum_{\boldsymbol{l}} a_{\boldsymbol{l}}\varphi_{\boldsymbol{l}}}\left(\sum_{\boldsymbol{l}} p_{\boldsymbol{l}}\varphi_{\boldsymbol{l}}\right)_x \\
&+\frac{1}{Re}\frac{1}{\sum_{\boldsymbol{l}} a_{\boldsymbol{l}}\varphi_{\boldsymbol{l}}}\left[\frac{4}{3}\left(\sum_{\boldsymbol{l}} b_{\boldsymbol{l}}\varphi_{\boldsymbol{l}}\right)_{xx} + \left(\sum_{\boldsymbol{l}} b_{\boldsymbol{l}}\varphi_{\boldsymbol{l}}\right)_{yy} + \left(\sum_{\boldsymbol{l}} b_{\boldsymbol{l}}\varphi_{\boldsymbol{l}}\right)_{zz}\right] \qquad (4.9)\\
&+\frac{1}{Re}\frac{1}{\sum_{\boldsymbol{l}} a_{\boldsymbol{l}}\varphi_{\boldsymbol{l}}}\left[\frac{1}{3}\left(\sum_{\boldsymbol{l}} c_{\boldsymbol{l}}\varphi_{\boldsymbol{l}}\right)_{xy} + \frac{1}{3}\left(\sum_{\boldsymbol{l}} d_{\boldsymbol{l}}\varphi_{\boldsymbol{l}}\right)_{xz}\right],
\end{aligned}$$

where subscripts denote partial differentiation. The result after completing steps ii)—iv) is the following:

$$\begin{aligned}
\sum_{\boldsymbol{k}} \dot{b}_{\boldsymbol{k}} \;+\; &\sum_{\boldsymbol{l},\boldsymbol{m}} b_{\boldsymbol{l}} b_{\boldsymbol{m}} B^{(1)}_{\boldsymbol{l}\boldsymbol{m},\boldsymbol{k}} + \sum_{\boldsymbol{l},\boldsymbol{m}} c_{\boldsymbol{l}} b_{\boldsymbol{m}} B^{(2)}_{\boldsymbol{l}\boldsymbol{m},\boldsymbol{k}} + \sum_{\boldsymbol{l},\boldsymbol{m}} d_{\boldsymbol{l}} b_{\boldsymbol{m}} B^{(3)}_{\boldsymbol{l}\boldsymbol{m},\boldsymbol{k}} = -\frac{1}{\gamma M^2}\frac{1}{\sum_{\boldsymbol{k}} a_{\boldsymbol{k}}}\sum_{\boldsymbol{k}} p_{\boldsymbol{k}} k_1 \\
-\;&\frac{Z}{Re}\frac{1}{\sum_{\boldsymbol{k}} a_{\boldsymbol{k}}}\left[\sum_{\boldsymbol{k}} b_{\boldsymbol{k}}|\boldsymbol{k}|^2 + \frac{1}{3}\sum_{\boldsymbol{k}} b_{\boldsymbol{k}} k_1^2 + \frac{1}{3}\sum_{\boldsymbol{k}} c_{\boldsymbol{k}} k_1 k_2 + \frac{1}{3}\sum_{\boldsymbol{k}} d_{\boldsymbol{k}} k_1 k_3\right]. \qquad (4.10)
\end{aligned}$$

In Eq. (4.10) $B^{(i)}_{\boldsymbol{l}\boldsymbol{m},\boldsymbol{k}}$, i=1, 2, 3 arise from Galerkin triple products, and it is assumed that any required normalizations have been absorbed into these coefficients. These triple products are defined as, for example,

$$B^{(1)}_{\boldsymbol{l}\boldsymbol{m},\boldsymbol{k}} = m_1 \int_\omega \varphi_{\boldsymbol{l}}\, \varphi_{\boldsymbol{m}}\, \varphi_{\boldsymbol{k}}\, dV\,, \qquad (4.11)$$

with analogous results for the others, wherein we have chosen to lump the wavevector component also into the definition. Z is a normalization constant arising from the fact that although the $\varphi_{\boldsymbol{k}}$ may be orthonormal, this is not necessarily true for their derivatives, but, the value of Z is generally set equal to unity.

We may view Eq. (4.10) as an infinitely accurate model (basically a DNS); but for our purposes, for its utilization as a subgrid-scale model for LES, we will proceed by deleting from consideration all but some finite number of wavevectors $\boldsymbol{k}$ as in shell model constructions

[60]. In fact, we will remove all but a single arbitrary wavevector $\boldsymbol{k}$. This results in

$$\dot{b} + b^2 B^{(1)} + bcB^{(2)} + bdB^{(3)} = -\frac{k_1}{\gamma M^2}\frac{p}{a} - \frac{1}{a}\frac{Z}{Re}\left[b|\boldsymbol{k}|^2 + \frac{1}{3}bk_1^2 + \frac{1}{3}ck_1k_2 + \frac{1}{3}dk_1k_3\right]. \quad (4.12)$$

Then employing a forward Euler time discretization yields

$$\begin{aligned} b^{n+1} \quad &= b^n - \tau(b^2)^n B^{(1)} - \tau b^n c^n B^{(2)} - \tau b^n d^n B^{(3)} - \frac{\tau}{a^n}\left[\frac{k_1}{\gamma M^2}p^n\right] \\ &\quad -\frac{Z}{Re}\frac{\tau}{a^n}\left[b^n|\boldsymbol{k}|^2 + \frac{1}{3}b^n k_1^2 + \frac{1}{3}c^n k_1 k_2 + \frac{1}{3}d^n k_1 k_3\right], \end{aligned} \quad (4.13)$$

where τ is an arbitrary time step parameter.

We next add and subtract $\tau Z b^n|\boldsymbol{k}|^2/Re$ in Eq. (4.13) to obtain a transformation which we shall use to incorporate the logistic map into our DDS:

$$\begin{aligned} b^{n+1} \quad &= \tau B^{(1)} b^n\left[\frac{1-\tau Z|\boldsymbol{k}|^2/Re}{\tau B^{(1)}} - b^n\right] - \tau b^n c^n B^{(2)} - \tau b^n d^n B^{(3)} + \tau\frac{Z}{Re}b^n|\boldsymbol{k}|^2 \\ &\quad -\frac{\tau}{a^n}\left[\frac{k_1}{\gamma M^2}p^n\right] - \frac{Z}{Re}\frac{\tau}{a^n}\left[b^n|\boldsymbol{k}|^2 + \frac{1}{3}b^n k_1^2 + \frac{1}{3}c^n k_1 k_2 + \frac{1}{3}d^n k_1 k_3\right], \end{aligned} \quad (4.14)$$

Observe that if we are to recover the logistic map as part of this DDS we must require (analogous to the transformation employed in [173])

$$\frac{1-\tau Z|\boldsymbol{k}|^2/Re}{\tau B^{(1)}} = 1, \quad (4.15)$$

which implies that

$$\tau B^{(1)} = 1 - \frac{Z}{Re}\tau|\boldsymbol{k}|^2. \quad (4.16)$$

This allows us to write Eq. (4.14) as

$$\begin{aligned} b^{n+1} \quad &= \quad \beta_1 b^n(1-b^n) - \gamma_{21}b^n c^n - \gamma_{22}b^n g^n + \alpha b^n - \frac{1}{a^n}\left[\alpha b^n + \psi_1 p^n\right] \\ &- \quad \frac{1}{3a^n}\left[\chi_1 b^n + \zeta_1 c^n + \zeta_2 g^n\right], \end{aligned} \quad (4.17)$$

in which the first term is the logistic map.

It is worthwhile to comment that insistence on including the logistic map has arisen for several reasons. First, is the analysis by Frisch [4] relating quadratic maps, in general, to the N.–S. equations and introducing the description, poor man's Navier–Stokes equation, as mentioned earlier. The second comes from the fact that initial work of this sort presented here was performed for the 2-D incompressible N.–S. equations, and the continuous dynamical system that resulted contained only two different equations, and hence could not exhibit behavior any more complicated than quasiperiodicity. Hence, it was decided to introduce a simple discrete dynamical system at the time of discretization of the ODEs. For the 3-D incompressible equations this is not completely necessary, but far wider ranges of

stable behavior are observed when the transformation is employed. Finally, for the compressible equations we have had difficulty obtaining any interesting stable behavior without introduction of the transformation Eq. (4.15) leading to the incorporation of the logistic map.

A completely analogous derivation for the other equations in Eq. (4.4), sans introduction of the logistic map into results results in a coupled system of logistic maps obtained directly from the N.–S. equations:

$$a^{n+1} = a^n - \gamma_{11} a^n b^n - \gamma_{12} a^n c^n - \gamma_{13} a^n d^n \tag{4.18a}$$

$$\begin{aligned} b^{n+1} &= \beta_1 b^n \left(1 - b^n\right) - \gamma_{21} b^n c^n - \gamma_{22} b^n d^n + \alpha b^n - \frac{1}{a^n}\left[\alpha b^n + \psi_1 p^n\right] \\ &\quad - \frac{1}{3a^n}\left[\chi_1 b^n + \zeta_1 c^n + \zeta_2 d^n\right] , \end{aligned} \tag{4.18b}$$

$$\begin{aligned} c^{n+1} &= \beta_2 c^n \left(1 - c^n\right) - \gamma_{31} c^n b^n - \gamma_{32} c^n d^n + \alpha c^n - \frac{1}{a^n}\left[\alpha c^n + \psi_2 p^n\right] \\ &\quad - \frac{1}{3a^n}\left[\chi_2 c^n + \zeta_2 b^n + \zeta_3 g^n\right] , \end{aligned} \tag{4.18c}$$

$$\begin{aligned} d^{n+1} &= \beta_3 d^n \left(1 - d^n\right) - \gamma_{41} d^n b^n - \gamma_{42} d^n c^n + \alpha d^n - \frac{1}{a^n}\left[\alpha d^n + \psi_3 p^n\right] \\ &\quad - \frac{1}{3a^n}\left[\chi_3 d^n + \zeta_2 b^n + \zeta_3 c^n\right] , \end{aligned} \tag{4.18d}$$

$$\begin{aligned} e^{n+1} &= e^n - \gamma_{51} e^n c^n - \gamma_{52} e^n c^n - \gamma_{53} e^n d^n - \frac{1}{a^n}\left[\eta_1 p^n b^n + \eta_2 p^n c^n + \eta_3 p^n d^n\right] \\ &\quad - \frac{1}{a^n}\left[\theta T^n\right] - \frac{4}{3a^n}\left[\chi_1 \left(b^n\right)^2 + \chi_2 \left(c^n\right)^2 + \chi_3 \left(d^n\right)^2\right] \\ &\quad - \frac{1}{3a^n}\left[\sigma_{12}\ b^n c^n + \sigma_{13}\ b^n d^n + \sigma_{23}\ c^n d^n\right] \\ &\quad - \frac{1}{a^n}\left[\left(b^n\right)^2 \left(\sigma_{22} + \sigma_{33}\right) + \left(c^n\right)^2 \left(\sigma_{11} + \sigma_{33}\right) + \left(d^n\right)^2 \left(\sigma_{11} + \sigma_{22}\right)\right] . \end{aligned} \tag{4.18e}$$

The above equations (4.18) are the "compressible poor man's Navier–Stokes (CPMNS) equation." This DDS is seven dimensional (when the equation of state and definition of internal energy are included to relate p^n to a^n and T^n to E^n), and it has a co-dimension of 35 (number of bifurcation parameters). Although it may appear at first that this imposes an almost insurmountable closure problem, all the bifurcation parameters are known in the sense that they can be evaluated "on the fly" at each grid point and at every time step of any typical LES procedure based only on the large-scale part of the solution. Finally, we comment that the form of this DDS and the nature of its construction suggest that it is related to a pseudodifferential operator of the compressible N.–S. system. This implies that is carries a significant part of the (local in space and time) behavior of these equations and should thus be appropriate as a SGS model of the type we are considering.

The 35 bifurcation parameters can be grouped into families based on their dependence on physical dimensionless parameters, or on velocity gradient components. This along with deconvolution leads to the straightforward theory for their evaluation which is described in the sequel.

4.2.2 Bifurcation parameters and amplitude factors—theory and evaluation

Recall that there are two main components in the subgrid-scale model: 1) the discrete dynamical system (DDS) which introduces temporal fluctuations at the subgrid-scale and 2) the amplitude factors for each fluctuating component. The derivation of the CPMNS equation (DDS) was discussed in fair detail in the previous section. In this section we provide details on the relationship between the bifurcation parameters in the CPMNS equation and the physics on the large-scale via the technique of deconvolution. Construction of the amplitude factors from an extension of Kolmogorov's theories is also discussed in brief.

Bifurcation parameters

By comparing Eq. (4.14) and Eq. (4.17), which is a part of the Galerkin procedure applied to the x-momentum equation, and going through an analogous derivation for the other four equations, it is straightforward to deduce that $\chi_i, \zeta_i, \sigma_{ij}$, $(i,j = 1,2,3)$ and α all depend on Re; ψ_i and η_i, $(i = 1,2,3)$ depend on M, and θ depends on Pe. For the sake of completeness we will explicitly write down the definitions of the bifurcation parameters mentioned above. Those associated with the Reynolds number are:

$$\beta_i = 4\left(1 - \frac{Z}{Re}\tau|\boldsymbol{k}|^2\right), \qquad \chi_i = \frac{\tau Z k_i^2}{Re}, \qquad \sigma_{ij} = \frac{\tau Z V^{(ij)}}{Re}, \qquad \alpha = \frac{\tau Z|\boldsymbol{k}|^2}{Re}$$
$$\zeta_1 = \frac{\tau Z k_1 k_2}{Re}, \qquad \zeta_2 = \frac{\tau Z k_1 k_3}{Re}, \qquad \zeta_3 = \frac{\tau Z k_2 k_3}{Re}, \tag{4.19}$$

where $i,j = 1,2,3$. Those containing Mach number are:

$$\psi_i = \frac{\tau k_i}{\gamma M^2}, \qquad \eta_i = \frac{\tau P^{(i)}}{\gamma M^2}, \qquad i = 1,2,3, \tag{4.20}$$

and the parameter providing Péclet number effects is defined as

$$\theta = \frac{\tau|\boldsymbol{k}|^2}{Pe}. \tag{4.21}$$

The γs defined as (*e.g.*, $\gamma_{21} = \tau B^{(2)}$) are set by the time stepping parameter and the Galerkin triple products corresponding to the selected wavevector. The Galerkin triple product carries Fourier space information associated with the velocity gradients. It is straightforward to check that $B^{(2)}$ arises from u_y in Eq. (4.4b), and this kind of relationship can be built for the other γs analogously. Even though this is somewhat complicated by wavevector dependence included in the triple products, we have lumped these into the definition of γs.

The basic feature of a subgrid-scale model is to account for the unresolved scales in a LES. The unresolved scales correspond to high-wavenumber content of the solution. We recognize that by performing the grid-scale calculation, hopefully, we are resolving wavenumber fluctuations that are approximately half-way through the inertial subrange (but probably not even that for high Re). To extract the high-wavenumber content from the solution components we need to perform a high-pass filtering of the grid-scale results. This corresponds to what is now termed deconvolution. In the present work this is achieved by using the Shuman filter [163], which is given by the formula $u_i = \left(u_{i+1} + \beta u_i + u_{i+1}\right)/\left(2+\beta\right)$, $\quad i = 2,\ldots,N-1$,.

We note that even though the Shuman filter is a low-pass filter (damps high-frequency oscillations) the high-frequency content of a signal can be extracted trivially by subtracting the Shuman filtered signal from the original signal.

At this point it is important to recognize that one has to specify a value for the filter parameter β. Moreover, one should expect this value to be different than the value employed to treat "aliasing" on the large-scale. On one end, at the large-scale the Shuman filter is used to remove high-wavenumber content, *i.e.*, as a low-pass filter, whereas at the small-scale it is employed to extract high-wavenumber content from the resolved-scale results (high-pass filter). Work done by Yang *et al.* [165] indicates that smaller the value of β lower the amount of high-wavenumber content left in the original signal. In the context of using the Shuman filter as a high-pass filter this would result in extracting more and more of the high-wavenumber content by lowering β. Moreover, filtering of the solution with a low value of β is somewhat similar to the second-filtering operation employed in implementations of dynamic SGS models, typically performed by employing a filter with a wider filter-width (generally $2\Delta x$). The reader would immediately recognize that setting the value of this parameter is important since it dictates the contribution from the SGS model. However, such free parameters, which have to be set are present in almost all filters that are widely used for LES; they are viewed as mathematical/numerical analytic quantities rather than as "closure constants."

We showed that the formal definition of the β_is is

$$\beta_i = 4\left(1 - \frac{Z}{Re_i}\tau|\boldsymbol{k}|^2\right), \qquad i = 1, 2, 3, \tag{4.22}$$

where Z is a normalization constant (usually set to unity); τ is the small-scale (dimensionless) time step; Re_i is a "directional" Reynolds number, which we will argue below to be roughly a Taylor microscale Reynolds number Re_λ. Finally, $\boldsymbol{k}$ is an arbitrary wavevector that must be estimated, by methods we will describe below.

We begin by estimating the time step τ on the sub-grid scales. Since we expect to be approximately half-way through the inertial subrange with the grid-scale calculations, it is natural to associate $\|\boldsymbol{S}\|^{-1}$ (inverse of the L^2 norm of the strain-rate tensor) with the Taylor microscale time, τ_T. Now since τ is dimensionless, and τ_T is not, we scale this with the resolved-scale time step size Δt; *i.e.,* we set

$$\tau = \frac{\tau_T}{\Delta t}. \tag{4.23}$$

We next consider the wavenumber $\boldsymbol{k}$. Our working hypothesis at this point is that we should use a wavevector consistent with, roughly, the middle of the inertial subrange. Thus, if we can compute a Taylor microscale Reynolds number and extract a length scale λ from this, we can obtain an appropriate value for $\boldsymbol{k}$ from its reciprocal.

Recall that the $Re_\lambda \sim Re_l^{1/2}$, the latter being the integral-scale Reynolds number defined by

$$Re_l = \frac{u'_{rms} l}{\nu}, \tag{4.24}$$

where l is a ("large-scale") length scale to be defined later; ν is kinematic viscosity (a function of density, locally in space and time), and u'_{rms} the root mean square velocity is defined as

follows. First let

$$u'(\boldsymbol{x},t) = u(\boldsymbol{x},t) - \langle u \rangle(t) \tag{4.25}$$

where, $\langle\cdot\rangle$ denotes a spatial average over some specified subdomain. Then u'_{rms} is given by

$$u'_{rms} = \langle u'^2 \rangle^{1/2} . \tag{4.26}$$

In general we will average over a 27 point stencil to perform the spatial averaging procedures. We observe that the length scale l is often viewed as the reciprocal of the wavenumber $\boldsymbol{k}$ at which $E(\boldsymbol{k})$, the energy spectrum achieves its (global) maximum. This generally occurs at relatively large spatial scales, typically on the order of about one-tenth of the size of the problem domain; that is, $l \sim 0.1L$. Now from the definitions $Re_\lambda \equiv u'_{rms}\lambda/\nu$ it follows that

$$\lambda = \frac{\nu}{u'_{rms}} Re_\lambda = \frac{\nu}{u'_{rms}}^{1/2} Re_l^{1/2} , \tag{4.27}$$

from which we obtain

$$\lambda = \left(\frac{\nu}{\langle u'^2 \rangle^{1/2}} \right) l^{1/2} . \tag{4.28}$$

Because of the manner in which this length scale is used (deducing a wavevector), it is advantageous to define the integral-scale Reynolds number in each separate direction—especially in cases of anisotropic turbulence. This will then permit calculation of the separate components of the wavevector as

$$k_i = \frac{1}{\lambda_i} , \qquad i = 1,2,3 . \tag{4.29}$$

The final step for completing the calculations of the β_is is to determine the appropriate Re for use in this context. We note that in the transformation leading to the CPMNS equation, the ability to define the β_is as in Eq. (4.17) comes from setting

$$\tau B^{(1)}_{\boldsymbol{lm,k}} = 1 - \frac{Z}{Re} \tau |\boldsymbol{k}|^2 \tag{4.30}$$

where $B^{(1)}_{\boldsymbol{lm,k}} = k_x B_{\boldsymbol{lmk}}$, with $B_{\boldsymbol{lmk}}$ being a Galerkin triple product—the Galerkin triple product carries Fourier space information associated with the velocity gradients. We note that we use the term Galerkin triple product to identify $B_{\boldsymbol{lmk}}$ since this corresponds to $\int_\Omega \varphi_{\boldsymbol{l}}\, \varphi_{\boldsymbol{m}}\, \varphi_{\boldsymbol{k}}\, dV$, (recall Eq. (4.11)). In particular, k_x comes from the Galerkin approximation of $\partial u/\partial x$. This provides us with a heuristic suggestion that the Re in the definitions of β_is should be the grid-cell Reynolds number, *i.e., Re* based on cell size.

In order to be somewhat more quantitative, we make the following approximate identification

$$|u'| = |u - \langle u \rangle| \sim h \left| \frac{\partial u}{\partial x} \right| . \tag{4.31}$$

We note that there are several choices of u (and v and w). Formally, u should be the complete velocity field (which would be available from the preceding time step). But we might also average the high-pass filtered squared velocity components. This approach is fairly consistent with the overall construction being presented here. Then we can write

$$\langle u'^2 \rangle^{1/2} \sim h \left| \frac{\partial u}{\partial x} \right| . \tag{4.32}$$

It follows that the Taylor microscale Reynolds number is of the same order as the cell Reynolds number if h is approximately the size of λ. In general, we should expect $h > \lambda$ to hold. Thus choosing $k = 1/\lambda$ and $Re = Re_h$ in the formula for β_is is fairly consistent. Then the appropriate definition for Re_h ought to be

$$Re_h \sim h_{x_i} \frac{|\partial u_i/\partial x_i|}{\nu} \tag{4.33}$$

From this we conclude that a reasonable approximation of the β_is is

$$\beta_i = 4\left[1 - \left(\Delta t \lambda_{x_i} ||\boldsymbol{S}|| Re_{h_{x_i}}\right)^{-1}\right], \qquad i = 1, 2, 3\,. \tag{4.34}$$

In addition, we note that we can now at least specify $Re_{h_{min}}$ by observing $\beta \geq 1$ must hold for the CPMNS to exhibit "interesting" behavior—meaning at least periodic. The precise limits on β also will depend strongly on the values of γs and the other bifurcation parameters, and these interrelationships will be investigated in the first half of the results section.

We further note that both M and Pe are calculated from their respective definitions. However, we should now use the high-pass filtered components in their constructions.

Considering the γs in the momentum equations we recall that

$$\begin{aligned} \gamma_{21} &= \tau m_2 B_{\boldsymbol{lmk}}\,, \qquad & \gamma_{22} &= \tau m_3 B_{\boldsymbol{lmk}}\,, \\ \gamma_{31} &= \tau m_1 B_{\boldsymbol{lmk}}\,, \qquad & \gamma_{32} &= \tau m_3 B_{\boldsymbol{lmk}}\,, \\ \gamma_{41} &= \tau m_1 B_{\boldsymbol{lmk}}\,, \qquad & \gamma_{42} &= \tau m_2 B_{\boldsymbol{lmk}}\,. \end{aligned} \tag{4.35}$$

The values of the triple products depend on the specific basis set chosen, but in general they can be expected to take $\mathcal{O}(1)$ values. We also known that the factor m_2 in γ_{21} arises as a part of the Galerkin representation of $\partial u/\partial y$; similarly, m_3 can be associated with $\partial u/\partial z$, *etc.* This suggests that we set

$$\begin{aligned} \gamma_{21} &= \tau \frac{\partial u}{\partial y}\,, \qquad & \gamma_{22} &= \tau \frac{\partial u}{\partial z}\,, \\ \gamma_{31} &= \tau \frac{\partial v}{\partial x}\,, \qquad & \gamma_{32} &= \tau \frac{\partial v}{\partial z}\,, \\ \gamma_{41} &= \tau \frac{\partial w}{\partial x}\,, \qquad & \gamma_{42} &= \tau \frac{\partial w}{\partial y}\,. \end{aligned} \tag{4.36}$$

Since we chose the non-conservation form of the governing equations to derive the CPMNS the γs in the continuity and total energy equations are given by

$$\begin{aligned} &\gamma_{11} = \tau\,(l_1 + m_1)\,B_{\boldsymbol{lmk}}\,, \qquad \gamma_{12} = \tau\,(l_2 + m_2)\,B_{\boldsymbol{lmk}}\,, \qquad \gamma_{13} = \tau\,(l_3 + m_3)\,B_{\boldsymbol{lmk}}\,, \\ &\gamma_{51} = \tau\,(l_1 + m_1)\,B_{\boldsymbol{lmk}}\,, \qquad \gamma_{52} = \tau\,(l_2 + m_2)\,B_{\boldsymbol{lmk}}\,, \qquad \gamma_{53} = \tau\,(l_3 + m_3)\,B_{\boldsymbol{lmk}}\,. \end{aligned} \tag{4.37}$$

where, as alluded to above m_i, $i = 1, 2, 3$ arises due to velocity gradients, and l_i, $i = 1, 2, 3$, arise due to spatial gradients of density in the case of γ_{11} through γ_{13} and total energy in the case of γ_{51} through γ_{53}. In these expressions the velocity and scalar gradients will be evaluated on the computational grid (using centered differencing) of the high-pass filtered components of the resolved-scale solutions.

With the detailed explanations given above for determining wavenumber components, Re, M, and Pe it is straightforward to evaluate the other parameters from their definitions.

Amplitude factors

We define local amplitude factors at each grid point (i, j, k) by assuming that locally the energy (per unit wavenumber) can be expressed as a power law of the form proposed by Kolmogorov but not necessarily having the well-known "universal constant" and $-5/3$ exponent. So, we can express the k^{th} mode contribution to energy as

$$E(k) = C_2 \langle \varepsilon \rangle^{\beta} k^{-(\beta+1)} \,, \tag{4.38}$$

where C_2 and β are the constant and exponent respectively. To compute C_2 and β locally we make use of the second-order structure function, which is defined as

$$S_2(\ell) \equiv \langle (u(\boldsymbol{x} + \boldsymbol{\ell}) - u(\boldsymbol{x}))^2 \rangle \,. \tag{4.39}$$

These were shown by Kolmogorov to satisfy a power law given by

$$S_2(\ell) = C_2 \langle \varepsilon \rangle^{\beta} \ell^{\beta} \,. \tag{4.40}$$

In the above equations $\langle \cdot \rangle$ represents a generic spatial average, which in our present formulation will be carried out spatially over the current grid point and its 26 nearest neighbors in 3D; $\boldsymbol{\ell}$ is a vector displacement from the current point having magnitude ℓ, and ε is turbulence kinetic energy dissipation rate given by $\varepsilon = \nu \|\boldsymbol{S}\|^2$, where $||\cdot||$ is the Euclidean norm, ν the kinematic viscosity (which varies spatio-temporally due to changes in density), and $\boldsymbol{S}$ is the strain rate tensor given by

$$S_{ij} = \frac{1}{2}\left(\frac{\partial u_i}{\partial x_j} + \frac{\partial u_j}{\partial x_i}\right) - \frac{1}{3}\frac{\partial u_k}{\partial x_k}\delta_{ij} \,, \tag{4.41}$$

where Einstein notation is used. For homogeneous, isotropic turbulence it is well-known that $\beta = 2/3$, while C_2 must be found from experiment.

Furthermore, by observing that $k \sim 1/\ell$ it is easily argued that

$$S_2(k) = C_2 \langle \varepsilon \rangle^{\beta} k^{-\beta+1} = E(k) \,. \tag{4.42}$$

This leads to the well-known $k^{-5/3}$ law. Now supposing that in each grid cell $S_2(\ell)$ and $\langle \varepsilon \rangle$ have been computed for N_ℓ values of ℓ (for each solution component), we seek the Kolmogorov constant C_2 and exponent β such that

$$Q(C_2, \beta) = \sum_{n=1}^{N_\ell} \left[S_2(\ell_n) - C_2 \langle \varepsilon \rangle^{\beta} \ell_n^{\beta} \right]^2 \tag{4.43}$$

is a minimum. Thus, we require

$$\frac{\partial Q}{\partial C_2} = 0 \,, \qquad \frac{\partial Q}{\partial \beta} = 0 \,. \tag{4.44}$$

Through considerable algebra one can show that this problem reduces to finding

$$C_2^* = \frac{(\sum A_n) \sum B_n^2 - (\sum A_n B_n) \sum B_n}{(N_\ell - 1)(\sum B_n^2) - (\sum B_n^2)} \,, \tag{4.45}$$

and

$$\beta = \frac{N_\ell \sum A_n B_n - \sum A_n \sum B_n}{(N_\ell - 1)\left(\sum B_n^2\right) - \left(\sum B_n^2\right)}. \tag{4.46}$$

C_2^* is related to C_2 via the relationship $C_2 = 10^{C_2^*}$. In the above equation $A_n = \log\ S_2(\ell_n)$ and $B_n = \log\left(\langle\varepsilon\rangle l_n\right)$.

Once C_2 and β have been obtained for each velocity component, the corresponding A_is are computed as

$$A_i^{*2} = \sum_{n=1}^{\infty} E_i^*\left(\boldsymbol{k}_n^{loc}\right)\ . \tag{4.47}$$

Here, $\boldsymbol{k}_n^{loc} \equiv (n+1)\boldsymbol{k}_c$. Then $n = 0$ gives $\boldsymbol{k}_0^{loc} = \boldsymbol{k}_c$, with $\boldsymbol{k}_c$ being the cut-off wavevector. This is known in advance from grid spacing on a uniform grid.

The extension of such calculations to the case of scalars is also direct. In particular, from the Kolmogorov–Obukhov–Corrsin theory (see Warhaft [179]) we can express the "energy" (the L^2 norm) associated with the fluctuations of a scalar as

$$E_{S,k} = C_{S,2}\langle\varepsilon\rangle^{-\beta/2}\langle\varepsilon_S\rangle^{\alpha} k^{(-\alpha-\beta+1)} \tag{4.48}$$

where $\langle\varepsilon_S\rangle$ is scalar dissipation rate. Thus, with β already determined from the velocity field, we can immediately calculate $C_{S,2}$ and α from scalar structure functions analogous to Eq. (4.39)

4.3 Results and Discussion

To characterize the different types of behavior produced by the CPMNS equations (4.18), we examine the time series and their corresponding power spectra. The time series are generated by performing 5×10^4 iterations of the DDS, with the last 8192 points of the time series being used to determine the power spectral density (PSD) using a standard radix-2 Fast Fourier Transform (FFT). To view the different states of the system in parameter space, we make use of the PSDs and time series, themselves, phase portraits and so called "regime maps" (2-D and 3-D bifurcation diagrams). In a final subsection we consider effects of initial conditions.

4.3.1 Solution regimes

One of the most important outcomes of this study was the identification of 14 different types of temporal behaviors that are produced by the DDS. We comment that the same behaviors have been reported for the incompressible case in [173] and that there are no further ones. We remark that, although this seems possibly counterintuitive with respect to the physical differences between compressible and incompressible flows, the fact remains that the DDSs obtained are quadratic maps in both cases. Thus, this result is not altogether unexpected due to the genericity of behaviors of such maps.

We proceed by first providing a list of the types of behaviors we have identified in the time series of Eqs. (4.18), by analyzing the respective PSDs: i) steady, ii) periodic, iii) periodic with different fundamental, iv) subharmonic, v) phase locked, vi) quasiperiodic, vii) noisy subharmonic, viii) noisy phase locked, ix) noisy quasiperiodic with fundamental, x) noisy

quasiperiodic without fundamental, xi) broadband with fundamental, xii) broadband with different fundamental, xiii) broadband without fundamental, and xiv) divergent.

It may be tempting to associate divergent behavior with employing a numerical time step parameter that is too large. Recall that the time step parameter τ is present in the definitions of the bifurcation parameters. However, dynamical systems tend to exhibit divergent behavior over certain ranges of values of their bifurcation parameters independent of how they are derived. Thus, we prefer not to associate divergent behavior specifically with numerical instability, especially since we do not assign values specifically to τ in the present context (but we must in the context of the complete SGS model).

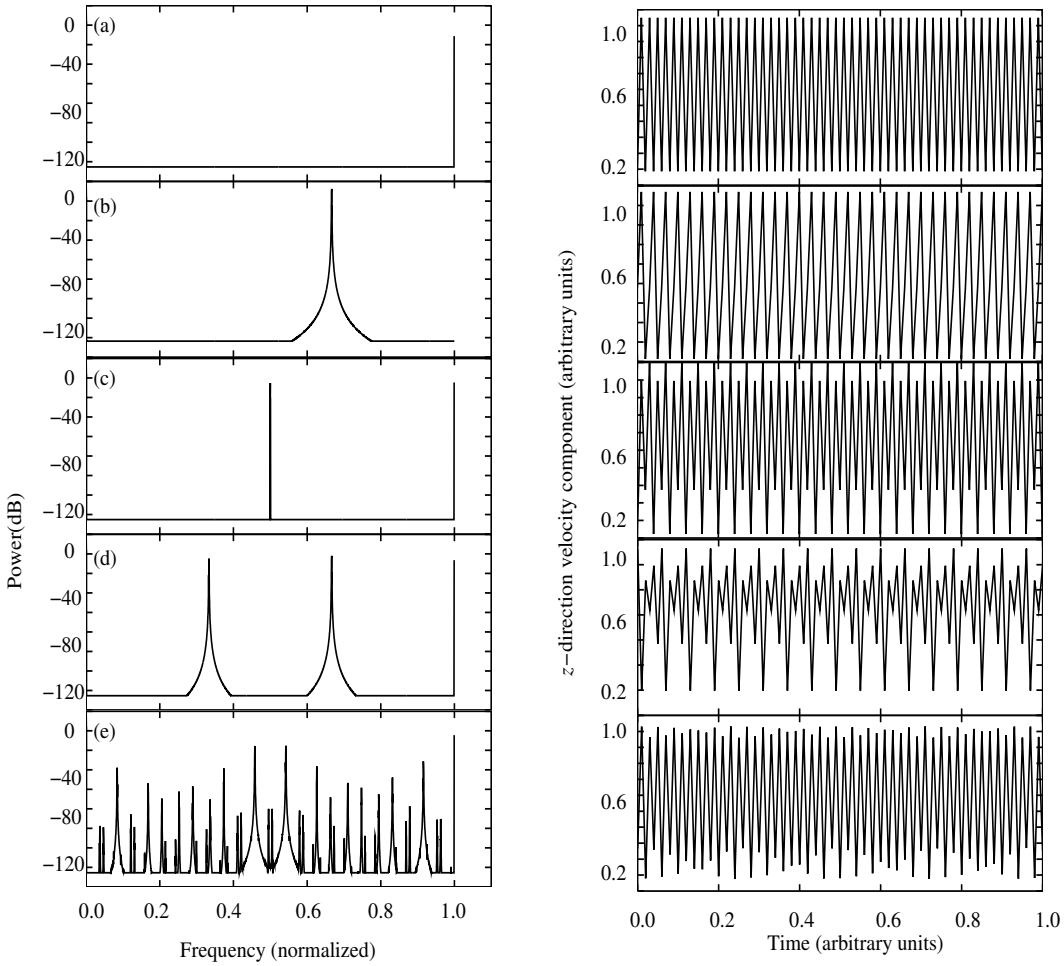

Figure 4.1 Example non-noisy power spectra and time series

Figure 4.1 displays power spectra and their corresponding time series in order of increasing complexity for each of the above "non-noisy" classifications except steady (a trivial case) and divergent, whose values go to infinity rapidly. Each of these PSDs has a sharp peak at zero frequency since we did not remove the average ("dc component"); but this cannot be seen in the plots. We note that the frequencies shown have been normalized because the time increments corresponding to map iterations are arbitrary. We further note that since the time increments are arbitrary, we started the abscissa on the time series plots from zero time, even though the data for these plots were taken from near the end of the computed

interval. In Fig. 4.1(a) we see a sharp peak at the highest possible frequency; this is the basic periodic case that arises via a pitchfork bifurcation of a quadratic map. In certain ranges of bifurcation parameters the system produces trajectories that are periodic with a different fundamental as shown in Fig. 4.1(b). It is well known that this occurs for the logistic map, and it has been observed for the incompressible PMNS equations as well. Figure 4.1(c) shows a subharmonic case, which has undergone one bifurcation beyond simple periodicity. The associated time series clearly displays the period doubling effect. In Fig. 4.1(d) we display a phase-locked PSD and time series which might also be identified as a period-tripling bifurcation following the initial periodic state. Phase locking occurs in quasiperiodic regimes when the two incommensurate frequencies of the quasiperiodic case (which begins as a bifurcation from a periodic state) become commensurate; however, we have presented this prior to the quasiperiodic case because its time series and PSD are noticeably simpler—clearly in the present case, a period-3 behavior. Finally, Fig. 4.1(e) corresponds to the PSD and time series of an example trajectory from the quasiperiodic classification. We note that a quasiperiodic signal has a seemingly (but not actually) nonperiodic, irregular aspect, suggestive of turbulence, and experimentalists sometimes classify it as such. However, Ruelle and Takens [61] proved that such a signal cannot be turbulent since it cannot be associated with a strange attractor; in particular, it is not sensitive to initial conditions (SIC). On the other hand, strange attractors may be arbitrarily nearby in bifurcation parameter space.

We note that distinguishing a phase lock from subharmonic behavior beyond the first bifurcation is difficult without knowing, *a priori*, the sequence of behaviors leading to a given state as a bifurcation parameter is varied. Borrowing from [173] our approach has been to characterize the behavior as subharmonic if the following criteria are met: 1) number of frequencies f_n is a power of two and 2) the power of all frequencies at the 2^{2m-1} level is less than that of either of their neighbors (in frequency) at the 2^m level. The same criteria are also applied to the noisy cases, where the attribute "noisy" implies some broadband aspects in the PSD (see [173] for details). We comment that these criteria are not always sufficient to make the distinction between phase lock and subharmonic based on a single time series; but in many situations (construction of regime maps shown below, or analysis of experimental data) this is all that is available. Moreover, the classification "n–periodic" might be applied to either case.

In Fig. 4.2 we present PSDs and time series for the remaining noisy classifications. Figure 4.2(a) displays a case of the noisy-subharmonic behavior. The spectral peaks are well defined, and they rise many tens of decibels from the base noise and are hence easily identifiable. On the other hand, although the basic feature of period doubling is still present in the time series for this case, the maxima and minima no longer exactly repeat (compare with Fig. 4.1(c)). In Fig. 4.2(b) we present a noisy phase lock wherein again we observe well-defined spectral peaks. Furthermore, the time series from which the PSD was generated is quite regular at the level of large amplitude oscillations, but non-repeatability is evident in the lower amplitude peak-to-peak behavior as the PSD suggests. We remark that experimentalists often attribute this to measurement noise; but this cannot be the case here—and possibly it is not in some experimental studies as well.

We note that as the bifurcation parameters are varied such that we move deeper into the noisy regime, classification of types of behavior becomes increasingly more difficult. Figures 4.2(c) and (d) are noisy quasiperiodic with and without, respectively, the fundamental fre-

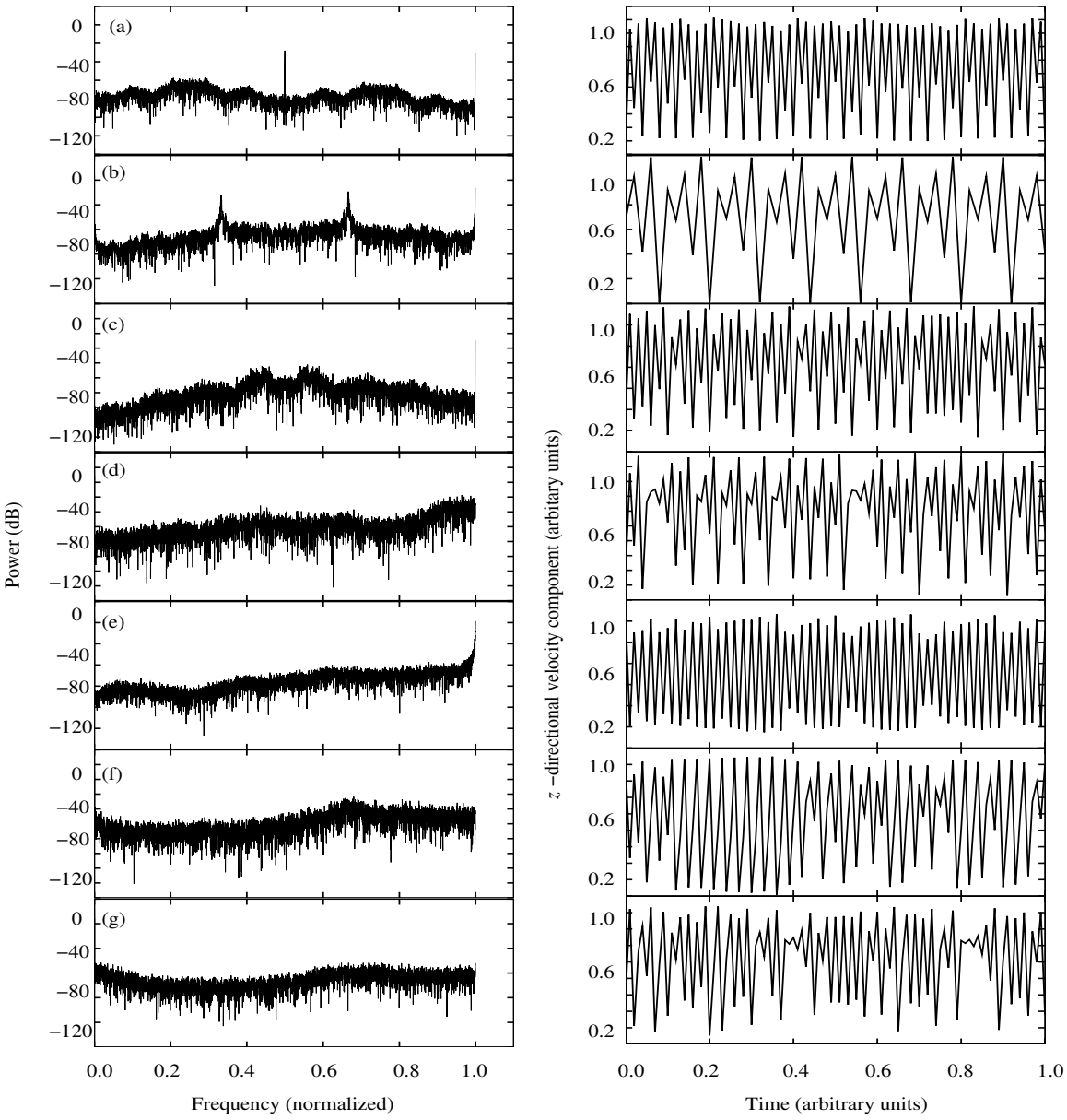

Figure 4.2 Example noisy power spectra and time series

quency. In the first of these, somewhat well-defined spectral peaks are present (*e.g.*, in the range between 0.4 and 0.6); but in the latter case the noise has continued to rise, and the peaks are far more difficult to distinguish. But evidence of such peaks can be seen scattered throughout the spectrum, *e.g.*, near the the frequencies 0.2 and 0.6. The temporal behavior, as seen in the time series is correspondingly less regular than in the case for which the fundamental is still present. Indeed, evidence of (physical) intermittency can be seen just preceding times $t = 0.1$ and 0.6, and the general nature of the oscillations and their timing have become much more "turbulent like."

The final three plots display behaviors involving broadband characteristics. In the first of these (Figure 4.2(e)), there is distinct peak and, hence, it is termed broadband with

fundamental (one might also call this noisy periodic). Aside from the peak at the highest possible frequency, the spectrum shows no distinguishing characteristics. The time series shows very regular peaks associated with this frequency, but their amplitudes are irregular. Moreover, one can see evidence of nonperiodic switching between short sequences of relatively lower amplitude oscillations to longer sequences of higher-amplitude behavior. The last two, broadband with different fundamental (Fig. 4.2(f)) and broadband without fundamental (Fig. 4.2(g)) are characterized by their lack of any defining spectral characteristics. There is clear evidence of this in their respective PSDs. However, in the case of the former there is some evidence of a peak at a frequency of 0.65. The corresponding time series displays some of the features contained in the time series of broadband with fundamental (see region between 0 and 0.4) and quasiperiodic with fundamental (see region between 0.4 and 1), which strongly suggests the presence of some fundamental frequency which is of a different amplitude. The time series of the broadband without fundamental classification displays a behavior that is somewhat less regular than the case for which the fundamental is still present. Furthermore one can clearly see some evidence of intermittent behavior at times preceding 0.4 and 0.8.

Before we end our discussion on time series and power spectra, it is also of interest to look at some of the associated "attractors" of the time series presented above. Attractors can be pictorially represented by making use of phase portraits. A phase portrait is a geometric representation of the time evolution of two or more dependent variables in phase space.

In Fig. 4.3(a) we display a three-dimensional phase portrait constructed using the three components of velocity for the broadband with different fundamental classification. The associated 2-D projections are presented in parts (b), (c) and (d). It is clear from the figure that, even after the initial transient, the trajectories of the discrete dynamical system display a highly irregular behavior, due to the wide range of frequencies present in the signal. From part (a) of the figure we observe that the phase points tend to align themselves at a 45 degree angle. Such alignments of the phase points suggests that there is good correlation between the u and v components of velocity (as verified in part(b) of the figure). However, correlations between the other two combinations of velocity components is not good. This is clearly evident from parts (c) and (d) of Fig. 4.3. As a result the trajectories of the system visit phase points that are widely separated thereby increasing the noise. But as observed in the time series (Fig. 4.2(f)) the presence of some fundamental has resulted in certain dominant features in the attractor. The harmonics can be somewhat discerned by looking at the dominant features of the attractor. However, the increase in the surrounding noise together with the lack of a strong fundamental has blurred the distinction between the dominant features.

4.3.2 Regime maps

The most appropriate method of studying a large number of cases (sets of bifurcation parameters) of Eqs. (4.18) is to view the so called "regime map." Regime maps can be thought of as multi-dimensional extensions of standard bifurcation diagrams typically used in the dynamical systems literature. The regime maps presented in this paper were created using a type of visual recognition algorithm that recognizes distinctive traits in the automatically calculated power spectrum. The power spectrum itself is run at each grid point

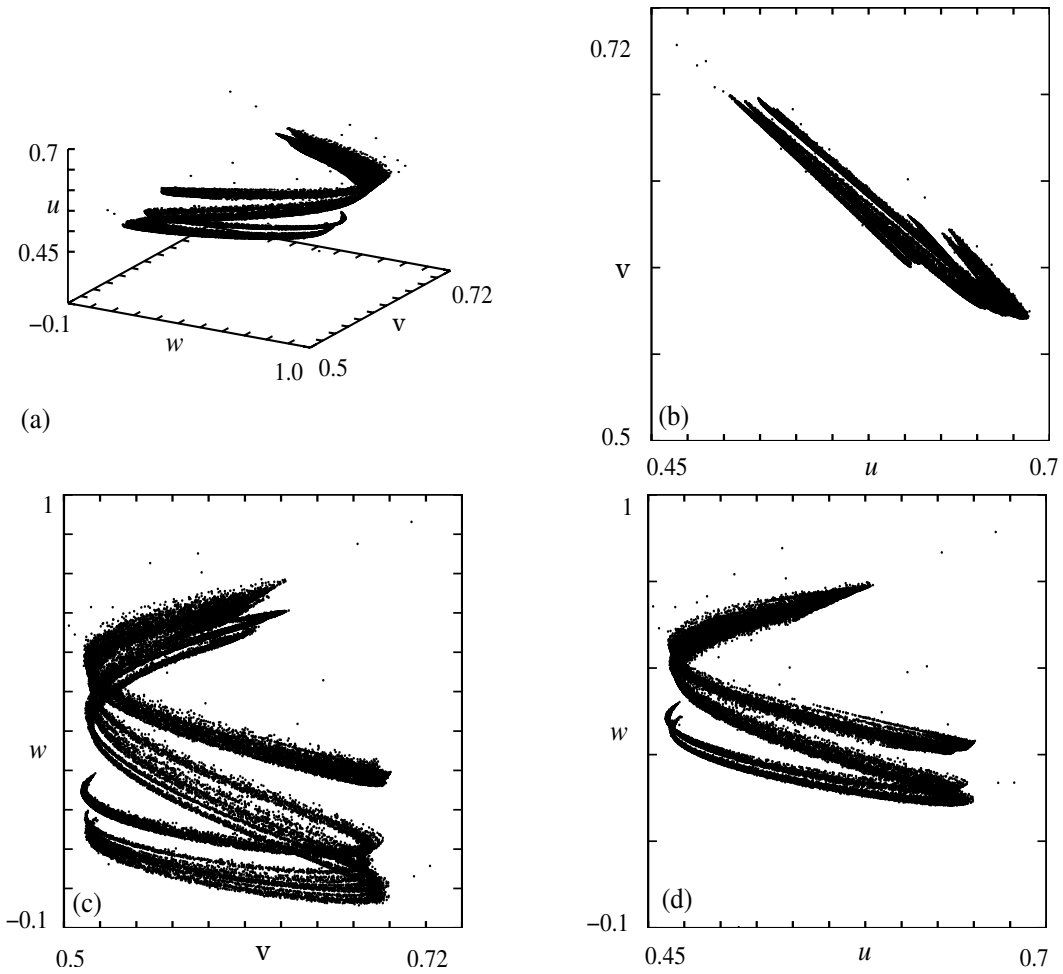

Figure 4.3 Phase portrait of broadband with different fundamental behavior. (a) 3-D phase portrait of the three velocity components (b) 2-D phase portrait of u and v components of velocity (c) 2-D phase portrait of v and w components of velocity and (d) 2-D phase portrait of u and w components of velocity

on a grid of bifurcation parameter values. The plots are then created, based on the result of the image processing algorithm, by color coding the 14 different types of behaviors that have been described in fair detail in the previous section. Moreover, regime maps provide us with a visual tool for the the easy identification of bifurcation sequences. For each 3-D regime map we used 145 points in each of the three coordinate directions, for a total of over 3 million combinations of bifurcation parameter values at which the DDS was iterated. To show details, we make use of more highly-resolved 2-D regime maps (in general, a slice of the overall 3-D domain) with a total of 1 million combinations per 2-D slice. We note that the power spectrum was computed (from the w-component Fourier coefficient) and the type of behavior was classified, recorded, and plotted. It is to be noted that it is generally (physically) not appropriate to equate the different sets of bifurcation parameters, and, hence, all bifurcation parameters have been assigned unique values. The same initial conditions were used in all calculations from which the regime maps were constructed: $a^{(0)} = 0.5$, $b^{(0)} = 0.45$, $c^{(0)} = 0.6$, $d^{(0)} = 0.75$ and $E^{(0)} = 0.95$, henceforth termed "standard," except

for results specifically associated with effects of initial conditions. With 35 bifurcation parameters it is nearly impossible to thoroughly study the behavior of the DDS for all possible combinations of these parameters. To make the task tractable, we present regime maps of combinations of the different families of bifurcation parameters, as identified in Sec. 4.2.2, by picking a bifurcation parameter from each family. This will at least give us an overall view of the behavior of the DDS.

The first regime map that we present, Fig. 4.4(a), is a 3-D map of β_1 *vs* γ_{22} *vs* ψ_1. Figure 4.4(b) is the color map which associates the 14 types of behaviors with the respective colors we have chosen to represent them. There are several observations to be made regarding Fig. 4.4(a). First, we see a relatively large region of divergent behavior at a value of ψ_1=1, particularly at high values of β_1. However, the plane on the 3-D plot displaying the behavior of β_1 *vs* ψ_1 suggests that this region decreases as the Mach number increases. Part(a) of the figure also suggests that as γ_{22} is increased (becomes less negative) the DDS produces complicated (noisy and broadband) behavior, indicating that the flow field is excited because of higher velocity gradients (recall the definitions of the γs). To make comparisons between the behavior of the system at different Mach numbers, we display a sequence of 2-D plots (Fig. 4.4(c)–Fig. 4.4(e)). These plots were produced by using values of ψ_1 in decreasing magnitude, thus simulating the effect of increasing Mach number. In Fig. 4.4(c) we present the system behavior at a value of ψ_1=0.896. Except for a very small region at the top left corner, which displays broadband behavior and a small patch at a value of $\beta_1 \approx 3.5$, the rest of the parameter space is comprised of relatively simple behavior. In the same region at high values of γ_{22} we see a series of "islands" where the DDS remains bounded even though it is divergent at most nearby points. Often present near these islands are "holes", which are regions of divergence completely surrounded by bounded behavior. As the value of ψ_1 is decreased to 0.555, the region at the top left hand corner moves inwards, increasing in size, and the corner region now displays noisy quasiperiodic behavior. We further notice a decrease in the area displaying periodic behavior and the appearance of a feather-like projection of quasiperiodic behavior at a value of β_1 around (but mostly below) 3.0. Also, note the noisy tip in this region. With further decrease in ψ_1 to 0.09 we see a marked increase in the region of broadband behavior especially in the low β region, *i.e.,* $1 \leq \beta_1 \leq 2.5$. Moreover, we also see an increase in the area displaying non-divergent behavior at values of $\beta_1 \geq 3.0$. In the low β region one can also easily discern the bifurcation sequence and the associated chaotic attractor as γ_{22} is increased. In particular, we see a period-doubling route to chaos:

$$\textit{steady} \rightarrow \textit{periodic} \rightarrow \textit{subharmonic} \rightarrow \textit{quasiperiodic} \rightarrow \textit{chaotic}\,.$$

We note that this is not the usual period-doubling route to chaos, since it contains a quasiperiodic state between the subharmonic and chaotic states. From both Fig. 4.4(d) and Fig. 4.4(e), we notice a bifurcation sequence going from *steady* $\rightarrow$ *periodic* $\rightarrow$ *quasiperiodic* in the feather-like region, which suggests that the CPMNS equations can also display the Ruelle–Takens–Newhouse (RTN) bifurcation scenario—*steady* $\rightarrow$ *periodic* $\rightarrow$ *quasiperiodic* $\rightarrow$ *chaotic*. However, in both plots the γ_{22} interval is not long enough to determine if this scenario occurs. Hence in Fig. 4.4(f) we display a map whose γ_{22} interval is $[-1.5, 2.5]$. We further note that our standard grid for 2-D plots, which contains a million grid points, was used to determine the behavior of the system on the domain $(\beta_1, \gamma_{22}) \in [1, 1.5] \times [4, 2.5]$. An obvious observation is that the system does not display the RTN bifurcation sequence.

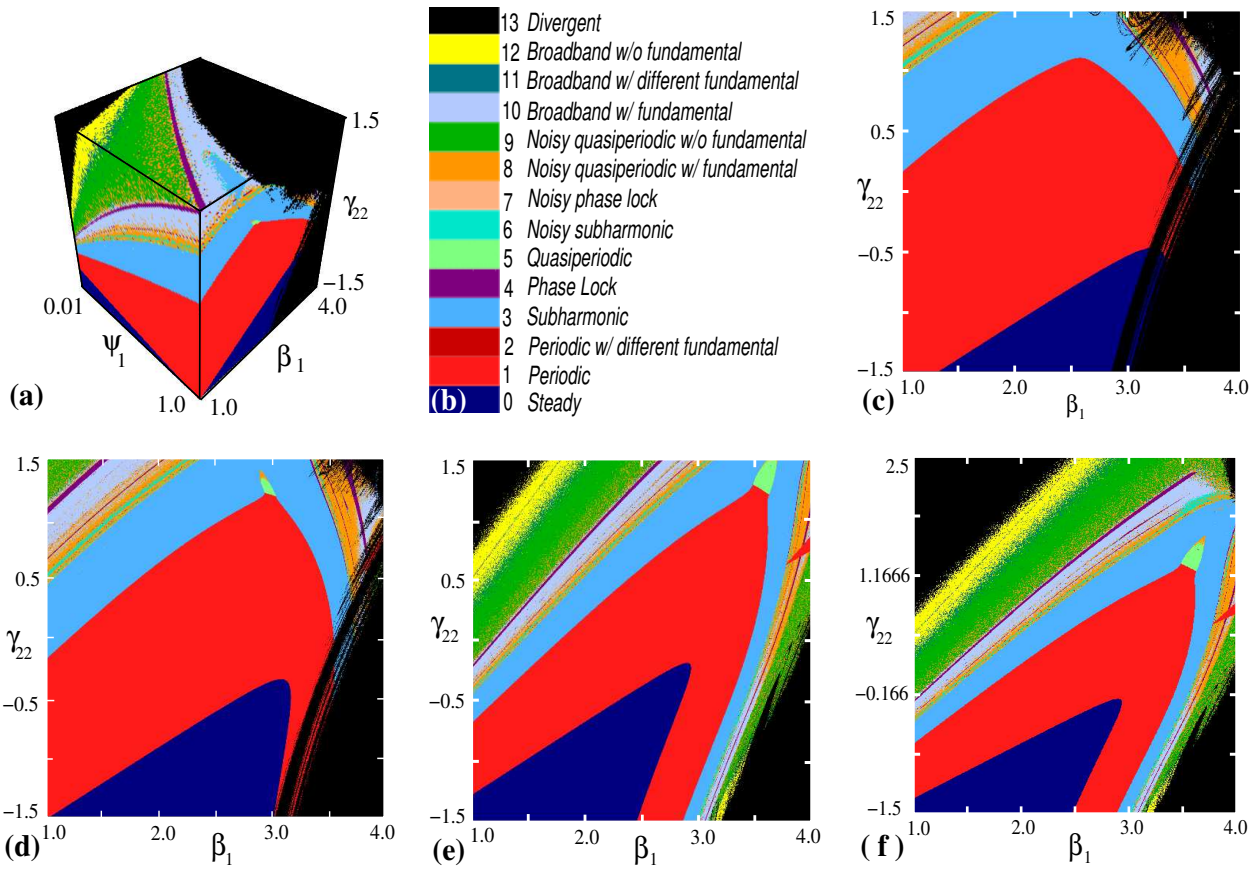

Figure 4.4 Regime maps displaying effects of M; (a) 3-D map of β_1 vs γ_{22} vs ψ_1, (b) Color table, (c) ψ_1=0.896, (d) ψ_1=0.555, (e) $\psi_1 = 0.09$, (f) $\psi_1 = 0.09$ and $-1.5 \leq \gamma_{22} \leq 2.5$.

The sequence does not proceed through the usual transition from quasiperiodic to chaotic directly; instead there is a region of subharmonic behavior before the eventual chaos. In particular, we observe the following bifurcation sequence:

$$steady \rightarrow periodic \rightarrow quasiperiodic \rightarrow subharmonic \rightarrow chaotic\,.$$

This region of subharmonic between the quasiperiodic and chaotic behaviors can physically be attributed to the phenomenon of relaminarization.

Figure. 4.5(a) displays a map of χ_2 *vs* γ_{31} *vs* ψ_2. We have chosen to show only a subspace of the overall domain because the behavior of the system at the extrema of the considered parameter values was divergent, and, hence not very interesting. In Fig 4.5(b) we present a 2-D slice of the entire computational domain at a relatively low value of M (ψ_2=0.569). It is evident that in the region $0.3 \leq \chi_2 \leq 1$ (recall that χ_2 is inversely proportional to Re) the system produces divergent behavior for all values of γ_{31}. However, in the region $0.001 \leq \chi_2 \leq 0.03$ we see the system producing relatively complicated behavior (although not yet chaotic). In Fig. 4.5(c), which is at a higher value of M (ψ_2=0.118), the system produces broadband (chaotic) behavior as Re is increased (decreasing values of χ_2), and, moreover, there is an overt decrease in the area of regions exhibiting divergent behavior. This is particularly encouraging from a modeling standpoint because it is at such regimes that we expect to have turbulence and, hence, our model to be active. Again, we see a

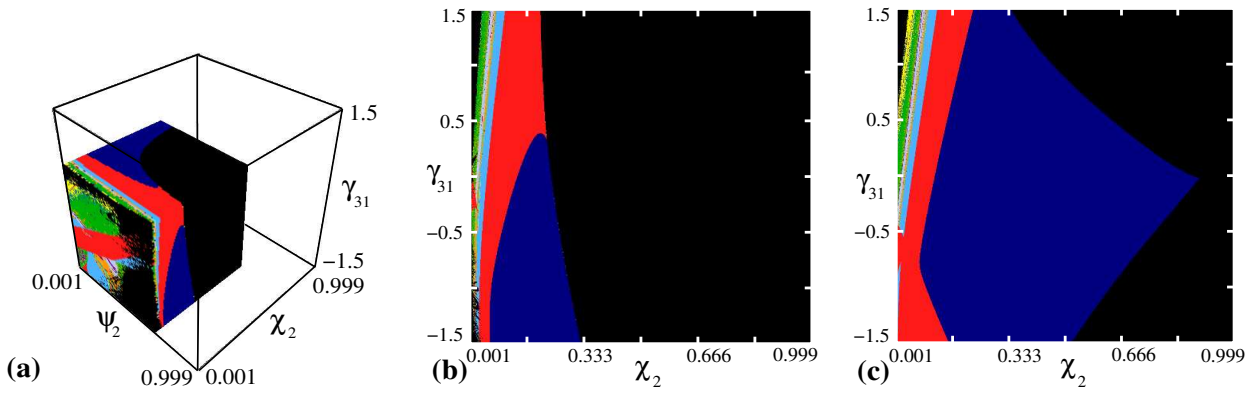

Figure 4.5 Regime maps displaying effects of Re; (a) 3-D map of χ_2 vs γ_{31} vs ψ_2, (b) ψ_2=0.569, (c) ψ_1=0.118.

period-doubling route to chaos as Re increases.

In Fig. 4.6 we present regime maps of β_1 *vs* β_2 *vs* β_3 at 7 different values of γ_{21} to γ_{42} (Fig. 4.6(c)–Fig. 4.6(i)). We note that the values of the γs were varied by integer factors from a set of values, henceforth termed baseline. The baseline values of the γ's were $\gamma_{21} = 0.025$, $\gamma_{22} = 0.01$, $\gamma_{31} = 0.031$, $\gamma_{32} = 0.021$, $\gamma_{41} = 0.019$ and $\gamma_{42} = 0.022$. At high negative values of the γs (-25 times the baseline values—Fig. 4.6(c)), there exists a large region of divergence surrounding a relatively small region of non-trivial behavior apart from steady. As the γs are increased to -15 times the baseline value, Fig. 4.6(d), the large region of divergence transitions to regions producing non-divergent behavior. The behaviors at moderate values of β_1 and β_2 ($1 \leq \beta_1 \leq 3$ and $1 \leq \beta_2 \leq 3$) are somewhat similar to those present in Fig. 4.6(c). However, transition to non-divergent, non-steady behavior is evident as values of β_1 and β_2 are increased. At the upper-right corner of the plot we clearly see the system undergoing the RTN bifurcation sequence. With further increase in the magnitudes of the γs, the large patch of steady behavior present in Fig. 4.6(e) begins to shrink in size, transitioning to periodic. However, the rim of interesting, generally chaotic, behavior surrounding the less complicated behavior still persists. At low positive values of the γs (5 times baseline value–Fig. 4.6(g)), the region of steady behavior becomes an island surrounded by a region of periodic behavior. When the γs reach a value of 15 times the baseline (Fig. 4.6(h)), the island of steady behavior completely transitions to a region of periodic behavior, and this region is surrounded by another region exhibiting subharmonic behavior. Further increases in γs (Fig. 4.6(i))result in the system producing noisy behavior (quasiperiodic and broadband) in most regions of the domain since the flow is excited by higher velocity gradients (hence, strain rates). Also, regions of divergent behavior reappear at high values of β_1 and β_2. When the value of the γs is raised to 35 times the baseline value (figure not shown), the flow is excited to such an extent that the regions of non-divergence almost completely disappear. The behavior in those regions which do produce non-divergent behavior is chaotic. In particular, we found broadband with a different fundamental and broadband without fundamental behavior in those regions.

In Figs. 4.4—4.6 we displayed regime maps involving bifurcation parameters mainly from the momentum equations. We will end the discussion on regime maps with illustrations of the system behavior as sets of bifurcation parameters from the continuity and energy equations

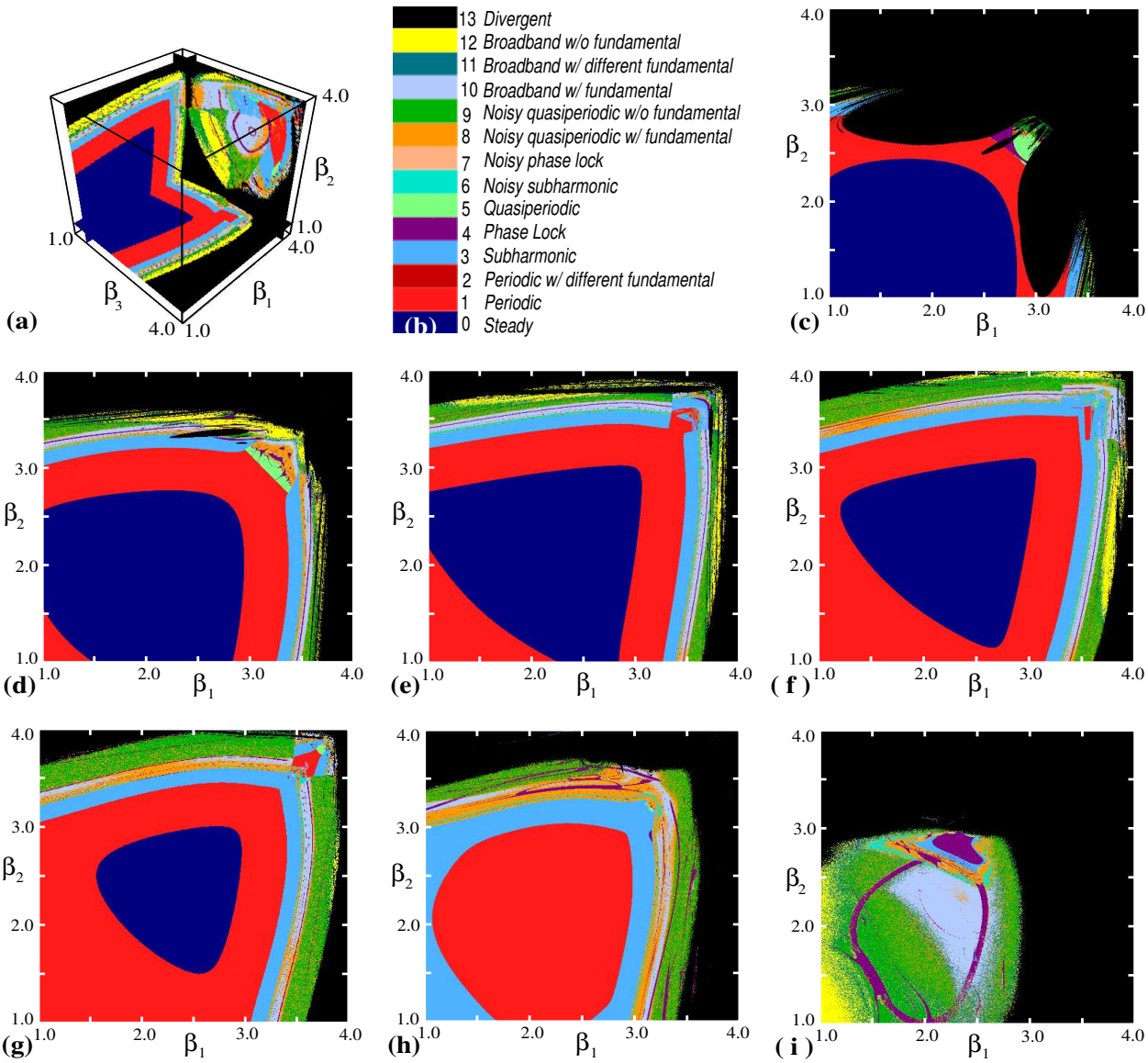

Figure 4.6 Regime maps displaying effects of velocity gradients; (a) 3-D map of β_1 vs β_2 vs β_2, (b) Color map, (c) $\gamma_{21} - \gamma_{42} = -25\times$ baseline, (d) $\gamma_{21} - \gamma_{42} = -15\times$ baseline, (e) $\gamma_{21} - \gamma_{42} = -5\times$ baseline, (f) $\gamma_{21} - \gamma_{42} =$ baseline, (g) $\gamma_{21} - \gamma_{42} = 5\times$ baseline, (h) $\gamma_{21} - \gamma_{42} = 15\times$ baseline, (i) $\gamma_{21} - \gamma_{42} = 25\times$ baseline.

are varied. We begin by presenting a case from the continuity equation. In particular, we display a map of β_2 *vs* γ_{11} *vs* γ_{12} in 3-D and the associated projections as 2-D plots in Fig. 4.7.

The figure illustrates the fact that there is a significant increase in regions of the domain that display divergent behavior as the values of γ_{11} and γ_{12} become negative. The reduction in the area of the region exhibiting non-divergent behavior as the γs become more and more negative can be clearly observed in Fig. 4.7(b). We further comment that there is a shortening of the intervals of the γs at which we obtain stable behavior when compared with those in the momentum equations. This is clearly seen in the plots presented. Derivation of

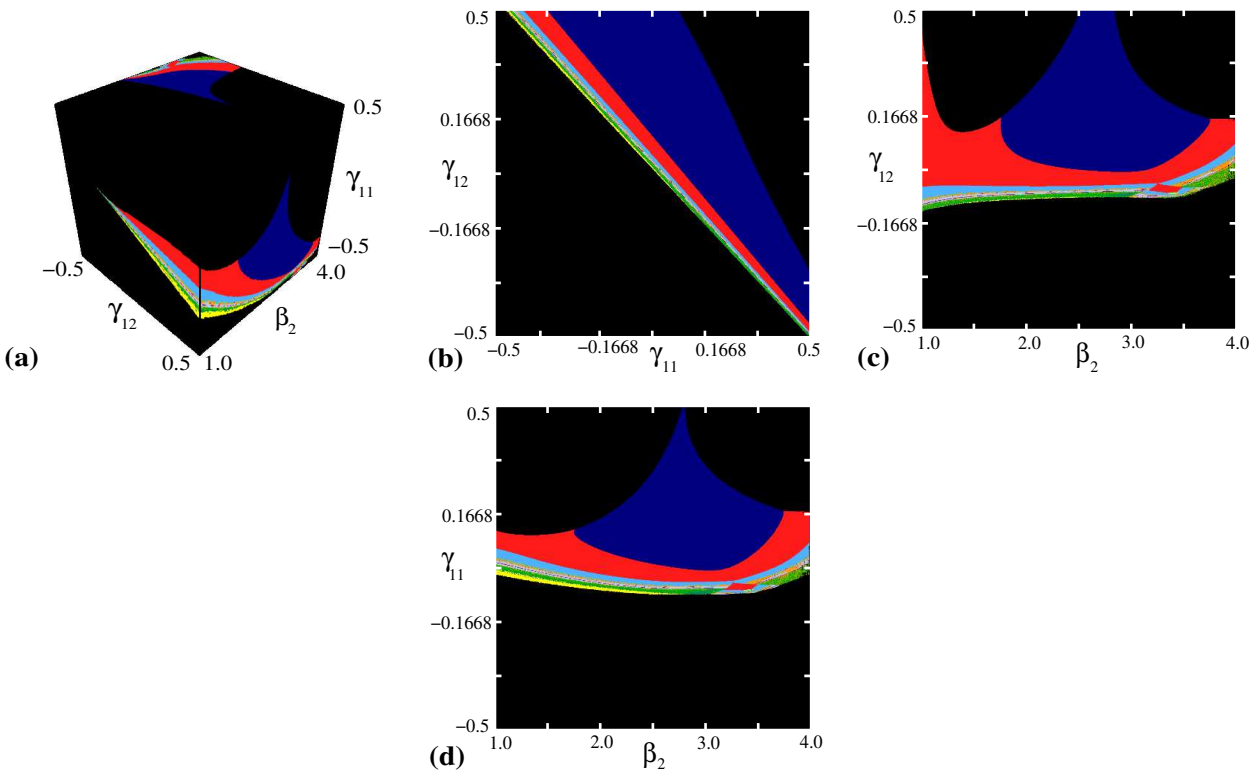

Figure 4.7 Regime maps involving parameters in the continuity equation; (a) 3-D map of β_2 vs γ_{11} vs γ_{12}, (b) γ_{11} vs γ_{12}, (c) β_2 vs γ_{12}, (d) β_2 vs γ_{11}.

the Galerkin form of the continuity equation analogous to that described in fair detail for the x-momentum equation allows us to observe that γs in the continuity equation depend on both the velocity and density gradients. From Fig. 4.7(c) and (d) we also see a transition to complicated behavior in both the low and high β regimes. Furthermore, we can also determine the tendency of the system to produce complicated behavior as the γs move towards negative values.

In Fig. 4.8(a) we present a map of σ_{11} *vs* γ_{51} *vs* θ for the energy equation. Recall that the σs depend on the Re and θ depends on the Pe number. From Fig. 4.8(b) we observe that for any constant value of θ the system transitions from *steady* $\rightarrow$ *periodic* $\rightarrow$ *noisy quasiperiodic without fundamental* as we increase the value of γ_{51}. We comment that this particular bifurcation sequence is generally not seen. To enhance our understanding about the system behavior in the region which displays the transition, we provide two successively zoomed views. The zoomed views are presented as insets in Fig. 4.8(b). We note that the zoom-ins were not merely created by using the visualization package Fieldview, but instead we re-ran the DDS on a 1000×1000 grid on the chosen sub-domain. In particular, for the second zoomed view (zoom 2) we ran on a domain $(\theta, \gamma_{51}) \in [0.587, 0.98] \times (0.59, 0.982)$ which provides a grid spacing of $\Delta\theta$=3$\times$ 10^{-6} and $\Delta\gamma_{51}$=2$\times 10^{-6}$. Even at such a high resolution, the inset (zoom 2) in part(b) of the figure clearly shows the direct transition alluded to above. In fact the PSD (part(e)) and phase portrait (part(f)) of a point in the noisy quasiperiodic regime from the zoom 2 inset is a classic example of the corresponding classification. The phase portrait clearly displays the two limit cycles characteristic of

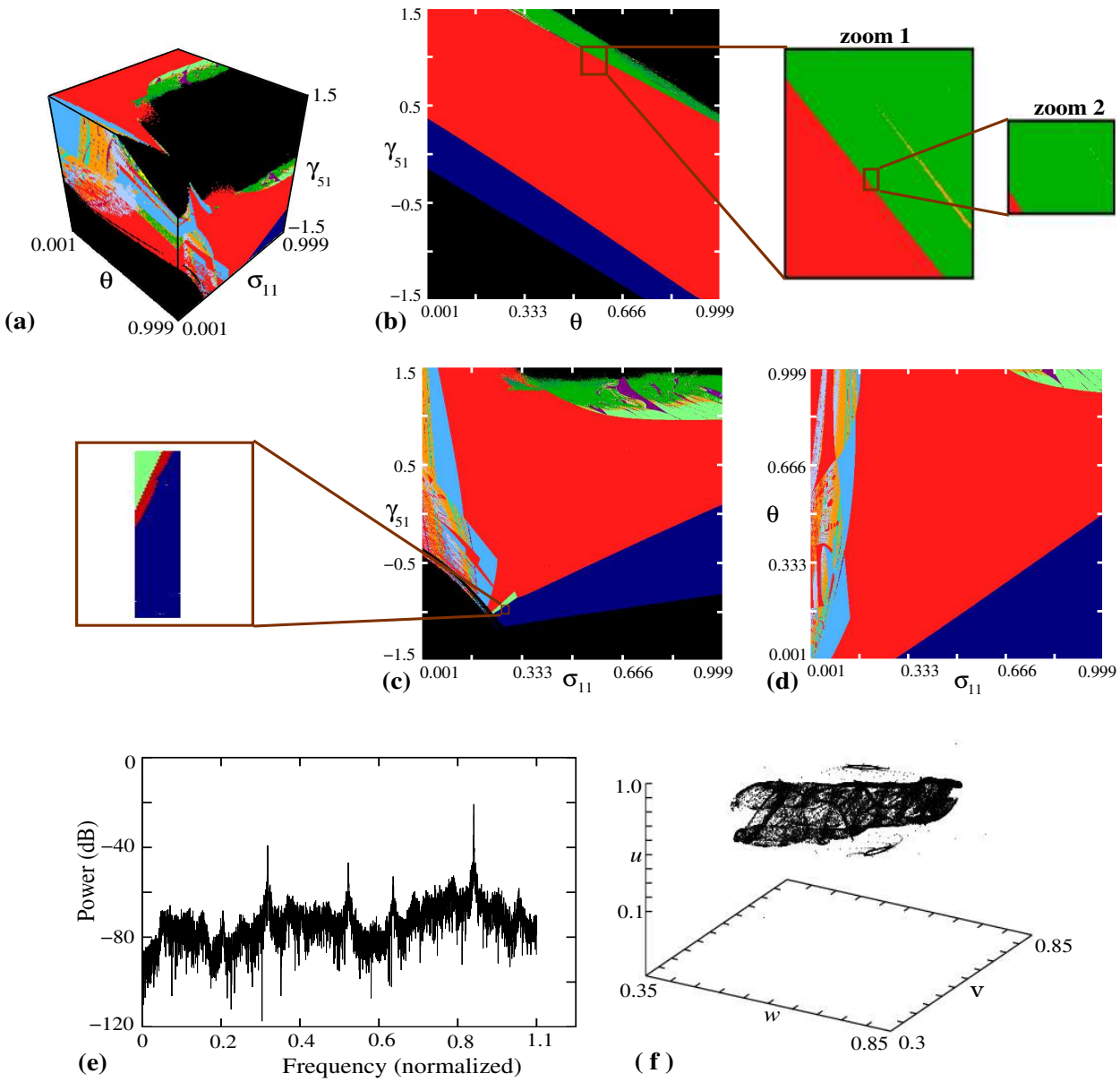

Figure 4.8 Regime maps involving parameters in the energy equation; (a) 3-D map of σ_{11} vs γ_{51} vs θ, (b) θ vs γ_{51}, (c) σ_{11} vs θ, (d) σ_{11} vs γ_{51}, (e) psd of a point in zoom 2 of part(b), (f) phase portrait of point in part(b).

quasiperiodic signals and also a large region of phase points separated from the limit cycles, that the individual trajectories of the system visit (hence, the attribute noisy).

In Fig. 4.8(c) we also see the transition from steady to quasiperiodic. The same exercise as described above for the periodic to noisy quasiperiodic without fundamental was carried out. However, for this case we noticed the emergence of a thin region of periodic with different fundamental behavior between the steady and quasiperiodic regions. Part(d) of the figure illustrates that the system undergoes a Hopf bifurcation at high values of σ_{11} and θ. In particular, for a fixed value of σ_{11} in this region we see a Hopf bifurcation sequence as the parameter θ is increased. Furthermore, we also see the period-doubling route to chaos

as the values of σ_{11} are decreased. At low values of σ_{11}, although we see regions exhibiting complicated behavior, we also see large regions where a return to periodicity is evident.

Effects of initial conditions

Until now we have studied the behavior of the CPMNS using only a particular set of initial conditions. However, it is well known that multiple attractors can exist for multi-dimensional dynamical systems. Hence it is necessary to study the effects of altering the initial conditions on the behavior on the system. One method of doing this would be to construct the regime maps presented in the previous subsection by changing the values of the initial conditions and comparing them to determine the effects. Undoubtedly this would be a painstaking process especially if one wants to study the effects of a large number of sets of the initial conditions. Another method of studying the effects of initial conditions is via the visualization of the basins of attraction for a particular set of bifurcation parameter values. A basin of attraction is the set of all initial conditions whose orbits converge to a specific attractor, in our case a specific behavior represented by a specific color on the color map. To study the basins of attraction of the CPMNS we implemented the same methodology we used for the regime maps, which should now be familiar to the reader. That is, we treat the initial conditions in the same way as we treated the bifurcation parameters. We further comment that we have used the same color coding to classify the behavior of the system on the initial condition grid.

The basins of attraction for a set of bifurcation parameter values, which produce broadband with fundamental behavior, is illustrated in Fig. 4.9. We investigated the behavior of the system by varying the initial data of the velocity vector between 0.001 and 0.999 for all three components ($u, v,$ and w). Projections of the 3-D domain onto three orthogonal planes are also shown as 2-D plots. It is evident from the figure that there is a growth of regions exhibiting divergent behavior as the values of the initial conditions approach 1, suggesting that such high values should not be used. In the zoomed view displayed as an inset in the figure we clearly see the existence of multiple basins. In particular, we see three different basins apart from broadband with fundamental, which are: i) noisy quasiperiodic with fundamental, ii) noisy quasiperiodic without fundamental, and iii) broadband with different fundamental. We comment that from a modeling standpoint we should expect the model to be driven by changes in values of the bifurcation parameters since they embody the physics of the flow. Hence, we do not want the system to produce drastically different behavior because of small changes in initial conditions, although the values of the bifurcation parameters remain the same. This favorable feature is evident from the figure, since we do not see for *e.g.,* any non-noisy behavior at any value of the specified initial conditions interval. Although the time series presented in Fig. 4.2 for the four types of behaviors seen on the initial condition grid are fundamentally different, they are all still sufficiently complex.

In Fig. 4.10 we display time series, which demonstrate the property of sensitivity to initial conditions (SIC). The time series in red corresponds to a series that was generated form the standard set of initial conditions and the one in green corresponds to initial conditions $b^{(0)} = 0.365167$, $c^{(0)} = 0.489167$, and $d^{(0)} = 0.503056$ (a^0 and E^0 were set to the standard values). We note that for both cases the values of the bifurcation parameters were set exactly the same (corresponding to broadband with fundamental for this case). It is evident from

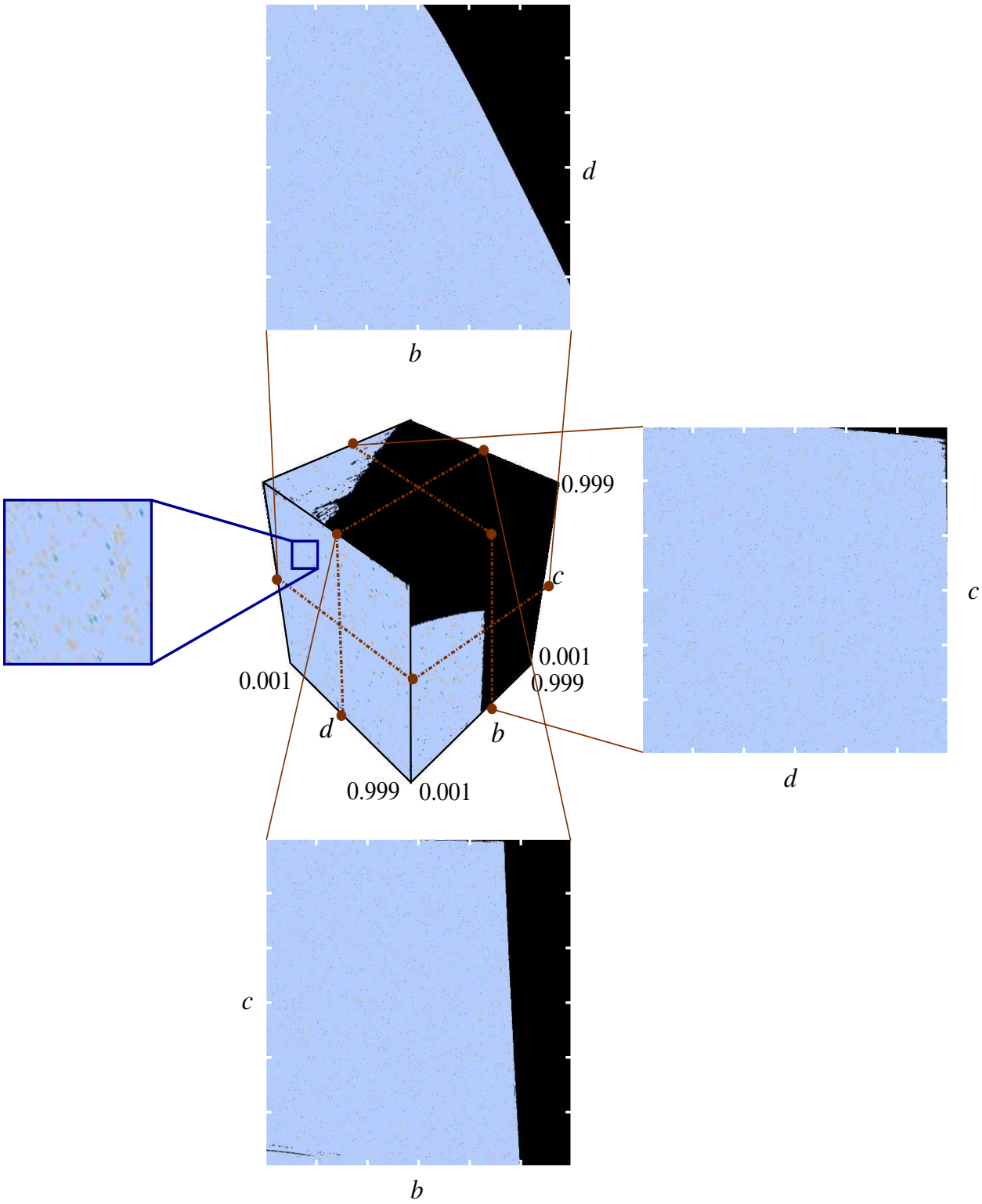

Figure 4.9 Basins of attraction for broadband with fundamental behavior.

the figure that the time series do not match point by point even though the bifurcation parameters are the same. Moreover, we see the time series going in and out of phase as

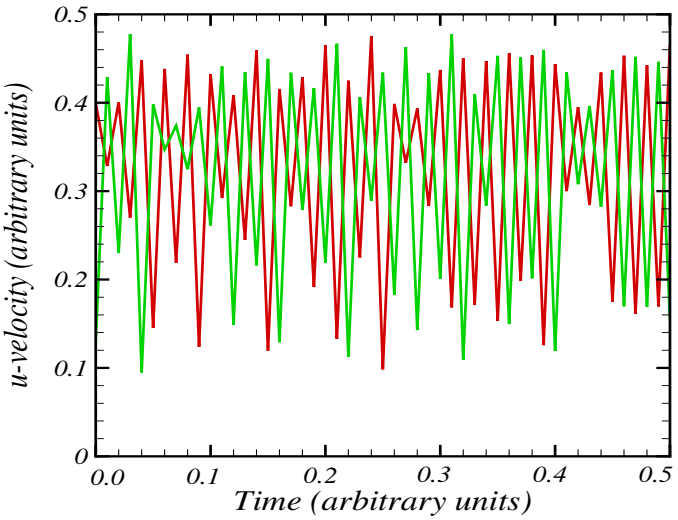

Figure 4.10 Depiction of SIC; red lines from standard initial conditions, green lines from alternative conditions.

time evolves. In the region between 0 and 0.1 we clearly see the out of phase nature of the time series. But as we proceed towards the end of the considered time interval, especially in the region between 0.4 and 0.5, we clearly see the time series getting back into phase. This demonstrates that the system produces time series that are different even though the only parameters that have changed are the initial conditions; *i.e,* the dynamical system produces time series that are sensitive to initial conditions. However, we remark that although the time series are different, the overall qualitative behaviors generated by them are not very different from each other. This is good from the subgrid-scale model point of view since the end result of the discrete dynamical system is to generate temporal fluctuations.

4.3.3 Preliminary testing of CPMNS turbulence model

To test the turbulence model we made use of a data set recorded at a particular time-step of the large-scale calculations. These data were then supplied to the small-scale algorithm to generate the different parameters that are present in the CPMNS equations.

To generate the large-scale field we considered a shock tube problem. The initial conditions in the left and right sections of the tube are presented in Table 4.1 (all entries are in SI units) This set up is similar to that of Test Case 1 in that it provides a pressure ratio of 10 across the diaphragm. The boundary conditions and computational domain are the same as considered previously in Chapter II. We ran the calculations on a grid consisting of $101 \times 41 \times 41$ points in x-y-z space with a time step $\Delta t = 1 \times 10^{-6}$s. The data set that was supplied to start the small-scale calculations was recorded at a time in the large-scale calculations when the shock was well established. In particular, we generated the large-scale data set at two specific times $t = 0.61$ms and $t = 0.6$ms.

Recall that the CPMNS equation was derived from a non-dimensional form of the N.–S. equations. However, the large-scale equations are in dimensional form; hence, solutions to these equations also have dimensions associated with them. This then suggests that we

Table 4.1 Initial conditions for shock tube problem employed to test CPMNS turbulence model.

Parameters	Left	Right
Velocity	0	0
Density	1	0.125
Pressure	10000	1000
Total Energy	2.5e5	2.5e4

would have to non-dimensionlize the large-scale field in a manner consistent with that used in deriving the CPMNS equations. In particular, the density, velocity components, and temperature are scaled by "typical" values. Pressure is scaled by the equation of state and the total energy E by the square of the velocity scale. Also, in this case we chose the typical length scale to be the length of the tube. This provides sufficient information to scale both dependent and independent variables and the spatial coordinates. The scaling parameters were set to be

$$\rho_s = 2\,, U_s = 400\,, T_s = 500\,, \text{and}\,, E_s = U_s^2\,, \tag{4.49}$$

with associated units. The scaling parameters were chosen such that their magnitudes were greater than the maximum values obtained by the corresponding variables in the large-scale field.

Once we obtain the non-dimensional large-scale field the next step is to extract the high-wavenumber content from these results. The high-wavenumber content is obtained by high-pass filtering the large-scale field using the Shuman filter as described in Sec. 4.2.2. This operation corresponds to implementing the second idea in the LES approach proposed by McDonough *et al.*, *i.e.,* filter solutions not equations. Previously, we alluded to the fact that the value of the filter parameter β at the small-scale should be set to a low-value. Moreover, we should also recognize that the value of β should be related to the grid-spacing in some fashion since in our setting the grid-size determines the extent of under-resolution in the LES simulation. Hence, we should expect that the coarser the grid, the greater will be the role played by the SGS model. This relationship between the computational grid and the SGS model then demands extraction of the maximum amount of high-frequency content from the grid-scale calculation. On coarse-grid simulations like the one being performed here, the extraction of the maximum amount of high-frequency content can only be obtained by using low values of β. Moreover, we conducted numerical tests and decided that a value of 10 for the filter parameter gave reasonable results. Nevertheless, it is clear that an automatic procedure for setting the parameter value would be a significant advantage in implementing this LES procedure, but this is beyond the scope of the present work.

Computed results of DDS bifurcation parameters

The large-scale flow field inside the shock tube at $t = 0.61$ms into the calculations at which we chose to generate the data set are presented in Fig. 4.11(a) for the non-dimensional u-velocity contour. This also provides a reminder of the location of the shock front, and the general physics associated with the shock tube problem. The distribution of the high-

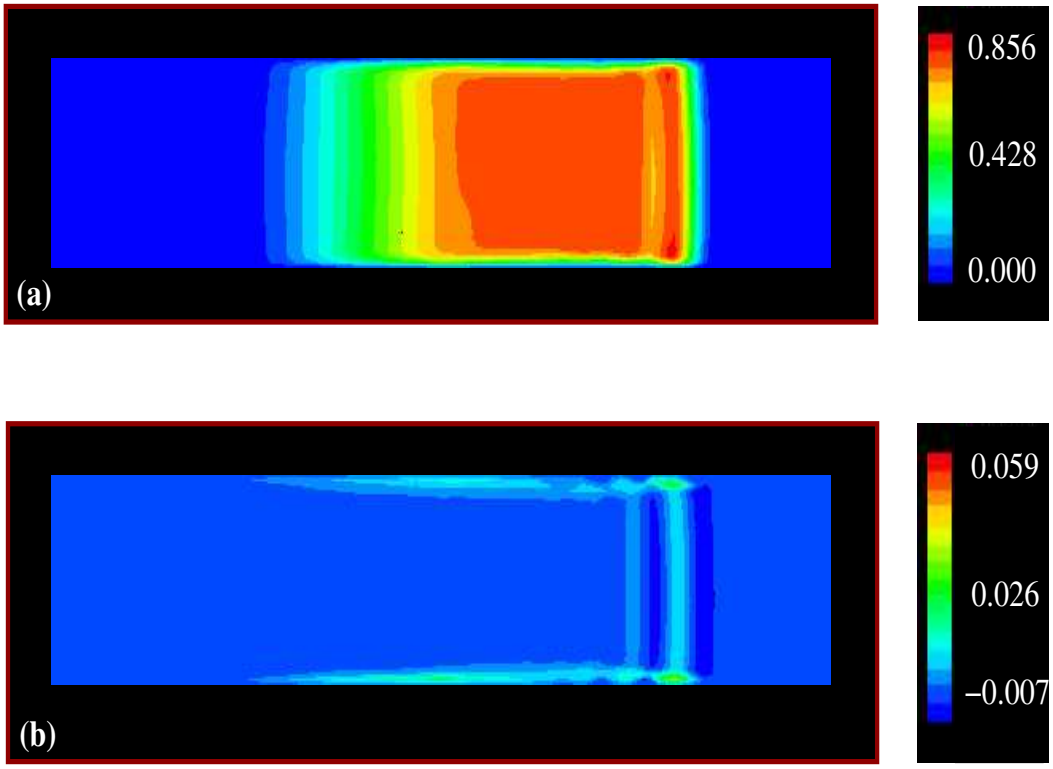

Figure 4.11 2-D contour plots of (a) u-velocity, and (b) highpass filtered u-velocity

wavenumber content of the velocity field (displayed in part(a)) is presented in part(b) of the figure. We observe that the regions near the tube walls and the shock display more high-wavenumber content than in found in the most of the remainder of the flow field. We comment that it is at these same regions that the effects of calculating on an under-resolved grid are most severe; thus the corresponding large-scale solutions will be significantly under-resolved. Hence, we would want the turbulence model to be active in these regions so that the model results can augment the under-resolved large-scale solution, and presence of high-wavenumber content in these regions is very encouraging from a modeling standpoint. However, one should expect the high-pass filtered field to be contaminated by the oscillations generated by the Gibbs phenomenon near the shock at the large-scale. Even though we are aware of this from the start, there is no *a priori* easy way to fix the problem, one would have to resort to using superior shock capturing schemes like ENO, WENO, *etc.*, to provide sharper shock-capturing with smaller overshoots and undershoots.

In Fig. 4.12 we display the distribution of the bifurcation parameters β_1, ψ_1, and γ_{21}. We have chosen to present results for β_1, ψ_1, and γ_{21} because they are associated with the horizontal component of velocity, which is the dominant flow direction in this case. In particular, β_1 is related to the grid-scale Re, ψ_1 is related to the M, and γ_{21} is related to $\partial u/\partial y$. In Figs. 4.12(a)–(c) we present results displaying the bifurcation parameters on a longitudinal plane running the length of the tube. The 2-D plane chosen to display the contours is the same plane used for the the 2-D contour plots in Chapter III (see Fig. 3.4). The distribution of the parameters within a planar cross section at a location corresponding to that of the shock front is presented in Figs. 4.12(d)–(e). We further note that the color

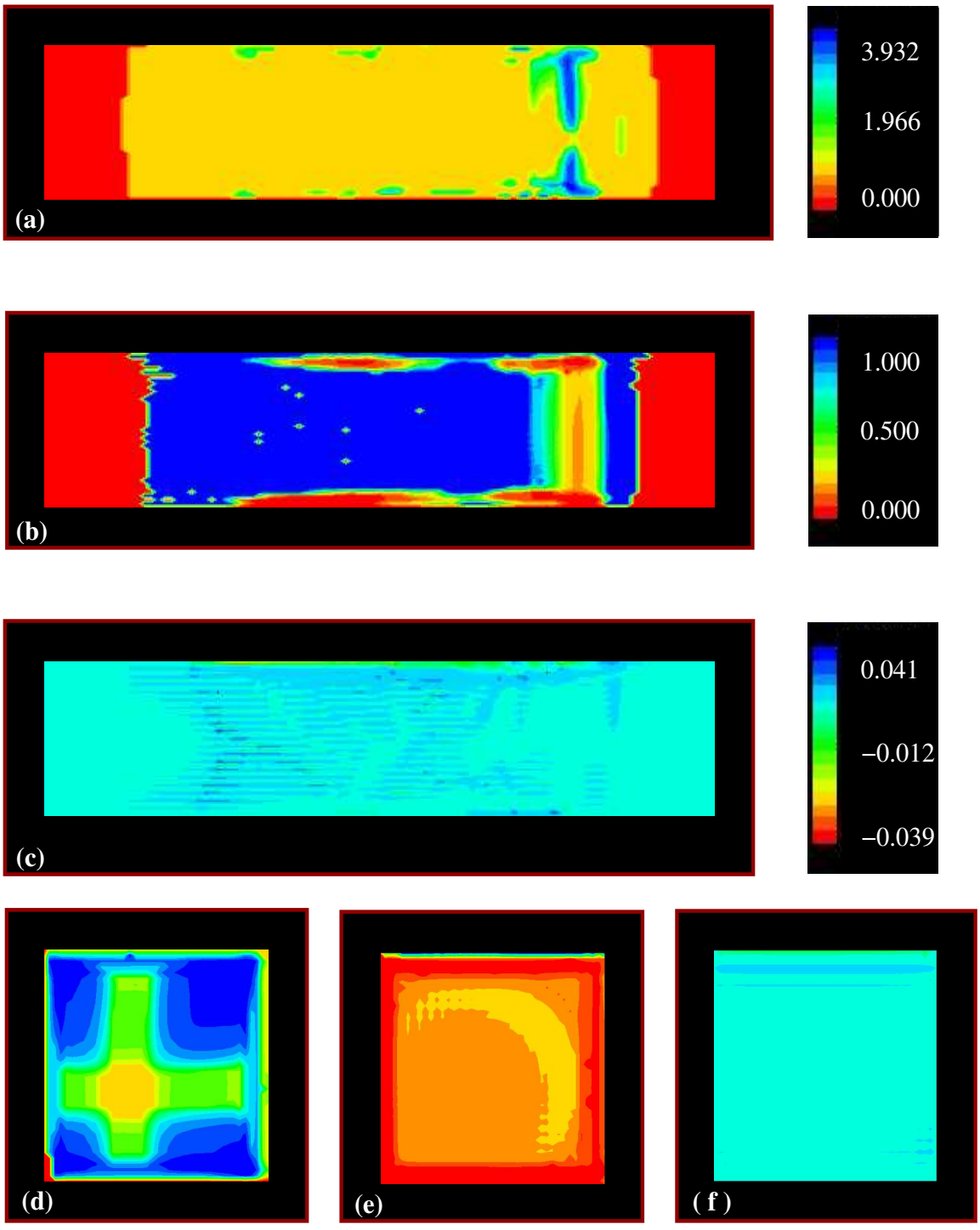

Figure 4.12 Distribution of bifurcation parameters along the length of the shock tube at $t = 0.61$ms; (a) β_1, (b) ψ_1, (c) γ_{21}. Distribution of the parameters at a cross section of the tube corresponding to the location of the shock front at $t = 0.61$ms; (d) β_1, (e) ψ_1, (f) γ_{21}.

code for this figure is inverted when compared to those used throughout this work. We chose to do this to provide better clarity for viewing results in the case of the bifurcation parameters.

Part(a) of the figure clearly shows that β_1 is zero in the quiescent regions of the domain that have not yet been passed by either the shock or rarefaction wave. We also see relatively high values of β_1 in regions near the wall and also near the position of the shock wave. Furthermore, within the region near the shock we see that β_1 is often close to its maximum value providing a high probability for chaotic, turbulent like behavior to be generated by the model. The parameter ψ_1 is also distributed in the same general way as β_1 in that the regions in the domain with activity is near the walls and the shock. Recall that the parameter ψ_1 is inversely proportional to M. In discussions on regime maps we presented results which indicated that at low values of ψ_1 the CPMNS equation displays complicated (turbulent like) behavior. From Fig. 4.12(b) we clearly see that the values of ψ_1 near the shock and near the walls are relatively lower when compared to those taken in other parts of the domain. Part(c) of the figure, on the other hand displays rather low values of γ_{21} throughout. However, we do observe that the parameter takes on a fairly wide range of values within the regions of interest, while it is constant, in fact equal to zero in the undisturbed right and left sections of the tube.

The distribution of β_1 and ψ_1 (part(d) and (e)) on the shock front suggests that there will be considerable activity from the turbulence model, especially at regions near the walls, since the value of β_1 is high and that of ψ_1 low. This scenario is interesting since it is in these regions that we would expect interaction between the shock and the boundary layer. From part(f) we notice that γ_{21} takes on constant values in most of the domain. Although this should be true in the interior since the shock is a normal shock wave taking on constant values on this plane, we should have seen some activity at near wall regions. We do see indications of this at some places but not in the others.

In Fig. 4.13 we present the distribution of the bifurcation parameters β_1, ψ_1, and γ_{21} at $t = 0.6$ms of the large-scale calculations. The figure clearly shows that the structure of the distribution of the bifurcation parameters within the length of the shock tube (parts (a)–(c)) are not very different from those obtained at $t = 0.61$ms (see Figs. 4.12(a)–(c)). This similarity is to be expected considering that only 0.01 ms has elapsed in time. We note that the although the time interval is only 0.01ms the position of the shock front will change, but only by a small distance. However, we observe that the distributions at the cross section corresponding to the location of the shock front are somewhat different (compare Figs. 4.12(d)–(f) and Figs. 4.13(d)–(f)). In particular, in Fig. 4.13(d) we see that the values of β_1 in the arms of the cross shaped region at the center of the cross section is slightly lower than that in Fig. 4.12(d). The yellow region in the middle of Fig. 4.13(e) seems to spread out as time progresses (see Fig. 4.12(e)). The distribution of γ_{21} is similar to that present at $t = 0.61$ms but the magnitude is reduced in most of the domain.

4.4 Concluding Remarks

In this chapter we outlined the construction of a novel subgrid-scale (SGS) model for an alternative approach to LES of compressible turbulence. The form of the SGS model that was proposed consists of modeling each dependent variable at the sub-grid scale as a product of two factors: i) an amplitude factor and ii) a discrete dynamical system that produces temporal fluctuations.

The amplitude factors A_i^*s were calculated locally (both in space and time) by utilizing

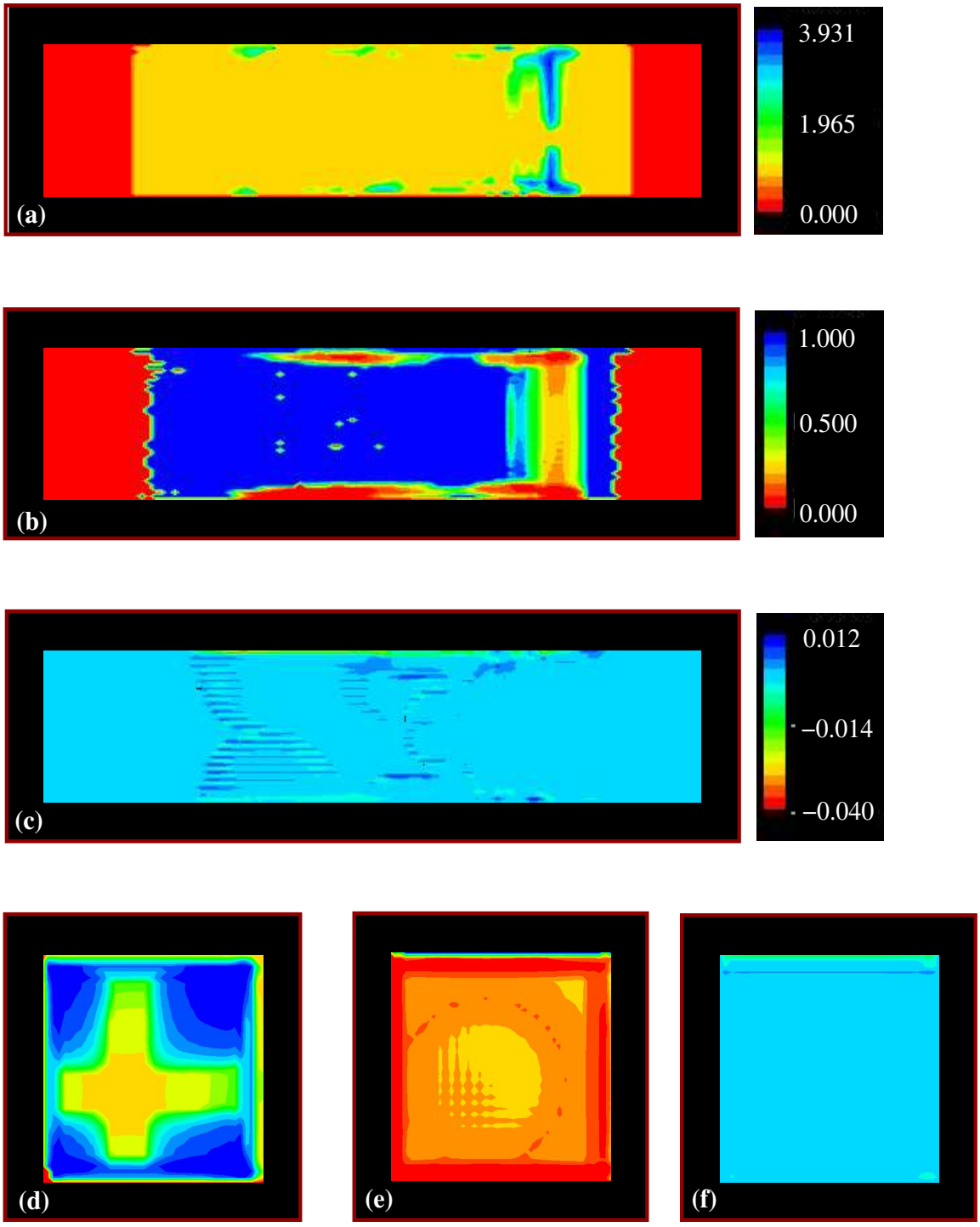

Figure 4.13 Distribution of bifurcation parameters along the length of the shock tube at $t = 0.6$ms; (a) β_1, (b) ψ_1, (c) γ_{21}. Distribution of the parameters at a cross section of the tube corresponding to the location of the shock front at $t = 0.6$ms; (d) β_1, (e) ψ_1, (f) γ_{21}.

results from an "extended" Kolmogorov's K41 theory, thus not limiting them to homogeneous, isotropic turbulence. In particular, the A_i^*s are calculated as the square-root of the total (cumulative) energy $E(\boldsymbol{k})$. $E(\boldsymbol{k})$ corresponds to the energy of all wavenumbers above

the cut-off. The cut-off is determined based on the resolution of the resolved-scale grid. Extension to non-homogeneous, nonisotropic flows was accomplished by assuming that the constant C_2 and the exponent β in the power-law representation of $E(\boldsymbol{k})$ are not constant, but instead vary in both space and time. We also described the technique employed to calculate C_2 and β at each grid-point and at each time-step of the small-scale calculations using a power-law formula derived by Kolmogorov for physical-space second-order structure functions $S_2(\ell)$.

To introduce turbulent-like fluctuations at the sub-grid scale we derived a new discrete dynamical system from the 3-D compressible N.–S. equations. The derivation, shown in fair detail for the x-momentum equation, is based on a Galerkin representation of the governing equations followed by the removal of all wavevectors except a single arbitrary one which is incorporated into the bifurcation parameters of the DDS. This DDS, which, we call the "compressible poor man's Navier–Stokes (CPMNS) equation" has a co-dimension of 35. Moreover, the bifurcation parameters were grouped into families based on their dependence on non-dimensional parameters or on velocity gradients. The derivation also provides us with formulae for the 35 bifurcation parameter values, permitting their evaluation "on the fly" at each grid point and at every time step of our LES procedure, thus overcoming the well-known "closure-problem" in turbulence simulations. This was discussed in some detail in Sec. 4.2.2

We further provided detailed characterizations of the possible behaviors that can be produced by the system via time series and power spectra. We identified 14 different types of behaviors (see Fig. 4.1 and Fig. 4.2) that the CPMNS equations are capable of producing. These different types encompass a wide range from relatively simple steady to behaviors displaying chaos. The complexity of the trajectories of the velocity components was illustrated by presenting a phase portrait of broadband with different fundamental behavior.

Employing so called "regime maps" (multi-dimensional bifurcation diagrams) we sought to provide a general overview on the dynamics of the CPMNS equations as various sets of bifurcation parameters are varied. In each 3-D regime map there were over 3 million combinations of bifurcation parameter values, and for the 2-D maps there were one million combinations at which the DDS was iterated. To determine the behavior of the system with changes in M we displayed a sequence of 2-D plots that were produced by successively decreasing the value of the associated bifurcation parameter ψ_1. As M increased the DDS displayed an increase in complexity of the behaviors it produced over the considered parameter range. This is seen clearly in the sequence of figures starting from Fig. 4.5(c) to Fig. 4.5(d). Furthermore, in Fig. 4.6 the DDS demonstrated an increase in the areas of non-divergence at increasing values of M. This is encouraging from the point of view of implementing the DDS in the SGS model since divergent turbulent fluctuations would complicate implementation. Hence, this increase in area of non-divergence provides a wider range of values that the bifurcation parameters can take on but still display interesting behavior. Moreover, the areas of divergence are typically adjacent to steady behavior, where the model would be turned off anyway. We further subjected the model to a gradual increase in strain rates. As would be expected in many physical flows, an increase in strain rate resulted in an increase in regions displaying turbulent behavior. This is evident at high β regions of Fig. 4.7. In Figs. 4.8 and 4.9 we presented regime maps constructed from bifurcation parameters associated with the continuity and energy equations, respectively. From Fig. 4.8 we observed

large increases in areas of divergence at negative values of both γ_{11} and γ_{12} at any value of β_1. This occurs because, near the regions of divergence the DDS produces complex behavior (noisy or broadband) indicating that the flow is already excited to a high degree and hence, any further increase beyond this produces divergent behavior.

The regime maps displayed in Sec. 4.3.2 also act as a visual tool for the identification of bifurcation sequences. These showed the CPMNS equation to be capable of producing both the period-doubling as well as the Ruelle–Takens–Newhouse routes to chaos. There were other routes to chaos also. Moreover, the presence of these various routes to chaos suggest that the CPMNS equation are capable of automatically transitioning to turbulence. This capability of the DDS should allow the SGS model to predict transition to turbulence without the need for separate and often *ad hoc* models for this purpose. We comment that even though the CPMNS equation is capable of predicting transition, we are still far from actually proving the accuracy of this for a given physical flow. But we believe that the ability of the CPMNS equation to produce deterministic chaos enhances its ability as a "synthetic-velocity" model for LES.

Effects of initial conditions on the DDS were studied via visualization of basins of attraction. In particular, we dealt with a specific case involving broadband with fundamental behavior. We showed that the DDS has multiple attractors even though the values of the bifurcation parameters were held constant. Making use of time series from two different sets of initial conditions we illustrated that the system is sensitive to initial conditions. We remark that even though the DDS displays SIC the time series generated by the DDS are not very different from each other in a qualitative sense. Moreover, one of the important findings in terms of implication of use of this DDS as a SGS model is the general understanding gained on the effects of initial conditions, including growth of regions of divergence at relatively high values of initial conditions.

Finally, we conducted a preliminary test of the CPMNS turbulence model by supplying it with a data set from the large-scale. A shock tube problem was employed for this purpose. Two-dimensional contour plots of the large-scale horizontal component of velocity and its corresponding high-pass filtered part were presented in Fig. 4.11. The distribution of the high-pass filtered velocity field was found to be at least qualitatively as should be expected, but one should keep in mind the contamination of this field by the Gibbs oscillations at the large-scale. Distribution of three bifurcation parameters (β_1, ψ_1 and γ_{21}) associated with the horizontal direction (dominant direction for the shock tube problem) were also displayed in Fig. 4.12.

Although the above observations could be better validated by making comparisons with experimental data, our attempts to do so have been inhibited by the lack of availability of detailed data (*e.g.* time series data) for compressible turbulence in the literature. However, the complicated parameter space structures that we have demonstrated are quite suggestive of the small-scale physics that can be reproduced by the use of the CPMNS equation. Furthermore, this provides the potential for the CPMNS equation to be used in constructing "synthetic-velocities" in the context of LES subgrid-scale models.

Chapter 5
SUMMARY AND CONCLUSIONS

Despite a tremendous expenditure of effort over the past century, the problem of turbulence is still not very well understood and remains an active area of research till the present day (and will probably remain so in the future). Advances in computing hardware towards the latter half of the 20th century provided an impetus to the development of computational approaches to turbulence. Several well-established numerical techniques are available at the present day, but large-eddy simulation (LES) is rapidly becoming the method of choice for industrial and environmental applications involving computation turbulent flows. This is witnessed by the fact that many commercial CFD code vendors are incorporating versions of LES into their software suites. However, application of LES to compressible flow have been significantly fewer owing to increased complexity (especially in 3-D) introduced by the need to solve an extra equation (for total energy), which in traditional LES would result in extra unclosed terms (correlations) that must be modeled in addition to the usual subgrid-scale stresses. Also, filtering the equations of motion in traditional LES leads to significant problems. This research effort was focused primarily on developing some of the key components for a novel three dimensional large-eddy simulation (LES) solver for compressible turbulent flow. The solver is based on a multi-scale approach and is designed to overcome most of the problems presented by traditional LES.

In the next section we will summarize the work presented in this thesis. Following this we will draw a list of conclusions from this research effort. Finally, a brief note on future work that can be undertaken based on the work conducted will be given.

5.1 Summary

1) In Chapter I, a brief introduction to turbulence was given. Included was a concise review on the history of turbulence research over the past century. We also specifically dealt with studies on compressible turbulence in brief. Furthermore, we outlined the problems that arise from filtering the governing equations as performed in traditional LES procedures. To circumvent most of the problems posed by traditional LES we proposed an alternative framework based on a multi-scale formalism. In this approach the numerous correlations that result from filtering governing equations do not occur, and thus need not be modeled. Instead, the physical variables are modeled on the small-scale utilizing a combination of Kolmogorov's theories and discrete dynamical systems.

2) In Chapter II, we presented some background information to enable the reader to understand the motivation behind this work as much as possible. In particular, relevant previous work on numerical procedures employed for turbulence simulations was presented. Included were discussions on classical techniques such as Reynolds-averaged Navier–Stokes (RANS) procedures, direct numerical simulation (DNS), and large-eddy simulation (LES). Emphasis was laid on LES, and a review on subgrid-scale modeling procedures was also presented. Two fairly recent numerical approaches, detached-eddy simulation (DES) and implicit large-eddy simulation (ILES), were also discussed. Since dynamical systems are

used in our SGS model, some background on the virtually untapped modern mathematical theory of dynamical systems and chaos was presented towards the latter half of Chapter II. Specific references (experimental and numerical) providing support to the "strange attractor theory of turbulence" were also cited. However, we noted that attempts to oversimplify turbulence by analogy with low-order dynamical systems is not entirely correct. But a subspace of fully developed turbulence, the small scales, may be effectively described locally in space and time by low-order dynamical systems without belying the complexity of fully developed turbulence. In addition we presented a brief review on a relatively new class of SGS models known as "synthetic-velocity" models, which allows one to explicitly evaluate the dependent variables on the sub-grid scale.

3) Chapter III dealt extensively with the numerical method employed to calculate the large-scale part of the solution, *i.e.,* $\boldsymbol{q}(\boldsymbol{x}, t)$. The algorithm is based on a predictor-corrector methodology. An explicit Euler method is used to solve the Euler (inviscid) equations at the predictor stage. This provides an initial guess to the corrector where the N.–S. equations are solved implicitly. Fairly standard numerical techniques such as δ-form quasilinearization and δ-form Douglas–Gunn time splitting are employed for the implicit solves. A detailed mathematical formulation and the corresponding pseudo-language algorithm were presented in Sec. 3.2. Several validation tests were performed to test the performance of the solver. In particular, the standard shock tube problem at three different initial conditions and the 3-D blast-wave problem were employed. 3-D and 2-D plots were used to describe the overall flow-field, and computed 1-D results were compared with the exact solution. Grid function convergence studies were performed for all four test cases to test the convergence of the numerical method.

4) In Chapter IV, we outlined the construction of a novel SGS model to represent the small-scale dependent variables for our LES procedure, *i.e.,* we model $\boldsymbol{q}^*(\boldsymbol{x}, t)$. The proposed model consists of modeling each dependent variable at the sub-grid scale as a product of two factors: i) an amplitude factor constructed from an extension of Kolmogorov's theories and ii) a DDS that produces temporal fluctuations. Discussions regarding the evaluation of the amplitude factors from the high-pass filtered resolved-scale solution was presented in fair detail. We also derived a new discrete dynamical system from the 3-D N.–S. equations and provided a detailed characterization of the possible behaviors produced by the system. We reported results in the form of regime maps to provide an overview on the dynamics of the CPMNS equations as various sets of bifurcation parameters were varied over ranges of stable behaviors. Effects of initial conditions on the DDS were studied via visualizations of basins of attractions for a specific case of broadband with fundamental behavior. Finally, we conducted some preliminary tests on the SGS model by qualitatively analyzing the distribution of some bifurcation parameters in the computational domain when the model was supplied with a large-scale scale data set recorded at a particular time step of the large-scale calculations.

5.2 Conclusions

In this section we will draw conclusions from results reported mainly in Chapters 3 and 4. From the validation tests conducted on the large-scale solver in Chapter 3 we learn that:

1) The inclusion of the predictor step in the large-scale algorithm weakens the stability properties of the algorithm, especially in cases involving strong shocks (*e.g.*, Test Case 3). Moreover, comparisons of total number of iterations through the full viscous N.–S. equations with and without the predictor indicated that we achieved only a 10 % decrease when the predictor is used. Even though this gives some reduction in total arithmetic, one can obtain the same (if not more) reduction by using standard code optimization procedures. These findings suggest that the predictor should not be used for the calculations.

2) Within the framework of employing artificial dissipation to capture shocks, comparisons of 1-D results with exact inviscid solutions indicate that the solver is able to resolve the shock wave and rarefaction fan with fairly reasonable accuracy.

3) Resolution of the contact discontinuity was found to be adequate for Test Case 1. However, a fair amount of smearing was seen in Test Cases 2 and 3. However, this smearing is inherent in almost all shock capturing methods, including high resolution methods, unless specific steps such as artificial compression or sub-cell resolution (see [160] for further options) are taken to combat it.

4) The solver demonstrated the ability to take into account effects of viscosity in the numerical solution. In fact, the solver was able to capture the general shape of the boundary layer for both transonic (Test Case 1) and supersonic (Test Case 2 and 3) cases, which is particularly encouraging.

5) One dimensional plots comparing computed solutions on three grids denoted as H_c, H_m, H_f—coarse, medium and fine, respectively, with the exact solution showed that the computed solution approaches the exact solution as grid-spacing is decreased, thus implying the convergence of the numerical solution at least in a qualitative sense.

6) Results from grid function convergence tests show that for Test Case 1 the convergence rate was within acceptable limits for problems whose solutions are inherently nonsmooth, *i.e.,* only $\mathcal{O}(h)$ accuracy is achieved even for formally higher-order methods (see [167] for details). However, there is a significant drop in convergence rates for Test Cases 2 and 3. This reduction is primarily caused by effects due to restrictions on number of grid points that could be employed. These effects combined with the roles played by increase in shock strength and aliasing further reduced the convergence rates.

7) Numerical results presented as 1-D and 2-D plots displayed the ability of the solver in simulating the complicated physics associated with the blast-wave problem (Test Case 4). The shock weakening effect as time evolves and the so called "suction phase," which are important features of fluid motion caused by explosions, can clearly be discerned in the plots presented.

8) The results for Test Case 4 also established the multi-dimensional capability of the solver. In particular, it was able to display the three-dimensional symmetries inherent in the solution to the blast-wave problem.

9) Grid function convergence tests for the blast-wave problem indicated that the convergence rates achieved were better than those obtained for the shock-tube problem. This increase is mainly due to fundamental differences between the physical flow scenarios in the two cases. These differences results in lower aliasing error in the blast wave problem, thus providing better convergence rates.

10) Overall, considering the performance of the solver over a wide range of test cases, we believe that the solver is reasonably accurate, robust and multi-dimensional. However, use of artificial dissipation to capture shocks implies that the numerical solution will always display oscillations due to Gibbs phenomenon. Hence, in the context of using this solver in our LES methodology one has to be judicious in analyzing the subgrid-scale results.

Probably the most significant achievement of this research was the derivation of the CPMNS equation, which provides turbulent fluctuations for the novel SGS model developed for LES of compressible turbulence. Given below is a list of conclusions drawn from analysis of the system conducted in Chapter IV:

1) The CPMNS equation can produce 14 different kinds of temporal behavior. These different types encompass a wide range from relatively simple steady to behaviors displaying chaos. The wide range of behaviors that have been identified provide a low-dimensional basis set from which practically any temporal behavior can be obtained as a linear combination.

2) The DDS also produced behaviors of increasing complexity when M, Re, or strain rate were increased. This is true for many physical flows; hence, implementation of the CPMNS equation in the SGS model should allow it to mimic the physics at the small scales. Moreover, the form of this DDS and the nature of its construction suggest that it is related to a pseudodifferential operator of the compressible N.–S. system. This relationship then implies that it carriers a significant part of the local in space and time behavior of these equations; *i.e.,* it inherently retains some of the small scale physics.

3) The CPMNS equation are capable of displaying both period-doubling and Ruelle-Takens-Newhouse (RTN) routes to chaos. Various other routes were also found. The presence of these different routes suggests that the CPMNS equation is capable of automatically transitioning to turbulence. This capability should enable the SGS model to predict transition to turbulence without separate and often *ad hoc* models which are implemented for this purpose. Even though we are far from proving the accuracy of predicting transition for a given physical flow, we believe that the ability of the CPMNS equations to produce deterministic chaos enhances the ability of the SGS model in this respect.

4) One of the important findings in terms of implications of use of the DDS in an SGS model is the general understanding gained on the effects of initial conditions on the behavior of the DDS. In particular, we found growth of regions of divergence at relatively high values of initial conditions, suggesting that such values should not be used in model implementation. In the same study we illustrated that even though the CPMNS equation displays sensitivity to initial conditions (SIC), the time series generated by the DDS are

not very different from each other in a qualitative sense. This is good from a SGS modeling standpoint since we expect the model to be driven by changes in values of the bifurcation parameters, which embody the physics of the flow.

5) Preliminary tests conducted on the SGS model showed that the distribution of the high-pass filtered velocity field was found to be at regions where the turbulence model results can augment the under-resolved large-scale solution. At the same time, one should bear in mind the contamination of the high-pass filtered field by oscillations due to Gibbs phenomenon at the large scale. The distribution of bifurcation parameters showed that there will be considerable activity near locations where we found the high-wavenumber content. But effects of these parameters on the small-scale field have not yet been studied and will be taken up in future work.

6) Even though our results could be better validated by making comparisons with experimental data, our attempts to do so have been inhibited by lack of availability of detailed experimental data (*e.g.,* time series data) for compressible turbulence in the literature. However, the complicated parameter space structures we have demonstrated is quite suggestive of the small-scale physics that can be reproduced by use of the CPMNS equation. Furthermore, this provides the potential for the CPMNS equation to be used in construction of "synthetic-velocity" forms of SGS models for LES like the one undertaken in this work.

5.3 Future work

As alluded to at the beginning of this thesis, this research effort was focused primarily on developing some of the key components for a LES solver based on a multi-scale approach to turbulent compressible flow. The results achieved at this stage of the development process are very encouraging, hence demanding immediate attention to the implementation of the complete multi-scale algorithm.

However, one should recognize that both the large-scale and small-scale parts themselves should be enhanced to increase the potential for the use of the LES solver over a wider range of flow scenarios. This would require a two-pronged approach, one dealing with including more physics, and the second with the numerical aspect, especially at the large-scale. Of interest in this regard would be the inclusion of chemistry into both the large- and small-scale algorithm, thus making the solver capable of dealing with combustion phenomena (deflagaration, detonation waves, *etc.*). The basic three-dimensional large-scale solver should be converted to generalized coordinates, so that it can incorporate complicated geometry and allow stretchable grids. Boundary conditions should also be enhanced so as to include complicated conditions such as supersonic inflows and outflows, shock reflection conditions, *etc.* The N.–S. equations should be solved in a fully-coupled manner as opposed to the present sequential approach since this would decrease CPU time and enhance robustness. Although the storage requirements are much greater for the fully-coupled approach, keeping in mind advances in computing hardware at the present day, this should not pose any problem in the future. Even though LES significantly reduces the amount of arithmetic when compared to DNS, the required arithmetic can still scale as badly as Re^2. This in turn results in very long run times; hence, the code needs to be parallelized. Preliminary investigation

into this has been undertaken in 2-D where we parallelized the large-scale algorithm using OpenMP. However, we found that the speedups obtained were sub-linear and not especially good. This lack of performance from OpenMP parallelization suggests that MPI should be used for parallelization in the future. A problem of a more serious concern is the presence of Gibbs oscillation in the large-scale solutions. We also recognize the fact that this effects the SGS model as well. In this regard use of post processing filters (*e.g.,* [166]) are probably the most promising and the simplest.

Even though some analysis was performed on the CPMNS equation in the present work, the presence of 35 bifurcation parameters made the task of obtaining appropriate limits on the values of bifurcation parameters to be used in model implementation not very thorough. Hence, more work needs to be done on the study of the CPMNS equation, itself. Moreover, with the inclusion of chemistry, which will add many corresponding equations to the CPMNS equation a detailed analysis of the system must be taken up.

BIBLIOGRAPHY

1. H. Lamb. *Hydrodynamics*, Cambridge University Press, Cambridge, 1916.

2. P. Bradshaw. Turbulence: The chief outstanding difficulty of our subject, *Exp. Fluids.,* **16**, pp. 203–216, 1994.

3. J. P. Richter. *The notes of Leonardo Da Vinci*, Dover, New York, 1989.

4. U. Frisch. *Turbulence: The legacy of A. N. Kolmogorov*, Cambridge University Press, Cambridge, 1995.

5. J. Boussinesq. Theorie de l' ècoulement Tourbillant, *Acad. Sci.,* Paris, 1877.

6. O. Reynolds. On the dynamical theory of turbulent incompressible viscous fluids and the determination of the criterion, *Phil. Trans. R. Soc. London A.,* **186**, pp. 123–161, 1894.

7. I. G. Currie. *Fundamental Mechanics of Fluids*, McGraw-Hill, New York, 1974.

8. John D. Anderson Jr., *Modern Compressible Flow*, *Third edition*, McGraw-Hill, New York, 2003.

9. Milton Van Dyke. *An album of fluid motion*, The Parabolic Press, Stanford, 1982.

10. Gary T. Chapman and M. Tobak. Observations, theoretical ideas, and modeling of turbulent flows—past, present and future, in *Theoretical Approaches to Turbulence*, Springer-Verlag, New York, pp. 19–49, 1985.

11. T. von Karman. The fundamentals of statistical theory of turbulence, *J. Aero. Sci.* **4**, pp. 131–138, 1937. Reprinted in *Centennial of Powered Flight: A Retrospective of Aerospace Research, AIAA J. Supplement,* **41**, 2003.

12. G. I. Taylor. Statistical theory of turbulence, I, II, III and IV *Proc. Roy. Soc. London A.,* **151**, pp. 421–478, 1935.

13. A. N. Kolmogorov. The local structure of turbulence in an incompressible viscous fluid at very high Reynolds numbers, *C. R. (Doklady) Akad. Nauk SSSR,* **30**, pp. 301–305, 1941. Reprinted in *Proceedings: Mathematical and Physical Sciences,* **434**, Turbulence and Stochastic Process: Kolmogorov's Ideas 50 Years On, 1991.

14. A. N. Kolmogorov. On degeneration (decay) of isotropic turbulence in an incompressible viscous fluid, *C. R. (Doklady) Akad. Nauk SSSR.,* **31**, pp. 538–540, 1941.

15. A. N. Kolmogorov. Dissipation of energy in locally isotropic turbulence, *C. R. (Doklady) Akad. Nauk SSSR,* **32**, pp. 16–18, 1941. Reprinted in *Proceedings: Mathematical and Physical Sciences.,* **434**, Turbulence and Stochastic Process: Kolmogorov's Ideas 50 Years On, 1991.

16. A. N. Kolmogorov. A refinement of previous hypotheses concerning local structure of turbulence in a viscous incompressible fluid at high Reynolds number, *J. Fluid. Mech.,* **13**, pp. 82–85, 1962.

17. A. M. Obukhov. On the distribution of energy in the spectrum of turbulent flow, *C. R. (Doklady) Akad. Nauk SSSR.,* **32**, pp. 136–139, 1941.

18. L. Prandtl. Bericht über Untersuchungen zur ausgebildeten turbulenz, *Zeitschrift für Angewandte Mathematik und Mechanik.*, **5**, pp. 136–139, 1925.

19. R. H. Kraichnan. The structure of isotropic turbulence at very high Reynolds numbers, *J. Fluid. Mech.,* **5**, pp. 497–543, 1959.

20. R. H. Kraichnan. Isotropic turbulence and inertial range structure, *Phys.of Fluids,* **8**, pp. 1728–1752, 1966.

21. A. S. Monin and A. M. Yaglom. *Statistical Fluid Mechanics: Mechanics of Turbulence*, MIT press, Cambridge, Mass., 1971.

22. A. Pouquet. Observations, theoretical ideas, and modeling of turbulent flows—Past, present and future, in *Theoretical Approaches to Turbulence*, Springer-Verlag, New York, pp. 19–49, 1985.

23. H. W. Liepmann. Aspects of the turbulence problem. *Z. Angew. Math. Phy.,* **3**, pp. 407, 1952.

24. G. B. Schubaeur and H. K. Skramstad. Laminar boundary-layer oscillations and transition on a flat plate. *NACA Report 909*, 1948.

25. Alan Townsend. *The Structure of Turbulent Flows*, Cambridge University Pres, Cambridge, 1956.

26. J. L. Lumley. The structure of inhomogeneous shear flows. *Atmospheric Turbulence and Radio Wave Propagation*, pp. 166, 1967.

27. J. L. Lumley. *Coherent Structures in Turbulence*. Academic Press, New York, 1981.

28. A. J. Grass. Structural features of turbulent flow over smooth and rough boundaries. *J. Fluid Mech.,* **50**, pp. 223–256, 1971.

29. A. Roshko. Dryden Research Lecture: Structure of turbulent shear flows: A new look. *AIAA J.,* **14**, pp. 1349–1357, 1974.

30. B. J. Cantwell. Organized motion in a turbulent flow. *Ann. Rev. Fluid Mech.,* **13**, pp. 457–515, 1981.

31. R. S. Rogallo. Numerical experiments on homogeneous turbulence. *NASA TM*-81315, 1981.

32. P. Moin and J. Kim. Numerical investigation of turbulent channel flow. *J. Fluid Mech.,* **118**, pp. 341-347, 1982.

33. A. Busemann. Compressible Flow in the Thirties. *Ann. Rev. Fluid Mech.,* **3**, pp. 1-12, 1971.

34. J. E. Moyal. The spectra of turbulence in a compressible fluid; eddy turbulence and random noise. *Math. Proc. Cambridge Philos. Soc.*, **48**, pp. 329, 1952.

35. G. F. Carrier and F. D. Carlson. On the propargation of small disturbances in a compressible fluid. *Quart. Appl. Math.,* **4**(1), pp. 1–12, 1946.

36. L. S. G. Kovàsznay. Turbulence in supersonic flow. *J. Aeronau. Sci.,* **20**(10), pp. 657–674, 1954.

37. B. T. Chu and L. S. G. Kovàsznay. Nonlinear interactions in a viscous heat conducting compressible gas. *J. Fluid. Mech.,* **3**(5), pp. 494–514, 1958.

38. S. Sarkar, G. Erlebacher, M. Y. Hussaini and H. O. Kreiss. The analysis and modeling of dilatational terms in compressible turbulence. *J. Fluid. Mech.,* **227**(5), pp. 473, 1991.

39. S. Sarkar. The pressure-dilatational correlation in compressibe flows. *Phys. of Fluids A,* **4**(12), pp. 2674–2682, 1992.

40. S. A. Orszag. Analytical theories of turbulence. *J. Fluid. Mech.,* **41**, pp. 363–386, 1970.

41. F. Bataille, Ye Zhou and Jean-Pierre Bertoglio. Energy transfer and triadic interactions in compressible turbulence. *ICASE Report.*, 1997.

42. P. Bradshaw. Compressible Turbulent Shear Layers. *Ann. Rev. Fluid. Mech.,* **9**, pp. 33–54, 1977.

43. M. V. Morkovin. *Studies in turbulence.* Mach number effects on free and wall turbulent structures in light of instability flow interactions., pp. 269–284, 1992.

44. Eric F. Spina, Alexander J. Smits and Stephen K. Robinson. The physics of supersonic turbulent boundary layers. *Ann. Rev. Fluid. Mech.,* **26**, pp. 287–19, 1994.

45. J. E. Green. Interactions between shock waves and turbulent boundary layers. *Prog. Aerosp. Sci.,* **11**, pp. 235–340, 1970.

46. T. C. Adamson, Jr. and A. F. Messiter. Analysis of two-dimensional interactions between shock waves and boundary layers. *Ann. Rev. Fluid. Mech.,* **12**, pp. 103–138, 1980.

47. Sanjiva. K. Lele. Compressibility effects on turbulence. *Ann. Rev. Fluid. Mech.,* **26**, pp. 211–254, 1994.

48. Ugo Piomelli. Large-eddy and Direct simulation of turbulent flows. in *e confèrence de la sociètè canadienne de CFD*, 2001.

49. J. M. McDonough. On intrinsic errors in turbulence models based on Reynolds–averaged Navier–Stokes equations. *Int. J. Fluid. Mech. Res.,* **22**, pp. 27–55, 1995.

50. Marcel Lesieur and Olivier Mètais. New trends in large-eddy simulations of turbulence. *Ann. Rev. Fluid. Mech.*, **25**, pp. 45–82, 1996.

51. Charles Meneveau and Joseph Katz. Scale-invariance and turbulence models for large-eddy simulation. *Ann. Rev. Fluid. Mech.,* **32**, pp. 1–32, 2000.

52. Ugo Piomelli. Large-Eddy Simulations: achievements and challenges. *Prog. Aerosp. Sci.* **35**, pp. 361–376, 2000.

53. M. Pino Martin, Ugo Piomelli, and Graham. V. Chandler. Subgrid-scale models for compressible large-eddy simulations. *Theoret. Comput. Fluid Dynamics.,* **13**, pp. 361–376, 2000.

54. J. A. Domaradzki and N. A. Adams. Direct modeling of subgrid scales of turbulence in large-eddy simulations. *J. Turbulence.,* **3**, pp. 1–19, 2002.

55. A. M. Guzmàn and C. H. Amon. Transition to chaos in converging-diverging channel flows: Ruelle-Takens-Newhouse scenario. *Phys. of Fluids,* **6**, pp. 1994–2002.

56. T. H. Pulliman and J. A. Vastano. Transition to chaos in open unforced 2-D flow. *J. Comput. Phys.,* **105**, pp. 133–149.

57. J. P. Gollub and S. V. Benson. Many routes to turbulent convection. *J. Fluid. Mech.,* **10**, pp. 449–470, 1980.

58. P. Wulf, C. Egbers,and J. H. Rath. Routes to chaos in wide-gap spherical Couette flow. *Phy. of. Fluids,* **11**, pp. 1359–1372, 1999.

59. John Guckenheimer. Strange attractor in fluids. *Ann. Rev. Fluid. Mech.,* **18**, pp. 15-31, 1986.

60. T. Bohr, M. H. Jensen, G. Paladin and A. Vulpiani. *Dynamical systems approach to turbulence.* Cambridge University Press, Cambridge, 1999.

61. D. Ruelle and F. Takens. On the nature of turbulence. *Commun. Math. Phys.,* **20**, pp. 167–192, 1971.

62. J. M. McDonough, Y. Yang and E. C. Hylin. Modeling time-dependent turbulent flow over a backward- facing step via additive turbulent decomposition and chaotic maps. *Proc. First Asian Conf. on Computational Fluid Dynamics.* eds. W. H. Hui, Y. K. Kwok and J. R. Chasnov, Hong Kong University of Science and Technology, Hong Kong, pp. 747–752, 1995.

63. J. Douglas, Jr. and J. E. Gunn. A general formulation of alternating direction implicit methods, part 1. parabolic and hyperbolic problems, *Numer. Math.,* **6**, pp. 428–453, 1964.

64. G. A. Sod. A survey of several finite difference methods for systems of nonlinear hyperbolic conservation laws, *J. Comput. Phys.,* **27**, pp. 1–31, 1978.

65. E. F. Toro. *Riemann solvers and numerical methods for fluid dynamics*, Springer, Berlin, 1999

66. A. Favre. Equations des Gaz Turbulents Compressibles. *Journal de Mecanique.,* **4**(3), pp. 361–390, 1965.

67. David C. Wilcox. *Turbulence Modeling for CFD*, DCW Industries, La Canada, 1993.

68. Charles. G. Speziale. Analytical methods for the development of Reynolds-Stress closures in turbulence. *Annu. Rev. Fluid. Mech.,*, **23**, pp. 107–157, 1991.

69. B. S. Baldwin and H. Lomax. Thin-layer approximation and algebraic model for separated turbulent flows. *AIAA paper.*, Huntsville, AL., pp. 257, 1978.

70. P. R. Spalart, and S. R. Allmaras. A one-equation turbulence model for aerodynamic flows. *AIAA paper no. 92-0439.*, 1992.

71. W. P. Jones and B. E. Launder. The prediction of laminarization with a two-equation model of turbulence. *Int. J. Heat and Mass Transfer.,* **15**, pp. 301–314, 1972.

72. M. W. Rubesin. Extra compressibility terms for Favre-averaged two-equation models of inhomogeneous turbulence. *NASA CR 177556.*

73. O. Zeman. Dilatation dissipation: the concept and application in modeling compressible mixing layers. *Phys. Fluids A.,* **2**, pp. 178–188, 1990.

74. S. Barre, J. P. Bonnet, T. B. Gatski, and N. D. Sandham. Compressible, high speed flows. *Closure Strategies for turbulent and transitional flows.* Cambridge University Press, Cambridge, pp. 522–581, 2002.

75. T. A. Zang, R. B. Dahlburg and J. P. Dahlburg. Direct and large-eddy simulation of three-dimensional compressible Navier–Stokes turbulence. *Phys. Fluids A,* **4**(1), pp. 127–140, 1991.

76. S. A. Orszag and G. S. Patterson. Numerical simulation of three-dimensional homogeneous isotropic turbulence. *Phys. Rev. Lett.,* **28**, pp. 76–79, 1972.

77. W. J. Feiereisen, W. C. Reynolds, and J. H. Ferziger. Numerical simulation of a compressible, homogeneous turbulent shear flow. *Rep. TF-13, Thermosci. Div., Dept. Mech. Eng., Stanford.,* 1981.

78. S. Lee, S. K. Lele and P. Moin. Eddy-shocklets in decaying compressible turbulence. *Phys. Rev. Lett.,* **3**, pp. 657–664, 1991.

79. R. Samtaney, D. I. Pullin, and B. Kosovič. Direct numerical simulation of decaying compressible turbulence and shocklet statistics. *Phys. Rev. Lett.,* **13**(5), pp. 1415–1430, 2001.

80. J. B. Freund, S. K. Lele, and P. Moin. Compressibility effects in a turbulent annular mixing layer. Part 1. Turbulence and growth rate. *J. Fluid. Mech.,* **421**, pp. 229–267, 2000.

81. C. Pantano and S. Sarkar. A study of compressibility effects in high-speed turbulent shear layer using direct simulation. *J. Fluid. Mech.,* **451**, pp. 329–371, 2002.

82. P. Moin and K. Mahesh. Direct Numerical Simulation: A tool in turbulence research. *Annu. Rev. Fluid Mech.,* **30**, pp. 539–578, 1998.

83. J. R. Ristorcelli and G. A. Blaisdell. Consistent initial conditions for the DNS of compressible turbulence. *ICASE Report TR-96-49.*, 1996.

84. A. Leonard. Energy cascade in large-eddy simulations of turbulent fluid flows. *Adv. Geophys. A,* **18**, pp. 237–248, 1974.

85. U. Piomelli. Large-eddy simulation: Achievements and challenges. *Prog. Aerospace. Sci.,* **35**, pp. 335–362, 1999.

86. J. Smagorinsky. General circulation experiments with primitive equations. I. *Mon. Weather Rev.,* **91**, pp. 99–164, 1963.

87. D. K. Lilly. The representation of small-scale turbulence in numerical simulation experiments. *Proc. IBM Scientific Computing Symposium on Environment Sciences.* Yorktown Heights, N. Y., pp. 195, 1967.

88. J. W. Deardoff. A numerical study of three-dimensional turbulent channel flow at large Reynolds numbers. *J. Fluid Mech.,* **41**, pp. 453, 1970.

89. A. Yoshizawa. Statistical theory for compressible turbulent shear flows, with application to subgrid modeling. *Phys. Fluids A,* **29**, pp. 2152–2164, 1986.

90. P. Moin, K. Squires, W. H. Cabot, and S. Lee. A dynamic subgrid-scale model for compressible turbulence and scalar transport. *Phys. Fluids A,* **3**, pp. 2746–2757, 1991.

91. M. Germano, U. Piomelli, P. Moin, and W. Cabot. A dynamic subgrid-scale eddy-viscosity model. *Phys. Fluids A,* **3**(7), pp. 1760–1765, 1991.

92. D. K. Lilly. A proposed modification of the Germano subgrid-scale closure method. *Phy. Fluids A,* **4**, pp. 633–635, 1992.

93. P. Sagaut. *Large Eddy Simulations for Incompressible Flows.*, Springer, Berlin, 2001.

94. J. Bardina, J. H. Ferziger, and W. C. Reynolds. Improved subgrid-scale models for large eddy simulation. *AIAA paper 80-1357*, 1980.

95. C. G. Speziale, G. Erlebacher, T. A. Zang, and M. Y. Hussaini. The subgrid-scale modeling of compressible turbulence. *Phy. Fluids A,* **31**, pp. 940–942, 1988.

96. G. Erlebacher, M. Y. Hussaini, C. G. Speziale, and T. A. Zang. Toward the large-eddy simulation of compressible turbulent flows. *J. Fluid Mech.,* **238**, pp. 155–185, 1992.

97. T. A. Zang, R. B. Dahlburg, and J. P. Dahlburg. Direct and large-eddy simulation of three-dimensional compressible Navier–Stokes turbulence. *Phy. Fluids A,***4**, pp. 127–140, 1992.

98. P. R. Spalart, W. H. Jou, M. Strelets, and S. R. Allmaras. Comments on the feasibility of LES for wings, and on a hybrid RANS/LES approach. *1st AFOSR Int. Conf. on DNS/LES*, Aug. 4-8, 1997.

99. P. R. Spalart. Strategies for turbulence modeling and simulations. *Int. J. Heat Fluid Flow,* **21**, pp. 252–263, 2000.

100. M. Shur, M. Strelets, L. Zaikov, A. Gulyaev, V. Kozlov, and A. Secundov. Comparative numerical testing of one- and two-equation turbulence models for flow with separation and reattachment. *AIAA paper no. 95-0863.*, 1995.

101. M. Strelets. Detached eddy simulation of massively separated flows. *AIAA paper no. 2001-0879.*, 2001.

102. F. R. Menter. Improved two -equation $k-\omega$ turbulence models for aerodynamic flows. *NASA-TM-103975.*, 1992.

103. F. R. Menter. Two-equation eddy-viscosity turbulence models for aerodynamic flows. . *AIAA J.*, **32**(8), pp. 1598–1605., 1992.

104. Y. B. Suzen, and K. A. Hoffmann. Investigation of supersonic jet flows by one- and two-equation turbulence models. *AIAA paper no. 98-0322*, 1998.

105. G. S. Constantinescu, and K. D. Squires. LES and DES investigations of turbulent flow over a sphere. *AIAA paper no. 2000-0540.*, 2000.

106. J. R. Forsythe, K. A. Hoffmamm, and F. F. Dieteker. Detached eddy simulation of a supersonic axisymmetric base flow with an unstructured solver. *AIAA paper no. 2000-2410.*, 2000.

107. Fedderik van der Bos and Bernand J. Geurts. Commutator errors in the filtering approach to large-eddy simulation. *Phy. of. Fluids,* **17** (3), pp. 2005.

108. A. Harten. High resolution methods for hyperbolic conservation laws. *J. Comput. Phys.,* **49**, pp. 357-393, 1983.

109. W. C. Reynolds. *Whither Turbulence? Turbulence at the crossroads*, ed. J. L. Lumely, Lecture Notes in Physics 357, Springer, Berlin, 1990.

110. J. P. Boris, F. F. Grinstein, E. S. Oran, and R. L. Kolbe. New insights into large-eddy simulation. *Fluid Dyn. Res.,* **10**, pp. 199–228, 1992.

111. J. P. Boris, and D. L. Book. Flux corrected transport. I. SHASTA, a fluid traansport algorithm that works. *J. Comput. Physics.,* **11**(1), pp. 38–69, 1973.

112. P. Colella, and P. R. Woodward. The piecewise parabolic method (PPM) for gas dynamical simulations. *J. Comput. Phys.,* **54**, pp. 174–201, 1984.

113. D. Drikakis. Advances in turbulent flow computations using high-resolution methods. *Progress Aero. Sci.,* **39**, pp. 405–424, 2003.

114. E. N. Lorenz. Deterministic nonperiodic flow. *J. Atmos. Sci.,* **20**, pp. 130–141, 1963.

115. H. Poincaré. *Les Methodes Nouvelles de la Mechanique Celeste. Vol. I and II.* Gauthier-Villars, Paris, 1897.

116. D. Aubin and A. D. Dalmedico. Writing the history of dynamical systems: *Longue durée* and revolution, discipline, and culture. *Historia Mathematica*, **29**, pp. 273–339, 2002.

117. L. D. Landau. Turbulence. *Akad. Nauk SSSR.,* **44**, pp. 339–342, 1944.

118. E. Hopf. A mathematical example displaying the feature of turbulence. *Commun. Pure Appl. Math.,* **1**, pp. 303–322, 1948.

119. L. D. Landau and E. M. Lifshitz. *Fluid Mechanics*, Pergamon, Oxford, 1959.

120. H. L. Swinney, and J. P. Gollub. The transition to turbulence. *Physics Today.,* **31**(8), pp. 41–49, 1978.

121. P. R. Fenstermacher, H. L. Swinney, and J. P. Gollub. Dynamical instabilities and the transition to chaotic Taylor-vortex flow. *J. Fluid Mech.,*, **94**(1), pp. 103–128, 1979.

122. M. J. Feigenbaum. The onset spectrum of turbulence. *Phys. Lett. A*, **35**, pp. 375-378, 1979.

123. Y. Pomeau and P. Manneville. Intermittent transition to turbulence in dissipative dynamical systems. *Commun. Math. Phys.,* **74**, pp. 189-197, 1980.

124. K. T. Alligood, J. A. Yorke, and T. D Sauer. *Chaos, an introduction to dynamical systems*, Springer, Berlin, 1996.

125. N. Aubry, P. Holmes, J. L. Lumley, and E. Sone. The dynamics of coherent structures in wall region of a turbulent boundary layer. *J. Fluid Mech.,* **192**, pp. 115–173, 1988.

126. J. M. McDonough, R. J. Bywater, and J. C. Buell. An investigation into strange attractor theory and small-scale turbulence. *AIAA paper no. 84-1674*, **24**, 1984.

127. J. M. McDonough and R. J. Bywater. Large-scale effects on local small-scale chaotic solutions to Burger's equation. *AIAA J.*, **24**, pp. 1924–1930, 1986.

128. J. A. Domaradzki and N. A. Adams. Direct modeling of subgrid-scales of turbulence in large-eddy simulations. *J. of Turbulence*, **3**, pp. 1–19, 2002.

129. A. Scotti and C. Meneveau. A fractal model for large-eddy simulation of turbulent flow. *Physica D*, bf 127, pp. 198–232, 1999.

130. A. R. Kerstein, W. T. Ashurst, S. Wunsch, and V. Nilsen. One-dimensional turbulence: vector formulation and application to free shear flows. *J. Fluid Mech.,* **447**, pp. 85–109, 2001.

131. A. R. Kerstein. One-dimensional turbulence: Model formulation and application to homogeneous turbulence, shear flows, and buoyant stratified flows. *J. Fluid Mech.,*, **392**, pp. 277–334, 1999.

132. J. A. Domaradzki and E. M. Saiki. A subgrid-scale model based on estimation of unresolved scales of turbulence. *Phys. of Fluids*, **13**, pp. 3510–3512, 1997.

133. J. A. Domaradzki and K. C. Loh. The subgrid-scale estimation model in physical space representation. *Phys. of Fluids*, **11**, pp. 2330–2342, 1999.

134. P. D. Lax. Weak solutions of nonlinear hyperbolic equations and their numerical computation. *Comm. Pure and Applied Mathematics,* **7**, pp. 159–193.

135. John D. Anderson Jr., *Computational Fluid Dynamics: The Basics with Application*, McGraw-Hill, New York, 1995.

136. G. Moretti. Computation of flows with shocks. *Ann. Rev. Fluid Mech.,* **19**, pp. 313–317, 1987.

137. C. Hirsch. *Numerical Computation of Internal and External Flows,* Vol. 2: Computation methods for inviscid and viscous flows, John Wiley and Sons, New York, 1984.

138. D. Gottlieb and Chi-Wang Shu. On the Gibbs phenomenon and its resolution. *SIAM Rev.,* **39**(4), pp. 644–668, 1997.

139. J. Von Neumann and R. D. Richtmyer. A method for the numerical calculations of hydrodynamical shocks. *Journal Mathematical Physics,* 21, 1950.

140. R. Courant, E. Isaacson and M. Reeves. On the solution of nonlinear hyperbolic differential equations by finite difference schemes. *Comm. Pure and Applied Mathematics,* **5**, pp. 243–255, 1952.

141. S. K. Godunov. A difference scheme for numerical computation of discontinuos solution of hydrodynamic equations. *Math. Sbornik,* **47**, 271-306 (in Russian). Translated US Joint Publ. Res. Service, *JPRS 7226*, 1969.

142. S. K. Godunov, A. Zabrodine, M. Ivanov, A. Kraiko, and G. Prokopov. *Resolution Numerique des Problems Multidimensionnels de la Dynamique des Gaz.,* Moscow, USSR: Editions MIR.

143. B. van Leer. Towards the ultimate conservative difference scheme, V. A second-order sequel to Godunov's method. *J. Comput. Phys.,* **32**, pp. 101–136, 1979.

144. Maurice Holt. Review of Godonov Methods. *ICASE Report No. 96-25*, 1996.

145. P. L. Roe. The use of the Riemann problem in finite difference schemes. *Lecture Notes in Physics.,* **141**, pp. 354–359, Berlin: Springer-Verlag, 1981.

146. S. Osher. Numerical solution of singular perturbation problems and hyperbolic systems of conservation laws. In O. Axelsson *et al.* (eds), *Mathematical Studies*, **47**, Amsterdam, Holland, 1981.

147. S. Osher and F. Solomon. Upwind difference schemes and boundary conditions with applications to Euler equations in general coordinates. *J. Compt. Phys.,* **50**, pp. 447–481, 1982.

148. J. L. Steger and R. F. Warming. Flux vector splitting of the inviscid gasdynamics equations with application to finite-difference methods. *J. Compt. Phys.,* **40**, pp. 263–293.

149. P. L. Roe. Characteristic-based schemes for the Euler equations. *Annu. Rev. Fluid Mech.,* **18**, pp. 337–365, 1986.

150. S. Osher and S. Chakravarthy. High resolution schemes and the entropy condition. *SIAM J. Numerical Anal.,* **21**, pp. 955–984.

151. A. Harten and S. Osher. Uniformaly high-order accurate non-oscillatory schemes. *Appl. Numer. Math.,* **2**, pp. 347–377, 1987.

152. A. Harten, S. Osher, B. Engquist and S. Chakravarthy. Uniformaly high-order accurate essentially non-oscillatory schemes III. *J. Compt. Phys.,* **71**, pp. 231–303.

153. C. W. Shu and S. Osher. Efficient implementation of ENO shock-capturing schemes. *J. Comput. Phys.,* **77**, pp. 439–447, 1988.

154. C. W. Shu and S. Osher. Efficient implementation of ENO shock-capturing schemes II. *J. Comput. Phys.,* **83**, pp. 32–78, 1989.

155. C. W. Shu, T. A. Zang, G. Erlebacher, D. Whitaker and S. Osher. High-order ENO schemes applied to two- and three-dimensional compressible flow. *Appl. Numer. Math.,* **9**, pp. 45–71, 1992.

156. X. D. Liu, S. Osher, T. Chan. Weighted essentially non-oscillatory schemes. *J. Comput. Phys.,* **115**, pp. 200–212, 1994.

157. R. W. MacCormack. A numerical method for solving the equations of compressible viscous flows. *AIAA Paper no. 81-0110*, 1981.

158. B. A. Fryxell, P. R. Woodward, P. Colella, and K. H. Winkler. An implicit-explicit hybrid method for Lagrangian hydrodynamics, *J. Comput. Phys.,* **63**, 283–318, 1986.

159. Wenglong Dai and Paul Woodward. Iterative implementation of an implicit-explicit hybrid scheme for hydrodynamics, *J. Comput. Phys.,* **124**, pp. 217–229, 1996.

160. C. B. Laney. *Computational Gas Dynamics*, Cambridge University Press, Cambridge, 1998.

161. L. V. Kantorovitch and G. P. Akilov. *Functional Analysis*, Pergamon Press, Oxford, 1982.

162. R. E. Bellman and R. E. Kalaba. *Quasilinearization and Nonlinear Boundary-value problems*, American Elsevier Oublishing Co., Inc., New York, 1965.

163. F. G. Shuman. Numerical methods in weather prediction: smoothing and filtering, *Mon. Weath. Rev.*, **85**, pp. 357–361, 1957.

164. R. Shapiro. Smoothing, filtering and boundary effects, *Rev. Geophys. and Space Phys.*, **8**, pp. 359–387, 1970.

165. T. Yang and J. M. McDonough. Solution filtering technique for solving Burger's equation, Special issue *Discrete and Continuous Dynamical Systems*, 2003.

166. T. Chan, S. Osher and J. Shen. The digital TV filter and nonlinear denoising, *IEEE Trans. Image Process.*, **10**, 2001.

167. Bjorn Engquist and Björn Sjögreen. The convergence rate of finitie difference schemes in the presence of shocks, UCLA Report. 2001.

168. R. Courant and K. O. Friedrichs. *Supersonic flows and shock waves*, Springer-Verlag, New York, unchanged reprint of original 1948 first edition, 1991.

169. E. C. Hylin and J. M. McDonough. Chaotic map models for the small-scale quantities in additive turbulent decomposition of the Navier-Stokes equations. Part1, Theory. *Mech. Engg. Report, CFD-01-94.,* University of Kentucky, Lexington, KY, 1994.

170. R. M. May. Simple mathematical models with very complicated dynamics. *Nature.,* **261**, pp. 459–467, 1976.

171. J. M. McDonough, V. E. Garzon and D. E. Schulte. Effect of film-cooling hole locationon turbulator heat transfer enhancement in turbine blade internal air-cooling circuits. Presented at *ASME TURBO EXPO.,* Indianapolis, IN, 1999.

172. J. M. McDonough and M. T. Huang. A low-dimensional model of turbulence-chemical kinetics interactions, *Proc. Third Int. Symp. on scale modeling.,* Nagoya, Japan, 2000.

173. J. M. McDonough and M. T. Huang. A 'poorman's Navier–Stokes equation:' Derivation and numerical experiments–the 2-D case. *Int. J. Numer. Meth. Fluids,* **44**, pp. 545–578, 2004.

174. S. A. Bible and J. M. McDonough. Basins of attraction of the two-dimensional 'poorman's Navier–Stokes equation,.' *Int. J. Bifur. Chaos,* **14**, pp. 2381–2386, 2004.

175. J. M. McDonough, S. A. Bible, and J. Scoville. Response to strain-rate in a discrete dynamical system model of the high-wavenumber Navier-Stokes equation. *J. Turbulence.,* **4**(31), 2003.

176. J. M. McDonough and D. L. Joyce. A discrete dynamical system model of turbulent convection. *AIAA paper.,* 8'th AIAA Thermophysics and Heat Transfer Conference, St. Louis, Missouri, 2002.

177. J. M. McDonough, A 'synthetic scalar' subgrid-scale model for large-eddy simulation of turbulent combustion, *Proc. 2002 Spring Tech. Mtg. Central States Sec.*, Combustion Inst., Knoxville, TN.

178. J. M. McDonough and J. C. Holloway. An alternative approach to subgrid-scale modeling of LES of turbulent combustion. *Proc. of Third Joint Meeting of the U.S. Sections of the Combust. Inst.,* The University of Illinois at Chicago, IL, 2003.

179. Z. Warhaft. Passive scalars in turbulent flows. *Annu. Rev. Fluid Mech.,* **32**, 2000.

VITA

Chetan Babu Velkur was born November 25, 1981 in Chittoor (A. P), India. He received a bachelors' degree from Visweshwariah Technological University, Karnataka, India in July of 2003. Currently he is completing work on a Masters degree in the Department of Mechanical Engineering at the University of Kentucky.

Professional Positions Held

Engineer, July 2003 - July 2004

Harita Infoserve Limited

Predictive Enginnering Practice, Bangalore, Karnataka, India.

Research Assistant, Spring 2005 - Spring 2006

Advanced Computational Fluid Dynamics Group

Department of Mechanical Engineering, University of Kentucky, Lexington, KY.

Scholastic Honors

Kentucky Graduate Scholarship, Fall 2004 - Fall 2006

University of Kentucky, Lexington, KY.

Professional Society Membership

American Physical Society

Papers and Conferences

1. C. B. Velkur and J. M. McDonough, "A parallel 2-D explicit-implicit compressible flow solver," 2006 Parallel CFD Conference, Busan, Korea, May 2006.

2. C. B. Velkur and J. M. McDonough, "A synthetic-velocity based subgrid-scale model for LES of compressible flow," Dayton-Cincinnati Aerospace Science Symposium, Dayton, OH, March 2006.

3. C. B. Velkur and J. M. McDonough, "A compressible 'poor man's Navier–Stokes equation' discrete dynamical system," 50th Annual Division of Fluid Dynamics meeting of the APS, Chicago, IL, November 2004.

4. C. B. Velkur and J. M. McDonough, "Application of discrete dynamical systems to compressible flow turbulence modeling," Dayton-Cincinnati Aerospace Science Symposium, Dayton, OH, March 2005.

Undergraduate Projects

1. Study and comparison of flow solves based on kinetic upwind methods [KFVS and PVU] for inviscid compressible flow, Indian Institute of Science, June 2003.